ORGANIC MOLECULES ON DIAMOND (001):
A SYNCHROTRON STUDY

QI DONGCHEN

(B. Sc, PEKING UNIV)

A THESIS SUBMITTED

FOR THE DEGREE OF DOCTOR OF PHILOSOPHY

DEPARTMENT OF PHYSICS

NATIONAL UNIVERSITY OF SINGAPORE

(2009)

DEDICATION

To my beloved wife and parents

ACKNOLEDGEMENTS

I would like to take this opportunity to acknowledge all the help, supports, discussions, and encouragements I have received while working on my thesis.

First and foremost, I would like to express my deepest gratitude to my supervisor Prof. Andrew T. S. Wee for his constant support, help and guidance over the past five years. Despite his busy schedule as the head of Physics department and then dean of Science faculty, he always managed to squeeze out time to discuss with me my research progress and give me valuable suggestions on experiments. He also reviewed and revised all my manuscripts word by word with greatest diligence. I also want to thank Prof. Wee for providing me research assistantship when my scholarship ended.

I am also indebted to my co-supervisor Dr. Gao Xingyu, who led me into the fantastic world of surface science and synchrotron radiation with his expertise, enthusiasm and great patience. He is the key person who builds and maintains the experimental endstation where my thesis work had been done. This thesis could not have come to fruition without his assistance and hard work. We almost spent everyday together over the last five years, and his great sense of humor makes everyday life enjoyable.

Certainly, none of the experiments discussed in this thesis would have been possible if without the diamond samples kindly provided by Dr. Loh Kian Ping in Chemistry department, who is the world-class expert in diamond society with profound knowledge and expertise. Although he is not my direct supervisor, he spared no efforts to instruct and advise on my research projects.

I am also grateful to Dr. Wang Li and Dr. Chen Wei for many useful discussions. Being experienced in synchrotron-based spectroscopies and molecular electronics, they give me a lot of suggestions and assistance on my research projects. In particular, an important part of my thesis work was originally inspired by Dr. Chen Wei's idea and supported by him with organic molecule sources.

I would like to thank Dr. Liu Lei for his help in conducting the DFT calculations for my research work. His work is indispensable to make the results consistent and convincing. I also want to express special thanks to Mr. Wong who has managed and organized our surface science lab so well that we can concentrate completely on research.

I am indebted to my colleagues and best friends, Mr. Chen Shi and Mr. Zheng Yi, for their constant help and discussions. We are the best partners in research and the best buddies in life. The badminton games we regularly played together were such a great time.

On personal levels, I am grateful to my parents for all their supports and love throughout my academic endeavors. Their love and supports are the impetus that drives me to work harder and stick to my goals. Finally, I offer my earnest thanks to my wife Amy, who has been such a great life companion walking besides me over the last two and half a year. I could not imagine what my life would be without her selfless care and love.

LIST OF PUBLICATIONS

(In relation with this thesis)

- *Tailoring the Electron Affinity and Electron Emission of Diamond (100) 2 × 1 by Surface Functionalization Using an Organic Semiconductor*
  Dongchen Qi, Xingyu Gao, Li Wang, Shi Chen, Kian Ping Loh, Andrew T. S. Wee
  CHEMISTRY OF MATERIALS, **20**, 6871 (2008)

- *Surface Transfer Doping of Diamond (100) by Tetrafluorotetracyanoquinodi-methane*
  Dongchen Qi, Wei Chen, Xingyu Gao, Li Wang, Shi Chen, Kian Ping Loh, Andrew T. S. Wee
  JOURNAL OF THE AMERICAN CHEMICAL SOCIETY, **129,** 8084 (2007)

- *Tuning the electron affinity and secondary electron emission of diamond (100) surface by Diels-Alder reaction*
  Dongchen Qi, Lei Liu, Xingyu Gao, Ti Ouyang, Shi Chen, Kian Ping Loh, Andrew T. S. Wee
  LANGMUIR, **23**, 9722 (2007)

- *Copper Phthalocyanine on Hydrogenated and Bare Diamond (001) 2×1: Influence of Interfacial Interactions on Molecular Orientations*
  Dongchen Qi, Jiatao Sun, Xingyu Gao, Li Wang, Shi Chen, Kian Ping Loh, Andrew T. S. Wee
  LANGMUIR, *submitted* (2009)

- *Surface transfer doping of diamond by organic molecules: a comparative study*
  Dongchen Qi, Wei Chen, Xingyu Gao, Li Wang, Shi Chen, Kian Ping Loh, Andrew T. S. Wee
  in preparation (2009)

- *Surface transfer doping of semiconductors* (an invited review article)
  Wei Chen[*], **Dongchen Qi**[*], Xingyu Gao, Andrew T. S. Wee
  PROGRESS IN SURFACE SCIENCE, **84**, 279 (2009)

- *Chemical Bonding of Fullerene and Fluorinated Fullerene on Bare and Hydrogenated Diamond*
  Ti Ouyang, Kian Ping Loh, **Dongchen Qi**, Andrew T. S. Wee, Milos Nesladek
  CHEMPHYSCHEM, **9**, 1286 (2008)

---

[*] Both authors contribute equally.

- *Surface Transfer P-Type Doping of Epitaxial Graphene*
  Wei Chen, Shi Chen, **Dongchen Qi**, Xing Yu Gao, Andrew T. S. Wee
  JOURNAL OF THE AMERICAN CHEMICAL SOCIETY, **129**, 10418 (2007)

- *Water-induced negative electron affinity on diamond (100)*
  Xingyu Gao, Lei Liu, **Dongchen Qi**, Ti Ouyang, Loh Kian Ping, Andrew T. S. Wee
  JOURNAL OF PHYSICAL CHEMISTRY C, **112**, 2487 (2008)

- *Surface-Transfer Doping of Organic Semiconductors Using Functionalized Self-Assembled Monolayers*
  Chen Wei, Xingyu Gao, **Dongchen Qi**, Shi Chen ,Zhikuan Chen, Andrew. T. S. Wee
  ADVANCED FUNCTIONAL MATERIALS, **17**, 1339 (2007)

- *Cycloadditions on diamond (100)-2×1: Observation of Lowered Electron Affinity due to Hydrocarbon Adsorption*
  Ti Ouyang, Xingyu Gao, **Dongchen Qi**, Andrew T. S. Wee, Kian Ping Loh
  JOURNAL OF PHYSICAL CHEMISTRY B, **110**, 5611 (2006)

- *High resolution electron energy loss and X-ray near edge absorption spectroscopic studies of diamond film functionalised with allyl alcohol*
  Kian Ping Loh, Chee Wei Lim, Xingyu Gao, **Dongchen Qi** and Andrew T. S. Wee
  DIAMOND AND RELATED MATERIALS, **15**, 711 (2006)

TABLE OF CONTENTS

ABSTRACT

This thesis describes experimental investigations of organic molecules adsorbed on diamond (001). This work has been conducted mainly using synchrotron radiation based spectroscopic techniques, namely photoemission spectroscopy (PES) and near-edge X-ray adsorption fine structure (NEXAFS), and complemented by other surface analytical probes and first-principle calculations. Particular emphasis is placed upon the interactions, electronic structures, and energy level alignments at the organic-diamond interface. The structural and electronic properties of bare and hydrogen-terminated diamond (001) have also been characterized as initial baseline studies.

Scanning tunneling microscope (STM) and low energy electron diffraction (LEED) studies confirm the 2×1 reconstruction with orthogonally oriented domains on both bare and hydrogenated diamond (001) surfaces. The electronic structures and properties probed by the combination of PES and NEXAFS are consistent with published work. In particular, the well-known negative electron affinity (NEA) of hydrogenated diamond is determined to be -1.1 eV, leading to a sharp and intense secondary electron emission peak in the low kinetic energy region of PES spectra.

The π-bonded surface dimers endow bare diamond surface with reactivity towards unsaturated organic molecules, which is indeed confirmed by the PES and NEXAFS studies of 1,3-butadiene adsorption. A reduction in diamond electron affinity by up to 0.7 eV is observed, as well as a greatly enhanced secondary electron emission yield accompanying the surface functionalization with 1,3-butadiene. Density functional theory (DFT) calculations reveals that this tuning effect is due to the surface dipole layer built up by the terminal heteropolar C—H bonds in the covalently bonded organics via cycloaddition reactions.

Copper phthalocyanine (CuPc), a prototypical organic semiconductor, is also investigated and compared on both bare and hydrogenated diamond (001). CuPc interacts weakly with hydrogenated diamond, whereas it undergoes chemical reaction with bare diamond dimers. A combination of interfacial charge transfer and intramolecular interface dipole created by the covalently attached molecules transform bare diamond surface from positive electron affinity (PEA) to NEA, with enhanced secondary electron emission intensity. A hot electron emission process from diamond conduction bands through covalently attached molecules to vacuum is described. Distinct supramolecular ordering and orientation within the CuPc films on both diamond (001) surfaces are revealed by NEXAFS, which is explained in terms of the interplay between intermolecular interactions and molecule-substrate interactions.

The last part of this thesis studies the *p*-type surface transfer doing of diamond, which relies on electron transfer from hydrogenated diamond to surface molecular adsorbates. The charge transfer and energy level alignments across the diamond/organic heterojunction is characterized by PES, which unambiguously demonstrates controlled *p*-type surface transfer doping of diamond by molecular acceptors. High areal hole density over 10^{13} cm^{-2} of diamond is readily achieved by tetrafluorotetracyanoquinodimethane (F_4-TCNQ) and highly fluorinated fullerene ($C_{60}F_{48}$) adsorption, which acts as effective acceptors even in isolated molecular form. Tetracyanoquinodimethane (TCNQ) and buckminsterfullerene (C_{60}), in comparison, induce moderate surface transfer doping (~ 10^{10} – 10^{12} cm^{-2}) only after the formation of condensed-phase molecular thin films. In contrast, CuPc films cause no observable interfacial charge transfer. Our study correlates their distinct surface transfer doping yields and efficiencies with their electron affinity values in both gas phase and condensed phase.

LIST OF TABLES

LIST OF FIGURES

LIST OF ABBREVIATIONS

AEY	Auger Electron Mode
BE	Binding Energy
BHJ	Bulk Heterojunction
CBM	Conduction Band Minimum
CMOS	Complementary Metal-Oxide-Semiconductor
CVD	Chemical Vapor Deposition
DFT	Density Functional Theory
DOS	Density of States
EA	Electron Affinity
EELS	Electron Energy Loss Spectroscopy
ESCA	Electron Spectroscopy for Chemical Analysis
EXAFS	Extended X-ray Absorption Fine Structure
FCC	Face-Centered Cubic
FET	Field Effect Transistor
FTIR	Fourier Transform Infrared Spectroscopy
FWHM	Full Width at Half Maximum
HOMO	Highest Occupied Molecular Orbital
IMFP	Inelastic Mean Free Path
IP	Ionization Energy
IPES	Inverse Photoemission Spectroscopy
ISFET	Ion-Sensitive Field-Effect
KE	Kinetic Energy
LED	Light Emitting Diode
LEED	Low Energy Electron Diffraction
LHC	Large Hadron Collider
LUMO	Lowest Unoccupied Molecular Orbital
MESFET	MEtal-Semiconductor Field Effect Transistor
ML	Monolayer
MOSFET	Metal-Oxide-Semiconductor Field-Effect Transistors

NEA	Negative Electron Affinity
NEXAFS	Near-edge X-ray Absorption Fine Structure
OFET	Organic Field Effect Transistor
PEA	Positive Electron Affinity
PES	Photoemission Spectroscopy
PEY	Partial Electron Yield
RT	Room Temperature
SAM	Self-Assembled Monolayers
SC	Surface Conductivity
SIMS	Secondary Ion Mass Spectrometry
SOMO	Singly Occupied Molecular Orbital
STM	Scanning Tunneling Microscopy
STS	Scanning Tunneling Spectroscopy
TEY	Total Electron Yield
TPY	Total Photoyield
UHV	Ultra-High Vacuum
UPS	Ultraviolet Photoelectron Spectroscopy
VBM	Valence Band Maximum
VL	Vacuum Level
WF	Work Function
XANES	X-ray Absorption Near Edge Spectroscopy
XAS	X-ray Absorption Spectroscopy
XMCD	X-ray magnetic circular dichroism
XPD	X-ray Photoelectron Diffraction
XPS	X-Ray Photoemission Spectroscopy

CHAPTER 1

INTRODUCTION

1.1 Carbon and its allotropes

Carbon (C), the sixth element in the periodic table, is the fourth most abundant chemical element. The relatively small size of a carbon atom as well as its ability to form strong covalent bonds with another carbon atom leads to a variety of carbon allotropes (Figure 1.1). When bonded to other elements such as hydrogen, nitrogen and oxygen, the carbon-based organic molecules constitute the great majority of all known chemical compounds. Notably, deoxyribonucleic acid (DNA) and ribonucleic acid (RNA), which are the very basis of all living organisms, are simply giant organic molecules. In fact, carbon is so essential to all terrestrial life that people have conjectured all life forms in the universe is carbon-based; this doctrine is known as *carbon chauvinism* [1].

The large number of carbon-based allotropes or compounds stems from the hybridizations of carbon valence orbitals. The ground state electronic configuration of carbon is $1s^2 2s^2 2p^2$, of which four are valence electrons (two in $2s$ orbital and two in $2p$ orbital). Upon hybridization, the $2s$ orbital can hybridize with one, two or three $2p$ orbitals to form sp, sp^2, or sp^3 hybridized orbitals respectively. The hybridized orbitals from two carbon atoms can overlap to form σ bonds. Together with partial overlapping of the unhybridized $2p$ orbitals, two carbon atoms can form a triple, double or single bond between them, leading to a great variety of carbon compounds. In particular, the sp^3 hybridized carbon forms the basis of one of the best known carbon allotropes: diamond.

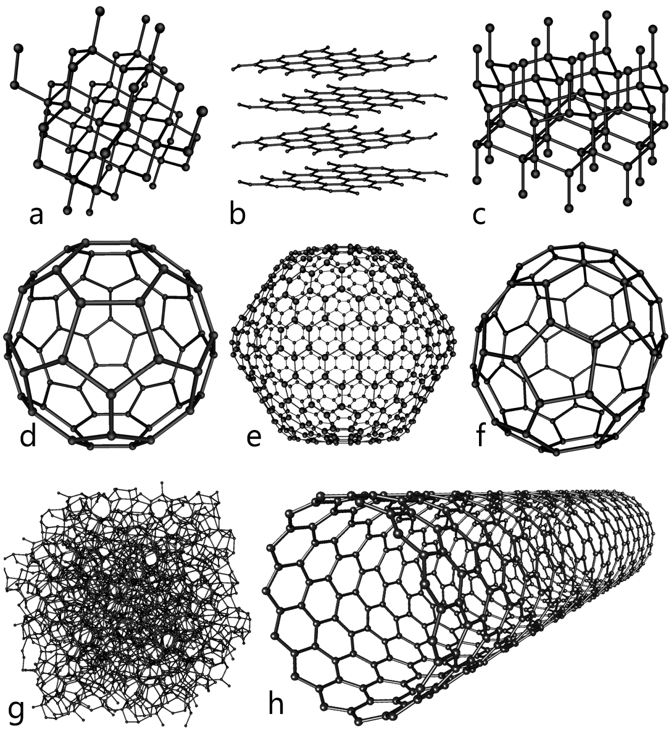

Figure 1.1. Eight allotropes of carbon: a) Diamond, b) Graphite, c) Lonsdaleite, d) C_{60} (Buckminsterfullerene), e) C_{540}, f) C_{70}, g) Amorphous carbon, and h) single-walled carbon nanotube [2].

1.2 Properties of diamond

1.2.1 General properties and applications

Diamond has been highly priced for centuries as a gemstone with exceptional brilliance and lustre. It is a solid crystalline form of carbon in which all carbon atoms are tetrahedrally coordinated and sp^3-bonded (Figure 1.2). The *diamond cubic* crystal structure is face-centered cubic (FCC) with a basis comprising two carbon atoms at each lattice point: one at (0 0 0) and another at $(\frac{1}{4}\ \frac{1}{4}\ \frac{1}{4})$, i.e. it can be viewed as two interpenetrating FCC lattices with an offset along a body diagonal by 1/4 of cubic length. The conventional cubic unit cell shown in Figure 1.2 has a lattice constant a_0 of 3.57 Å at room temperature (RT) [3]. The C−C center-to-center distance d is therefore one quarter of the cubic body diagonal length, where $d = \sqrt{3}a_0 / 4 \cong 1.54\,\text{Å}$.

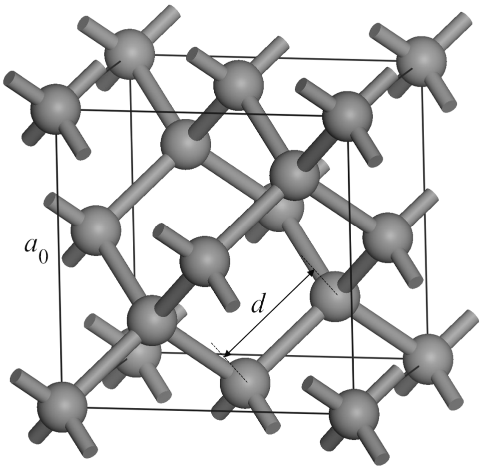

Figure 1.2. Ball-and-stick model of the conventional unit cell of diamond, where a_0 is the cubic lattice constant.

Each conventional unit cell contains eight equivalent carbon atoms, giving an atomic number density $8/a_0^3 \approx 1.76 \times 10^{23}$ cm^{-3}, which is the highest among all terrestrial materials.

The extremely strong sp^3 bonding and tight lattice structure endow diamond with a long list of outstanding mechanical, electrical, thermal, optical and chemical properties (cf. Table 1.1 and Table 1.2), enabling a broad range of applications, particularly when these properties are combined. The incompressibility of C−C bonds and stability of the tetrahedral lattice arrangement lead to diamond's most renowned property of extreme hardness; this is used as the maximum (10, hardest) in the calibration of the Mohs scale of mineral hardness. In fact, the name of *diamond* is derived from ancient Greek ἀδάμας (adámas), literally meaning *invincible* or *indestructible*. Its resistance to scratching (except by another diamond) underscores diamond's suitability as a gemstone because it can maintain its polish extremely well against daily wear. Industrial use of diamond has historically been mainly associated

Table 1.1. General properties of diamond [3-8].

Properties	**Value**
Crystal structure	Diamond Cubic
Space group	$Fd\bar{3}m$
Lattice constant (300 K)	3.56683 Å
Bond length (300 K)	1.54448 Å
Density (300 K)	3515.25 kg/m^3
Relative hardness (Mohs scale)	10
Modulus of elasticity	700-1200 Gpa
Young's modulus ([111])	1223 Gpa
Coefficient of friction	0.05
Atomic number density (300 K)	1.763×10^{23} cm^{-3}
Thermal expansion coefficient (300 K)	1.05×10^{-6} K^{-1}
Melting point	3773 K
Debye temperature	2067 °C
Thermal conductivity (300 K)	2200 Wm^{-1}K^{-1}
Refractive index (visible range)	2.40 - 2.46
Dielectric constant (300 K, 1-10 KHz)	5.70

with their hardness, which makes diamond the ideal material for cutting, grinding, polishing, and drilling applications.

Diamond possesses the highest thermal conductivity (*k*) of any material known. High *k* is very unusual for ordinary semiconductors due to the lack of electrons in conduction band to transfer energy through the crystals. However, the rigid sp^3 bonding is responsible for the extremely high thermal conductivity of diamond, as they can transfer lattice vibrations with great efficiency. Consequently, the measured *k* of natural diamond at RT is in the range of 900 ~ 2300 Wm^{-1}K^{-1} [7-8], several times higher than the metallic copper (~ 400 Wm^{-1}K^{-1}) [8]. This extremely high thermal conductivity enables diamond-based devices to work under high power and high temperature conditions. In particular, with its low thermal expansion coefficient (Table 1.1), diamond serves as a superb window material.

The gorgeous luster of diamond, which results from its undistorted reflection from properly cut diamond facets and flashes of prismatic colors, is probably the most valuable optical property viewed from a jeweler's perspective. Another exceptional optical property of diamond is its superb optical transparency from deep ultraviolet (UV), through the visible to far-infrared (IR), owing to its large, indirect band gap of 5.47 eV. This unique property is valued by scientists and engineers and used in various optical applications such in IR laser windows.

Diamond also has remarkable chemical inertness due to its strong bonding energy, making diamond an excellent material for devices that work in harsh chemical environments. Furthermore, owing to its wide chemical potential window [9] and inherent biocompatibility [10], diamond is an ideal platform material for hybrid bio-inorganic interfaces in applications such as biosensors [11], biomedical implants [5], and organic/biomolecular electronics [12].

1.2.2 Diamond as an electronic material

With rapid development in the synthesis of large diamond thin films (both polycrystalline and single crystalline) with very high quality by chemical vapor deposition (CVD) technique [4, 13], diamond is increasingly recognized as a promising electronic material [14-15] for active devices such as field-effect transistors (FETs). Although intrinsic diamond is a *bona fide* insulator due to its wide band gap, its numerous exceptional electronic properties (Table 1.2) endow doped-diamond with tremendous potential as an electronic material capable of operating in extreme conditions beyond the scope of conventional semiconductor materials such as silicon. In particular, diamond-based electronic devices can potentially operate at high frequency, high power, high temperature conditions, and can function under harsh chemical environments and severe radiation exposure. These unprecedented device possibilities are opened by diamond's unique electronic properties such as high carrier mobility, high saturation velocity, long carrier lifetime, high dielectric breakdown field and wide band gap.

Single-crystal diamond possesses the highest electron and hole mobilities at RT among common inorganic semiconductors. Extremely high electron mobility (4500 $cm^2V^{-1}s^{-1}$) and hole mobility (3800 $cm^2V^{-1}s^{-1}$) have been measured in intrinsic, single-crystal CVD diamond at RT [16], far exceeding carrier mobilities in other conventional semiconductor materials (Table 1.2). High carrier mobility is essential to realize devices with fast switching speed. Diamond also exhibits very high saturation velocity for both electrons and holes ($v_s \sim 0.8\text{-}2 \times 10^7$ cm/s under electric field of 10 kV/cm). Such high saturation velocity is important for FETs working at high frequencies (>10 GHz). Another extraordinary electronic property of diamond is its high electric breakdown field of 10 MV/cm [15]. Combined with its high thermal conductivity, diamond is made a dream material for high voltage and high power devices, with performance surpassing other competing wide gap materials such as SiC and GaN for high-frequency and high power electronic device applications (Table 1.2).

Diamond's wide band gap finds applications in diamond-based UV light emitting diodes (LED) [17]. Combined with its radiation hardness and high breakdown field, diamond is used for radiation detectors of UV radiation, X-rays, γ-rays to ultrahigh energy elementary particles [18]. For example, diamond is incorporated as core-components into the detector system of the Large Hadron Collider (LHC) [19], playing crucial roles in arguably the greatest experiment till today.

Table 1.2. Important electronic properties of diamond in comparison with other commonly used semiconductors [14-16].

	Natural diamond	**CVD diamond**	**Si**	**4H-SiC**	**GaN**
Band gap (eV)	5.47	5.47	1.1	3.2	3.44
Electron mobility ($cm^2V^{-1}s^{-1}$)	200-2800	4500	1450	900	440
Hole mobility ($cm^2V^{-1}s^{-1}$)	1800-2100	3800	480	120	200
Electron saturation velocity (cm/s)	2×10^7	2×10^7	0.86×10^7	3×10^7	2.5×10^7
Hole saturation velocity (cm/s)	0.8×10^7	0.8×10^7	N/A	N/A	N/A
Electric breakdown field (MV/cm)	10	10	0.3	3	5

Negative electron affinity (NEA), another unique property of diamond, leads to the high electron emission yield of diamond, because electrons in the conduction bands experience no energy barrier to escape into vacuum. This property makes diamond an ideal material for electron-emitting devices such as field-emission devices [20], electron multipliers [21] and cold cathodes [22]. The NEA property of diamond is explored in detail in Chapter 3. In particular, the electron affinity (EA) and electron emission properties of diamond can be tailored through interactions with organic molecules, which are the central subjects of Chapter 4 and Chapter 5.

When terminated by hydrogen atoms, diamond exhibits unexpected *p*-type surface conductivity by forming a quasi-two-dimensional hole gas at the surface [23]. Several surface conductive-channel devices based on this property have been realized, such as surface-channel FETs [24]. Its sensitivity to pH variations of solutions is also exploited in diamond-based pH sensors [25].

Diamond even finds application in the burgeoning field of quantum computation. Because of the long decoherence time of its nitrogen-vacancy (NV) impurity center, the electron spin state of individual NV center can be read out and manipulated even at RT [26]. This revolutionary property enables the construction of the most fundamental building block of a quantum computer, a quantum bit or qubit in reality. Furthermore, a single NV center when deexcited, emits a single photon, which is utilized in diamond-based single-photon source for applications such as quantum cryptography.

With so many unprecedented properties and applications, there is no wonder that diamond is called "*a 21st century material*" [13]. However, its own unique properties also present a number of challenges for device applications. Among them, the lack of reliable *n*-type dopant for diamond severely restricts diamond device designs to unipolar devices in which holes are the only available charge carrier. Even the *p*-type dopants for diamond suffer from low activation at RT, leading to low conductivity. Moreover, the extreme hardness and chemical inertness of diamond requires unconventional fabrication processes. A novel surface transfer doping scheme that relies on charge exchange between surface dopants and semiconductor surface holds the promise for overcoming some of these challenges. Chapter 6 is devoted to this subject.

1.3 Objective and scope of this investigation

Studying molecules on solid surfaces is one of the major topics in surface science. It is central to many surface phenomena with applications in heterogeneous catalysis, tribology, surface functionalization, material engineering, etc. [27]. Earlier studies mainly focused on the adsorption and chemical reaction kinetics of simple inorganic molecules (e.g. H_2, O_2, N_2) on a wide range of solid surfaces including metals, metal oxides and semiconductors. More recently, there is growing interest in the adsorption of complex organic molecules on solid surfaces, particularly on metal [28] and group IV semiconductor surfaces [29], in view of potential applications such as organic electronics [30] and hybrid organic/inorganic devices [31]. This is because the interface between the active organic layer and inorganic substrate plays a crucial role in device performance.

The study of organic molecules on diamond has received less attention as compared to its silicon or germanium counterpart, but is important for both fundamental surface science and practical applications. Diamond can be viewed as a "*big organic molecule*" [32], but in the solid state. Studying its interactions with organic molecules can help us to answer some fundamental and compelling questions such as how the solid state effect influences chemical reactions. Furthermore, coupling organic molecules to diamond surfaces allows versatile organic functionalities to be integrated with diamond's extraordinary material properties, which can be harnessed to design and fabricate diamond-based molecular electronic devices.

This thesis aims to investigate the interactions between diamond surface and different organic molecules. I will focus on how these interactions alter the electronic structures and electronic properties at the interface by synchrotron-based spectroscopies. The synopsis of this thesis are:

1. To characterize the surface reconstructions, electronic structures and electronic properties of diamond (001) with different surface terminations (i.e. bare and hydrogen-terminated); this serves as a starting point for subsequent adsorption studies. (***Chapter 3***)
2. Investigating the cycloaddition reaction on bare diamond (001) with a model alkene-containing organic molecule (1,3-butadiene), To clarify how the covalent attachment of organic molecules onto diamond alters its electronic structures, energy level alignment, work function, electron affinity and secondary electron emission yield. (***Chapter 4***)

3. To compare the interactions of hydrogenated and bare diamond surfaces with a prototypical organic semiconductor molecule (copper phthalocyanine), and to address how the interplays between molecule-substrate interactions and intermolecular interactions influence the supramolecular organizations and molecular orientations. (***Chapter 5***)
4. To examine surface transfer doping of diamond by organic molecules which provides a novel route for engineering *p*-type surface conductivity of diamond. Spectroscopic insights of the charge transfer process at the interface between hydrogenated diamond and several carefully selected molecular acceptors with varying electron-accepting capabilities are addressed. The correlation between doping efficiency and molecular electron affinity is discussed. (***Chapter 6***)

The diamond sample used in this study is a single crystal diamond with (001) orientation grown by the CVD technique. The (110) and (111) orientational sample are not the subject of the present study, because diamond (001) is the most easily grown crystallographic face by CVD with high quality and also the most technologically important single crystalline diamond surface.

This thesis emphasizes the electronic structures and energy level alignment at diamond/organic interfaces, therefore synchrotron based spectroscopies (i.e. photoemission spectroscopy and X-ray absorption spectroscopy), which provide complete information on the occupied and unoccupied electronic states, are employed throughout. The working principles and instrumentations of these techniques, along with the experimental stations where this study was carried out, are introduced in the next chapter.

CHAPTER 2

EXPERIMENTAL TECHNIQUES

2.1 Principles of experimental techniques

2.1.1 Scanning tunneling microscopy

Scanning tunneling microscopy (STM) is a powerful technique for studying surface structures with atomic resolution. It is also capable of manipulating a single atom or molecule on a surface. In 1981, G. Binnig, H. Rohrer et al at the IBM Zurich Research Laboratory invented the first STM system [33], the advent of which brings on the era of nanoscience and nanotechnology.

The general principle underlying the operation of a STM is the quantum mechanical tunneling effect. A voltage is applied between a sharp tip (e.g. tungsten) and a conductive surface. Tunneling of the electrons through the vacuum barrier between the tip and surface occurs when the tip is extreme close to the surface (~ 1 nm) yet not touching. The tunneling current through the vacuum barrier can be expressed as:

$$I \propto V \exp(-2kd) \tag{2.1}$$

where V is the voltage between the tip and the surface, d the distance between the tip and the surface. The parameter k is $\frac{\sqrt{2m(\Phi - E)}}{\hbar}$, where Φ is the average work function (WF) and E the energy of state with respect to the Fermi level. The average WF can be calculated from the WF of the tip and the surface. From Eqn. (2.1), it is easily seen that the tunneling current is extremely sensitive to the distance d. If the distance is decreased by 0.1 nm, the tunneling current will be increased by approximately one order of magnitude.

By scanning the tip over the surface while keeping the tunneling current constant by means of a feedback loop, one can obtain a three-dimensional image of the surface corrugation by monitoring the vertical position of the tip as a function of the lateral position. This imaging mode is referred as constant current mode. STM also can work under constant height mode. During the scanning process, the vertical position of the tip is kept constant and the topography of the surface is acquired through monitoring changes in the tunneling current. When STM is working in constant height mode, the surface must be quite flat with roughness smaller than 1 nm to avoid crashing the tip into surface protrusions.

STM is capable of atomic level resolution: ~ 0.1 nm in the direction parallel to the surface and ~ 0.01 nm in the direction perpendicular to the surface. Moreover, when combined with scanning tunneling spectroscopy (STS), information on the electronic structure of the surface, such as the density of states (DOS) of both occupied and unoccupied levels, local charge density and band gap etc., can also be obtained by STM.

2.1.2 Low energy electron diffraction

In contrast to STM which probes the local surface structures within a small area (from several tenths of nm^2 to thousands of nm^2), the low energy electron diffraction (LEED) technique reveals a long-range order in surface structures. The LEED electron gun emits a beam of electrons with a well-defined low energy (typically in the range 20 - 200 eV) incident normally on the sample. The sample itself must have a well-ordered surface structure in order to generate a back-scattered electron diffraction pattern. A typical LEED experimental set-up is sketched below.

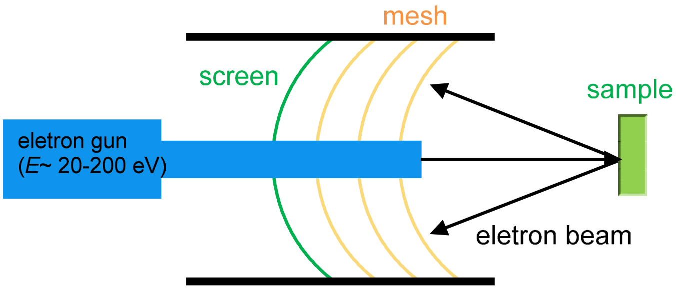

Figure 2.1. Above: Schematic set-up of a LEED experiment. Below: a LEED optics assembly produced by Omicron (picture courtesy of Omicron).

The backscattered electrons from the sample surface first encounter the meshes which impose a series of retarding potentials to filter out inelastically scattered electrons before falling on the fluorescent screen. The electron diffraction pattern follows the Bragg diffraction condition:

$$a \sin \theta = n\lambda \tag{2.2}$$

where a is the surface lattice parameter, θ is the angle between surface normal and the direction of reflected electron beams, and n is a integer. λ is the wave length of electrons which is related to the pre-defined incident electron energy E,

$$\lambda = \frac{h}{p} = \frac{h}{\sqrt{2mE}} \tag{2.3}$$

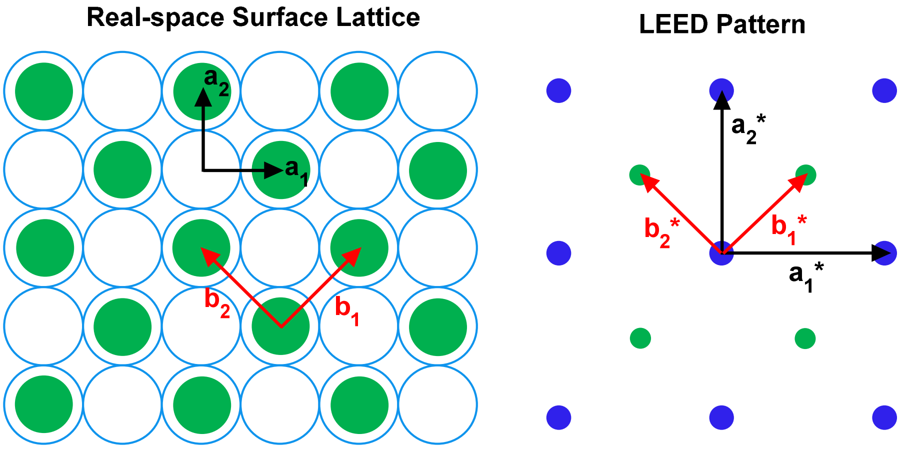

Figure 2.2. Left: A schematic representation of (100) surface of a FCC single crystal covered with an overlayer with c(2×2) superstructure. ($\boldsymbol{a_1}$, $\boldsymbol{a_2}$) and ($\boldsymbol{b_1}$, $\boldsymbol{b_2}$) are the surface lattice vectors of the substrate and the adsorbate overlayer, respectively. Right: corresponding diffraction pattern observed in LEED. ($\boldsymbol{a_1}^*$, $\boldsymbol{a_2}^*$) and ($\boldsymbol{b_1}^*$, $\boldsymbol{b_2}^*$) are the reciprocal lattices.

In this way, the position of a diffraction pattern on the screen is explicitly related to the 2-D surface lattice structure. In fact, the observed LEED pattern directly reflects the reciprocal lattice of a surface structure.

Figure 2.2 shows a typical LEED pattern observed on the (100) surface of a FCC single crystal covered with a c(2×2) overlayer. By analyzing the observed LEED pattern, we can obtain qualitative information on the relative size, symmetry and rotational alignment of the adsorbate superstructures with respect to the substrate unit cell. Moreover, by recording the intensities of various diffraction spots as a function of the incident electron beam energy to generate the so-called *I-V* profiles and comparing them with theoretical multiple scattering calculations, we can quantitatively evaluate surface atom positions, interlayer spacings and other important structural information [34].

2.1.3 Photoemission spectroscopy

Photoemission spectroscopy (PES), also known as photoelectron spectroscopy [35], refers to kinetic energy (KE) measurement of electrons emitted from solids, gases or liquids by the photoexcitation at a specific photon energy, in order to determine the binding energies (BEs) of electrons in a substance. The fundamental principle underlying PES is the well-known photoelectric effect, contributed by Albert Einstein [36]. It describes the phenomenon that when a photon with a specific energy ($h\nu$) is incident on a material, the electrons in the materials that occupy a certain initial energy state (E_{i}) can absorb the photon and escape from the material to vacuum as photoelectrons with a certain KE (E'_{k}). Defining the energy difference between the initial energy state of electrons and the Fermi energy as electron binding energy (E_{b}), or more precisely the energy difference of *total energies* between the final state (excited state, N-1 electrons) and the initial state (ground state, N electrons), the relationship between BE and the KE of emitted photoelectrons can be expressed according to energy conservation as,

$$E_b = h\nu - E'_k - \phi_s \tag{2.4}$$

where ϕ_{s} is the WF of the sample.

Several models have been proposed to theoretically treat the photoemission process. Among them, a phenomenological description that splits the process into three separate steps is the most commonly used model to understand the complex photoemission process. In this three step model developed by Berglund and Spicer [37], optical excitation between two Bloch states, transport of the excited electron to the surface and escape of the electron from the surface to the vacuum are treated separately (Figure 2.3). As a result, the total photoemission intensity is then given by the product of the three independent probabilities associated with each step. Among them, the optical excitation of an electron is described by the Fermi Golden rule transition probability [38], which is dependent on $\left|\langle f,k|H|i,k\rangle\right|^2$ where $|i,k\rangle$ and $\langle f,k|$ are states with negligible change in wavevector k. The perturbation operator H, is : $H=\frac{e}{2m}(A\bullet p+p\bullet A)$ where A is the vector potential of the incident light and p the momentum operator. Therefore, by measuring the energy distribution of the photoelectrons at fixed photon energy, the features of the occupied DOS weighted by the matrix element are reproduced in PES. In addition to the three-step description of the PES process, a more recent one-step process [39] which considers the excitation from a one-electron Bloch wave state into a damped final state near the surface has been widely accepted as an efficient model for photoemission related calculations.

The typical experimental set-up for PES measurements is schematically shown in Figure 2.4. The main components of a PES system is a photon source which emits photons at a specific energy, an electron energy analyzer (spectrometer) which is

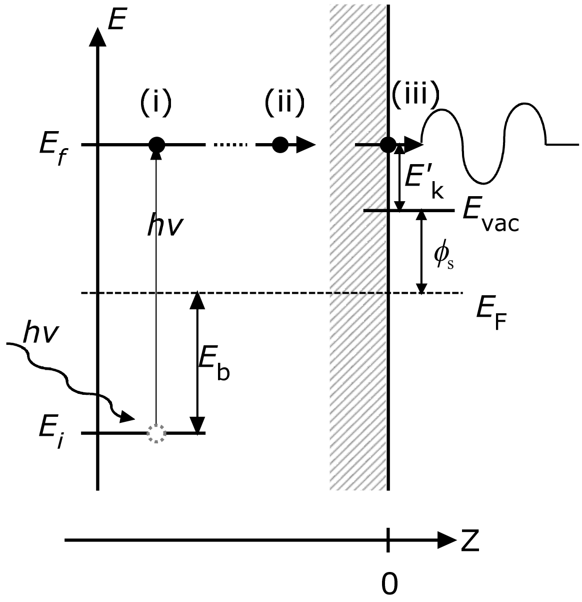

Figure 2.3. Illustration of three-step model in photoemission process: (i) photoexcitation of a electron from an initial state to a final state; (ii) transport of excited electrons to the surface; (iii) escape from surface to the vacuum.

aligned in a proper direction facing the sample surface and measures the KE of emitted electrons, and a data collection system which records the measured electron KE as well as photoelectron intensity simultaneously. The measurement system is encapsulated in an ultra high vacuum (UHV) system to minimize the inelastic scattering of photoelectrons by gas molecules. The sample used in PES measurements can be any solid as long as it has enough conductivity to avoid charge accumulation on the surface. The photoelectron spectrum, or energy distribution curve (EDC), is obtained by sweeping a range of KEs with the electron analyzer and keeping the photon energy constant. It should be noted that the KE measured by the spectrometer (E_k) is not directly equal to the KE of photoelectrons (E'_k) in most cases due to the WF difference between that of the spectrometer (ϕ_a) and that of the sample (ϕ_s), and Eqn. (2.4) is then rewritten as:

$$E_b = h\nu - E_k - \phi_a \tag{2.5}$$

This eliminates the need of prior knowledge of the sample WF, and facilitates a direct comparison of the BE of a specific element between different samples.

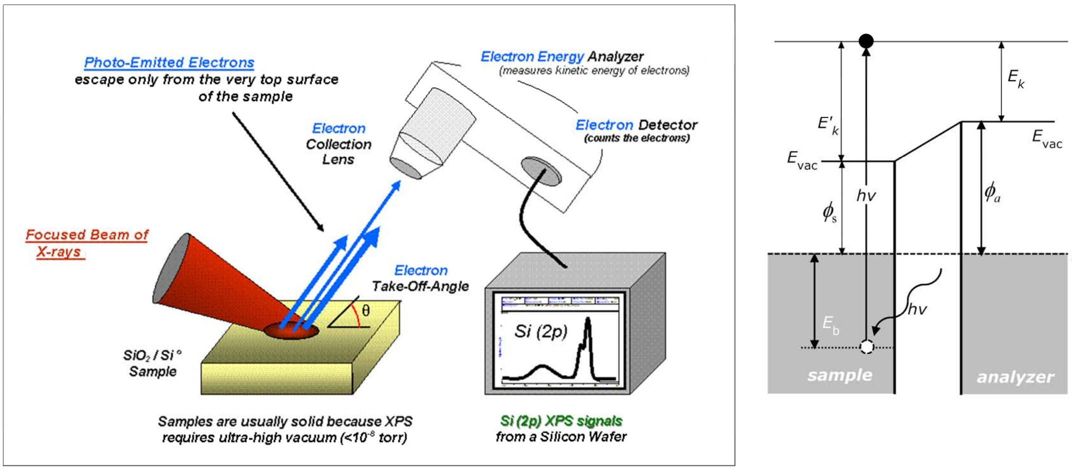

Figure 2.4. A typical experimental set-up for PES measurements. Shown at the right is the energy level alignment between sample and the electron energy analyzer assuming sample and analyzer are in good electric contact so their Fermi energies coincide with each other [40].

According to the photon energy of the exciting radiation source, PES can be divided into two categories, namely ultraviolet photoelectron spectroscopy (UPS) and X-ray photoelectron spectroscopy (XPS) as shown in Figure 2.5. They have different applications in the characterization of materials. Laboratory-based UPS utilizes a vacuum UV radiation source ($h\nu$ = 10 ~ 100 eV) which is normally a noble gas discharge lamp, such as a helium discharge lamp emitting He-I radiation at 21.2 eV or He-II radiation at 40.8 eV. Because of the relatively low photon energy of UPS, it is only capable of ionizing valence electrons from the outermost levels of the atom. Therefore, UPS is sometimes referred as valence band spectroscopy as well. One advantage of UPS is it can offer ultrahigh resolving resolution (several meV) owing to the very narrow line width of the radiation light. Because UPS is optimized to probe the valence electron states, by doing a detailed angle resolved study (ARUPS), the complete valence band structures in the *k*-space can be mapped out. Another major application of UPS is to study the bonding orbitals of molecules either absorbed on solid surfaces or condensed as molecular solids. By sweeping the energy region close to the Fermi level, various frontier molecular bonding orbitals including the highest occupied molecular orbital (HOMO) can be resolved.

UPS is also often used to measure the sample WF (ϕ_s) for metals or ionization potential (IP) for semiconductors by measuring the spectral width (*W*). As shown in Figure 2.5, the spectral width *W* is defined as the energy distance between the cut-off position of the secondary electron emission in the low KE region and the Fermi energy position. For materials other than metals, there is no DOS at the Fermi energy, and the upper edge of the spectra width is then replaced by the spectral feature that has the highest KE (i.e. valence band maximum or HOMO edge). It is straightforward to obtain the sample work function as $\phi_s = h\nu - W$ for metals. For semiconductors this gives the IP instead. It should be noted that when the sample WF is smaller than that of the spectrometer ($\phi_s < \phi_a$), the low KE photoelectrons with energies just above the vacuum level (VL) of sample cannot be detected by the electron analyzer (see Figure 2.4), and the spectral width measured by analyzer is underestimated, leading to

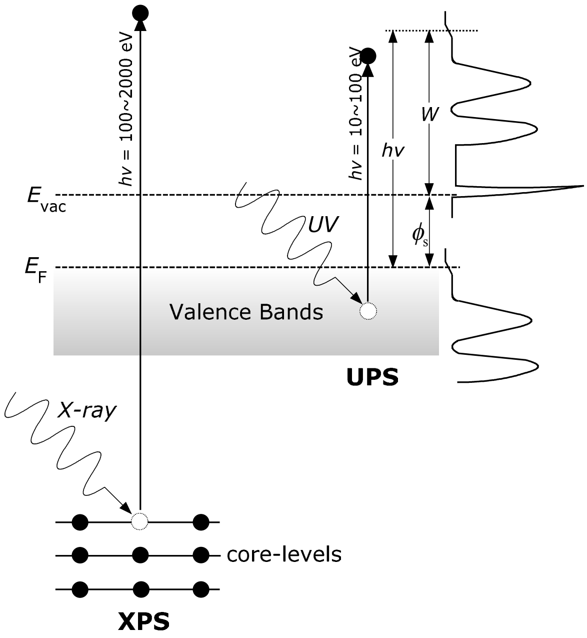

Figure 2.5. Schematic diagram of XPS and UPS. The spectra shown on the right side shows a typical valence band density of states (DOS) and it corresponding UPS spectrum.

incorrect value of sample WF or IP. In order for these low KE electrons to overcome the WF of analyzer, a small negative bias (U ~ 3-10 eV) is usually applied to the sample, which shifts the measured spectrum to higher kinetic energies. The WF or IP measured in this way represents the intrinsic properties of samples, eliminating the influence of the spectrometer.

Owing to the higher photon energy of X-rays, XPS can excite the core-level electrons residing in much deeper energy states than those in valence bands. Because the BEs of core-level electrons are usually element specific, each element gives rise to a characteristic set of peaks with specific BE in the XPS spectrum (e.g. 1*s*, 2*s*, 2*p* …). Therefore, XPS can provide information on the chemical composition of the studied materials by examining the presence of characteristic peaks associated with different elements. Furthermore, the intensity of the peaks is related to the concentration of the element within the sampled region. Thus, the technique provides a quantitative analysis of the surface composition and is so sometimes referred as Electron Spectroscopy for Chemical Analysis (ESCA). XPS can also distinguish between different chemical states (or valence states) of a specific element. The local chemical (e.g. number of valence electrons) or physical environment (i.e. crystal symmetry) around the excited atom can alter the BE of its core-level electrons, and is represented in XPS spectrum as a BE shift, termed the “chemical shift”. For example, oxidized atoms which lose their valence electrons lead to higher BE of core-level electrons, while adding electrons to the valence orbital lowers the core-level BE. This ability to discriminate between different oxidation states and chemical environments is one of the major strengths of the XPS technique. In principle, XPS can also excite electrons from the valence bands, but the photoionziation cross section of valence band elec-

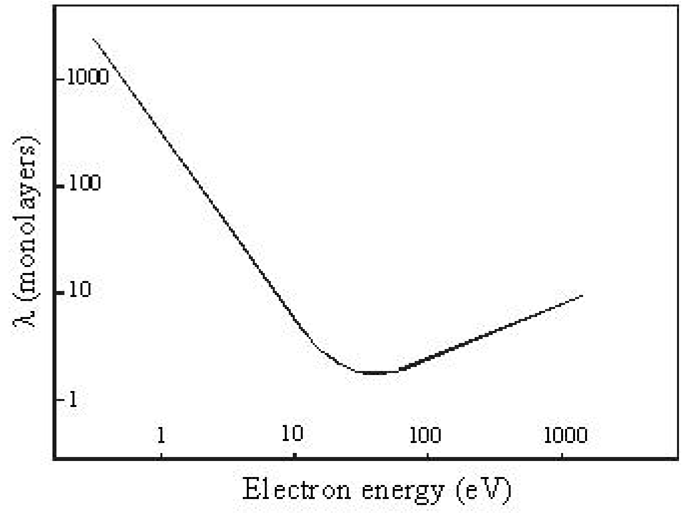

Figure 2.6. The typical inelastic mean free path of an electron as a function of its KE [35].

trons at XPS photon energy is much lower than that in UPS, making it less suitable for probing the valence band information of studied materials.

The most commonly employed commercial Lab-based X-ray sources in XPS experiments are the Mg K_α radiation (hv = 1253.6 eV) as well as the Al K_α radiation (hv = 1486.6 eV). However, they suffer from an inherent low energy resolution due to large line width of X-ray source. The last several decades have witnessed a rapid development in synchrotron radiation facilities, producing synchrotron radiation with high brilliance, high energy resolution and wide energy range. In particular, the tunable photon energy of synchrotron radiation source enables much improved flexibility in PES measurements. For example, one can greatly enhance the cross section for a specific energy level of an element by intentionally choosing a photon energy close the BE.

One of the many advantages of PES is its surface sensitivity. As described in the three-step model, an electron excited by absorbing a photon must travel to the surface before escaping the solid surface. During the transport, the electron may lose its energy due to inelastic scatterings. The inelastic scattering process is very complex and determined by many different mechanisms. At low kinetic energies, photoelectrons have insufficient energy to initiate scattering processes, and at high energies, the cross section of scattering events is low. The escape depth of the electron, or the so-called inelastic mean free path (IMFP) varies with its KE as shown in Figure 2.6, and is extremely short (of the order of a few angstroms) when the KE of the electron is just in the range 50-200 eV. Thus, photoemission spectra reflect the electronic and chemical properties of the top few atomic layers rather than those in the bulk. In addition, the surface sensitivity of the photoemission measurement can be further enhanced by a proper choice of parameters such as the photoelectron emission angle. These advantages have made PES an exceptionally important and powerful tool in the surface and interface analysis.

2.1.4 Near edge X-ray absorption fine structure

While PES offers an experimental approach to the occupied electron states, NEXAFS (near edge X-ray absorption fine structure) also named XANES (X-ray absorption near edge spectroscopy) is another widely used surface characterization technique that probes the unoccupied electronic states [41]. The fundamental principle underlying NEXAFS is similar to the photoemission process, in which an electron residing in the core-level of an atom (initial state) absorbs an incoming photon and is excited into an unoccupied final energy state. But unlike the extended, free electron final state of the emitted photoelectrons, the final state of the excited electron in NEXAFS is a bound state. For an electron in a core level of an atom, a specific amount of energy is required to excite this electron to the unoccupied states near the Fermi level. In a simple picture, when the incident X-ray photon energy just reaches the energy gap between the core-level and the unoccupied state, the absorption of X-ray photons is significantly enhanced due to the emergence of the corresponding excitation channel. However, the absorption will slowly decrease if the energy of the incident X-ray photon increases further. It is reasonable to expect that absorption thresholds vary for different chemical elements. Thus, X-ray absorption can also be used to detect elemental composition.

In fact, the absorption of X-rays is more complicated than the simple picture outlined above. A real X-ray absorption spectrum is measured by sweeping the incident photon energy (Figure 2.7). The structure close to the absorption edge (10 - 50 eV) is known as the NEXAFS region. The structures located at higher photon energies (50 - 1000 eV above absorption edge) are the extended X-ray absorption fine structure (EXAFS) that exhibits weak oscillations due to interference between back-scattered electron waves with forward-propagating electron waves. We focus on NEXAFS region in this study.

In NEXAFS, an electron is excited from the occupied state, the core level, to the discrete unoccupied state by an X-ray photon. The density of the unoccupied states dominates the measured spectrum. Moreover, the nature of the unoccupied state (e.g. symmetry) also has a very important effect on the intensity of the transition through the transition probability between these two states. In molecules, the relative direction between the transition dipole moment of various chemical bonds (π^* and σ^*) and light polarization has a strong influence on the intensities of related resonant transitions. Therefore, by performing angular-dependent NEXAFS measurements, the orientation of absorbed molecules relative to the substrate can be determined [41].

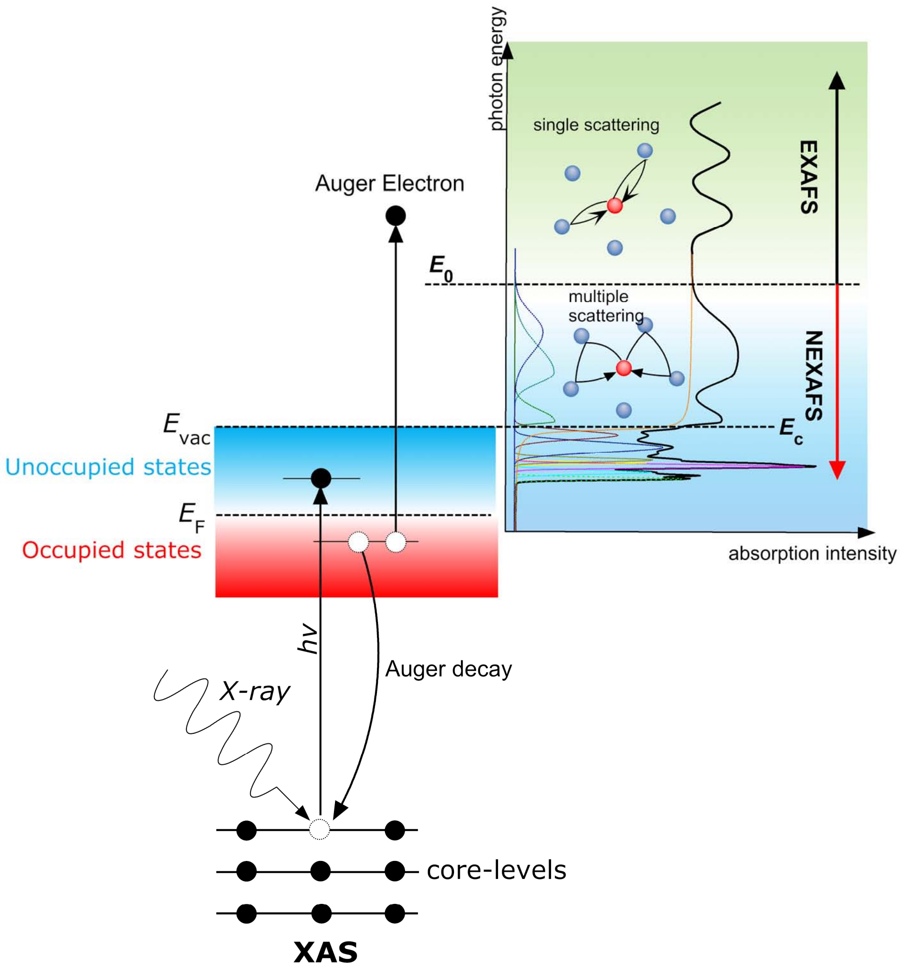

Figure 2.7. Schematic diagram of the X-ray absorption transition and the associated Auger decay channel. Showing on the right is a typical XAS spectrum with distinguishable parts: the low-energy NEXAFS region with discrete structure originating from core electron transitions to unoccupied states (dotted lines shows the deconvolution fittings), the NEXAFS region with multiple scattering processes in the continuum states (between E_0 and E_c), and the EXAFS region with single scattering processes at higher energies.

In principle, NEXAFS may be measured directly by detecting the transmitted radiation, according to the simple absorption relation:

$$I = I_0 \bullet e^{-\mu z} \tag{2.6}$$

where μ is the absorption coefficient, and z is the sample thickness. However, the necessity to prepare very thin samples makes this direct measurement approach unrealistic for many samples. As shown in Figure 2.7, the electron in the excited state created by photon absorption is unstable and will undergo certain decay processes to a state with lower energy. Auger decay is one of the most common decay processes: after a valence electron falls into the core hole created by x-ray photon absorption, an electron in another valence band state may be “kicked out” and its KE is independent of the incident x-ray photon energy. An NEXAFS spectrum thus can be achieved by measuring the flux of electrons from a particular Auger process as a function of photon energy (Auger electron mode). Fluorescence is another process for core-hole decay in which characteristic photons are emitted instead of electrons, but it occurs with a much lower probability. NEXAFS with excellent signal to noise ratios are also commonly achieved in so-called total electron yield (TEY) mode by detecting the sample current or partial electron yield (PEY) mode by using an electron yield detector.

The above techniques give yields proportional to the absorption coefficient. However, the probing depth varies between different techniques. Transmission and fluorescence modes have a large probing depth comparable to the X-ray penetration depth, while the Auger electron mode and PEY are more surface sensitive (~ 1 nm). The TEY signal is more bulk sensitive than AEY and PEY, but is still considered a surface characterization technique. Finally, because NEXAFS measurements require an intense and continuously tunable radiation source, they must be performed at a synchrotron facility.

2.2 Sample preparation

2.2.1 CVD diamond (001)

The diamond sample used throughout the experiments is a 4 mm × 4 mm, 1 mm thick, single crystal diamond grown epitaxially with (001) orientation on a High Pressure

High Temperature (HPHT) synthetic type IIb[1] single crystal diamond substrate. The epitaxial layer with a thickness about 1 μm was grown by microwave plasma assisted CVD (MPCVD) technique using 0.1% methane in hydrogen [4, 13]. To enhance the film conductivity for the PES measurement, the CVD epitaxial layer is doped with boron (10^{16} cm^{-3}) by using diborane (B_2H_6) gas during the CVD process at a concentration of 1 ppm relative to hydrogen.

2.2.2 Sample treatment-*ex situ*

Before experiments, the diamond sample is routinely cleaned and treated by acid and hydrogen plasma. Metallic impurities are first dissolved in hot aqua regia (HNO_3:HCL = 1:3), followed by removing organic adsorbates from diamond sample by hot "piranha" solution of $1H_2SO_4$:$3H_2O_2$ for 10 minutes at 90 °C [42]. After acid treatment, the sample is rinsed thoroughly in acetone solution to remove the acid. After the sample dries, it is transferred to a microwave plasma chamber for hydrogen plasma treatment. It is known that the hydrogen plasma treatment can etch away the oxygen containing species left behind by acid and in the meantime makes the diamond surface atomically smooth with hydrogen-termination [43-45]. The hydrogen plasma treatment (Figure 2.8) is performed at the microwave power of 1000 W, 30 torr hydrogen pressure, and 300 sccm of hydrogen gas flow with diamond heated around 800-1000 °C (appearing red hot during treatment) for 10-15 minutes in a 2.45 GHz microwave plasma reactor (*Astex*). After sample temperature cools down to RT, the diamond sample is taken out for the next step of experiments.

---

[1] A type II b diamond contains very low or undetectable amount of nitrogen impurities so that the boron acceptors are uncompensated and diamond behaves as a *p*-type semiconductor.

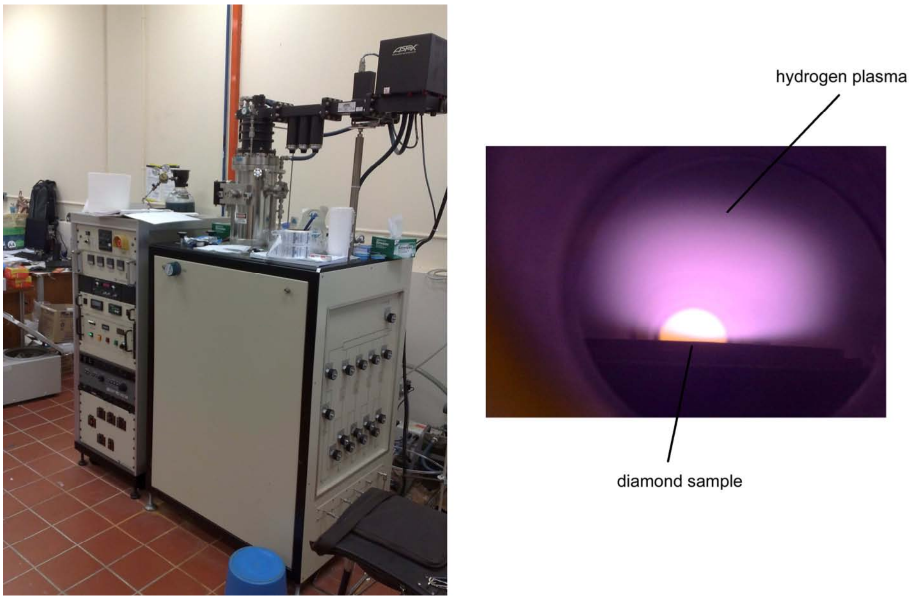

Figure 2.8. Left: microwave hydrogen plasma reactor. Right: diamond sample viewed through one of the viewports during plasma treating.

2.2.3 Sample treatment-*in situ*

After the plasma treatment, the hydrogen termination of diamond surface protects it from reacting with atmospheric species. The diamond sample is then clamped with Ta foil on top of a diamond coated highly doped silicon substrate. Together they are mounted on an *Omicron* direct-heating sample holder (upper left in Figure 2.9). When annealing, the current will mainly pass through the underlying highly conductive silicon ($R \sim 1 - 2\ \Omega$) to produce heat which anneals the diamond sample. The sample is then transferred to our UHV (ultra-high vacuum) analysis chamber at the SINS (acronym for **S**urface, **I**nterface and **N**anostructure **S**cience) [46] beamline of SSLS (Singapore Synchrotron Light Source) for further treatment. After pumping down to a pressure of 10^{-9} mbar in the fast-entry load-lock system attached to the main chamber, the sample is transferred to the sample stage of the manipulator inside the main analyzing chamber with a base pressure of 1×10^{-10} mbar (right in Figure 2.9). Before experiments, the sample is annealed by direct-heating at the current of 0.5 A (T ~

100 °C) for several hours or overnight to desorb water and other weakly adsorbed contaminations. If required, the sample can be further annealed by direct-heating at higher current with temperature as high as 1200 °C. The sample temperature is monitored by two different methods. Below 400 °C, it is given by a thermocouple attached to the back side the sample stage. It needs long time for the sample stage to reach thermal equilibrium with the sample, and so the temperature reading is underestimated by around 50 °C. At higher temperatures, the silicon substrate becomes dim red and the temperature is determined by an optical pyrometer that directly measures the thermal radiation from silicon. This method is fast and accurate but limited to the high temperature range.

2.2.4 Organic molecule adsorption and deposition

Depending on the type of organic molecules, two different approaches are adopted for molecular adsorption or deposition on diamond. All chemicals are directly purchased from chemical companies such as *Sigma Aldrich* with highest available purity. For simple organic molecules in the form of compressed gas or liquid with high vapour pressure (e.g. 1,3-butadinene), they are introduced into the UHV chamber as a vapour through a precision leak valve without further purification. The dosing was usually carried out at RT unless specified otherwise. During molecular dosing, the chamber pressure is monitored by an ion gauge. The dosing pressures are normally in the range of 10^{-8}-10^{-6} Torr and are not corrected to account for the relative positions of the leak valve with respect to the sample and ionization gauge. All dosages are expressed in Langmuir (L), where $1\ \mathrm{L} = 1\times10^{-6}\ \mathrm{Torr} \cdot \mathrm{s}$.

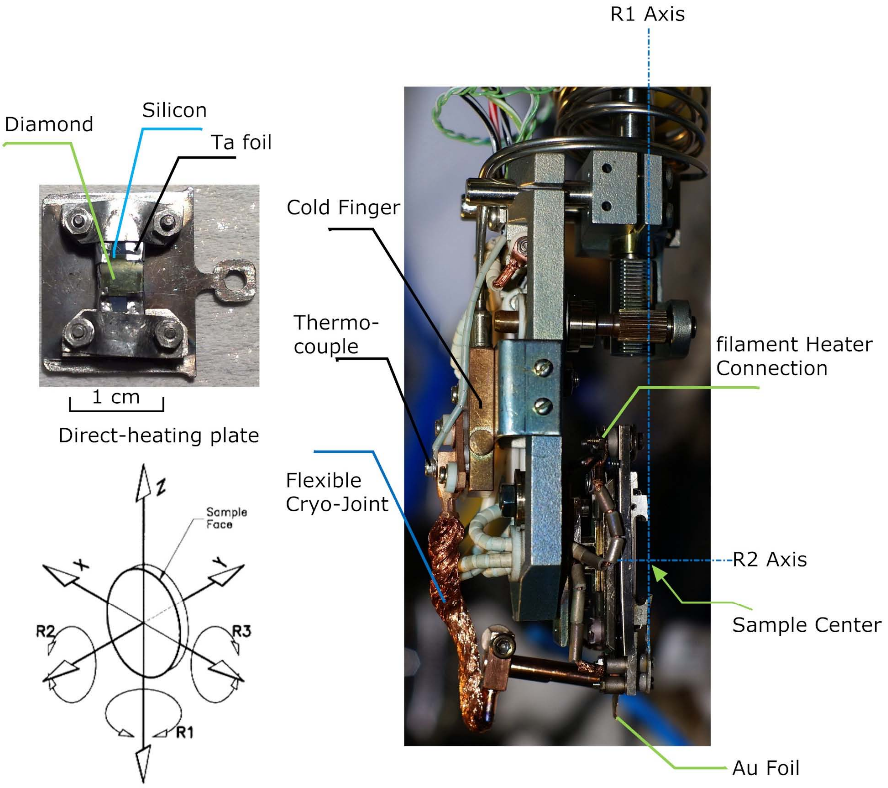

Figure 2.9. Upper left: direct-heating sample plate with diamond sample mounted. Lower left: rotational axis and translational axis of sample on sample stage. Right: key components of the sample stage for sample handling in vacuum.

A standard effusion cell (*MBE Komponenten*, Figure 2.10) is used to *in-situ* sublime solid organic molecular sources (e.g. fullerene, copper phthalocyanine) which are put into pre-degassed PBN or quartz crucibles. The diamond sample is directly facing the effusion cell at a distance of around 20 cm, and is kept at RT during the entire deposition process. The organic sublimation temperature varies with different organic sources, and is usually in the range of 100 °C to 500 °C (c.f. Table 2.1). Accurate temperature control is realized through a feedback loop, consisting of a thermocouple inside the effusion cell and a power supply that controls the output power of the heating elements. Upon loading into the effusion cell, the source is thoroughly degassed around 100 °C overnight. Before actual deposition, the source undergoes several heating-cooling cycles up to the sublimation temperature for further

Table 2.1. The sublimation temperature for organic molecule sources.

Molecules	CuPc	F_4-TCNQ	TCNQ	C_{60}	$C_{60}F_{48}$
Temperature	360 ~ 440 °C	100~150 °C	100~150 °C	350~450 °C	180~200 °C

purification. To avoid overheating the source which could lead to decomposition of the molecules, the maximum output power is limited at slightly above the sublimation power, and the temperature set-point in controller is increased stepwise in small intervals until it reaches the desired sublimation temperature.

The nominal thickness of deposited organic films on diamond is estimated from the attenuation of the PES intensity of diamond C 1*s* main line by assuming a near layer-by-layer (Frank-van der Merve) growth mode for organic layers:

$$I(d) = I_0 \exp(-\frac{d}{\lambda \cos\theta}) \tag{2.7}$$

where I_0 is the initial C 1*s* intensity of pristine diamond, $I(d)$ is the intensity after deposition, d is the nominal thickness of organic films, and θ is the angle between analyzer detecting direction and sample surface normal direction. λ (in nanometer) is

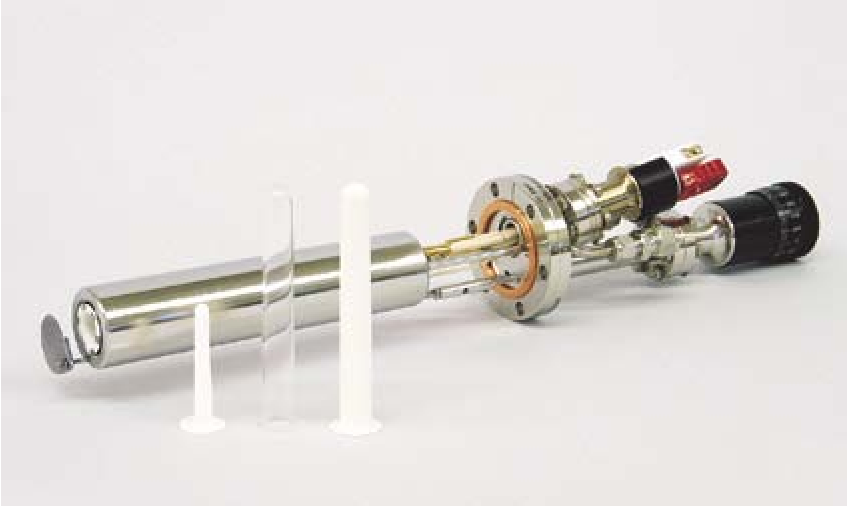

Figure 2.10. The effusion cell for solid organic molecular sources. In front are the crucibles made from PBN and quartz (picture courtesy of *MBE Komponenten*).

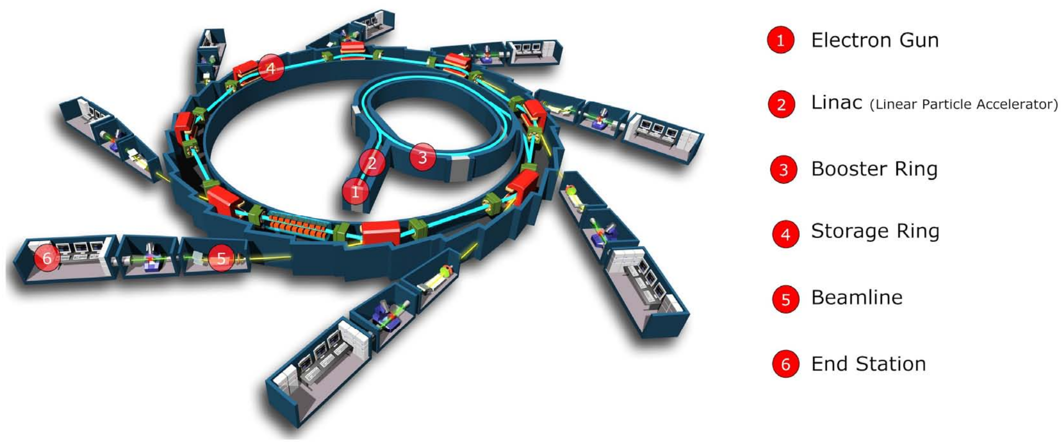

Figure 2.11. A schematic of synchrotron facility [48].

the IMFP of photoelectrons in organic films which depends on the KE of photoelectrons (E_{kin} in eV) and the density of organic films (ρ in g/cm^{-3}) according to the following empirical relation [47]:

$$\lambda = (49E_{\mathrm{kin}}^{-2} + 0.11E_{\mathrm{kin}}^{1/2}) / \rho \ . \tag{2.8}$$

2.3 Experimental system

2.3.1 Synchrotron radiation

Synchrotron radiation is an intense light source of electromagnetic radiation with tunable photon energy. It utilizes the physical phenomenon that when charged particles (usually electrons) accelerated at velocities close to the speed of light are forced to bend in their trajectories by strong magnetic fields, they emit extremely bright light in a narrow cone in the forward direction tangent to the electron orbit. Synchrotron radiation has numerous unique properties, such as high intensity and brilliance, wide energy spectrum from infrared to hard X-rays, high polarization and very short pulse, making it one of the most powerful scientific instruments with wide applications spanning almost every scientific field. In particular, its wide energy spectrum enables us to continuously tune the wavelength of the photon beam to desired values, facilitating the PES and XAS measurements introduced above.

As shown in Figure 2.11, the central part of a synchrotron facility is the electron storage ring, where electrons circulate for many hours. UHV is required to limit the loss of electrons due to collisions with residual atoms or molecules in the ring. Along the storage ring are the light emitting devices comprising of bending magnets or undulators (Figure 2.12). To keep electrons traveling in closed trajectories around the storage ring, a number of superconducting bending magnets are required to deflect the trajectory of the electrons. Because of the defection, an electromagnetic wave is generated and propagates. The bending magnet was the only emitting device in the first and second generation synchrotron facilities.

To further boost the flux and brightness of synchrotron radiation, 3rd generation synchrotrons use insertion devices known as undulators. An undulator is a periodic magnet array inserted in a straight section of the storage ring. Each magnet slightly deviates the moving electron and induces an oscillation of the electron in the plane parallel to direction of motion of the electron. Compared to the bending magnet, the undulator emission spectrum is quite sharp, emitting a narrow band around the fundamental wavelength with several orders of magnitude higher flux.

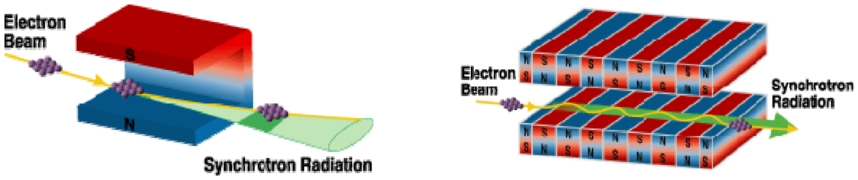

Figure 2.12. Two common synchrotron light emitting devices: a bending magnet (left) and an undulator (right) [49].

Table 2.2. Key parameters of Helios 2 [50].

Parameter	Unit	Value
Electron Energy	MeV	700
Magnetic Field	T	4.5
Charateristic photon energy	keV	1.47
Charateristic photon wavelength	nm	0.845
Current (typical)	mA	500
Circumference	m	10.8
Lifetime	h	>10
Emittance	µmrad	1.37
Source diameter horizontal	mm	1.45-0.58
Source diameter vertical	mm	0.33-0.38
Number of beam ports		20 + 1
Horizontal angular aperture of port	mrad	60

2.3.2 Singapore Synchrotron Light Source

The Singapore Synchrotron Light Source (SSLS) is a second generation light source comprising a compact 700 MeV superconducting storage ring (Helios 2) with 4.5 T bending magnets to produce synchrotron radiation. The key parameters of the synchrotron facility are listed in Table 2.2. The radiation spectrum extends from about 10 keV down to the far infrared at wavenumbers of less than 10 cm^{-1}.

Although the SSLS is smaller as compared to other major synchrotron facilities in the world in terms of dimensions and beam energy, it has developed a broad scope of research activities ranging from materials characterization, micro/nanofabrication, environmental sciences, to archaeology and even forensic science. Till now, five beamlines have been built and running in SSLS, with several new beamlines proposed in the coming years. The five existing beamlines (Figure 2.13) include XDD beamline

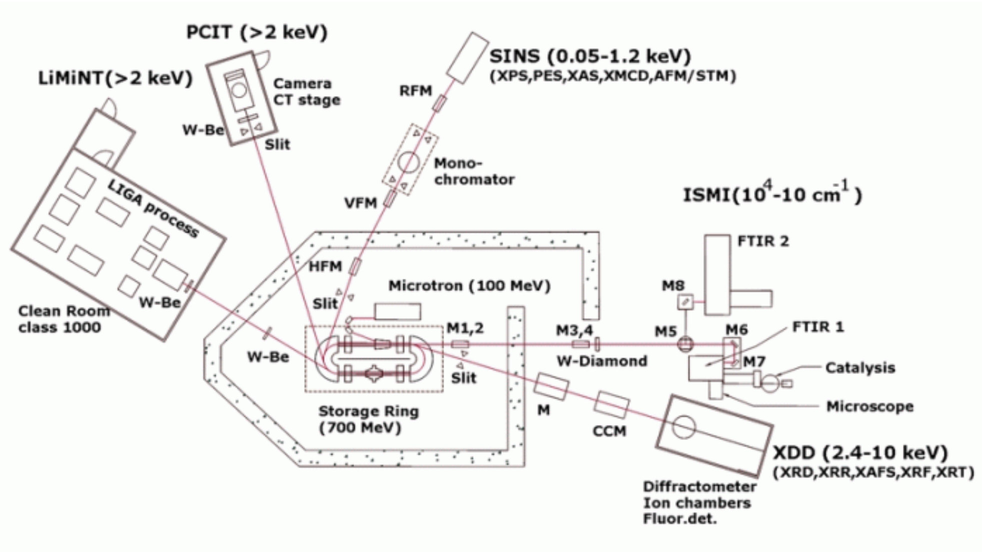

Figure 2.13. Schematic layout for the storage ring and beamlines of SSLS [50].

for X-ray diffraction and XAS, ISMI beamline for infrared spectroscopy, LiMiNT beamline for X-ray deep lithography and LIGA process, PCI beamline for phase contrast image, and finally SINS for surface and interface studies with soft X-ray spectroscopies [51]. As this thesis work has been mainly carried out at the end station of the SINS beamline, it will be introduced in more detail.

2.3.3 SINS beamline and end-station

The SINS beamline provides synchrotron radiation in the range of 50 eV to 1200 eV for surface science experiments [46]. It is a typical dragon-type beamline (Figure 2.14) with a monochromator comprising four interchangeable spherical gratings delivering tunable monochromatized photons in the range of 50-110 eV, 110-220 eV, 220-440 eV and 440-1200 eV respectively. Three mirrors are used for beam focusing: two sit before the monochromator and decouple the focusing action into the horizontal and vertical directions, while a re-focusing mirror (RFM) behind the monochromator allows for small focusing adjustments at the experimental end-station. Two slits (entrance and exit slits) along the beamline provide control over the photon flux and

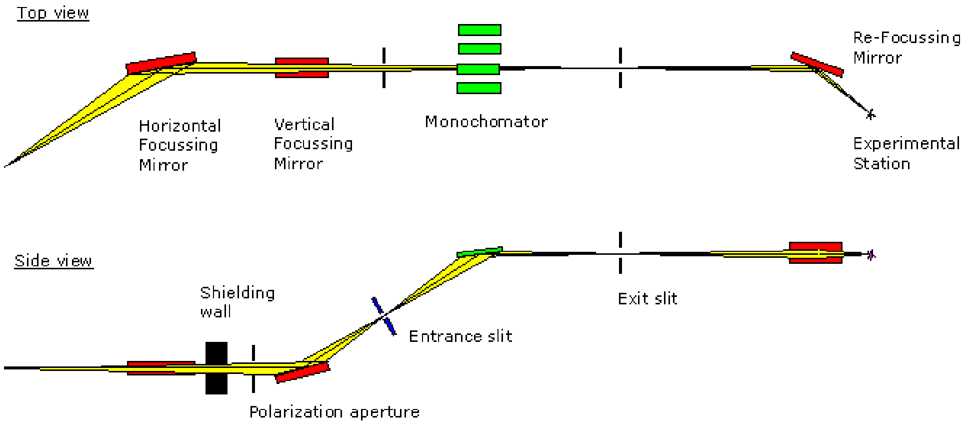

Figure 2.14. Schematic layout of the SINS beamline [50].

energy resolution. The radiation intensity of monochromatized light I_0 is determined by a Keithley which measures the photocurrent at the gold-coated RFM. The beamline has an energy resolving power better than 2000 with a photon flux of about 10^{10} photons/s/100 mA delivered into a spot size of 1.5×0.2 mm^2 (FWHM). By adjusting the polarization aperture and vertical position of the vertical focusing mirror, the polarization of light can be tuned from linear polarization (parallel to incident plane) to circular polarization (both left and right helicity).

The beamline has a fixed end-station consisting of an analytical chamber and a preparation chamber (Figure 2.15). The two chambers are interconnected through a gate valve and are pumped separately by turbo-molecular pumps, ion pumps and sublimation pumps. The base chamber pressure after the baking out is better than 2.0×10^{-10} mbar. The end-station is equipped with a number of surface analytical instruments that include an ion sputtering gun to clean the sample, LEED optics, twin anode (Mg, Al) standard x-ray source (as back-up), *Omicron* STM/AFM, an *Omicron* hemisphere energy analyzer with 7 channeltron electron multipliers for angular-resolved photoemission. A sputtered clean gold foil in electric contact with the sample is used to calibrate the photon energy. BE of all PES spectra are thus referenced to the

Fermi level of the gold foil. The end-station also has *in-situ* material deposition capabilities with two e-beam evaporators for molecular beam epitaxy (MBE) of metals (Co, Fe, Ni, etc.), and several standard effusion cells (*MBE Komponenten*) for the growth of organic materials. A transfer system with fast-entry load lock is installed in order to change samples without breaking the UHV condition. Another long transfer arm allows the transfer of samples between the two end-station chambers. Sample annealing can be achieved by direct heating as well as resistive heating using heating filaments. The end-station has the capability to perform several synchrotron-based spectroscopy measurements including angular-resolved PES, NEXAFS, XPD (X-ray photoelectron diffraction), XMCD (X-ray magnetic circular dichroism). The overall energy resolution for PES is better than 100 meV at a 5 eV analyzer pass energy, and for NEXAFS is better than 300 meV.

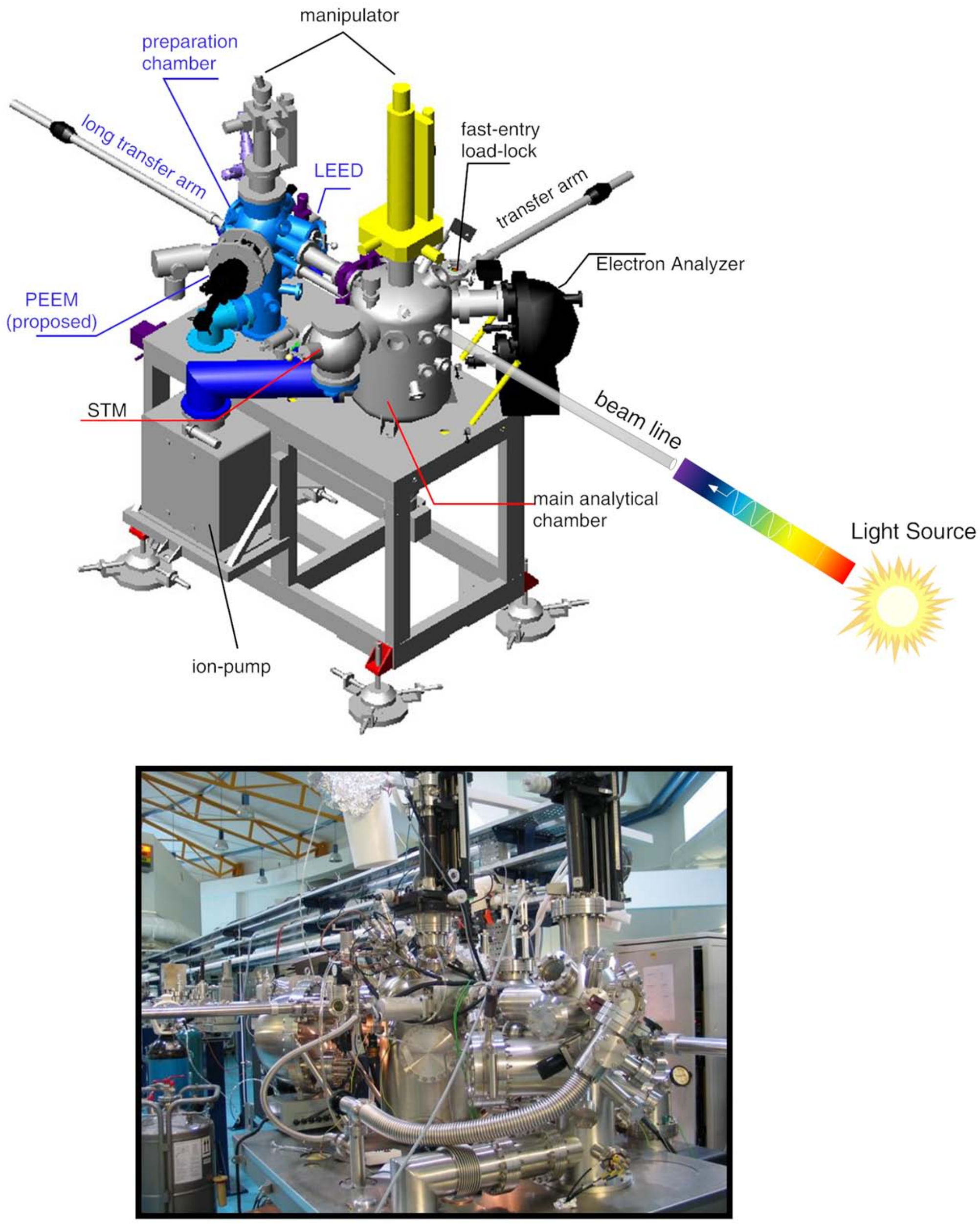

Figure 2.15. A schematic drawing (upper panel), and photograph (lower) of the end-station of SINS beamline.

CHAPTER 3

DIAMOND (001) SURFACE: STRUCTURES AND PROPERTIES

3.1 Introduction

Surfaces are sometimes referred as the largest defects in real materials. The transition from bulk material to vacuum, gas, liquid overlayers or other adsorbates inevitably introduces dangling bonds, broken symmetry, impurity-atom termination, atomic reconstruction or surface dipoles, which lead eventually to surface or interface states. For semiconductors, these surface or interface states define the remarkable electronic and structural properties of semiconductor surfaces, which are closely related to the properties of semiconductor electronic devices. As a result, semiconductor surface and interface science has become a fascinating field of research for both experiment and theory.

A remarkable property of a semiconductor is its surface reconstruction (i.e. atomic rearrangement of surface atoms), by which the ideally truncated semiconductor surfaces reduces the density of dangling bonds and therefore its total surface energy [52-53]. The surface adsorbates or overlayers can further lower the total surface energy by forming chemical bonds with the remaining dangling bonds of semiconductor surface atoms.

Figure 3.1 shows the ball-and-stick models of the ideally terminated C (001) surface, as well as the reconstructed bare and hydrogenated C (001) surfaces. On the ideally-truncated diamond (001), each surface atom exhibits two dangling bonds as illustrated in Figure 3.1a. As with surfaces of other IV-group semiconductor such as Si(001) and Ge(001), the surface atoms of diamond (001) in neighboring rows pair up to form C=C dimers in a 2×1 reconstruction symmetry as shown in Figure 3.1b [54-

55]. The dimers on diamond are untilted and symmetric [55], in contrast to the tilted dimers on silicon and germanium surfaces [53]. The formation of dimers on diamond (001) reduces the number of dangling bonds by a factor of two and thus effectively lowers the electronic surface energy. By bonding hydrogen atoms to the bare surface, the double bonds of dimers are saturated and thus the surface electronic energy is further lowered. The resulting monohydrogenated diamond (001) surface (Figure 3.1c) has the same 2×1 reconstruction symmetry as the bare surface, but is relatively inert and stable due to the elimination of surface dangling bonds. The introduction of hydrogen as an impurity-atom termination on diamond (001) not only alters the surface structures, but also brings about several unique electronic properties including true NEA and *p*-type surface conductivity, which will be discussed in the following sections.

(a) ideal truncated-bulk C(001) 1x1

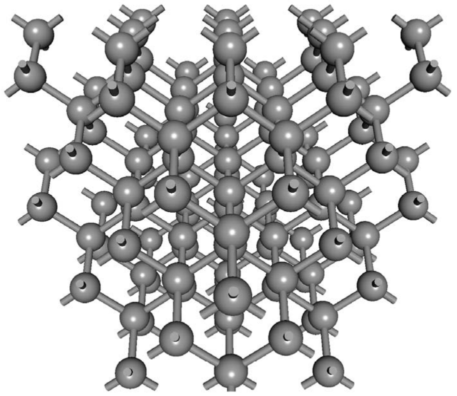

(b) C(001) 2x1

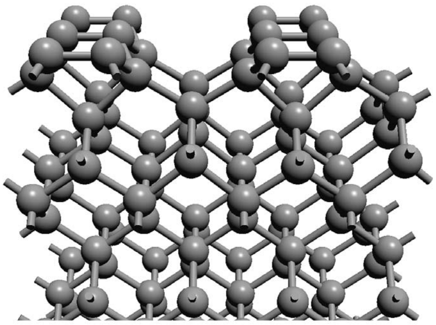

(c) C(001) 2x1:H

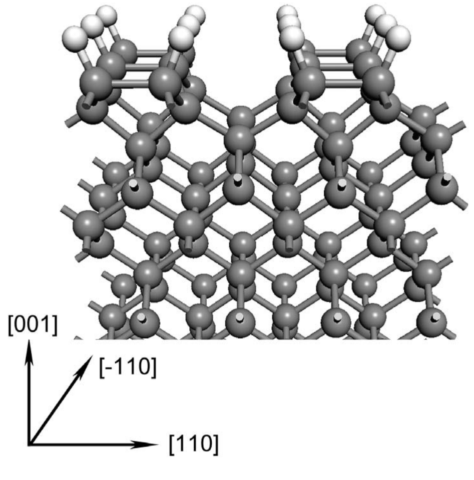

Figure 3.1. Perspective views of the atomic geometries for (a) the ideally-truncated, (b) the 2×1 reconstructured bare and (c) hydrogenated diamond (001) surfaces.

3.1.1 Band bending

Band bending is a common phenomenon at semiconductor surfaces and interfaces. It refers to the gradual changes in the electron energy levels from the surface/interface region to the bulk interior. Band bending arises from the spatially extended space-charge layers due to charge transfer at surfaces or interfaces. The width of band bend region is usually large, which is a result of the large screening lengths of semiconductors (due to low densities of free charge carriers). Band bending also occurs on diamond surfaces (bare and hydrogenated), and they are technologically important to diamond based device applications that exploit diamond surface properties.

In general, the band bending mechanism can be understood as the following: for *n*-type (*p*-type) semiconductors, the bulk Fermi energy (E_F) is largely determined by the bulk doping level. However, the surface electronic states, which are inherently related to the surface reconstruction and geometry, are fixed within the band gap. As a result, the surface Fermi energy (E_F^{sur}) is also pinned at a relatively stable position above the valence band maximum (VBM) irrespective of whether the samples are *p*-type or *n*-type doped. Such *pinning of the Fermi level at the surface* causes E_F^{sur} and the bulk Fermi level E_F to not typically coincide, facilitating electron transfer between bulk dopant and surface states. The resulting charge residing at the surface states is compensated by an equal amount of charge with opposite sign forming in a certain extended depth into the semiconductor interior. At the same time, the electric field created by the charge build-up alters the energy band from surface to bulk. The mechanisms are illustrated more clearly in Figure 3.2 and Figure 3.3.

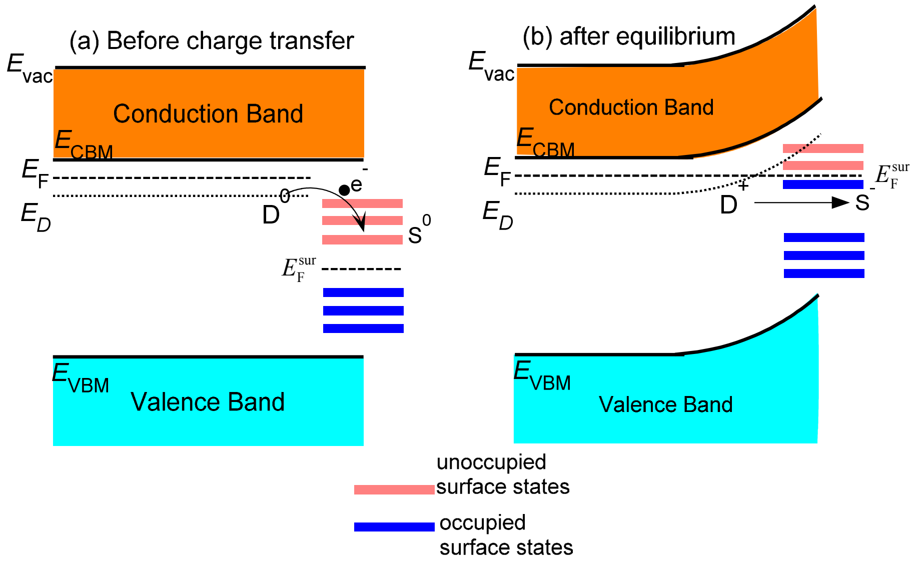

Figure 3.2. Schematic of the mechanism for band bending in a typical *n*-type semiconductor. (a) Bulk Fermi level E_F is far above surface Fermi level, favoring electron transfer from neutral donor impurities (D^0) to unoccupied surface states (S^0). (b) During charge transfer, an electric field is thus created between the negatively charged surface states (S^-) and ionized donor states (D^+), which bends the energy bands upward toward the surface. This process ends after equilibrium is reached where the bulk and surface Fermi levels are aligned.

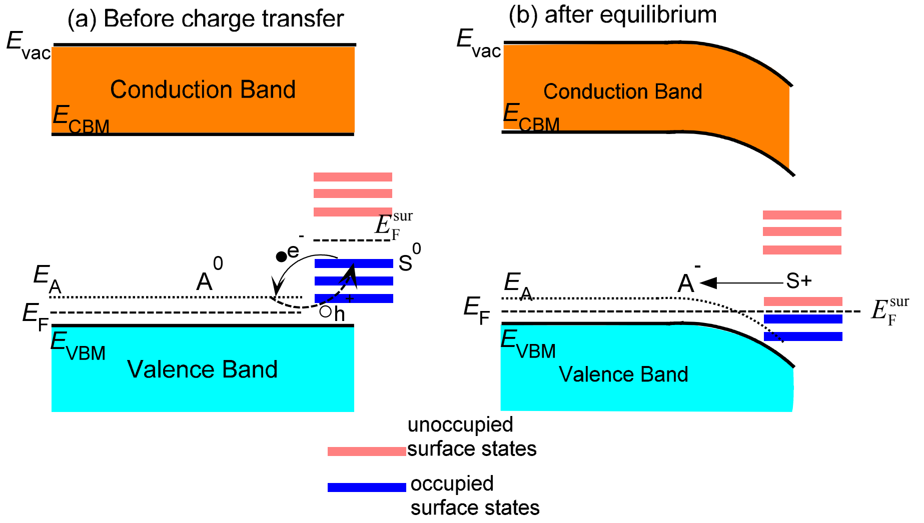

Figure 3.3. Schematic of the mechanism for band bending in a typical *p*-type semiconductor. (a) Bulk Fermi level E_F is far below surface Fermi level, favoring electron transfer from neutral occupied surface states (S^0) into neutral acceptor impurities (A^0). (b) During charge transfer, an electric field is thus created between the positively charged surface states (S^+) and negatively charged acceptor states (A^-), which bends the energy bands downward toward the surface. This process ends after equilibrium is reached where the bulk and surface Fermi levels are aligned.

In the above-mentioned *n*-type and *p*-type semiconductors, the band bending depletes the majority carriers. The exact position of E_F at the surface within the bands of surface states, the amount of band bending and the depth of the space charge layer is determined by charge neutrality and Poisson's equation [52]. As described in CHAPTER 2, the diamond sample used in this study is boron-doped (*p*-type). Therefore, the expected band bending should be downward towards the surface as depicted in Figure 3.3.

3.2 Hydrogenated diamond C(001)-2×1:H surface

3.2.1 Surface reconstruction

The monohydrogenated diamond C (001)-2×1:H surface is prepared by hydrogen plasma treating in a microwave reactor as described in Chapter 2. Alternative surface treatments for hydrogenated diamond surface include *in-situ* exposure of the surface to atomic hydrogen produced by a hot tungsten filament as well as by acid etching; however, the surface order and smoothness are not as good as in hydrogen plasma treating. The atomic arrangement of the hydrogenated (001)-2×1:H diamond surface is shown in Figure 3.4a, where the top view can better illustrate the 2×1 reconstruction symmetry. In general, the monohydride diamond dimers are symmetric, analogous to its counterparts of monohydride Si and Ge (001) surface dimers. The bond length of the hydrogenated C–C dimer is 1.60±0.05 Å as determined by *I-V* LEED [56], as well as by theoretical calculations (1.61 Å) [55, 57], which is slightly larger than a single C–C bond in a hydrocarbon molecule (e.g. *d*(C–C) = 1.55 Å). The relaxed C–H bond length is determined to be 1.11 Å, with the angle between C–H bond and surface normal at 24.5° [55, 57].

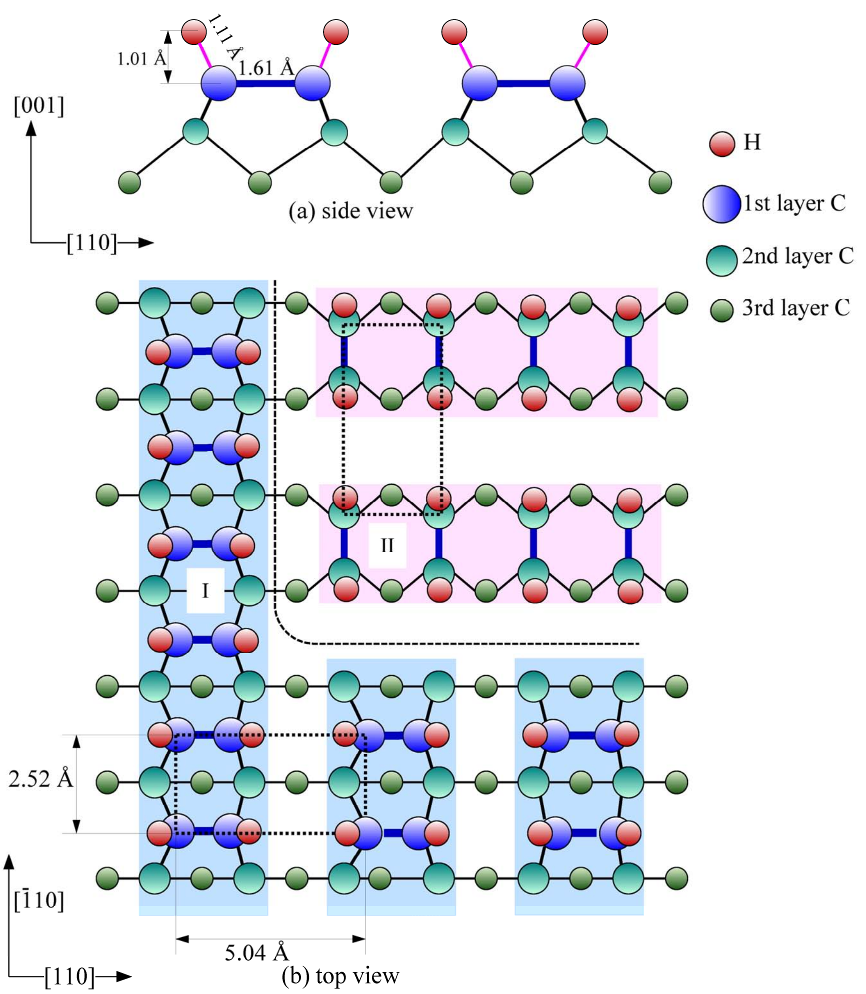

Figure 3.4. (a) Side view of atomic arrangement of the monohydrogenated diamond (001)-2×1:H surface. The colored circles with different size represent hydrogen atoms and carbon atoms belonging to the top four surface layers. The dimer bonds are represented by thick blue sticks. (b) Top view of a two-domain 2×1 reconstructed surface containing a monoatomic step. The domain labeled I and II represent the upper and lower terrace, respectively. The dimer rows in each domain are highlighted by colored shadings. The dashed line schematically indicates the domain boundary. The surface lattice meshes in each domain are indicated by a rectangular with dotted border.

The 2×1 reconstruction is formed by paring of adjacent rows of surface atoms; therefore the periodicity is doubled either along the [110] or [$\bar{1}$10] direction depending on which surface layer they belong to, and the dimer rows run along [$\bar{1}$10] or [110] accordingly as schematically shown in Figure 3.4b with different color shadings. These two 2×1 domains are therefore rotated by 90º from each other and separated by monoatomic step of height *a*/4 (*a* is the lattice constant of diamond). Since the domain

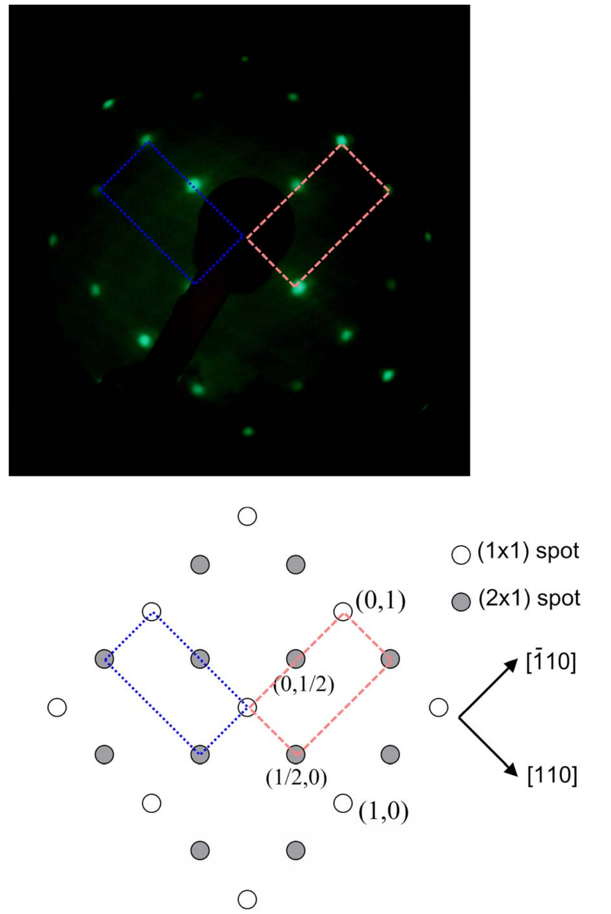

Figure 3.5. LEED pattern (upper panel) and its schematic representation of the hydrogenated C(001)-2×1:H diamond surface (electron beam energy 165 eV). The dashed rectangular boxes represent the reciprocal lattices of the two orthogonally oriented 2×1 domains.

sizes are usually much smaller than the LEED probing area, both orthogonally oriented 2×1 domains can be observed in the diffraction patterns as shown by the (0, 1/2) and (1/2, 0) LEED spots with similar intensities (Figure 3.5). It should be noted that the absence of the (1/2, 1/2) spots explicitly distinguishes it from a 2×2 reconstructed surface.

The hydrogenated diamond (001)-2×1 surface is most clearly visualized by the STM in Figure 3.6. The bright lines correspond to the CH–CH dimer rows. The existence of two different surface domains (terraces) separated by a monoatomic step is demonstrated by the dimer rows running in orthogonal directions. The distance

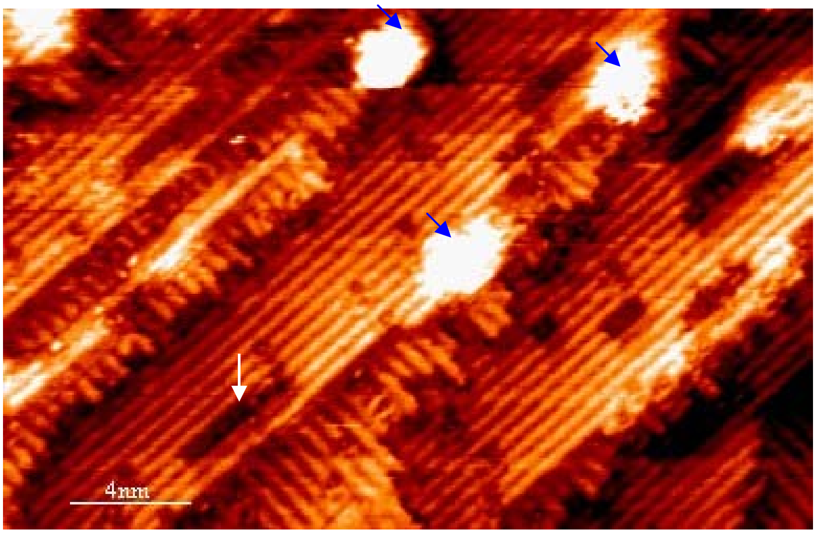

Figure 3.6. STM topographies of the hydrogenated diamond C(001)-2×1:H surface (U_{bias} = 1.5 V, I_t = 1.0 nA). The scale bar indicates the length of 4 nm.

between the bright lines roughly corresponds to the expected inter-row distance (5.04 Å) of the surface dimers. However, due to limits to resolution, individual dimers in the dimer rows cannot be resolved. Defects structures, such as the missing row marked by the white arrow in Figure 3.6, are also commonly observed. The bright features (as marked by blue arrows) which are most often observed at the step edges might be due to dangling bonds caused by local hydrogen desorption [58].

3.2.2 Electronic structures

3.2.2.1 PES of hydrogenated diamond surface: surface core-levels and valence band structures

Surface reconstruction not only alters the surface atomic arrangement, but it also influences the electronic structures of the surface atoms, making them remarkably different from those of corresponding bulk atoms. Hence, the surface atoms of semi-conductors often exhibit surface-induced shifts of core-level BE as well as the appearance of surface states within the bulk band gaps. Therefore, the study of surface electronic structures can provide valuable information about the structure and bonding

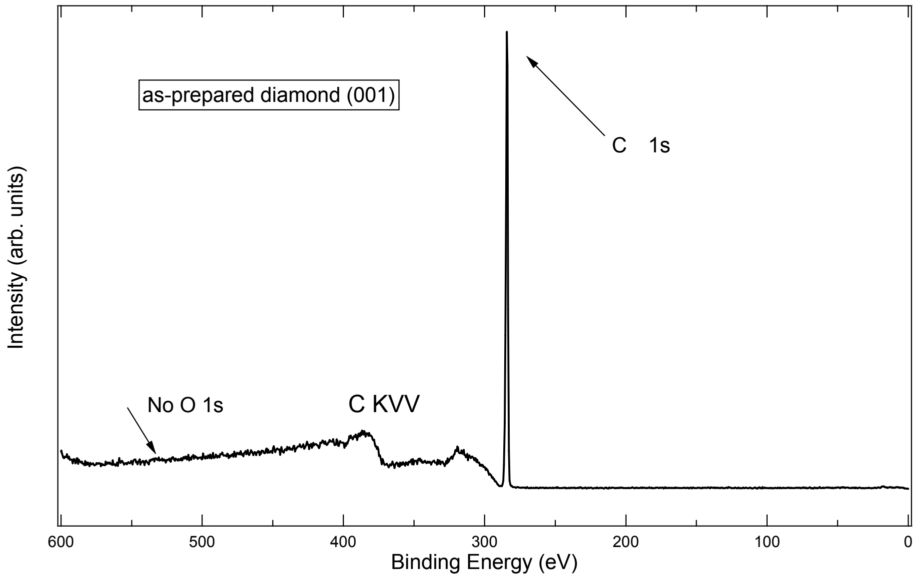

Figure 3.7. PES wide scan of an as-prepared hydrogenated diamond (001)-2×1:H surface with photon energy of 650 eV. The peak origins are labeled in the graph. The emitted photoelectrons are collected at surface normal direction.

arrangements at the surface, giving insights into numerous surface related macroscopic effects and phenomena [52-53]. High-resolution synchrotron-based PES with high surface sensitivity is a powerful tool for the investigation of the surface electronic structures of solids.

The surface cleanliness of freshly prepared hydrogenated diamond sample after hydrogen plasma treatment is demonstrated by the wide scan photoelectron spectrum recorded at the photon energy of 650 eV as shown in Figure 3.7, where no extrinsic species other than carbon are present within PES detection limit of less than 1%, indicating the inert and stable nature of this surface. Although it is well known that a physisorbed water adlayer is naturally present on solid surfaces exposed to atmosphere, the water molecules apparently desorb in ultrahigh vacuum, as revealed by the absence of any prominent peak in the O 1*s* spectral region (BE around 531 eV).

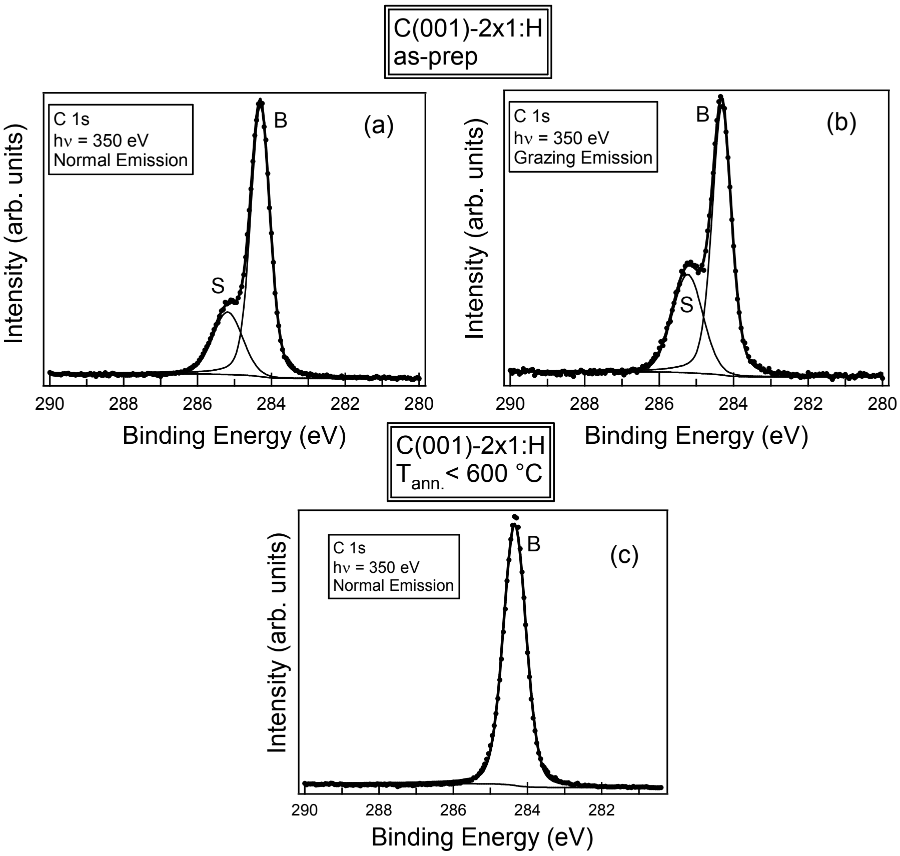

Figure 3.8. C 1*s* core-level spectra of a hydrogenated diamond (001) surface (*hv* = 350 eV). **Top**: as-prepared sample after a microwave hydrogen plasma treating with (a) normal emission angle (bulk sensitive) and (b) 50º emission angle relative to surface normal (surface sensitive). **Bottom**: annealed at 400~600 ºC in vacuum. Solid lines through experimental points demonstrate the result of least-square fitting.

Figure 3.8 shows the C 1*s* core-level PES spectra of hydrogenated diamond (001). The spectra components are fitted with the sum of Gaussian and Lorentzian line shapes (pseudo-Voigt functions) with Shirley background removed. The fitting results are summarized in Table 3.1. The high surface sensitivity of PES spectra was achieved by selecting a photon energy of 350 eV, which yields C 1*s* photoelectrons at kinetic energy of about 65 eV with a short electron IMFP well below 10 Å. The upper two spectra in Figure 3.8 show the C 1*s* core-level spectra of diamond (001) as-prepared after hydrogen plasma treatment. In addition to the main bulk C 1*s* peak (labeled *B*) at 284.30 eV, a component (labeled *S*) shifted by 0.9 eV towards higher

Table 3.1. Summary of the C 1*s* core-level fitting analysis for the diamond (001) with different surface conditions. θ refers to the photoelectron emission angle relative to the surface normal, E_B to the BE of each component, FWHM to the width of the component line-shape, L/G to the Lorentzian- Gaussian mixing ratio of the fitted line-shape, and area ratio to the relative contribution of each component to the total emission intensity.

(001) surface	**Emission angle θ**	**Component**	**E_B (± 0.05 eV)**	**FWHM**	**L/G (%)**	**Area ratio (%)**
as-prepared *hydrogenated*	0°	Bulk *B*	284.30	0.61	27	75
		Surface *S*	285.20	0.94	10	25
	50°	Bulk *B*	284.30	0.61	33	66
		Surface *S*	285.20	0.96	10	34
ann. at 400~600 ºC *hydrogenated*	0°	Bulk *B*	284.30	0.72	22	100
ann. at 1050 ºC *bare*	0°	Bulk *B*	284.90	0.77	14	69
		Surface S_D	283.95	0.84	14	31

BE is clearly distinguishable. By comparing the spectra at different electron emission angles, it is evident that the *S* component relative to the total C 1*s* emission intensity increases as the emission angle (θ) changes from normal emission (bulk sensitive) to grazing emission (surface sensitive) (c.f. Table 3.1), which clearly confirms that this additional component stems from the diamond surface. This surface component is attributed to adsorbed hydrocarbons which are the by-products from hydrogen plasma treatment [59]. These hydrocarbons are only weakly adsorbed on the diamond surface, as *in-situ* mild annealing at 400~600 ºC is enough to remove these adsorbates, leaving the C 1*s* bulk component *B* only (Figure 3.8c). It should be noted that although the chemical environment of dimer carbon atoms bonded with hydrogen is slightly different from that of subsurface bulk carbon atoms, they are essentially indistinguishable in the C 1*s* spectra due to their small BE difference (< 0.1 eV) [59].

Valence band structures of hydrogenated diamond surface after mild annealing are probed by PES recorded with a photon energy in the ultraviolet energy range (*hv* = 60 eV), as shown in Figure 3.9. Theoretical calculations of bulk diamond band structures predict four occupied valence bands with different atomic-like characters [6]. To distinguish the different atomic-like characters in the valence bands, Figure

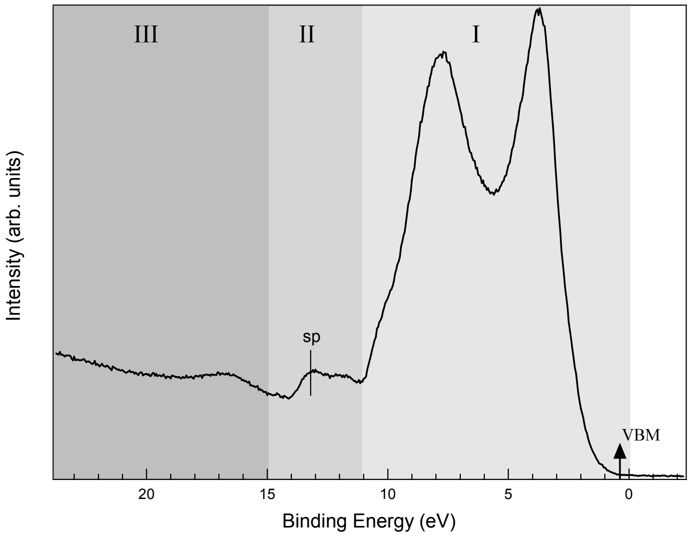

Figure 3.9. Valence band spectra of hydrogenated diamond (001)-2×1:H surface recorded with photon energy of 60 eV at normal emission angle. Different grey shading regions represent different atomic-like character of valence band structures.

3.9 is divided into different regions accordingly. The top two bands that extend to 11 eV below Fermi level (region I) have mostly *p*-character, and the lowest band after 15 eV in region III has mostly *s*-character, leaving a band of mixed *sp* character in region II between 11 eV to 15 eV with a sharp peak centered around 13.2 eV (labeled *sp* in spectra) reflecting the sp^3 bonding nature of bulk diamond lattice. Although there should be CH-CH dimer related occupied surface states as predicted by a number of theoretical calculations [55, 57], they actually reside within the valence band, and therefore are difficult to resolve in the valence band spectrum due to strong overlapping with the bulk valence bands of diamond [60].

The determination of the position of the valence band maximum (VBM) relative to the Fermi level can provide important information about the semiconductor electronic properties, such as degree of band bending, ionization potential (IP) and electron affinity (EA). Although the VBM is not directly visible in the valence band spectra, its separation from experimentally accessible spectral features such as the C

1*s* core-level line (Figure 3.8) and the *sp* peak in the valence band spectrum (Figure 3.9) are constant and thus can be used to infer its energy position. The energy difference of the VBM from the C 1*s* core-level (E_B = 284.30 eV) and *sp* peak (E_B = 13.2 eV) were previously determined by an independent calibration experiment to be 283.9 ± 0.1 eV and 12.8 ± 0.1 eV respectively [61]. The VBM is thus determined to be 0.4 ± 0.1 eV below the Fermi level (E_F) in the surface region. It is known that boron forms an acceptor level in diamond with an ionization energy of E_A = 0.36 eV. By requiring charge neutrality, the bulk Fermi level E_F was calculated by Bandis and Diederich at 0.30 eV above the VBM (E_{VBM}) for B doping level of 10^{16} cm^{-3} [62-63]. By comparison with the value of $E_F - E_{VBM}$ as determined above, the band bending (φ_{BB}) value of hydrogenated diamond (001) should be within 0.1 eV. Such a small band banding is consistent with the model in Figure 3.3, since the surface states of hydrogenated diamond lie within the bulk valence band and therefore electron transfer from occupied surface states to boron acceptors level (E_A) is not favored.

3.2.2.2 *Negative electron affinity and energy level diagram*

One remarkable property of diamond is its NEA when its surface is terminated by hydrogen. The EA in a material is defined as the energy difference between the vacuum level (VL) and conduction band minimum (CBM). For most materials, the EA value is positive, which means that secondary electrons thermalized to the CBM have to overcome an energy barrier equal to the EA in order to be emitted into vacuum, and as a result the secondary electron emission yield is relatively low. With the lowering of the barrier height (EA), more and more secondary electrons can escape from the surface resulting in increased secondary electron emission intensity. In certain specially engineered materials, the CBM can even be above the VL. With this

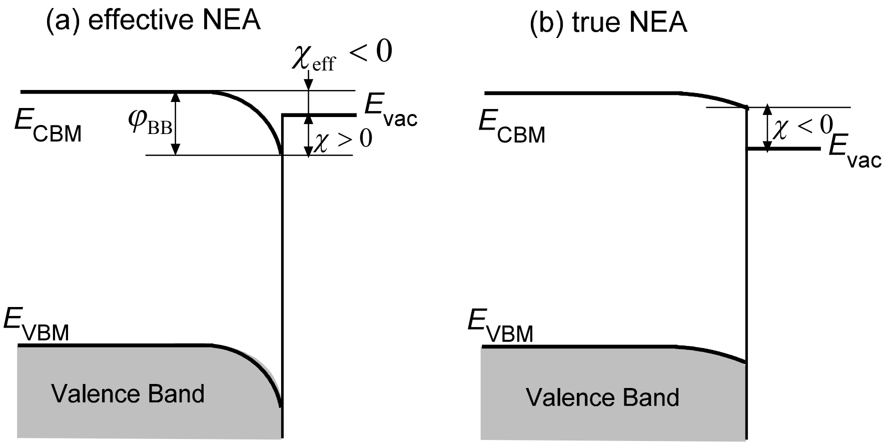

Figure 3.10. Schematic energy level diagram of a semiconductor which exhibits (a) effective negative electron affinity and (b) true negative electron affinity.

NEA, secondary electrons can be easily emitted into vacuum without experiencing any energy barrier, leading to very strong secondary electron emission yield. Therefore, semiconductors with NEA are widely used as photocathode and cold-cathode emitters.

NEA semiconductor surfaces are normally prepared by combining strong downward band bending with a monolayer cesium surface coating [64]. The band bending forces the bulk CBM to lie above the VL, thereby producing an NEA surface (Figure 3.10a). Since there is still a potential barrier at the surface (χ), it is referred to as effective NEA. The realization of effective NEA critically relies on a large enough downward band bending ($\chi_{\text{eff}} = \varphi_{\text{BB}} - \chi > 0$) as well as a very short band bending length *l* so that CBM electrons in the bulk can ballistically tunnel through the band bending region without experiencing inelastic scattering. Therefore heavy *p*-type doping is often required to fulfill these requirements. On a true NEA surface, the EA (χ) is negative at the surface (Figure 3.10b), and bend bending is not a critical requirement for NEA activation but it affects the emission efficiency.

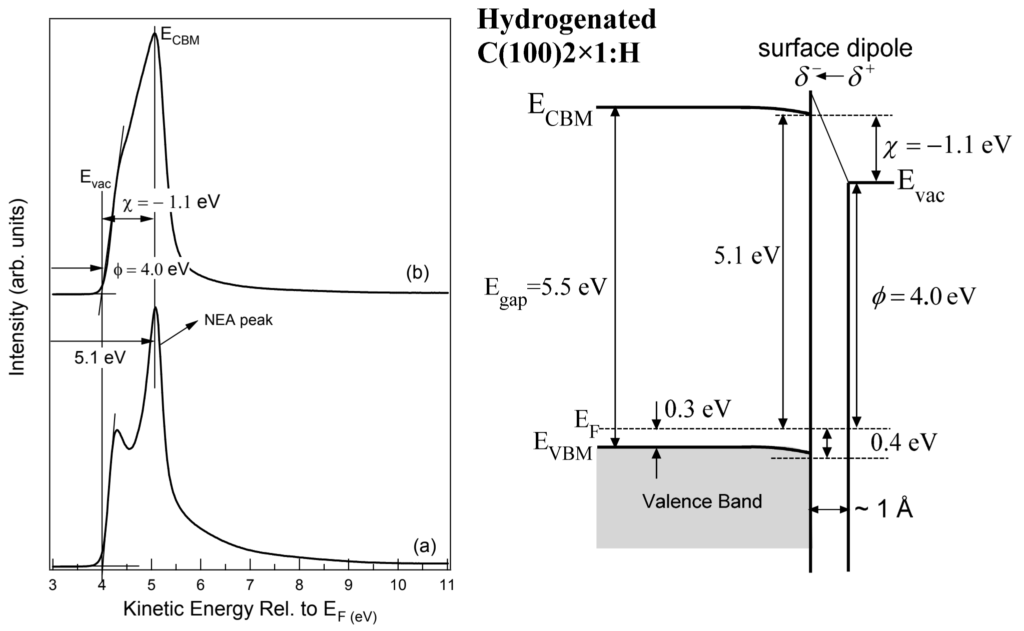

Figure 3.11. Left: Low-kinetic energy part of the PES spectra for hydrogenated diamond (001) surface recorded using photon energy of 60 eV at normal emission angle with two typical structures in (a) and (b). The KE scale has been corrected for the -5 V applied bias. The vertical lines represent the energy position of VL (E_{vac}) and CBM (E_{CBM}), respectively. The cut-off position of the emission peak is determined by extrapolation of the rising edge to zero intensity. **Right:** schematic diagram of the energy level of hydrogenated diamond (001). All energy scales are estimated within an uncertainty of 0.1 eV.

The hydrogenated diamond surfaces exhibit true NEA [61, 65-69]. This NEA arises from a surface dipole layer formed by the heteropolar bonds between surface carbon terminated by hydrogen, where the C-H bonds are polarized with a positive charge δ^{+} on the H atom side as hydrogen exhibits a lower electronegativity ($\chi_{H} = 2.20$) than carbon ($\chi_{C} = 2.55$). This separation of charge over a distance of C-H bond length (1.11 Å) naturally presents a dipole momentum pointing towards the vacuum side, and eventually provides a potential step that pulls down the vacuum level below the CBM [61, 68].

NEA in hydrogenated diamond is characterized by an intense and sharp secondary electron emission peak in the low KE part of the UPS or in the secondary electron spectrum, as the majority of low kinetic energy electrons are directly emitted from diamond CBM to vacuum with a narrow energy distribution. The left panel in Figure 3.11 shows secondary electron emission in the low-kinetic energy part of the UPS spectra. In order to detect those low KE electrons, a -5V bias was applied to the sample to overcome the electron analyzer WF (4.3 eV). The emitted electrons are collected by the analyzer at normal emission relative to the sample surface. Such a set-up is chosen based on two considerations: first, the CBM is located in the [001] direction (along Γ-X) [6] and therefore the emitted CBM electrons possess a momentum perpendicular to the surface; second, the applied bias voltage tends to force these low-kinetic-energy electrons normal to the surface [67]. The lower spectrum (a) in Figure 3.11 is a typical low-KE electron distribution for the hydrogenated diamond (001) surface, which exhibits fine structures within the KE range between 3.5 eV to 6 eV. The highest peak at around 5.1 eV is referred to as the NEA peak with high intensity and narrow line-width (w~0.3 eV). The NEA peak comprises electrons directly emitted from the CBM of diamond, and therefore is often regarded as a signature of the NEA surfaces [63, 65-66, 70-71], although it was pointed out by Yater that the sharply peaked low-kinetic energy electron emission can also be attributed to a small but positive electron affinity (PEA) [72]. In addition to the NEA peak, there is another peak located around 4.5 eV with its cut-off (4.0 eV) well below the CBM, which in some cases is not so well resolved and merged into the high intensity tail of the NEA peak as a shoulder (upper spectrum b in Figure 3.11). In both cases, the cut-offs of this peak are at the same position. Two possible mechanisms could contribute to such electron emission below the conduction band. One is the inelastic scattering of the CBM electrons at the surface region, and the other is the transitions of electrons from the CBM to unoccupied surface states. The latter mechanism, however, is favored, as theoretical calculations predict such unoccupied states related to CH-CH dimers fall below the bulk conduction band down to the VL [57]. With either mechanism, the cut-off position of the lower energy peak reflects the VL (E_{vac}), which equals to the WF (ϕ = 4.0 eV) when it is referenced to the Fermi level.

The observation of a sharp and intense NEA peak, together with the observation of electron emission originating from populated surface states down to the VL, unambiguously demonstrate the NEA property of the hydrogenated diamond (001)-2×1:H surface. However, a quantitative determination of the EA value χ still requires knowledge of the position of CBM (E_{CBM}) relative to the VL E_{vac}. In the previous section, the VBM of diamond (E_{VBM}) is determined to be 0.4 eV below E_{F}. With the known band gap of diamond (E_g = 5.5 eV), the position of CBM can be deduced relative to E_{F} according to $E_{\mathrm{CBM}} - E_{\mathrm{F}} = E_g - (E_{\mathrm{F}} - E_{\mathrm{VBM}}) = 5.5 - 0.4 = 5.1$ eV with an uncertainty of 0.1 eV. The position of the CBM coincides with the NEA peak position as labeled in Figure 3.11, which is consistent with the nature of the NEA peak. However, it should be pointed out that since both the process of electron transport to the surface and the process of electron emission into vacuum play important roles in the formation of the NEA peak [72], which is also highly dependent on the amount of band bending at the surface [73], the NEA peak position cannot be exclusively taken as the CBM position.

With the determination of the E_{CBM} and E_{vac}, the EA of hydrogenated diamond (001) is easily calculated as $\chi = (E_{\mathrm{vac}} - E_{\mathrm{F}}) - (E_{\mathrm{CBM}} - E_{\mathrm{F}}) = \phi - (E_{\mathrm{CBM}} - E_{\mathrm{F}}) = 4.0 - 5.1 = -1.1$ eV ± 0.1 eV. The obtained EA value of -1.1 eV is in good agreement with reported values. Using PES, L. Diederich et al. [62, 67] obtained an EA value of -1.0 ± 0.1 eV on hydrogenated diamond (001). F. Maier and Cui et al. reported an EA of -

1.3 ± 0.1 eV for hydrogenated diamond (001) [61] and (111) [68] surfaces by combining PES with Kelvin probe measurements. More recently using total photoyield (TPY) experiments, D. Takeuchi et al. [69] explicitly determined an EA value of -1.1 eV for hydrogenated diamond regardless of the doping and face orientation. The results also qualitatively agree with theoretical calculations made for diamond surfaces by Rutter et al. [74], Zhang et al. [75] and Sque et al. [57], although the obtained EA values are systematically larger than experimentally determined ones

With the knowledge of the positions of different energy levels in hydrogenated diamond (001), the schematic energy band diagram is plotted in the right panel of Figure 3.11. As can be seen, the surface dipole layer created by C-H bonds over a distance of 1.0 Å effectively lowers the vacuum level down to 1.1 eV below the CBM. In spite of the large band gap of diamond, NEA leads to an exceptionally low IP ($I = \phi + (E_F - E_{VBM}) = 4.0 + 0.4 = 4.4$ eV), which is indeed the lowest among all semiconductors. As a consequence, when surface adsorbates with high enough EA are present, electron transfer from the valence band to physisorbed adsorbates is energetically favorable. Such electron transfer at the hydrogenated diamond surface is the mechanism underlying the *p*-type surface conductivity of hydrogenated diamond, another unique property of diamond, which will be discussed in more detail in Chapter 6.

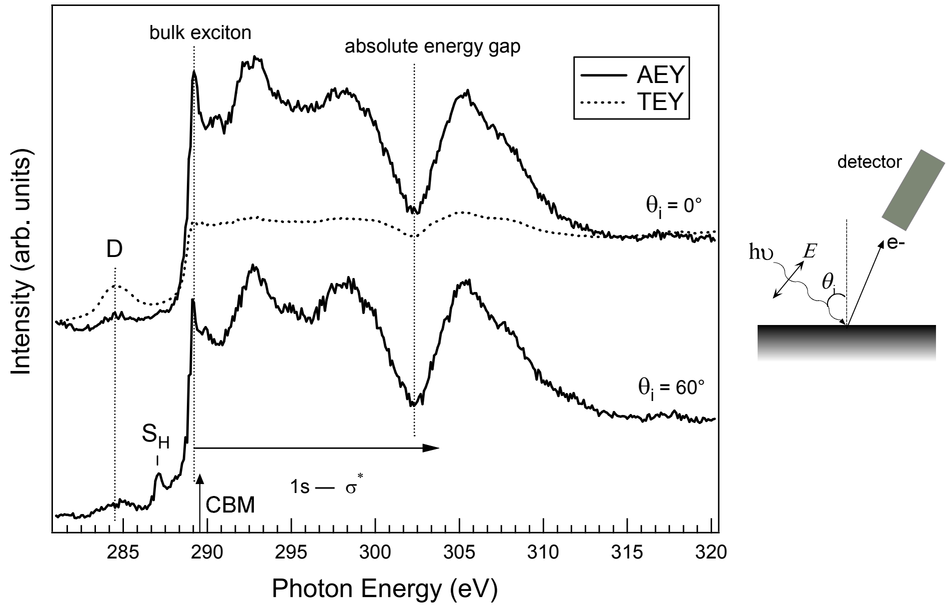

Figure 3.12. C *K*-edge NEXAFS spectra of hydrogenated diamond (001) at different incidence angle of incoming light. The inset illustrates relative positions and orientations of the incident light, electron analyzer, and the sample surface.

3.2.2.3 NEXAFS spectroscopy of hydrogenated diamond surface: probing the unoccupied states

PES studies provide detailed information on the electronic structures of occupied states, from core-levels to valence bands, but a comprehensive understanding of the electronic structures requires knowledge of the unoccupied states. NEXAFS spectroscopy, as described in the Chapter 2.1.4, monitors the resonant excitation of electrons from core-level to unoccupied states of an atomic specie. Figure 3.12 shows the C *K*-edge NEXAFS spectra of hydrogenated diamond with different detection modes (TEY and AEY) and light incidence angles. The overall spectral shapes agree well with previous studies [76-80]. The most noticeable features of all three spectra include a dip at 302.4 eV which is caused by the absolute energy gap in the conduction-band structure of diamond and its position is used here to calibrate the photon energy [76]. The sharp peak located at 289.2 eV is attributed to the creation of bulk core excitons of diamond (i.e. electrons in the conduction band bounded to core holes) [76]. Adding the diamond band gap to the known energy difference between C 1*s* and VBM, the position of CBM is deduced at the photon energy of 289.4 eV (i.e. 5.5 eV + 283.9 eV), which is 0.2 eV above the excitonic peak at 289.2 eV. This 0.2 eV difference specifies the bulk core excitonic BE, in excellent agreement with the value of 0.19 ± 0.015 eV reported by Morar et al [76].

The appearance of the excitonic peak marks the onset of bulk excitations C $(1s)\rightarrow\sigma^*$, whereas the pre-edge features below the bulk excitation threshold are surface resonances in the band gap. The sharp peak S_H at 287.2 eV is associated with the transition to unoccupied σ^* anti-bonding state of the surface C-H bonds [78-79], which is theoretically predicted to be located within the diamond band gap [57]. The intensity of this surface resonance is significantly reduced when the incident light direction changes from $\theta_i = 60^\circ$ to $\theta_i = 0^\circ$, due to the polarization dependence of the optical transitions. When linearly polarized synchrotron light is incident at a grazing angle (e.g. $\theta_i = 60^\circ$), its electric-field vector $\boldsymbol{E}$ has a larger component in the C-H antibonding orbital direction which is out of the sample plane, therefore this resonance is enhanced. At the photon energy of 284.5 eV, we also detect a broad absorption resonance *D* at both normal and grazing incidence, and the energy position resembles a C $(1s)\rightarrow\pi^*$ transition commonly seen in graphite as well as molecules with π-electrons [41]. Since single crystalline diamond contains sp^3 bonding only, we attribute this resonance to transitions into empty defect states not intrinsic to the diamond surface [78].

In Figure 3.12 we also show NEXAFS in TEY mode. Compared to the spectrum taken in AEY mode at the same incidence angle, the TEY spectrum exhibits very different shape with most of the fine structures unresolved. This phenomenon can be attributed to the saturation effect in the XAS [81], which implies the measured current signal is no longer proportional to the X-ray absorption coefficient as the photon energy varies, and the intensities of prominent absorption features are reduced or saturated. Saturation effect occurs when the probe depth of the detected signal is comparable to or even larger than the X-ray penetration depth. It is known that in TEY mode, the absorption signal is largely contributed by secondary electrons as a result of secondary processes which fill the *K*-shell holes following the primary absorption process. In hydrogenated diamond, these secondary electrons are mainly comprised of CBM electrons which are emitted freely into vacuum due to diamond NEA. Using TPY technique, it is determined that the CBM electrons in diamond have a unusually large diffusion length between 150 and 250 μm [82], which is considerably larger than the X-ray penetration depth of 1.5 μm at the C *K*-edge in diamond [83]. Therefore, this strong saturation effect suggests that TEY mode is not suitable as a detection technique for NEXAFS measurements in hydrogenated diamond.

3.3 Bare diamond C(001)-2×1 surface

3.3.1 Surface reconstruction

Annealing the hydrogenated diamond *in situ* above 1000 ºC for several minutes leads to the desorption of hydrogen, yielding a hydrogen free, bare diamond C(001)-2×1. Although it has been reported that hydrogen starts to desorb at around 800 ºC, to achieve a complete hydrogen-free surface, annealing temperatures above 1000 ºC is necessary [59]. However, the annealing procedure should be performed with caution, because overheating to 1250 ºC will lead to graphitization of the diamond surface [59]. In practice, the annealing procedure was started at 900 ºC for 10 minutes and UPS measurements at photon energy of 60 eV were used to monitor the presence of the NEA peak in the low KE part of the spectra (see Figure 3.11). If the NEA peak was

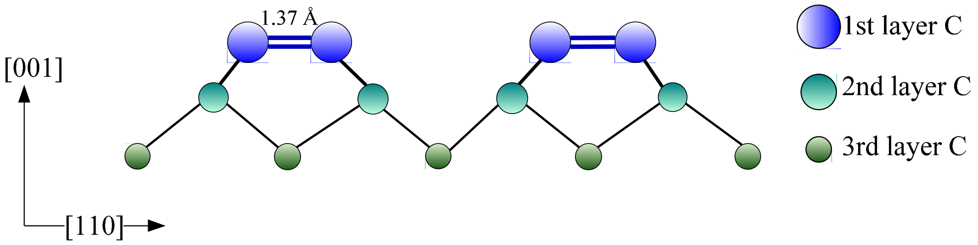

Figure 3.13. Side view of atomic arrangement of the bare diamond (001)-2×1 surface. The colored circles with different size represent carbon atoms belonging to the top three surface layers. The dimer double bonds are represented by blue sticks.

observed, annealing was repeated at 50 ºC higher until the NEA peak disappeared completely and the low KE electrons display a broad, low intensity distribution with its cut-off at higher KE (see below). This careful annealing procedure with hydrogen coverage monitoring, fully dehydrogenates the diamond surface while at the same time avoids graphitization of diamond surface due to possible overheating. In addition to the annealing temperature, the vacuum condition, which should be maintained below 1×10^{-9} mbar, is also critical to obtain a high-quality bare diamond surface.

Hydrogen desorption leads inevitably to the reconstruction and relaxation of diamond surface. The two dangling bonds of each surface dimer due to hydrogen desorption partially overlap and form a weak π bond. Together with the existing σ bond between surface dimer atoms, they form a strained C=C double bond. The atomic arrangement of bare diamond (001) 2×1 is shown schematically in Figure 3.13, and its top view is analogous to that of hydrogenated diamond surface (Figure 3.4b) with orthogonally oriented 2×1 domains. The relaxed bond length of C=C dimer is 1.37 Å as determined by theoretical calculations [55, 57], resembling the length of the C=C double bond in common unsaturated organic molecules such as C_2H_4 ($d = 1.38$ Å).

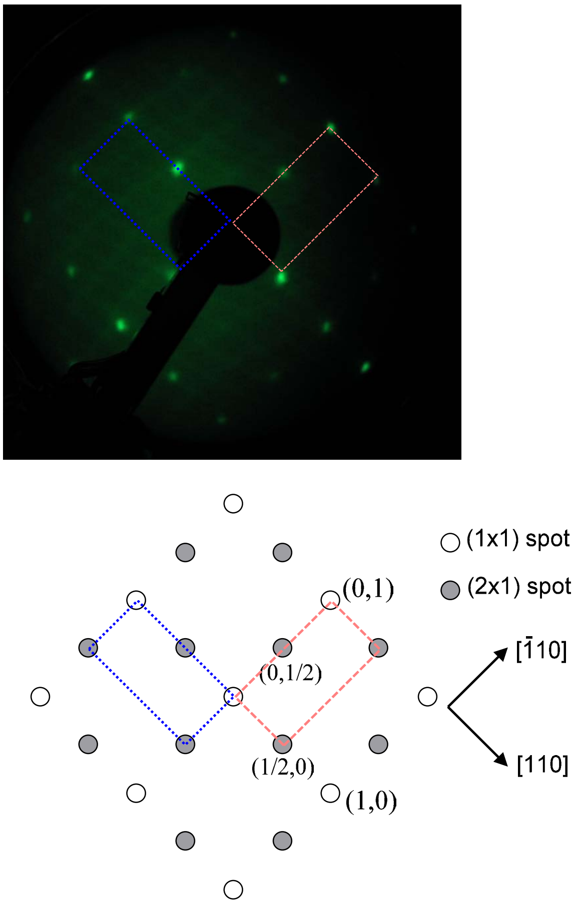

Figure 3.14. LEED pattern (upper panel) and its schematic representation of the bare C(001)-2×1 diamond surface (electron beam energy 170 eV). The dashed rectangular boxes represent the reciprocal lattices of the two orthogonally oriented 2×1 domains.

Since the 2×1 reconstruction symmetry is still retained on bare diamond surface, its LEED pattern (Figure 3.14) is essentially the same as that of hydrogenated diamond (Figure 3.5). However, we failed to image STM topographies on bare diamond with resolved dimer rows. The loss of surface conductivity due to hydrogen desorption prevents the investigation of bare diamond surface by normal STM technique, but it has been successfully imaged by STM with atomic-scale resolution using an unconventional resonant electron injection mode [84].

3.3.2 Electronic structures

3.3.2.1 PES of bare diamond surface: surface core-levels and valence band structures

Figure 3.15 shows the C 1*s* PES spectrum of bare diamond (001)-2×1, which comprises a bulk diamond C 1*s* line *B* and a surface component S_D. The surface component, which shifts by 0.95 eV towards lower BE, is attributed to the π-bonded surface dimers [59, 62, 67]. This rather large BE shift of the surface component S_D, in spite of the relatively small initial state difference between surface C atoms and bulk C atoms, arises from the more effective final-state core-hole screening by the π-electrons in surface dimers compared to the bulk [59]. The intensity of the surface component accounts for about 31% of the total emission intensity. Comparing the BE of the bulk components in bare diamond with that in hydrogenated diamond (Table 3.1), the bulk C 1*s* line is shifted 0.6 eV to higher BE during the transition from hydrogenated to bare surface, indicating an increase of downward band banding of the same amount [59, 85-86]. This large band banding on bare diamond, which signifies further hole depletion in the *p*-type diamond surface region, arises from the fact that the occupied surface states related to the π-bonded dimers reside above the valence band within the band gap [55, 57] and act as effective donor-type surface states as depicted in Figure 3.3. Adding the 0.6 eV shift to the existing band bending in hydrogenated diamond (0.1 eV), the band bending of bare diamond is estimated to be 0.7 ± 0.1 eV. The width of the band bending region could be estimated using the following formula [7]:

$$D = \sqrt{2\varepsilon\varphi / qN_A} \tag{3.1}$$

where ε is the dielectric constant ($\varepsilon = 5\times10^{-11}$ F/m for diamond), φ is the band bending in eV , q is the elementary charge, and N_A is the acceptor concentration assuming

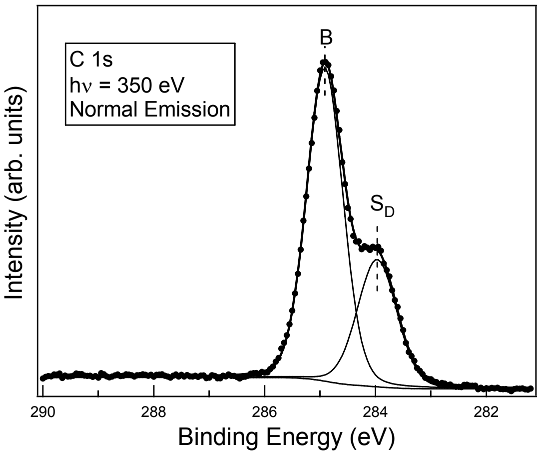

Figure 3.15. C 1*s* core-level spectra of a bare diamond (001) surface (*hv* = 350 eV) after annealed at 1050 ºC at normal emission angle. Solid lines through experimental points demonstrate the result of least-square fitting.

complete ionization of dopants. For the doping concentration of 10^{16} cm^{-3} and band bending of 0.7 eV in bare diamond, the band bending width is calculated to be around 2100 Å, which is much larger than the PES detection depth for C 1*s* signal (below 10 Å). Therefore, using PES we measure only the surface area of the whole band-bending region, corroborating the effectiveness of using C 1*s* BE shift to estimate the amount of band bending as presented above.

The occupied surface π bonding states of bare diamond can be clearly identified in valence band spectra using photon energy of 60 eV (Figure 3.16), where the pronounced emission peak S_D located 1.35 eV below Fermi level denotes the π-bonding surface state originating from dimers. The rest of the emission peaks resemble bulk valence band structures as seen in hydrogenated diamond (Figure 3.9) but with a rigid shift to higher BE due to increased band bending. It should be noted that a photon energy larger than 50 eV is critical in resolving the surface state emission S_D from the bulk valence band emission due to the degeneration of the surface state with bulk states at the surface Brillouin zone center ($\bar{\Gamma}$) [57, 87]. For example, the previously reported surface state feature by Wu et al. [85] and Francz et al. [86] using a photon energy of about 40 eV is a mixture of the surface state and bulk valence band emission. Theoretical calculations predict the occupied π surface state resides in the bulk band gap with a heavy dispersion in the regions away from the zone center [55, 57]. The surface state dispersion is manifested by the different BE of the surface emission peak S_D when the electron emission angle changes from normal emission to grazing emission, as shown in Figure 3.16, in qualitative agreement with angle-resolved PES results [87]. In addition, the surface state emission is more prominent at normal emission than at grazing emission. The position of the VBM in the valence band spectra is simply determined by adding the 0.7 eV band bending amount to the known energy difference of 0.3 eV between bulk Fermi level and VBM, giving 1.0 eV for the VBM below Fermi energy.

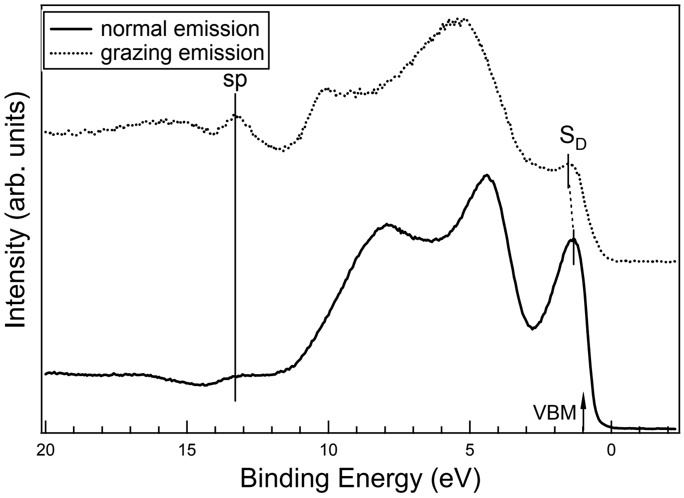

Figure 3.16. Valence band spectra of bare diamond (001)-2×1 surface recorded with photon energy of 60 eV at two emission angles. The spectra are all normalized to the same height for better viewing.

3.3.2.2 Work function, electron affinity and energy level diagram

The WF and EA of bare diamond are determined from the measurement of low-KE part of the UPS spectra (Figure 3.17). The spectrum shape of secondary electrons emission from bare diamond is characterized by a low intensity and relatively broad distribution, in contrast to the sharp and intense emission from hydrogenated diamond (see the inset of Figure 3.17 and Figure 3.11a). In fact, the secondary electron emission intensity from bare diamond is so low that it is merely comparable to the background intensity of the emission from hydrogenated diamond (Figure 3.17 inset). The emission threshold also shifts to higher kinetic energy by as much as 1.3 eV, indicating a lifting of the VL after hydrogen desorption, and the WF of bare diamond surface is therefore determined to be 5.3 eV. The position of the CBM is determined according to $E_{\mathrm{CBM}} - E_{\mathrm{F}} = E_{\mathrm{g}} - (E_{\mathrm{F}} - E_{\mathrm{VBM}}) = 5.5 - 1.0 = 4.5$ eV, clearly below the VL of bare diamond. The EA χ of bare diamond is thus positive with a value of 0.8 ± 0.1 eV. This is in good agreement with theoretical predictions of 0.8 eV [75], and is also in reasonable agreement with other measured values ranging from 0.5 eV [61], 0.75 eV [88], and to 1.3 eV [62]. The small deviations may be due to different diamond quality, annealing temperature and measurement techniques. However, all measurements explicitly indicate the PEA nature of bare diamond. Additional features located at higher kinetic energy around 10–13 eV are identified and labeled as E_1 and E_2, and are turning points or threshold energies representing rapid changes of intensity. These two threshold energies, E_1–first threshold energy for the creation of electron-hole pairs with phonon assistance, and E_2–second threshold energy for the creation of electron-hole pairs without phonons, are inherently related to the position of CBM through a consideration of electron scattering and emission mechanisms in the material ($E_1 = E_{\mathrm{CBM}} + E_{\mathrm{g}}$; $E_2 = E_{\mathrm{CBM}} + 1.5E_{\mathrm{g}}$) [65, 72]. It is worth mentioning that these two

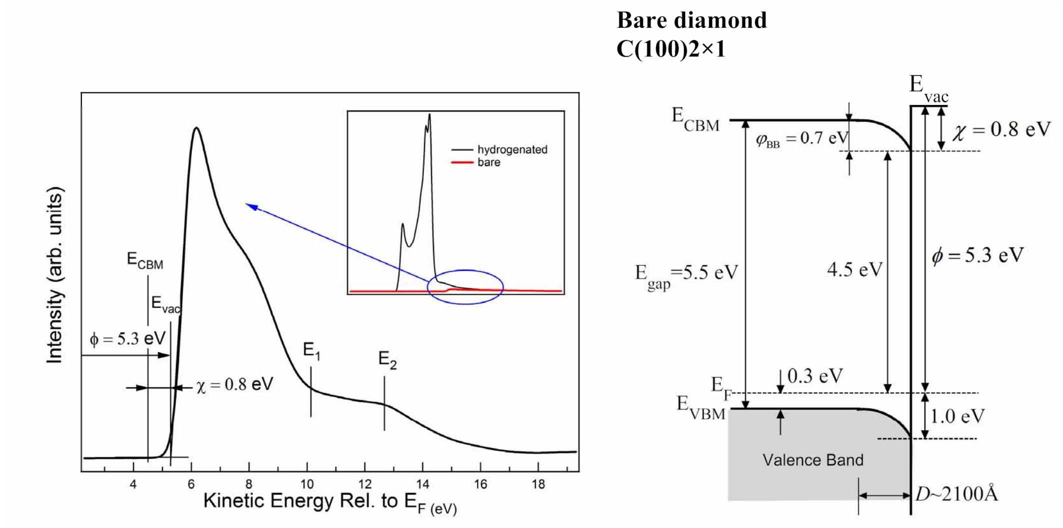

Figure 3.17. Left: Low-kinetic energy part of the PES spectra for bare diamond (001) surface recorded using photon energy of 60 eV at normal emission angle. The kinetic energy scale has been corrected for the -5 V applied bias. The vertical lines represent the energy position of vacuum level (E_{vac}) and CBM (E_{CBM}), respectively. The cut-off position of the emission peak is determined by extrapolation of the rising edge to zero intensity. The inset shows both low-kinetic energy electron emissions of both hydrogenated and bare diamond surface. **Right:** schematic diagram of the energy level of bare diamond (001). All energy scales are estimated within an error value of 0.1 eV.

features are also visible in emission spectra of hydrogenated diamond, although it is largely masked by the ultra high NEA peak.

The schematic energy band diagram of bare diamond (001) is plotted in the right panel of Figure 3.17. A large downward band bending of 0.7 eV towards the surface is present, with its depletion layer extending 2100 Å into the bulk. Hydrogen desorption by annealing also eliminates the surface dipole layer along with its step potential. As a result, the VL on bare diamond is lifted above its CBM, leading to a PEA surface. Consequently, the majority of low KE electrons (hot electrons) that accumulate at diamond CBM are now blocked by an energy barrier of 0.8 eV imposed by the VL, resulting in the low intensity and broad secondary electron emission. The IP I increases to 6.3 eV, much larger than that of the hydrogenated surface (4.4 eV). The change of EA $\Delta\chi$ or IP ΔI of 1.9 eV from hydrogenated to bare surface highlights the magnitude of the electrostatic potential step caused by the surface dipole layer due to hydrogen termination. The surface dipole induced EA change could be theoretically evaluated according to a simple electrostatic dipole model [61, 68]:

$$\Delta\chi = \frac{ep_z n}{S(n)\varepsilon_0} \tag{3.2}$$

where p_z is component of the dipole moment of an isolated surface bond (C-H in this case) perpendicular to the surface, n is the areal density of surface dipoles, e and ε_0 are elementary charge and vacuum permittivity respectively. The denominator $S(n)$ which depends on dipole density n accounts for the mutual interaction of dipoles which tends to reduce the contribution of each dipole to the total potential drop for high dipole densities. It has a simple expression in the following form [89]:

$$S(n) = 1 + \frac{9\alpha n^{3/2}}{4\pi\varepsilon_0} \tag{3.3}$$

where α is the polarizability of C-H dipoles. The dipole moment p_z of isolated C-H bond could be estimated in the point charge approximation by $p_z = d_z\Delta q$ where d_z is the C-H bond length projected perpendicular to surface (d_z = 1.01 Å) and Δq is the charge transfer from the C to the H atom due to their different electronegativity. Using the Pauling electronegativities for C (2.55) and H (2.2), we can obtain Δq for C-H bond as follows [53]:

$$\Delta q = e(0.16|\chi_\mathrm{C} - \chi_\mathrm{H}| + 0.035|\chi_\mathrm{C} - \chi_\mathrm{H}|^2) = 0.07e \tag{3.4}$$

Together with d_z we obtain p_z = 0.07 e·Å = 1.13×10^{-30} A·s·m. Given $n = 1.57\times10^{15}$ cm^{-2} for fully hydrogenated diamond (001) surface, and polarizability $\alpha = 1.0\times10^{-40}$ A·s·m^2/V [61] to Eqn. (3.2) and Eqn. (3.3) , we arrive at the EA change $\Delta\chi$ = 1.4 eV due to hydrogen termination, in reasonable agreement with the experimentally determined $\Delta\chi$ value of 1.9 eV.

3.3.2.3 NEXAFS spectroscopy of bare diamond surface: probing the unoccupied states

The C *K*-edge NEXAFS spectra of bare diamond are displayed in Figure 3.18 with different light incidence angles. The spectra are all taken using AEY mode to achieve maximum surface sensitivity. The overall spectra profiles resemble that of hydrogenated diamond with a sharp bulk core-exciton at 289.2 eV as well as the dip at 302.4 eV. However, the pre-edge region below the bulk excitonic peak exhibits dramatically different structures. The absence of a resonance at around 287.2 eV related to surface C-H bonds, as well as a peak at around 282.5 eV associated with single dangling bonds of surface dimer atoms due to partial hydrogen desorption [77], confirm the complete dehydrogenation of diamond surface by annealing at 1050 ºC. Two new absorption resonances at 283.8 eV (Ex_1) and 286.0 eV (Ex_2) respectively, are observed. These two surface resonances in the band gap were previously reported by NEXAFS measurements made on bare diamond [77-78]. However, their assignments of these two resonant features are controversial. Graupner et al. [78] interpreted both resonances to be surface core excitons associated with the π-bonded dimers on bare diamond (001)-2×1, whereas Bobrov et al. [77] assigned Ex_1 to a surface core-excitonic state and Ex_2 to the transition to the unoccupied π^* anti-bonding state in the band gap as predicted by theoretical calculations [55, 57].

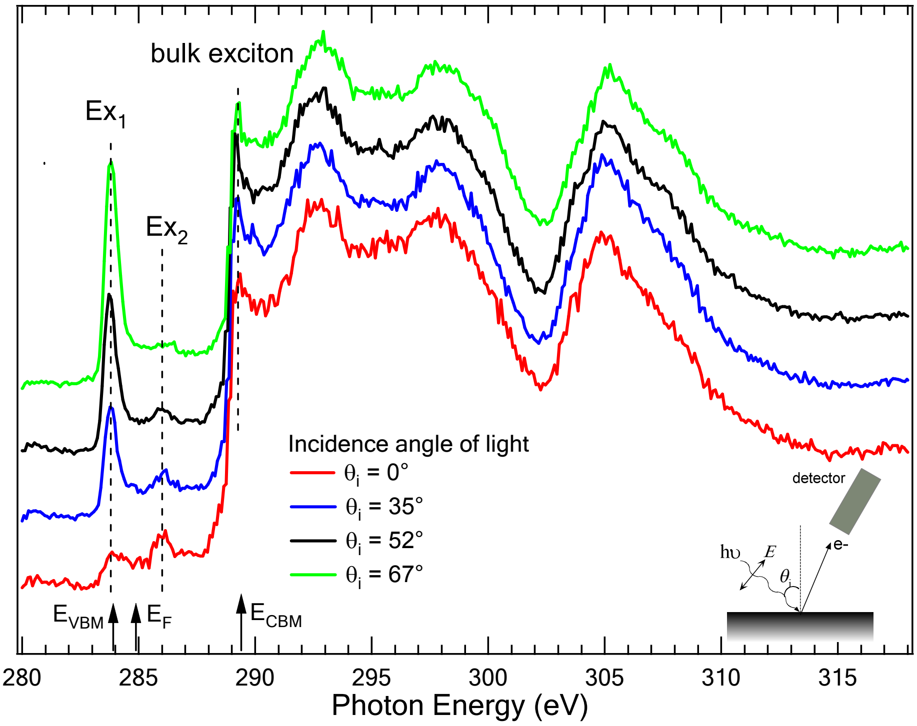

Figure 3.18. C *K*-edge NEXAFS spectra of bare diamond (001) at different incidence angles of incoming light. Spectra are taken in AEY mode by detecting the C Auger electrons at 265 eV. The energy position of VBM, CBM and Fermi level are marked by vertical arrows in the bottom axis. The inset illustrates relative positions and orientations of the incident light, electron analyzer, and the sample surface.

In order to correctly interpret the origins of these two surface resonances, the position of the Fermi level in the absorption spectra, which has important implications on the excitation nature of the surface resonances, must be determined appropriately. As demonstrated by Morar et al. [80], if the electronic states are lying below the Fermi level, they are indisputably classified as surface core excitons whose energy is highly influenced by the strong electron-hole Coulomb interactions. Alternatively, if the states are lying above the Fermi level, they are most likely to be due to transitions into unoccupied surface states, although their excitonic nature cannot be ruled out if the exciton BE is relatively small. For hydrogenated diamond, it is straightforward to determine the position of the Fermi energy as the BE of the bulk component (284.3

eV) in the photon energy scale of NEXAFS spectra. However, for bare diamond, the additional C 1*s* surface component is shifted by 0.95 eV to lower BE bringing ambiguity in determining the Fermi level. Intuitively, one may want to use the BE of the surface C 1*s* component (283.95 eV) to set the Fermi level, since the transitions occur at surface dimers. But such an assignment is only valid if the initial-state effect (i.e. chemical shift) accounts for the surface component shift. As discussed above, the surface component is indeed due to final-state effects (i.e. more effective core-hole screening by π-electrons), and therefore the BE of the bare diamond bulk component (284.9 eV) should be used to determine the Fermi level exclusively. In this way, the Fermi level, along with VBM (283.9 eV) and CBM (289.4 eV), are all determined and labeled in Figure 3.18. Therefore, the surface resonance Ex_2 lying above the Fermi level most probably corresponds to the electronic transition into unoccupied π^* anti-bonding state of surface dimers as suggested by Bobrov et al. [77].

However, the assignment of the Ex_1 resonance is more complicated. As shown in Figure 3.18, the Ex_1 state lies below the Fermi level, indicating its excitonic nature. Two different scenarios could give rise to the Ex_1 state. **In one scenario**, the Ex_1 resonance is still associated with transitions into the π^* anti-bonding state of the surface dimers, but with a strong electron-hole bound by forming surface core excitons. In this situation, the energy difference between Ex_1 and Ex_2 simply gives an exciton BE of 2.2 eV. Such a large excitonic BE, which corresponds to rather localized Frenkel-type surface core excitons, are the result of the two-dimensional nature of the surface excitons as well as the reduced screening at the surface with diamond's relatively low dielectric constant (ε = 5.7) [78]. **In the other scenario**, electron transfer from occupied surface states to bulk boron acceptors should be taken into account to explain the origin of Ex_1 resonance. This charge transfer process inevitably empties or partially empties some of the original occupied π bonding states of surface dimers (c.f. Figure 3.3). These emptied or partially emptied π surface states could then be probed by NEXAFS as a resonant excitation (Ex_1), whereas resonance Ex_2 still corresponds to the transitions to the relaxed π^* surface state. In this case, the energy difference of 2.2 eV between Ex_1 and Ex_2 should be equal to the average energy splitting of the π–π^* surface bands in the band gap region. The energy difference between the maximum of the π surface state and the minimum of the π^* surface state was predicted by theoretical calculations to be 1.86 eV [57], which is in reasonable agreement with our deduced value from the above scenario considering a large dispersion of surface states and the excitonic nature of Ex_1. However, at present it is difficult to discriminate which of the two described scenario would be responsible for the formation of Ex_1, or it might be even a combination of both two scenarios. Future NEXAFS measurements on *n*-type bare diamond (001) will be useful in identifying the origins of these surface resonances, since the latter scenario would be ruled out in *n*-type diamond.

Now we turn our attention to the polarization dependence of these surface resonances. As shown in Figure 3.18, the intensity of Ex_1 exhibits a strong polarization dependence on the light incident angle. It has the highest intensity at grazing incidence (θ_i = 67°) but becomes weakest at normal incidence. The polarization dependence of the Ex_1 signal is less prominent but with an opposite trend. Considering the π-electron (or π^*) nature of the Ex_1 state in either scenario mentioned above, the π-orbital (or π^*) formed by linear combinations of dangling *p* orbitals centered at the two C atoms of each surface dimer is essentially out-of-plane. Therefore, when the incident synchrotron light has a larger component projected on the π-orbital (or π^*) direction (i.e. grazing incidence), the resonant excitation Ex_1 is enhanced. However, despite a similar π^*-electron nature, the peculiar opposite angular dependence of resonance Ex_2 seems to be inexplicable. Graupner et al. observed a similar polarization dependence of these two surface resonances, which they describe as due to the different point group symmetries of the excited states [78]. Whether the polarization dependence follows the dipole selection rule of excited states orbital direction or the specific point group symmetry remains an open question which is beyond the scope of the present study.

3.4 Chapter summary

In this chapter, we focus on the surface reconstruction and electronic structures of diamond (001) in two different surface conditions: hydrogenated and bare. LEED patterns and STM topographies confirm the (2×1) reconstruction symmetry on both surfaces with two orthogonally oriented (2×1) domains. In particular, hydrogen termination on diamond, which passivates the dimer dangling bonds, leads to further relaxations of the surface structures with elongated dimer bond length.

High surface sensitivity PES reveals different electronic structures on these two surfaces. C 1*s* core-level spectra of freshly prepared hydrogenated diamond uncover the existence of hydrocarbon residuals on the surface due to the hydrogen microwave plasma treatment. *In-situ* mild annealing of the sample at 400~600 ºC removes these adsorbates, and leaves the single bulk C 1*s* spectrum. Valence band structures of hydrogenated diamond exhibit only bulk diamond valence band structures, while the surface states related to CH-CH dimers resides below the VBM of bulk diamond and therefore are unable to be resolved. The lack of occupied surface states within the band gap also results in flat bands in hydrogenated diamond. In contrast, the unoccupied σ^* antibonding state of the surface C-H bonds, appearing in the band gap as predicted by theoretical calculations, is identified by NEXAFS in the pre-edge region.

Annealing hydrogen terminated diamond at 1050 ºC leads to desorption of hydrogen and conversion to bare diamond surface. The corresponding C 1*s* core-level spectrum shows a surface component shifting to lower BE which is related to the π-bonded dimers. The bulk C 1*s* component is also shifting to higher BE compared to hydrogenated diamond, indicating an increased downward band bending towards diamond surface. This large downward band bending is inherently related to the emergence of occupied π-bonding surface states in the band gap, which shows up as a prominent emission peak close to the Fermi level in the valence band spectra. NEXAFS exhibits two surface resonances in the band gap region. Two possible scenarios are proposed to interpret these two resonant excitations, which involve surface core excitons. In addition, their polarization dependence could be related to the direction of bonding orbitals or to the point group symmetry of excited states.

Notably, the hydrogen termination creates a dipole layer with an electrostatic potential step as large as 1.9 eV which effectively lowers the VL below the CBM and thus transforms PEA of bare diamond surface to a true NEA surface, enabling a large number of electrons accumulating at the CBM to escape into the vacuum without any energy barrier in the electron emission processes. These electrons constitute a sharp, intense peak in the low-kinetic energy region of the UPS spectra. Information about various electronic properties (e.g. E_{CBM}, E_{VBM}, E_{VAC}) are extracted from the PES measurements and depicted schematically in the energy band diagram for hydrogenated and bare diamond surface, respectively.

In conclusion, the different surface conditions of diamond (001) result in distinct electronic properties, providing us a versatile system to study the interactions of organic molecules with diamond surfaces, as will be discussed in the following chapters. On one hand, the π-bonded dimers on bare diamond are structurally analogous to those C=C bonds in organic molecules such as alkenes and olefins, and are therefore expected to exhibit reactivities towards other unsaturated organic molecules, which will be explored in Chapter 4 and 5. On the other hand, the very low IP due to hydrogen termination will favor electron transfer from diamond valence band to surface adsorbates. This surface transfer doping scheme, which is the underlying mechanism for diamond surface conductivity, provides us opportunities to dope and manipulate the surface conductivity of diamond. This possibility is explored in Chapter 6.

CHAPTER 4

CYCLOADDITIONS ON BARE DIAMOND (001) 2×1 SURFACE: TUNING THE ELECTRON AFFINITY AND ELECTRON EMISSION BY SURFACE FUNCTIONALIZATION

4.1 Introduction

With the rapid development of microelectronics and the continuing shrinkage of device dimensions, hybrid organic-inorganic systems are expected to revolutionize future technologies and devices [29, 90-91]. Through combining the best properties and features of both inorganic and organic materials, we have an unparalleled opportunity to construct functional systems with tunable chemical, electric, mechanical and biological properties. Based on this concept, a wide range of applications (biosensing, optoelectronics, drug delivery etc.) are being developed, and many routes towards such functional systems are being pursued. Among them, surface organic functionalization, which incorporates organic materials onto semiconductors surfaces through direct, covalent attachment is emerging as an important approach for the development of robust, nonvolatile hybrid materials and devices. Unlike metals, the covalent nature of semiconductor surface lattices permits suitable reactivity that can be exploited to form covalent bonding with unsaturated organic molecules. In particular, the cycloaddition reaction, a widely used reaction scheme in organic synthesis to form new carbon-carbon bonds and rings [92], provides a powerful route to the controlled organic functionalization of semiconductor surfaces [93].

Cycloaddition is a pericyclic chemical reaction mechanism, in which two π bonded molecules react to form a new cyclic molecule by losing two π bonds and forming two new σ bonds. According to the number of π electrons in each molecule involved in the reaction, cycloaddition reactions are classified into two types as shown in Figure 4.1, namely [2+2] cycloaddition and [4+2] cycloaddition (the latter is also known as the Diels-Alder reaction). These two types of cycloadditions, however, are subject to the so-called Woodward-Hoffmann selection rules, which rely on the symmetry of the frontier highest occupied and lowest unoccupied molecular orbitals (i.e. HOMO and LUMO) of the reactants [94]. As a result, [2+2] cycloadditions are found to be “symmetry forbidden”, and the Woodward-Hoffmann selection rule dictates that this reaction should not occur without significant energy activation such as photochemical activation. In contrast, [4+2] cycloadditions are “symmetry allowed” with much less activation barrier. Indeed, Diels-Alder reactions are more commonly used in organic synthesis to than its [2+2] counterparts.

Inorganic semiconductor surfaces such as Si(001) and Ge(001) have surface dimers (Si=Si, Ge=Ge) resembling an alkene group, and cycloadditions with unsaturated organic molecules are expected to proceed on these surfaces. However, a solid surface dimer is not identical to a true double bond system, and the Woodward-Hoffmann selection rules cannot be simply applied since distortion, tilting and solid state effect of surface dimers need to be taken into consideration. Indeed, both [4+2] and [2+2] cycloadditions with a number of different alkene-containing molecules (e.g. ethylene, butadiene, cyclopentene) are found to readily occur on Si (001) and Ge (001) surfaces [91, 93]. In particular, [2+2] cycloadditions, which are not allowed according to the symmetry selection rules, can readily occur quite fast on both surfaces at RT due to the tiled asymmetric surface dimers that relax the symmetry restrictions [93, 95-96].

As discussed in the previous chapter, the diamond (001) surface also exhibits a 2×1 reconstruction with surface dimers consisting of a highly strained double bond with σ and π components. These strained alkene-like double bonds make diamond surface reactive with unsaturated organic molecules. Indeed, the Diels-Alder reaction with 1,3-butadiene on bare diamond C(001)-2×1 has been established by electron energy loss spectroscopy (EELS) [97] and Fourier transform infrared spectroscopy (FTIR) [71]; these studies show that 1,3-butadiene is readily chemisorbed on C(001) predominantly via the [4+2] cycloaddition reaction route, whereas [2+2] cycloadditions are not favored because of a much higher activation barrier. The high activation barrier for [2+2] cycloaddition is considered a result of the symmetric dimer geometry of diamond which lacks the low-symmetry pathway to initiating a [2+2] cycloaddition [98]. These findings are further supported by the FTIR study of the reaction of cyclopentene with diamond by Hovis et al. [99]. They report a very low sticking coefficient of cyclopentene on diamond surface of the order of 10^{-3}, several orders of magnitudes lower than that on silicon and germanium. Despite the low sticking coefficient, Hovis et al.'s work still suggests the feasibility of [2+2] cycloadditions on diamond. Indeed, combining high-resolution EELS (HREELS) and synchrotron-based spectroscopies, Loh K. P. and co-workers, including the present author, unambiguous demonstrated [2+2] cycloaddition of allyl organics (i.e. allyl alcohol, acrylic acid and ally chloride) and acetylene on diamond (001) surface [100]. The successful attachment of allyl group molecules via cycloadditions is particularly significant because it provides a powerful and tunable route to functionalize diamond by simply varying the functional group of allyl organics. The exceptions to the Woodward-Hoffmann rules for surface [2+2] cycloadditions of diamond is not unexpected, because diamond is an extended solid-phase system with continuum band structures, which is considerably different from the discrete frontier molecular orbitals of gas phase reactants in regular cycloadditions.

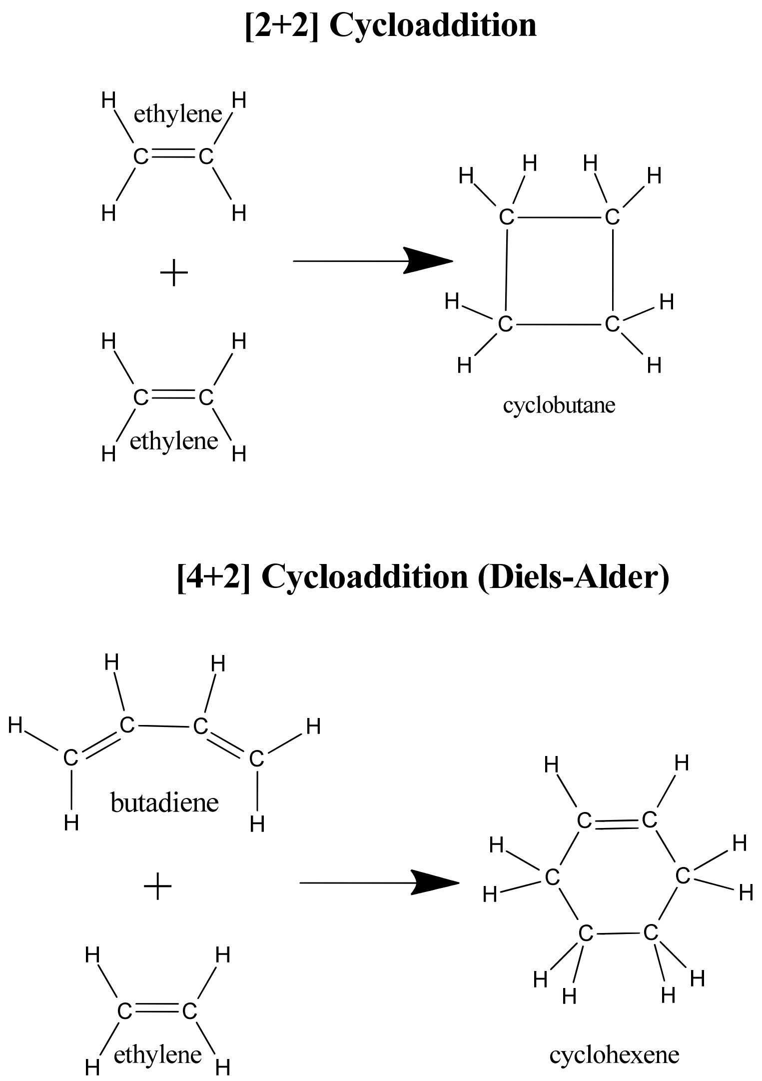

[2+2] Cycloaddition

[4+2] Cycloaddition (Diels-Alder)

Figure 4.1. Examples of cycloaddition reactions. [2+2] cycloaddition between two alkenes forms a four-membered ring, whereas [4+2] cycloaddition between a diene and alkene forms a six-membered ring.

Surface functionalization of diamond is especially promising from the surface science point of view. Unlike germanium or silicon, both the diamond surface and the functionalizing agents are carbon-based, and the interface formed by direct C—C covalent coupling is therefore homogeneous. In this case, the diamond surface can be considered as a solid organic template, and the bonding interface can be viewed as a natural extension of the diamond surface lattice, leading to minimum influence on the properties of diamond. It thus enables a perfect matching of organic functionality with the numerous exceptional properties of diamond. Although many studies have been devoted to studying the cycloaddition reactions on diamond surface, most are focused on understanding the chemical reaction mechanism and dynamics, while little attention is paid to the modification of surface electronic structures induced by cycloadditions. It is known that the incorporation of organic layers at the interface can significantly modify the surface electrostatic potential by giving rise to an interface dipole layer [101-102]. Such a dipole layer, which either results from the internal dipole moments of the grafted molecules themselves or from the charge transfer or charge rearrangement between substrate and molecules, can in turn modulate the surface electronic properties such as WF, EA as well as secondary electron emission yield.

This chapter will discuss in detail the cycloaddition reactions of a prototypical alkene-containing molecule (1,3-butadiene) with bare diamond (001) surface. The surface electronic structures will be investigated by synchrotron-based spectroscopies. The tailoring of diamond surface electronic properties by surface functionalization and its underlying mechanism will be explored by both experiments and density functional theory (DFT) calculations. Choosing 1,3-butadiene as the model organic molecule is based on two considerations. First, the Diels-Alder reaction of 1,3-butadiene on bare diamond C(001)-2×1 surface is already well established by several researchers [71, 97, 100], and shows the highest sticking coefficient among all the functionalizing organics on diamond. Second, the relatively simple and symmetric chemical structure of 1,3-butadiene reduces the complexity in modeling the reaction product by DFT calculations.

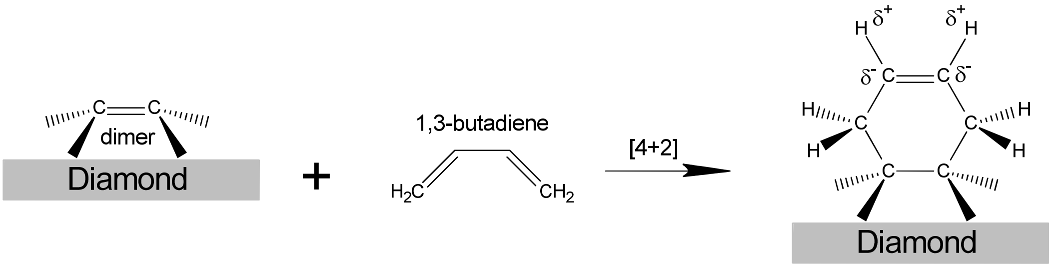

Figure 4.2. Diels-Alder reaction of 1,3-butadiene with bare diamond C(001)-2×1 surface.

4.2 Diels-Alder reactions on bare diamond (001) 2×1 surface

The Diels-Alder reaction scheme of a 1,3-butadiene with a bare diamond surface dimer is shown schematically in Figure 4.2. Upon reaction, the 1,3-butadiene molecules break the diamond dimer π bonds and form cyclohexene-like structures on the surface [71, 97]. With dimer π bond breaking, its related π-bonding (occupied) and π*-antibonding (unoccupied) surface states are expected to diminish, which is indeed confirmed by PES (Figure 4.3) and NEXAFS (Figure 4.4) respectively. Figure 4.3(i) shows the changes to the valence band spectra of bare diamond after exposures to 1,3-butadiene. There is an obvious intensity decrease of the peak labeled *SS* with increasing 1,3-butadiene dosage. As described in the previous chapter, this peak near the Fermi energy represents the dimer π bond induced surface state. In contrast, the peak at 13 eV which is a fingerprint of the sp^3 bonding in bulk single crystalline diamond is only slightly attenuated. Hence the gradual decrease of the *SS* peak directly indicates a chemical reaction on diamond surface that breaks the dimer π bonds rather than a simple attenuation of the *SS* peak photoemission intensity due to physisorbed molecular overlayers. Besides the surface state diminishing, there is a slight intensity enhancement of the broad region at 5-10 eV, which originates from the C 2*p* states of

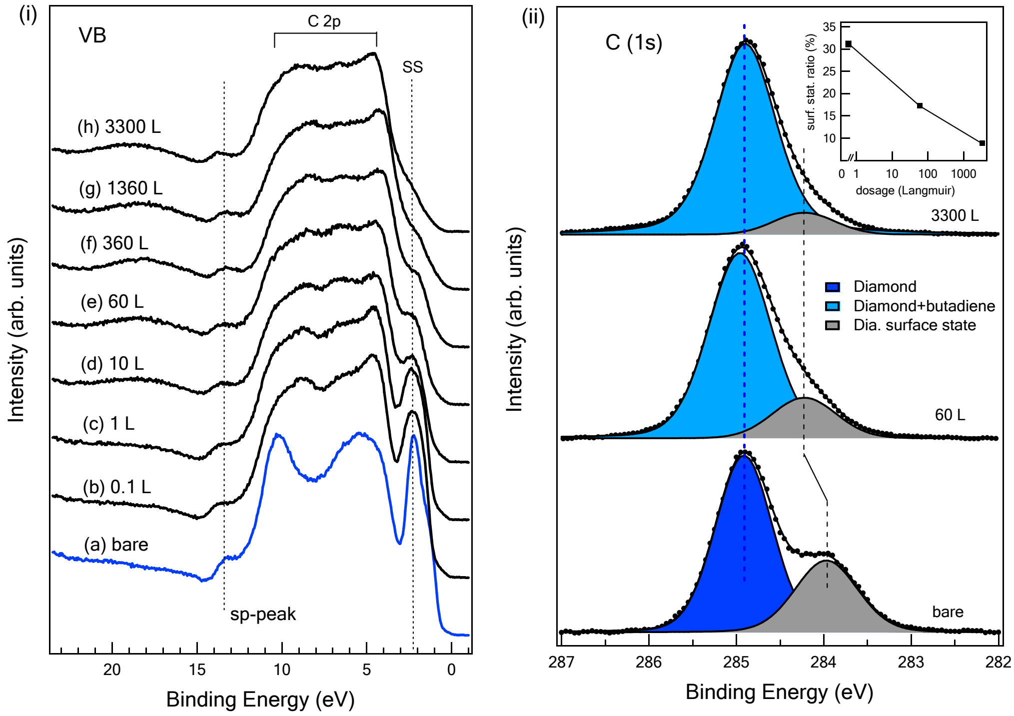

Figure 4.3. PES spectra of (i) valence band of diamond with increasing molecular dosages (photon energy, 60 eV) and (ii) C 1*s* core-levels (photon energy, 350 eV). Solid line through the experimental data points in (ii) demonstrates the results of the least-squares fitting using Voigt shapes. The inset shows the surface state intensity ratios as a function of dosage (in logarithmic scale).

absorbed molecules. Above the dosage of 1360 L, the valence bands barely change, indicating the saturation dosage is reached.

Similarly, the surface component intensity in the C 1*s* core-level spectra (Figure 4.3ii) drops significantly with increasing dosage. The ratio of the surface component intensity to the total C 1*s* PES intensity declines from 31% for bare diamond to about 9 % at saturation dosage (3300 L) as shown in the inset, which cannot be caused by simple physisorption[2]. Meanwhile, the position of the surface component shifts to higher BE after 60 L 1,3-butadiene dosing, and remain unchanged afterwards. It is

---

[2] In a simple physisorption model, assuming the relative intensity ratio between surface component and bulk component of diamond is invariant, from the attenuation of bulk component the thickness of 1,3-butadiene physisorbed overlayers is then estimated to be over 10 Å which is equivalent to about 2-3 monolayers.

known that the energy difference between the surface component and bulk component arises from the more effective core-hole screening by the π-electrons in surface dimers [59]. The bonding of molecules on the surface, however, greatly reduces the π-electron densities and hence the core-hole screening effect, resulting in decreased energy separation. Even at saturation dosage, we are unable to resolve 1,3-butadiene related emission signals due to large energy overlap with the diamond main line at 284.90 eV. However, the spectral width of this peak after deconvolution shows a noticeable increase after reaction ($\mathrm{FWHM_{bare}}$ = 0.75 eV, $\mathrm{FWHM_{reacted}}$ = 0.85 eV), indicating the incorporation of molecular components. Nevertheless, emission from bulk diamond still dominates this peak, and its energy position remains unchanged after the chemical reaction. Since the BE of diamond main line is related to the band bending in bulk diamond associated with space charge layers, its invariance after reaction thus indicates the cycloaddition on diamond surface involving homopolar C—C bond formation does not induce interfacial charge transfer.

In addition to the changes brought to the occupied states by cycloaddition, the unoccupied states of diamond surface are equally influenced. Figure 4.4 presents the NEXAFS of the C *K*-edge before and after gas exposure of 1360 L in surface sensitive AEY mode. Both spectra are characteristic of bulk diamond [76, 78-79] (also see Chapter 3). However, they are different in the pre-edge region. In the bare diamond spectrum, two surface excitonic peaks ($\mathrm{Ex_1}$ and $\mathrm{Ex_2}$) appear in the band gap below the bulk core excitation threshold (289.3 eV). They are explicitly related to resonant transitions to the π*-antibonding states of surface dimers (see Chapter 3.3.2.3). After exposure to 1,3-butadiene, the two surface resonances $\mathrm{Ex_1}$ and $\mathrm{Ex_2}$ disappear and a new resonance peak at 285.0 eV appears which is at typical energy of the $\mathrm{C}(1s)\rightarrow\pi^*$ transition in C=C bonds [41]. This newly formed peak is attributable to the remaining

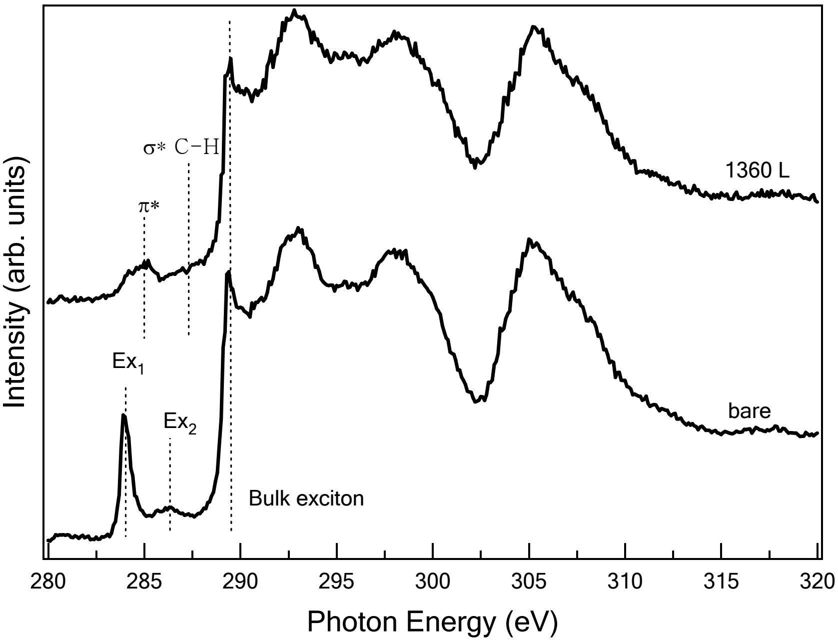

Figure 4.4. NEXAFS spectra of bare diamond (001)-2×1 and diamond surface exposed to 1360 L 1,3-butadiene. NEXAFS spectra were collected in AEY mode. The photon incidence angle was 50° from surface normal, and the auger electron (C *KVV*) collection angle was in normal direction.

C=C bonds of the cyclohexene-like products on the surface (see Figure 4.2). A subtle shoulder at around 287.5 eV corresponds to the C(1*s*)→σ* resonance within the C-H bonds of surface products [41]. The present NEXAFS results are thus consistent with the Diels-Alder reaction scheme shown in Figure 4.2.

4.3 Enhanced secondary electron emission and reduced electron affinity by Diels-Alder reaction

Combining PES and NEXAFS, the chemisorption of 1,3-butadiene on diamond via Diels-Alder reaction is successfully demonstrated. We now turn our attention to analysis of the tuning effect of cycloadditions on several important surface electronic properties of diamond. The secondary electron emission of the diamond surface under different 1,3-butadiene dosages is investigated by recording the low KE regions of UPS spectra at a photon energy of 60 eV, as shown in Figure 4.5a. The emission spectra of the bare diamond surface as well as that exposed to 1,3-butadiene below 10 L dosage are almost identical, featuring a very broad and low intensity peak above 5.3 eV kinetic energy, which is typical of a PEA surface (see Chapter 3.3.2.2). At the dosage of about 10 L, a very sharp and intense peak centered at 5.10 eV with a FWHM of 0.23 eV appears, and the intensity of the emission peak, which is the integrated area over the range 4 eV to 10 eV, is about 4 times larger than that from the bare diamond. Meanwhile the onset of emission shifts about 0.42 eV to lower KE. Considering this low KE cut-off as the position of the VL (E_{vac}), the WF of the reacted diamond is therefore reduced by 0.42 eV accordingly. With further dosages, the secondary electron emission increases continuously but at a much slower rate, and the WF decreases correspondingly as shown in Figure 4.5b. The FWHM of the secondary electron peak increases from 0.23 eV at 10 L to 0.40 eV at 3300 L as well. The effects of the emission peak intensity and WF by cycloadditions appear to saturate above 3300 L from the trends in Figure 4.5b. At saturation dosage, the secondary electron emission intensity experiences over 13 times enhancement as compared to pristine bare diamond. However, even at the highest dosage, the WF of the functionalized surface ($\phi = 4.6\ \text{eV}$) is still 0.6 eV higher than that of hydrogenated diamond, and the corresponding intensity of the sharp secondary electron emission peak reaches 60% of the hydrogenated diamond surface after proper normalization.

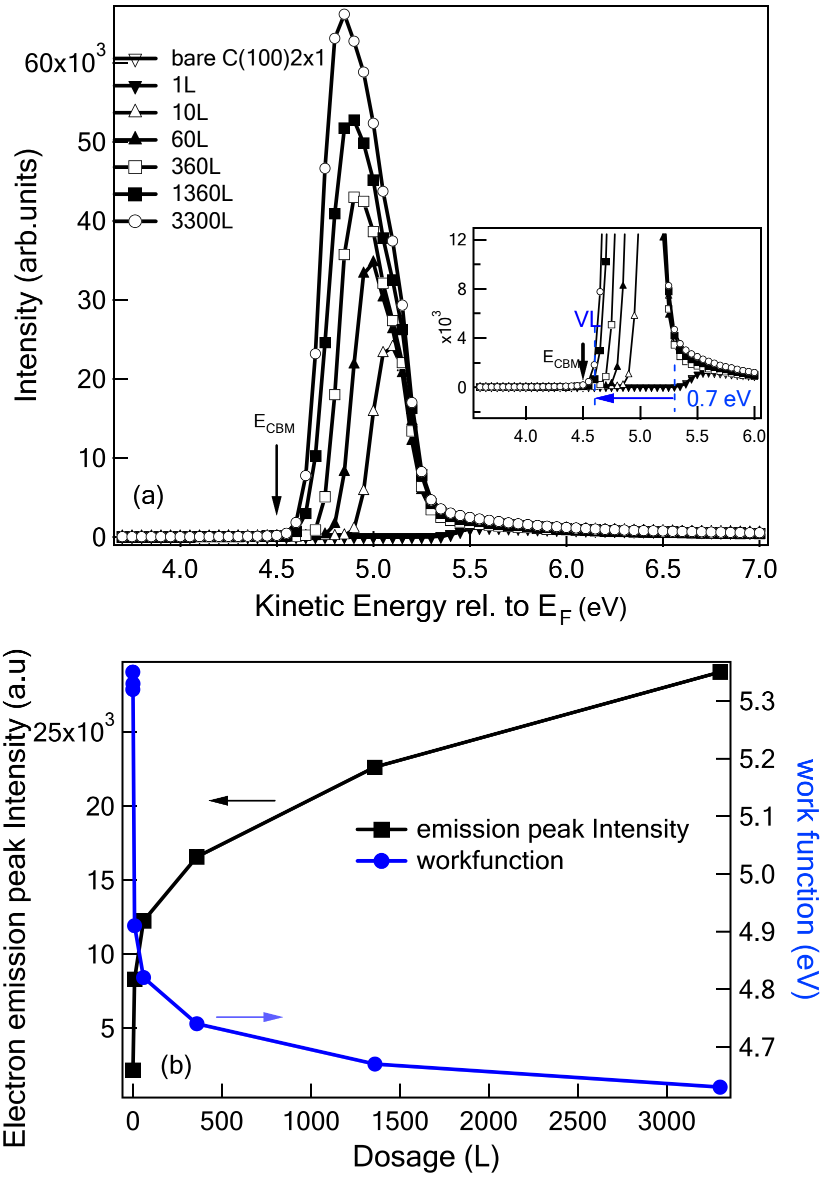

Figure 4.5. (a): Low KE region of normal emission UPS spectra (*hν*=60 eV) of diamond sample under different surface conditions. The KE scale is corrected for an applied bias voltage of -5 V. The inset is a magnification of the onset of emission part illustrating the shift of VL. The vertical dashed lines indicate the position of VL. The arrow represents the position of CBM as discussed in text. (b): The dependence of the secondary electron emission intensity (area of the sharp emission peak from 4 eV to 10 eV) and the WF on 1,3-butadiene dosages.

Table 4.1. The EA value χ_E and the WF ϕ_E for different diamond surface conditions determined by the low KE part of the UPS normal emission spectra in Figure 4.5. χ_C is the EA value determined by DFT calculation.

Diamond	ϕ_E **(eV)**	χ_E **(eV)**	χ_c **(eV)**
C(001)-2×1	5.3±0.1	0.8±0.15	0.28
Dose 1L	5.3±0.1	0.8±0.15	
Dose 10L	4.9±0.1	0.4±0.15	
Dose 60L	4.8±0.1	0.3±0.15	
Dose 360L	4.7±0.1	0.2±0.15	
Dose 1360L	4.7±0.1	0.2±0.15	
Dose 3300L	4.6±0.1	0.1±0.15	
25% coverage			-0.72

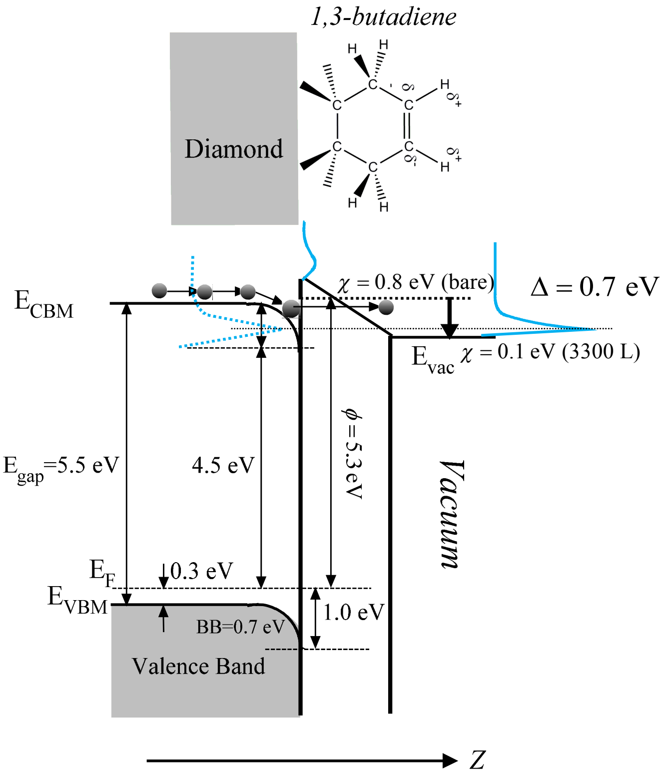

Figure 4.6. Energy band diagram of bare diamond (001) with subsequent 1,3-butadiene adsorption. An interface dipole of 0.7 eV after 1,3-butadiene saturation dosage is present which lowers the VL by the same amount. All values are estimated to lie within an error of 0.10 eV. The secondary electron emission process is also schematically presented. The internal energy distribution profile of secondary electrons as well as the experimentally measured secondary electron emission spectra at different surface EA (blue curves) is schematically presented.

This sharp and intense emission peak after reaction seems to suggest that the cycloadditions with 1,3-butadiene transform bare diamond to a NEA surface, Indeed, many earlier electron-emission studies interpreted the presence of a sharp peak in the secondary electron emission spectra as the sole evidence of a NEA surface without actually determining the EA χ [66, 70, 103]. However, it has been recently pointed out by Yater *et al.* that the sharply peaked energy distribution can also be attributed to a small but positive EA [72], because the internal energy distribution of the impact-ionized secondary electrons may be sharply peaked above the CBM. Consequently, the quantitative value of EA needs to be derived from experimental results in order to clarify the tuning effect of cycloaddition.

The detailed procedure of deriving EA from the relative position of CBM and VL is described in Chapter 3.2.2.2, which uses the BE of diamond C 1*s* bulk component to indirectly deduce the position of CBM (E_{CBM}) relative to the Fermi level (E_{F}). It should be noted that cycloadditions with 1,3-butadiene do not lead to shifts of the diamond main line (Figure 4.3ii), indicating the position of CBM also remains unchanged. Table 4.1 lists the as-determined WF and EA for bare diamond with increasing molecular dosages. This explains how the EA quantitatively decreases with increasing dosage of 1,3-butadiene, and a reduction of EA up to 0.7 eV is reached at saturation dosage. However, the EA of diamond sample at the saturation dosage is still about 1.2 eV higher than that of hydrogenated diamond. From the above analysis, we are able to sketch the energy diagrams for bare diamond surface with 1,3-butadiene adsorption. As shown in Figure 4.6, an interface dipole with magnitude up to 0.7 eV brings down the VL very close to conduction band edge.

As discussed in the previous chapter, the EA in a material is defined as the energy difference between the VL and CBM. For most materials, the EA value is positive, which means that the secondary electrons thermalized to the CBM have to overcome an energy barrier equal to the EA in order to be emitted into vacuum, and as a result the secondary electron emission is relatively low as in the case for bare diamond. With the lowering of the barrier height (EA), more and more secondary electrons can escape from the surface with increased secondary electron emission intensity. In wide band gap materials such as diamond, the conduction band can be close to or even above the VL. With this small or even negative EA, secondary electrons can be emitted into vacuum with little or no energy barrier, leading to very high secondary electron emission in the form of a sharp peak as for hydrogenated diamond. It should be noted that the band bending in diamond also play a role in the enhanced secondary electron emission, because the downward band bending potential helps to accelerate electrons that are excited into the conduction band toward the interface, leading to increased electron density accumulated at surface CBM region. In such a case, the emitted secondary electron energy distribution from UPS can be simply viewed as the energy profile of the secondary electrons that reach the surface. This energy profile is influenced by both the density of available states in the conduction band, band bending, and the complex multiple-scattering and recombination mechanisms during diffusion to the surface [72]. Thus, the peak of the emission spectra may not coincide with the position of CBM. Consequently, for diamond surfaces undergoing Diels-Alder reaction with 1,3-butadiene, despite its small PEA, we could still observe sharp and intense secondary electron peaks up to EA of +0.4±0.15 eV for 10 L dosage. This is because the secondary electron energy distribution which is related to the internal energy distribution of impact-ionized electrons is actually sharply peaked at ~0.3-0.7 eV above E_{CBM} for reacted diamond surfaces (as seen from Figure 4.5a). The ability to probe those electrons by the analyzer is highly dependent on the position of VL at the

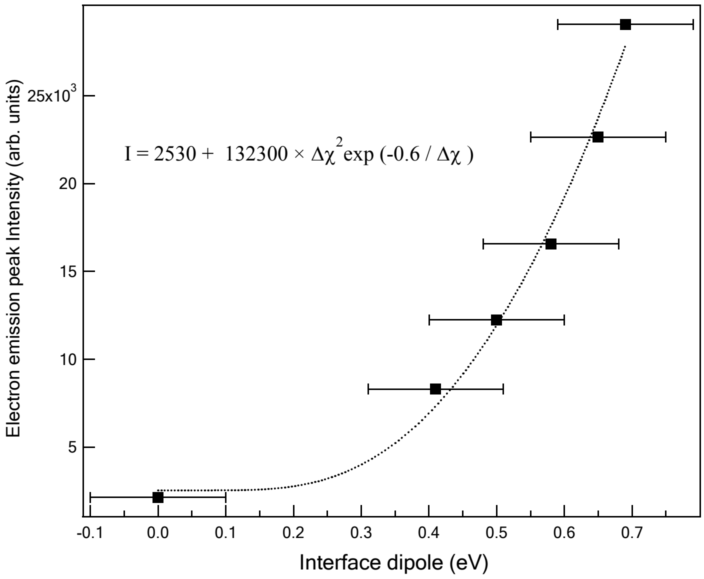

Figure 4.7. The secondary electron emission intensity I as a function of interface dipole which is the change of EA ($\Delta\chi$) compared with pristine bare diamond. The data points are fitted by a dotted line, with the equation shown in the graph.

surface (see illustration in Figure 4.6). Therefore, as long as the VL E_{vac} lies within or below this distribution ($\chi<0.7$ eV), the so-called NEA peak will be observed. As χ increases and more secondary electrons are blocked by a higher energy barrier, the peak becomes narrower and lower in intensity, until it finally vanishes with sufficiently large EA.

The enhanced secondary electron emission process in the presence of a strong interface dipole can be understood in a way similar to the field emission process which is the emission of electrons from the surface of a condensed phase into another phase due to the presence of high electric fields. The only difference is in field emission the emitted electrons are from the Fermi level, while in this case the electrons are mainly hot electrons accumulated at the CBM of diamond. The fundamental mechanism underlying field emission is the quantum mechanical tunneling process called Fowler-Nordheim tunneling [7]. The electric field, which helps to reduce the potential barrier (WF) at the surface, should be on the order of 10^6 V/cm for efficient field emission.

The interface dipole of 0.7 eV over several Angstrom in the present case results in a strong electric field of the order of 10^7 V/cm, which easily exceeds this requirement. Consequently, the intensity of secondary electron emission I can be related to the magnitude of interface dipole $\Delta\chi$ (i.e. change of EA) by adopting the Fowler-Nordheim tunneling relationship:

$$I \propto \Delta\chi^2 \exp\left(\frac{-b}{\Delta\chi}\right). \tag{4.1}$$

The continuous tuning of diamond EA by cycloadditions provides a unique opportunity for us to quantitatively model the dependence of secondary electron emission intensity on the EA. The data points extracted from Figure 4.5 and Table 4.1 is plotted in Figure 4.7, and they can be well fitted by Eqn. (4.1) with fitting parameters listed in the graph. This relationship could be generally applied to other systems as well.

4.4 Origin of the tuning effect of Diels-Alder reaction on electron affinity

The WF (EA) variation induced by adsorbates (both physisorption and chemisorption) on solid surfaces is a common phenomenon. The adsorbed atoms and molecules generally have a significant influence on the electronic structure of a surface [52]. They can rearrange the electronic charge on the surface; they can induce interfacial charge transfer that leads to charge separation; they can form chemical bonds with electronic charge rearrangement within the bond; or they can add elementary dipoles if the adsorbed molecule has its own static dipole moment [104]. In every scenario, an interface (surface) dipole is present on the surface which abruptly shifts the VL. For example, for close-shell adsorbates such as Xe atoms and most conjugated molecules physisorbed on metal surfaces, an exchange-like Pauli-repulsion of electronic clouds of adsorbates pushes back the metal surface electron tailings leading to an interface dipole layer with abrupt reduced WF [105]. However, this push-back effect is negligible on semiconductor surfaces due to the much more localized surface electron densities, whereas chemical bond formation and interfacial charge transfer are the leading causes.

For Diels-Alder reaction with 1,3-butadiene on bare diamond, the interfacial charge transfer can be neglected since no energy shift of the diamond component is observed. Furthermore, covalent bonds formed at their interface are homopolar C—C bonds which should not induce any dipole moment. This argument is further corroborated by a control experiment of adsorption of fullerene (C_{60}) adlayers on bare diamond (Figure 4.8). A C_{60} molecule, being nothing more than a strained polyalkene, can react as both a diene or a dienophile in Diels-Alder reactions [106]. Therefore, they can react with bare diamond dimers in a way similar to 1,3-butadiene, which is indeed experimentally verified [107]. But unlike 1,3-butadiene, C_{60} is made up of carbon atoms only and has no internal dipole. As shown in Figure 4.8, the adsorption of C_{60} induced a VL change of less than 0.1 eV. The shape and intensity of the emission peak after reaction is also close to pristine bare diamond, in clear contrast to the absorption of 1,3-butadiene. This convincingly demonstrates that C—C bond formation at the diamond/molecule interface by cycloadditions alone cannot contribute to the observed tuning effect, whereas the internal dipole moment of the reaction product is the most cause.

Inspection of the reaction scheme in Figure 4.2 suggests the cyclohexene-like reaction product might provide such a dipole moment. If we view the attached molecular adducts as an extension of the diamond surface lattice, its terminal C—H bonds have dipole moments pointing from the more electronegative C (δ^-) to less electro-

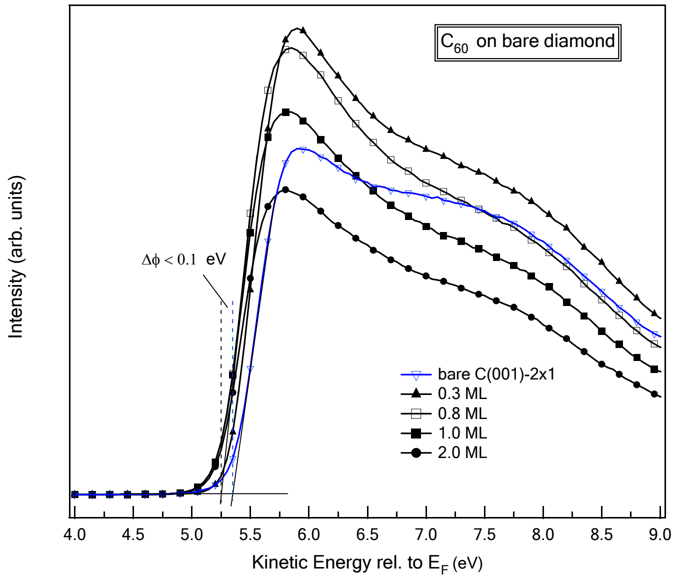

Figure 4.8. Low KE region of normal emission UPS spectra (*hv* = 60 eV) of bare diamond with increasing fullerene coverage (in monolayers). The KE scale is corrected for an applied bias voltage of -5 V. The vertical dashed lines indicate the position of VLs.

negative H (δ^+). For this interpretation to be plausible, the dipole moments must point toward the vacuum side to give rise to a surface electrostatic potential drop in a way similar to NEA of hydrogenated diamond. This argument would require a specific geometry of the reaction product to contribute a net perpendicular component of the dipole moment relative to the surface. Since the C—H bond orientation cannot be derived from present spectroscopic studies, DFT calculations[3] are needed to optimize the geometries of the reaction products [108-109].

4.4.1 Optimization of surface geometry by DFT calculations

The optimized surface structure is shown in Figure 4.9, with the bond lengths and angles listed in Table 4.2. The [4+2] product has a six-member ring containing one

---

[3] The first-principles DFT calculations using the plane wave basis VASP code within the generalized gradient approximation (GGA) is performed by Dr. Lei Liu in Department of Physics, NUS. Ultrasoft pseudopotentials were employed as the ionic potential for all the elements. Sampling *k*-points with 0.05 Å^{-1} separation in the Brillouin zone were used. All structures were optimized and relaxed such that the change in energy upon ion displacement was less than 1 meV.

double bond at the top. The C—C bond lengths are typical of molecular single and double bonds with the exception of the reacted surface dimer bond, consistent with previous calculations [55, 75, 98, 110]. The coverage of 1,3-butadiene used in the calculation is 25%, corresponding to one adsorbed molecule for every four surface dimer sites. A higher coverage was found to significantly increase the total energy due to the steric repulsion between hydrogen atoms of adjacent molecules, and this causes the system to become energetically unstable [110]. At 25% coverage, the plane of the six member ring is perpendicular to the diamond surface at its energy minimum. This vertical configuration is attributed to the repulsive interaction of adjacent unreacted dimers with the π bond of the [4+2] cycloaddition product [98]. In this configuration, the two terminal C—H bonds (C2—H2 and C3—H3) that lie in the six-member ring plane are directly pointing to the vacuum side, with a tilting angle of 29.4° from surface normal (Table 4.2), similar to that of the C—H bonds on hydrogenated diamond (24.5°) [55, 57]. Therefore, the lowering of VL and EA through adsorption of 1,3-butadiene molecules is indeed analogous to the hydrogenated diamond (001) surface in which the dipole moments from terminal C—H bonds form a planar dipole layer. With increasing coverage of adsorbed molecules, the planar average of the electrostatic potential field of this dipole layer will continuously lower the VL until the molecules reach saturation coverage, at which the total interface dipole due to molecular adsorbates reaches 0.7 eV. It should be noted that the other four C—H bonds (C1—H1, C1—H1', C4—H4, C4—H4' in Figure 4.9) lie parallel to the diamond surface and thus do not contribute to the surface dipole layer.

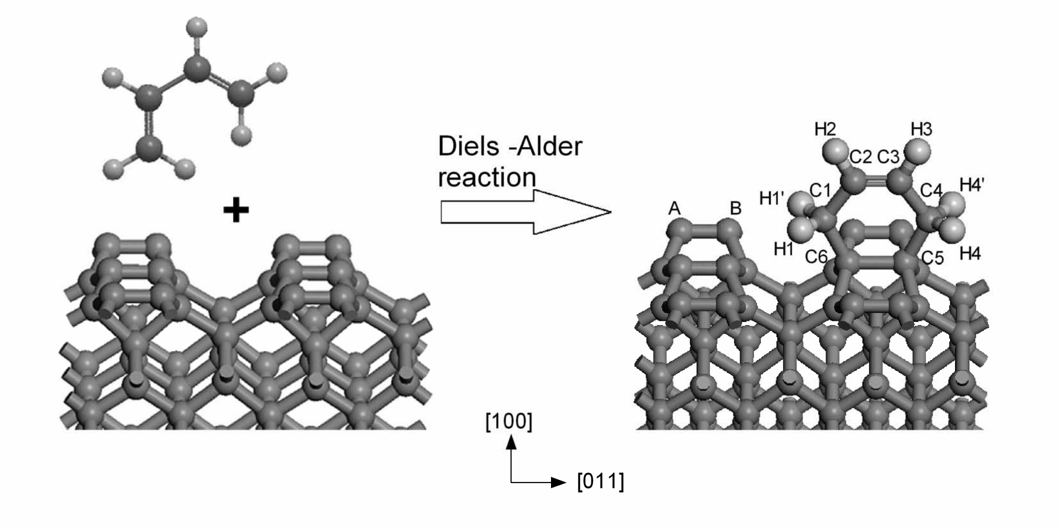

Figure 4.9. Ball-and-stick models show the side view of Diels-Alder reaction of 1,3-butadiene with C(001)-2×1 surface. Dark gray and light gray balls represent C and H atoms respectively. These models have been relaxed so that the structure shown reflects the actual geometry.

Table 4.2. Bond lengths, angles for the Diels-Alder reaction product in Figure 4.9.

bond length (Å)								angle(deg)
A-B	C5-C6	C6-C1	C1-C2	C2-C3	C3-C4	C4-C5	C2-H2	C3-C2-H2
1.38	1.66	1.56	1.51	1.33	1.51	1.56	1.09	119.4

4.4.2 DFT calculations of the electron affinity

The lowering of VL via attachment of 1,3-butadiene molecules is further supported by DFT calculations of the plane-averaged electrostatic potentials for the bare, hydrogenated and 1,3-butadiene adsorbed diamond surfaces. The diamond structure was modeled by a supercell containing twenty layers of diamond and a 20 Å vacuum region, to avoid interactions between periodically repeated slabs. Both surfaces of the slab were kept equivalent, so the calculated electrostatic potentials can be well aligned in the central bulk region.

In Figure 4.10, we plot the plane-averaged potential for different diamond (001) surface conditions. All the potentials agree well inside the bulk and flatten out in the vacuum region, indicating good convergence with respect to the number of diamond layers and the size of the vacuum layers adopted in the calculation. The position of the VBM (E_{VBM}) is computed using bulk diamond calculations. By adding the experimental band gap E_{gap} = 5.47 eV, the position of the CBM (E_{CBM}) can be determined. As seen in Fig. 5, the bare C(001)-2×1 has the largest potential barrier; its VL (indicated by the flat potential region) lies above the CBM, giving an EA of +0.28 eV. With the attachment of 1,3-butadiene, the VL is indeed significantly lowered by 1.0 eV with an EA of -0.72 eV. The hydrogenated surface has the lowest VL with a NEA of -2.32 eV, in agreement with previous calculations [74-75] which are known to be significantly overestimated. Moreover, the flattening out region for 1,3-butadiene attached surface begins several Å father away from center than those of bare and

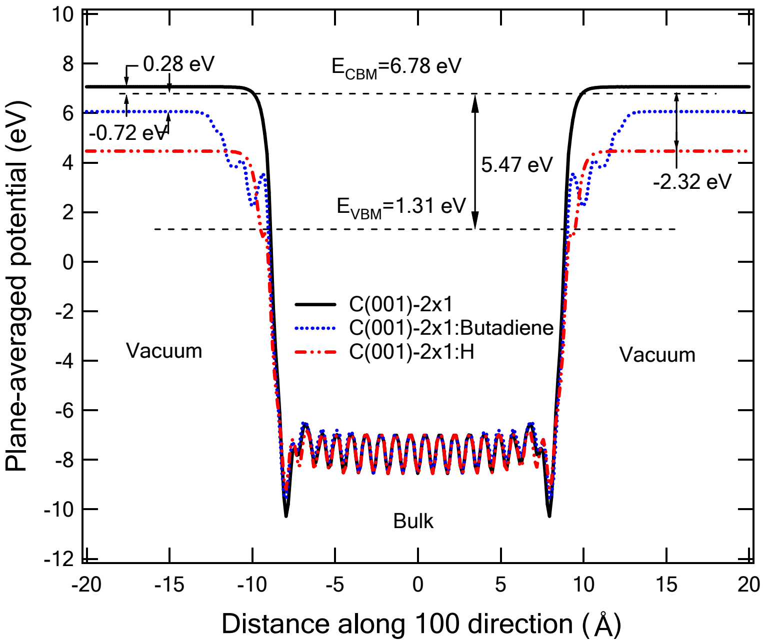

Figure 4.10. Calculated plane-averaged, self-consistent potentials of bare, 1,3-butadiene adsorbed and hydrogenated diamond (001) surfaces.

hydrogenated diamond, consistent with the position of the outer C—H bonds of the reaction product (Figure 4.9). When these calculated values are compared to the experimentally determined EA values as listed in Table 4.1, large discrepancies can be found. The inconsistency may arise from the following two reasons. First, the positions of E_{CBM} and E_{VBM} labeled in Figure 4.10 are calculated using bulk diamond lattices without considering possible band bending near the surface region. Figure 4.6 shows that the band bending is 0.7 eV for the bare diamond surface. Taking this band bending into account, the calculated EA for bare diamond is increased to 1.0 eV, in good agreement with the experimental value of 0.8±0.15 eV (Table 4.1). Second, the change of EA due to the attachment of molecules is proportional to the potential step caused by the surface dipoles and can be expressed by the basic electrostatics equation Eqn. (3.2). The depolarization factor $S(n)$ which depends on n takes the mutual electrostatic interaction of the dipoles into account and approximately equals to 1 at present low dipole density. From Eqn. (3.2), it is obvious that the change of EA is thus directly proportional to the surface dipole density, which in turn is proportional to the 1,3-butadiene coverage. The coverage of butadiene used in the theoretical calculations is 25%, which may be substantially higher than the actual coverage in the experiments leading to the overestimated EA changes. By comparing the measured $\Delta\chi$ (0.70 eV) at saturation dosage with the calculated one (1.00 eV) for 1,3-butadiene adsorbed surface, we can estimate the coverage of 1,3-butadiene to be about 17% at saturation dosage. This low coverage is responsible for the higher EA and lower secondary electron emission than that of the fully hydrogenated surface. It should be noted that change in EA does not scale linearly with the coverage of the adsorbates at high coverages (e.g. >50%). On one hand, at high dipole densities the depolarization factor $S(n)$ cannot be approximated to 1 any more and it tends to decrease the electrostatic potential drop induced by the dipole layer. On the other hand, at high coverages the geometry of adsorbed molecules is reoriented due to the need to minimize steric repulsion between neighboring molecules. This causes their terminal C—H bonds to be tilted toward the surface plane, thus reducing the perpendicular component of the dipole moments [110].

4.5 Chapter summary

In this chapter, the tuning of EA and secondary electron emission by Diels-Alder reaction of 1,3-butadiene with bare diamond surface is investigated by synchrotron-based spectroscopies and DFT calculations. A significant reduction in EA up to 0.7 eV and enhancement of secondary electron emission were observed after 1,3-butadiene absorption. The lowering of VL via 1,3-butadiene is supported by DFT calculations. It was found the terminal C—H bonds in the covalently bonded organics on diamond contribute to the enhanced secondary electron emission and reduced EA in a mechanism similar to C—H bonds on hydrogenated diamond surface with a field emission-like emission process. This mechanism for tuning electron affinity by cycloadditions can be applied to other hydrocarbon molecules on diamond as well, where similar phenomenon have been observed [100].

CHAPTER 5

ORGANIC SEMICONDUCTOR ON DIAMOND: A COMPARATIVE STUDY OF COPPER PHTHALOCYANINE ON HYDROGENATED AND BARE DIAMOND (001) 2×1 SURFACES

5.1 Introduction

In the previous chapter, we examined the cycloadditions with 1,3-butadiene on bare diamond surface and its tuning effect on surface electronic properties. Being a simple organic molecule with two unsaturated double bonds, 1,3-butadiene serves as a simple but good model organic system to investigate cycloadditions on solid substrates. However, its structural simplicity also limits its functionalities. From a technological point of view, functionalization of diamond with more complex organic molecules, especially those with conjugated π-electron systems are of great interest. These organic molecules, when assembled into thin films or crystals, often behave as semiconductors [111-112] and may therefore have the potential to function as active components in diamond-based organic electronic devices.

In recent years, organic semiconductors have attracted much attention for low-cost, large-scale and flexible electronic device applications [30, 113-118], encompassing organic light emitting diodes (OLEDs), organic solar cells, organic field effect transistors (OFETs) and organic spintronics. Intensive research effort has been devoted to studying the growth of organic thin films with well-controlled properties, such as molecular orientation [119-121], supramolecular organization [122-126] and well-defined surface or interface morphologies or nanostructures [127-131]. It is widely accepted that the interface between the active organic layers and the substrate, *i.e.*, molecule-electrode or molecule-dielectric interface, plays a crucial role in achieving good device performance. Consequently much effort has been spent to understand energy level alignment and the formation of interfacial dipoles at the interface between molecules and metals, semiconductor or conducting polymers [104, 132-133]. Moreover, the supramolecular organization at the interface, which can in turn influence the crystalline structure and orderliness of subsequent grown molecular films, is found to be governed by a delicate interplay between the intermolecular interactions and the molecule-substrate interactions [134-136]. Understanding their relationships is crucial to optimize the morphology, structures and electronic properties of organic thin films for device applications. Till now, most of the research efforts have been devoted to studying the interfaces between organic semiconductors and several technologically important substrates including metals and conducting polymer electrodes, organic heterojunctions, and inorganic semiconductors such as silicon. Much less attention has been paid to understanding interfacial interactions between organic semiconductors and diamond.

Diamond (001) provides an excellent platform to examine how the interfacial interaction strength influences the electronic structure, energy level alignment and molecular organization at their interfaces. The surface reactivity of diamond can be easily tuned by varying the surface termination. As discussed in the previous chapters, bare diamond surface exhibits reactivity towards unsaturated molecules via cycloadditions; and hence this interface is dominated by strong covalent bonding interactions. On the contrary, hydrogen termination passivates all the dangling bonds of reactive dimers, rendering the hydrogenated diamond surface chemically inert. As a result, the interfacial interactions between hydrogenated diamond surface and organic semiconductors are expected to be dominated by weak Van-der-Waals-type interactions.

Diamond thus provides a unique opportunity to realize these two distinct interfacial interactions on the same substrate, which can be exploited in different device

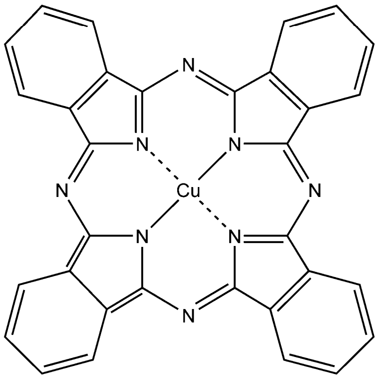

Figure 5.1. Chemical structure of CuPc.

architectures. Covalent interactions at interfaces can strongly couple the organics onto the substrate lattice, integrating properties and features of both organic and inorganic semiconductors. This is vital for the realization of organic-inorganic hybrid devices. Weak van-der-Waals-type interactions at interfaces, on the other hand, can better retain the structural and electronic integrity of organic semiconductor molecules, which is important for devices that rely on the charge transport in organic active layers close to the interface, such as OFETs. Clarifying the interfacial properties between diamond and organic semiconductors, therefore, has important implications for understanding and engineering organic/inorganic interfaces.

Copper(II) phthalocyanine (CuPc) is traditionally used as an organic pigment [137]. It is now a widely adopted organic semiconductor with high chemical stability and remarkable electronic properties (e.g. high hole mobility [138], superconducting upon alkali doping [139]), and represents one of the most promising candidates for organic electronics [140-143]; it therefore serves as an excellent archetypical organic semiconductor for the present study. The CuPc molecule has a planar structure with fourfold-symmetry, and is comprised of four aromatic rings around a porphyrin-like central ring with a copper ion (Cu^{2+}) at its center (Figure 5.1). It belongs to the phthalocyanine family with different metal centers (or metal free Pc). The phthalocyanine ligand has a complex electronic structure which is further complicated by the introduction of the transition metal ion into the system. The overlapping of the Cu 3*d* electronic states with ligand 2*p* states produces a combination of both localized and delocalized molecular frontier orbitals near the Fermi level [144-145]. Among them, the peculiar singly occupied molecular orbital (SOMO) is largely derived from Cu $3d_{x2-y2}$ orbital (with b_{1g} symmetry), making CuPc distinct from the other metal-Pcs [144-146].

Depending on the growth parameters, bulk CuPc molecular solids exist in several different crystalline polymorphs, and the two most important monoclinic crystalline forms are denoted *α* and *β* forms (c.f. Figure 5.2 and Table 5.1) [143]. In general, films in *α*-form can be more easily grown by vacuum deposition on substrates at RT, whereas the *β*-form is observed if the substrate is kept at elevated temperatures (>210 ºC) during deposition. Moreover, the $\alpha \rightarrow \beta$ phase transition can be achieved by annealing the film in N_2 ambient at 350 ºC [147]. In both polymorphs, the molecules form molecular columns along the *b* axis with molecular plane parallel to each other (π—π stacking), while the adjacent columns are arranged into a herringbone-like structure. The major difference between the two polymorphs is the angle between the normal direction of molecular plane and the stacking direction (*b* axis), which is about 26º in the *α*-form and 45º in the *β*-form. As a result, despite of different Cu-Cu distances (equal to *b*), the interlayer distance (*d*) within the molecular column is almost the same (~3.4 Å) for both forms. The herringbone packing of molecular crystals often leads to anisotropic electronic properties, such as electric conductivity. Along the π—π stacking direction (*b* axis), the intermolecular interactions are stronger due to larger overlapping of π-orbitals between adjacent molecules than in the per-

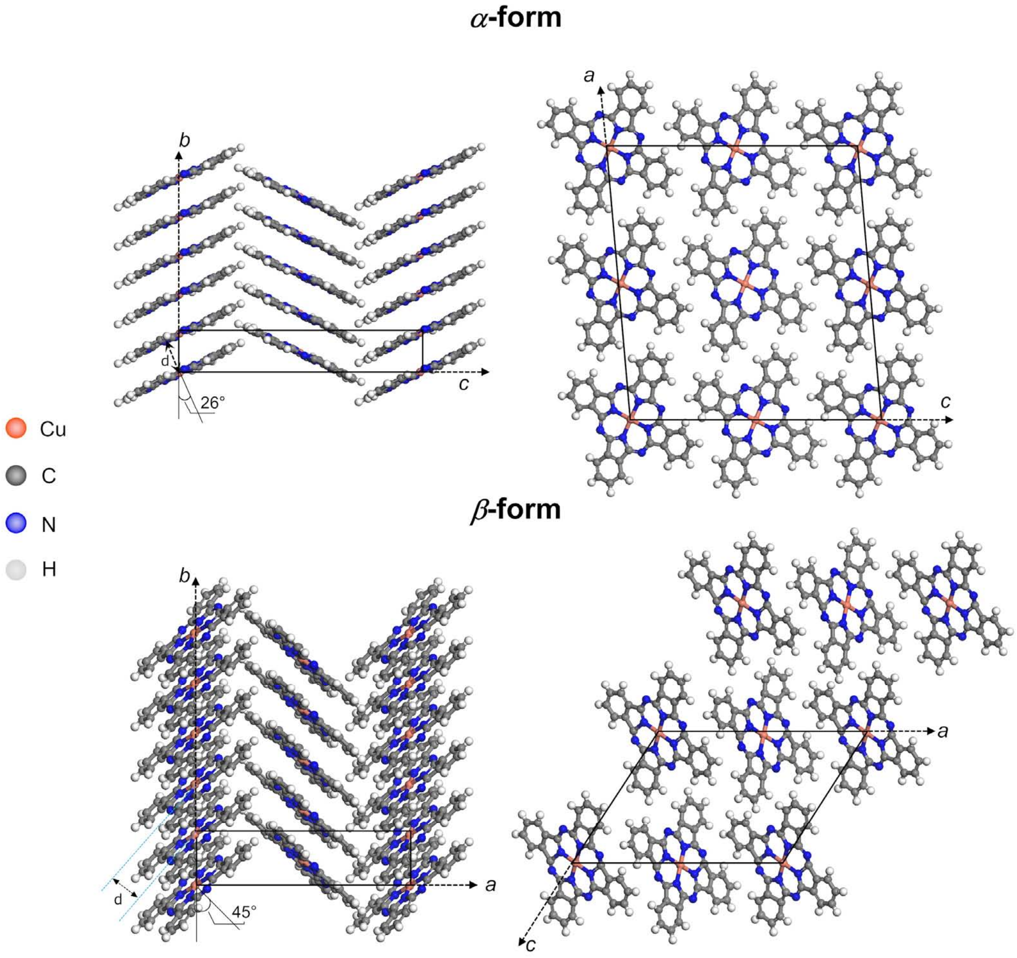

Figure 5.2. Crystalline structures of *α* and *β* forms of CuPc crystals.

pendicular direction, resulting in more dispersed orbital-derived intermolecular electronic bands with enhanced charge carrier mobilities [148].

Table 5.1. Lattice parameters of *α* and *β* form of CuPc crystals.

	a (Å)	*b* (Å)	*c* (Å)	*β* (deg)	mol/unit cell
***α*-form**	25.92	3.79	23.92	90.4	4
***β*-form**	19.6	4.79	14.6	120.6	2

The electronic structures and growth mode of CuPc films on various substrates (metals, inorganic and organic semiconductors) have been extensively investigated [149-173]. Its numerous unsaturated bonds are expected to readily react with reactive inorganic semiconductor surfaces with dangling bonds. This is already confirmed by PES and STM studies of the adsorption and bonding of CuPc molecules on Si(111) and Si(100) surfaces [149-152, 162]. However, to our knowledge no studies have been carried out on diamond (001) 2×1 which bears similarities to the Si(100) 2×1.

In this chapter, I will discuss and compare the *in-situ* adsorption of CuPc molecules on hydrogenated diamond C(001) 2×1:H as well as on bare diamond C(001) 2×1, focusing on the differences in interfacial electronic structures and supramolecular organizations. The different interactions between molecules and the two diamond surfaces are mainly explored by synchrotron-based PES. I will also systematically show how the different nature of molecule-substrate interactions influences the ordering and molecular orientation at different coverages using angular-dependent NEXAFS spectroscopy.

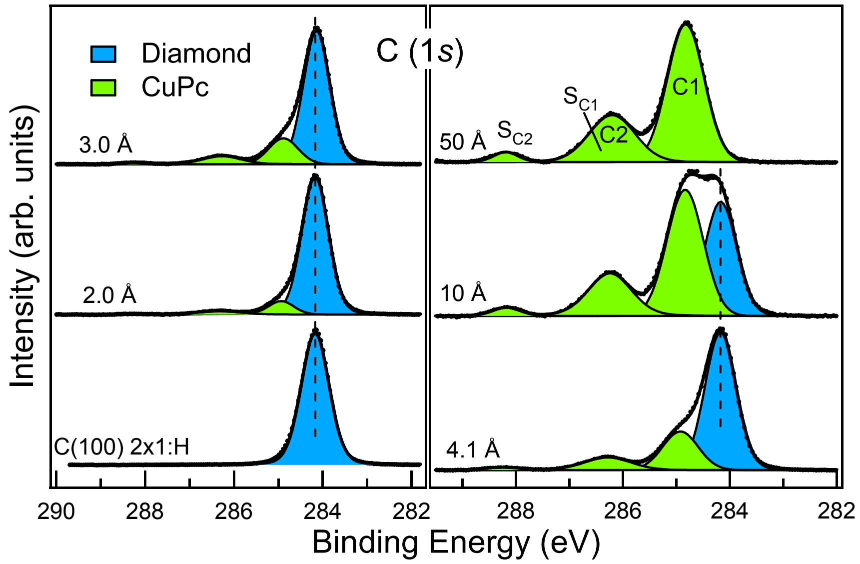

Figure 5.3. C 1*s* PES spectra (photon energy, 350 eV) of CuPc on hydrogenated diamond with increasing thickness. C 1*s* spectra are all normalized to the same height for better viewing. Solid lines through the experimental data points demonstrate the results of the least-squares fitting.

5.2 CuPc on hydrogenated diamond surface

5.2.1 C 1*s* and N 1*s* core level PES spectra

The evolution of C 1*s* PES spectra with increasing CuPc thickness is shown in Figure 5.3. The cleanliness of pristine hydrogenated diamond surface after mild annealing (400 ~ 600 ºC) to desorb loosely adsorbed hydrocarbon molecules is confirmed by the single C 1*s* bulk component located at 284.3 eV. Subsequent step-by-step deposition of CuPc leads to continuous changes to the C 1*s* line shape from that of the diamond substrate to that of the deposited CuPc film. At large thickness (50 Å), the signal from diamond substrate is completely attenuated and the C 1*s* spectrum is characteristic of CuPc films with three distinctive peaks (labeled C1, C2, S_{C2} in Figure 5.3). Both the relative peak positions and area ratios of individual CuPc components agree well with previous studies of CuPc films [151, 153-156]. They are attributed to the aromatic carbon of the benzene rings (C1), pyrrole carbon linked to

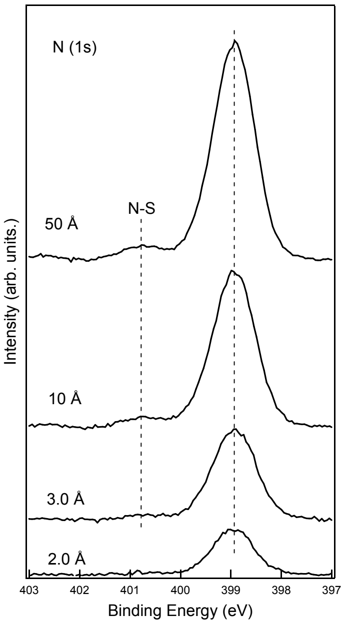

Figure 5.4. N 1*s* PES spectra (photon energy, 500 eV) of CuPc on hydrogenated diamond with increasing thickness.

nitrogen (C2) and a shake-up satellite of C2 carbon (S_{C2}) related to intramolecular π-π* transitions, respectively. Although there should be an additional satellite feature associated with the aromatic carbon (C1) hidden within the C2 feature, the C2 peak can be fitted very well using a single voigt-shape peak. During the fitting process, the energy separations and the intensity ratio of individual peaks of CuPc were fixed, whereas their absolute energy positions and widths were free fitting parameters. As shown in Figure 5.3, the C 1*s* spectra measured after each deposition step of CuPc on hydrogenated diamond surface can be satisfactorily fitted by a superposition of spectra from diamond and CuPc with different spectral weights. Additional components are not necessary in the fitting process. After each deposition step, there were no observable BE shifts for both diamond component and CuPc components within experimental error of 0.05 eV.

The corresponding N 1*s* spectra of CuPc on hydrogenated diamond appear as one dominant peak with its corresponding satellite located at 1.6-1.7 eV higher in BE (N-

S), typical of CuPc bulk films (Figure 5.4) as well [156]. The FWHM of the main peak is around 1.0 eV at all coverages of CuPc, indicating the integrity of Cu-N bonds and hence the molecular structure. Its energy position also remains the same at different thicknesses. It should be noted that the chemical states of the aza-bridging nitrogens (the outer four nitrogens bonded with two carbon atoms) and the pyrrolic nitrogens (the inner four nitrogens bonded with carbon atoms and the central Cu metal atom, see Figure 5.1) are very similar and thus they cannot be separated in the main peak [156].

In both the C 1*s* (Figure 5.3) and N 1*s* (Figure 5.4) spectra, the absence of additional components other than those from bulk diamond and CuPc films, especially at the earliest stages of CuPc deposition, clearly indicates that no chemical reaction occurs at the interface due to the hydrogen passivation. More importantly, the diamond C 1*s* main line exhibits no shifts upon CuPc deposition. This suggests that the electronic levels of the hydrogenated diamond substrate remain essentially unperturbed by CuPc deposition. In particular, the interfacial charge transfer, which is generally observed between semiconductor/metal or semiconductor heterojunctions due to their Fermi energy difference [52], is negligible at this interface. Otherwise, the charge redistribution across the interface would modify the space charge layer in hydrogenated diamond, causing electrostatic band bending which would be manifested as a BE shift of diamond core-level states.

5.2.2 Valence band spectra and work function measurements

Valence band spectra of hydrogenated diamond with deposited CuPc films at different thicknesses are shown in Figure 5.5a. The spectrum of hydrogenated diamond is typical for a diamond C(100) 2×1:H surface (see Chapter 3.2.2.1). Subsequent depositions of CuPc lead to gradual attenuation of diamond-associated valence band features and the emergence of several new components originating from CuPc. At a nominal thickness of 50 Å, various molecular orbitals derived states can be clearly resolved, while diamond features completely disappear. The spectrum of 50 Å CuPc film is typical of that for bulk CuPc with the HOMO peak at 1.70 ± 0.05 eV and its edge at 1.25 ± 0.05 eV (indicated by the vertical dashed lines in Figure 5.5) [154, 156]. No additional spectral structures close to the Fermi level, which would otherwise indicate

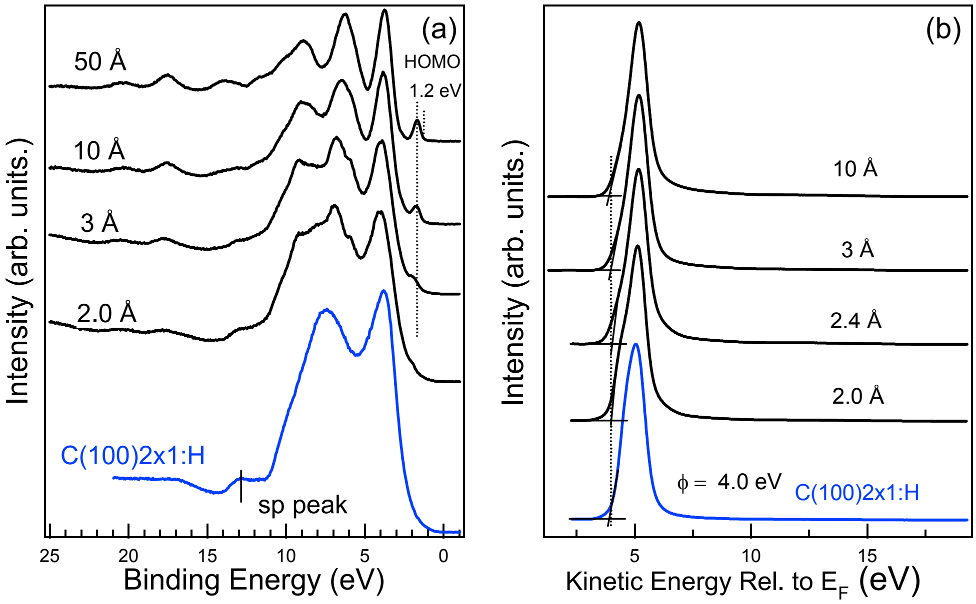

Figure 5.5. (a) UPS spectra (photon energy, 60 eV) of hydrogenated diamond after CuPc deposition of increasing thickness; (b) the corresponding secondary electron emission at the low KE region. The KE scale in (b) is corrected for an applied bias voltage of -5 V and the cut-offs (vertical line) indicate the positions of the VL relative to the Fermi level (E_F). The secondary electron emission peaks are all normalized to the same height.

the appearance of interfacial gap states associated with chemical bond formations or strong charge transfer, can be identified in Figure 5.5a. Therefore, the evolution of the valence band spectra is consistent with the non-reactive nature of the heterojunction between CuPc and hydrogenated diamond as concluded from the core-level PES spectra.

Figure 5.5b shows the secondary electron emission recorded in the low KE part of the UPS spectra. Pristine hydrogenated diamond exhibits a strong and sharp secondary emission peak with a WF of 4.0 ± 0.1 eV, which is typical of a NEA diamond surface (also see Chapter 3.2.2.2). This cut-off position barely changes with subsequent CuPc depositions, indicating a common VL alignment across the CuPc/diamond interface, in contrast to most organic/metal interfaces where a pronounced shift of VL is observed as a result of interface dipole formation [104, 132-

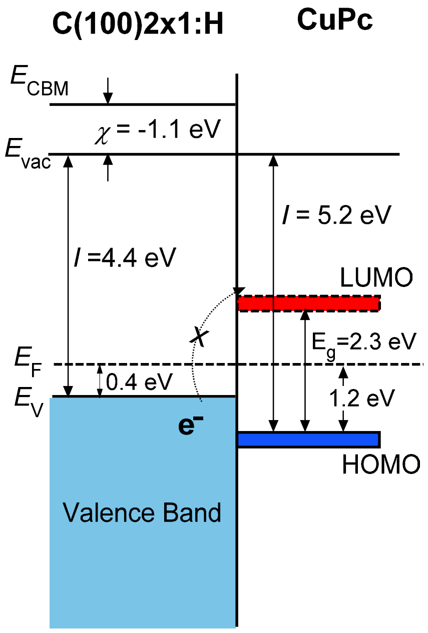

Figure 5.6. Schematic energy level diagram of CuPc on hydrogenated diamond surface. The LUMO position of CuPc film is estimated by adding the CuPc transport band gap of 2.3 eV [158]. All values are estimated to within an error of 0.1 eV.

133]. Since the formation of interface dipole is commonly associated with charge transfer and charge redistribution (e.g. chemical bond formation, Pauli-repulsion) at the interface, the absence of an interface dipole barrier at the interface between hydrogenated diamond and CuPc corroborates our previous conclusion that neither chemical reaction nor charge transfer occur at the interface.

Figure 5.6 shows the energy level alignment across the heterojunction. The determination of energy levels of diamond is described in Chapter 3. Hydrogenated diamond surface exhibits a pronounced NEA of -1.1 eV, with nearly flat bands towards the surface. After the deposition of CuPc molecules, a common VL is achieved across the interface. The passivation of hydrogen effectively prevents diamond from reacting chemically with adsorbed organic molecules, and the energy levels in diamond are unperturbed. Meanwhile, the apparent large energy barrier between the diamond VBM and molecule's LUMO excludes electron transfer at the interface. On the molecular side, there is also no observable bending of molecular energy levels in the CuPc film. The IP, which is the distance between HOMO and VL is estimated to be about 5.2 eV by adding WF (4.0 eV) to the HOMO-E_F energy difference (1.25 eV), in agreement with the literature [156]. It is interesting to note that a downward molecular level bending in CuPc films on metal surface is usually observed, which is due to the more effective screening effect of photoholes by the metal substrate for molecules in the vicinity of the metal than those farther away from the interface, thereby reducing the BE of molecular energy states [154, 156]. However, this final state effect is almost negligible on hydrogenated diamond surface due to its much lower density of conduction electrons (i.e. low dielectric constant) compared with metals.

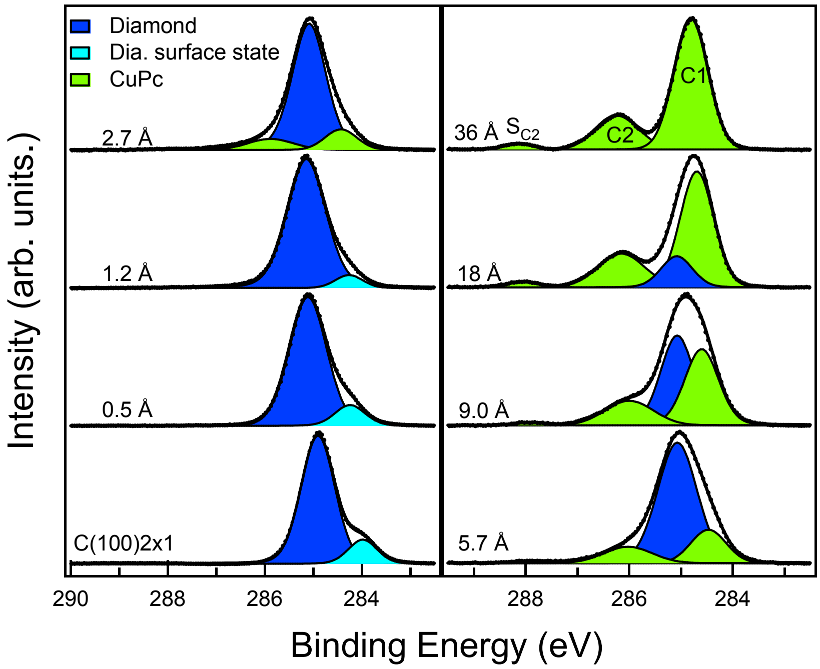

Figure 5.7. C 1*s* PES spectra (photon energy, 350 eV) of CuPc on bare diamond with increasing thickness. C 1*s* spectra are all normalized to the same spectral height for better viewing. Solid lines through the experimental data points demonstrate the results of the least-squares fitting.

5.3 CuPc on bare diamond surface

5.3.1 C 1*s* and N 1*s* core level PES spectra

As discussed in Chapter 4, the highly strained double bonds (π plus σ) of bare diamond (001) dimers are reactive towards alkene-containing organic molecules through cycloaddition reactions. Similarly, a CuPc molecule can be viewed as a giant alkene-like molecule with numerous unsaturated double bonds, thereby allowing chemical reactions to proceed on bare diamond. The chemical reaction occurring at the CuPc and bare diamond interface is confirmed by C 1*s* and N 1*s* PES spectra. Figure 5.7 shows the C 1*s* PES spectra of bare diamond with increasing CuPc thickness. Upon the deposition of CuPc molecules, there is an apparent intensity decrease of the dimer related surface state, which totally disappears with the emergence of C1 and C2 peaks from CuPc at a thickness of 2.7 Å. Following the same rationale in the discussion of Diels-Alder reaction with 1,3-butadiene in Chapter 4, the radical suppression of the bare diamond surface state is attributed to the cycloaddition-like reaction that breaks the dimer π-bonds. However, neither the CuPc component nor additional components related to newly formed bonds between diamond and CuPc can be resolved below the thickness of 2.7 Å, possibly due to overlaps with the dominant diamond components. Subsequent depositions lead to further attenuations of the diamond main line, and CuPc components become dominant. The well-formed CuPc components (C1, C2, and S_{C2}), especially the existence of the π-π^* shake-up satellite of C2 carbon (S_{C2}), clearly indicate the integrity of CuPc molecules deposited after all diamond dimers are passivated by the first CuPc monolayer. During the least-squares fitting procedure, it was found that fixing both the relative energy positions and intensities of individual peaks of CuPc cannot yield satisfactory fitting results. This is attributed to the reacted first monolayer of molecules which is expected to be structurally different from unreacted molecular overlayers; therefore the intensity ratios of CuPc components were treated as free fitting parameters in the fitting process. In contrast to a constant intensity ratio between C1 and C2 (C1/C2 = 2.3) of CuPc on hydrogenated diamond, the ratio of C1 to C2 on bare diamond increases from 1.3 at low coverage of CuPc (2.7 Å) to 3.0 at high coverage (36 Å). The increase in C1/C2 ratio is attributable to the change of CuPc molecular orientation, resulting in different attenuations of the pyrrolic (C2) and aromatic carbon (C1) signals respectively. When CuPc molecules lie flat on the surface, the C 1*s* PES signals from pyrrolic and aromatic carbon atoms are similarly attenuated, whereas for molecules standing up on the surface the electrons from the pyrrolic C atoms (C2) are attenuated by aromatic rings (C1) closer to the vacuum interface [159, 171]. Therefore, the apparent increase in C1/C2 ratio as a function of film thickness suggests a change of

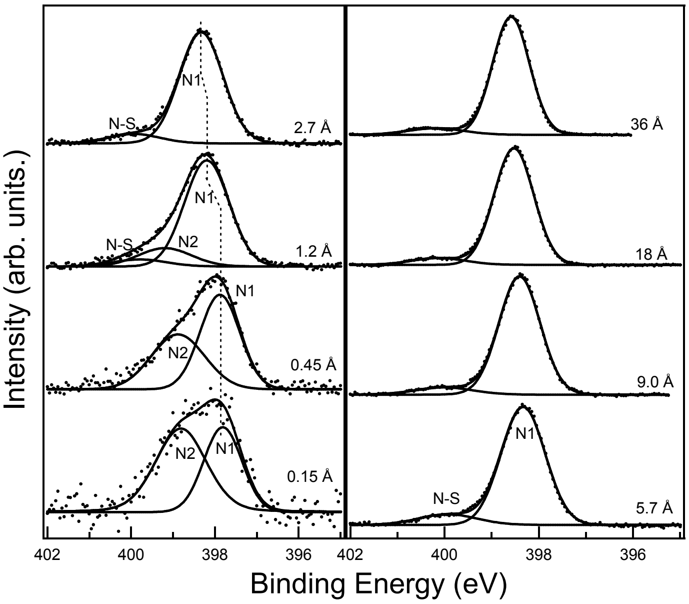

Figure 5.8. N 1*s* PES spectra (photon energy, 500 eV) of CuPc on bare diamond with increasing thickness. N 1*s* spectra are all normalized to the same spectral height for better viewing. Solid lines through the experimental data points demonstrate the results of the least-squares fitting.

CuPc molecular orientation from lying-down at monolayer coverage to standing up in multilayers.

The corresponding N 1*s* spectra are shown in Figure 5.8. The spectral shape of sub-monolayer CuPc deposited on bare diamond contrasts strongly with those of the multilayer films (right panel of Figure 5.8). The initial deposition of 0.15 Å CuPc already leads to the formation of two distinct peaks located at around 397.8 eV (peak N1) and 398.8 eV (peak N2), respectively. Subsequent depositions lead to gradual diminishing of the N2 intensity until it completely vanishes at a thickness of 2.7 Å. Beyond the thickness of 2.7 Å, the spectra is dominated by peak N1 with a small shake-up satellite peak located at 1.7 eV higher BE (N-S), resembling that of CuPc on hydrogenated diamond as well as bulk CuPc films [156]. The N1 component is hence attributed to nitrogen atoms of pristine CuPc molecules, while N2 is related to the interfacial species of nitrogen atoms covalently bonded to diamond surface dimers. It should be noted that the N1 and N2 components at submonolayer coverages may originate from the two inequivalent types of nitrogen atoms (aza-bridging and pyrrolic) within the same CuPc molecule. Indeed, nitrogen atoms at the aza-bridging sites are known to exhibit a higher reactivity than the pyrrolic ones. This was demonstrated previously in potassium-doped CuPc, where it was found the K^+ ions are prone to be bonded close to the aza-bridging sites [160]. More recently, using STM combined with DFT calculations, Baffou *et. al* demonstrated the anchoring of phthalocyanine (Pc) molecules on the 6*H*-SiC(0001)3×3 surface through the formation of Si-N bonds between two adjacent Si dangling bonds of SiC and two opposite aza-bridging N atoms of the Pc molecule, while the inner pyrrolic N atoms remain intact [161]. Therefore, in our case it is very likely that a few aza-bridging nitrogen atoms within a CuPc molecule are directly forming covalent bonds with the diamond dimers at the interface and constitute the N2 component in Figure 5.8, whereas the remaining unreacted nitrogen species including both the pyrrolic and aza-bridging ones form the N1 component. However, the involvement of pyrrolic nitrogen in the interfacial chemical reaction cannot be completely ruled out at the present stage.

Previous studies on the adsorption of CuPc on Si(111) 7×7 and Si(100) 2×1 have shown strong chemical interactions between molecules and silicon dangling bonds through the formation of Si-C and Si-N bonds which lead to a planar adsorption geometry of CuPc molecules [149-152, 162]. Similarly, our PES results also indicate that chemical reactions occur between diamond and CuPc molecules. The reaction breaks the highly strained π bonds of surface dimers and directly couples the dimer atoms to C and N atoms of CuPc molecules through cycloaddition-like reactions, thus functionalizing the diamond surface. Although a detailed reaction scheme and configuration of CuPc on diamond cannot be formulated at the present stage, the

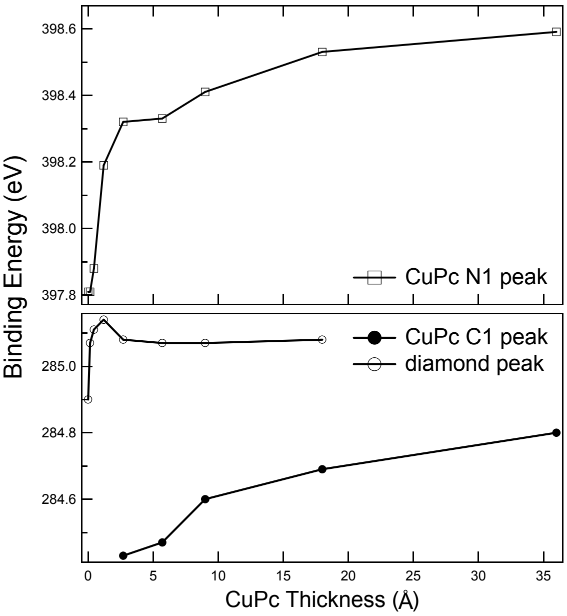

Figure 5.9. The binding energy shifts of C1, N1 and diamond peak (Figure 5.7 and Figure 5.8) as a function of CuPc thickness on bare diamond.

observation of covalent bonding between nitrogen atoms and diamond dimers clearly points to a lying-down geometry of CuPc molecules upon adsorption [152, 162], which is in agreement with the evolution of C1/C2 ratio in C 1*s* PES spectra discussed previously.

Figure 5.9 summarizes the BE shifts of the CuPc and diamond core-level components as a function of CuPc thickness. Below a thickness of 3 Å, the N1 peak shifts abruptly by 0.5 eV (Figure 5.8). The N1 peak continues to shift to higher BE at a much slower rate with increasing coverage, and stabilizes above the thickness of 18 Å. As the CuPc components can only be resolved beyond the thickness of 2.7 Å in the C 1*s* spectra (Figure 5.7), data points for C1 peak are not available at submonolayer coverage. Nevertheless, the trend of the C1 core-level shift is consistent with that of the N1 peak in at higher thicknesses, indicating a downward “band bending” like molecular level shift in the CuPc film away from the interface. Similar energy shifts of the CuPc film have been previously observed on gold [154], and they are attributed to the final state photohole screening effect [174]. But the screening ability of metal is much greater owing to its infinitely large dielectric constant as compared to ordinary semiconductors. Therefore this effect can be neglected on diamond surface. Instead, a partial charge transfer across the interface accompanying covalent bond formation should contribute to the observed energy shifts. It is clear from Figure 5.9 that the core-level BE shifts occur most significantly within the submonolayer regime (below 4 Å), in agreement with the scenario of charge transfer induced by an interfacial chemical reaction [104]. Moreover, the "band bending" direction within the CuPc film indicates that electrons are transferred from CuPc to diamond, leaving the CuPc layers at the interface positively charged (hole accumulation) which moves the Fermi level in the gap towards the HOMO. Away from the reaction interface, the molecular layers become neutral and the Fermi level moves back into the mid-gap region. Similar interfacial charge transfer and *p*-doping of CuPc films has been observed on certain organic substrates, such as on conducting polymers (CPs) [175] and on self-assembled monolayers (SAMs) [176]. The proposed charge transfer direction is further corroborated by the subtle increase in diamond C 1*s* BE after CuPc deposition (Figure 5.7 and Figure 5.9) indicating electron accumulation. In retrospect, the cycloadditions with 1,3-butadiene on bare diamond do not induce any interfacial charge transfer or charge rearrangement. However, the chemical reaction with CuPc involves the formation of heteropolar C-N bonds between CuPc and surface dimers. The π-electrons of CuPc participating in the reaction are also delocalized on a much larger scale than those of 1,3-butadiene. Consequently, charge transfer and charge rearrangement across the interface as a result of a chemical reaction are not surprising.

5.3.2 Valence band spectra and work function measurements

Valence band spectra of bare and CuPc-covered diamond are shown in Figure 5.10. Similar to its corresponding C 1*s* spectrum, the valence band spectrum of bare diamond is characterized by a significant surface state (*ss*) near the valence band edge (1.2 eV from E_F) attributed to the π-bonded surface dimers. Therefore, the rapid intensity decrease of the surface state after the initial depositions of CuPc is consistent with an interfacial chemical reaction. Further depositions lead to an overall attenuation of the diamond features and the emergence of CuPc orbitals with the HOMO state resolved (above the thickness of 5.7 Å). A closer inspection of the HOMO state also reveals a continuous shift towards higher BE with increasing CuPc deposition, consistent with the shift of CuPc core-level components.

The position of VL across the interface is very sensitive to interfacial charge transfer and the formation of interface dipoles which are expected to arise as a result

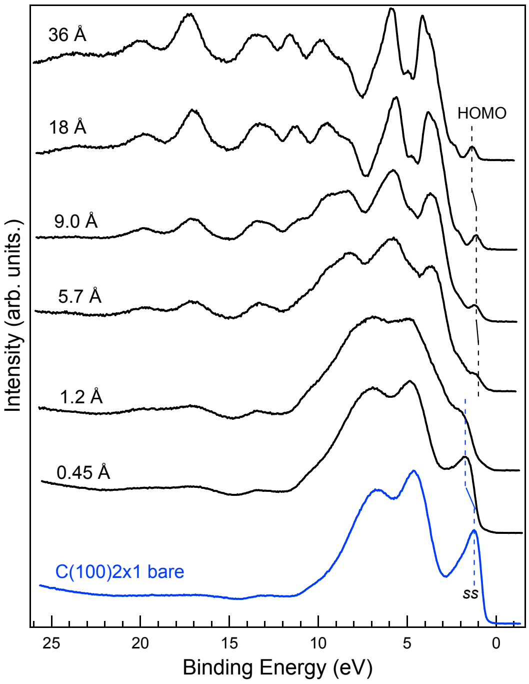

Figure 5.10. Valence band spectra (photon energy, 60 eV) of bare diamond with CuPc of increasing thickness.

of chemical reactions. Consequently, the surface WF serves as a useful indicator for these processes. Figure 5.11a shows the secondary electron emission of bare diamond with increasing CuPc thickness. The emission from bare diamond surface is characterized by a broad and low intensity distribution with emission cut-off at 5.3 eV. In contrast to the scenario of CuPc on hydrogenated diamond where the VL barely shifts at all thicknesses, the initial deposition of CuPc (0.15 Å) on bare diamond already significantly shifts the VL by 0.55 eV to lower KE, indicating a drastic reduction of diamond WF by the same amount. Meanwhile, the secondary electron emission becomes a sharp peak centered around 5.3 eV with its peak height enhanced over 3 times as compared to that of bare diamond. Subsequent depositions lead to further reduction of the WF which eventually drops to 3.6 eV at the thickness of 36 Å, a value lower than that of hydrogenated diamond (i.e. 4.0 eV). The emission peak has the narrowest FWHM of about 0.5 eV at the thickness of 0.45 Å, and becomes moderately broadened with subsequent depositions.

Following the same derivation procedure described in Chapter 3 and Chapter 4, we determined the EA values χ after CuPc depositions (Table 5.2). The dependence of EA against CuPc thickness is plotted in Figure 5.11b. It is obvious that both the WF and the EA are continuously reduced with increasing CuPc coverage, and after the deposition of 1.2 Å CuPc the bare diamond surface is transformed from PEA to NEA. The lowest attained EA is -0.7 eV, slightly larger than that of the hydrogenated diamond surface (χ = -1.1 eV). Figure 5.11b also displays the secondary electron emission peak height as a function of CuPc thickness. In the submonolayer range (below 4 Å), the emission intensity rises sharply with CuPc thickness and reaches about 30-times that of bare diamond at the thickness of 1.2 Å. Further depositions cause the emission intensity to decline quickly with the film thickness, and it becomes comparable to that of bare diamond after the formation of CuPc multilayers but with the sharp emission peak still present, indicating of a narrow energy distribution for secondary electron emission.

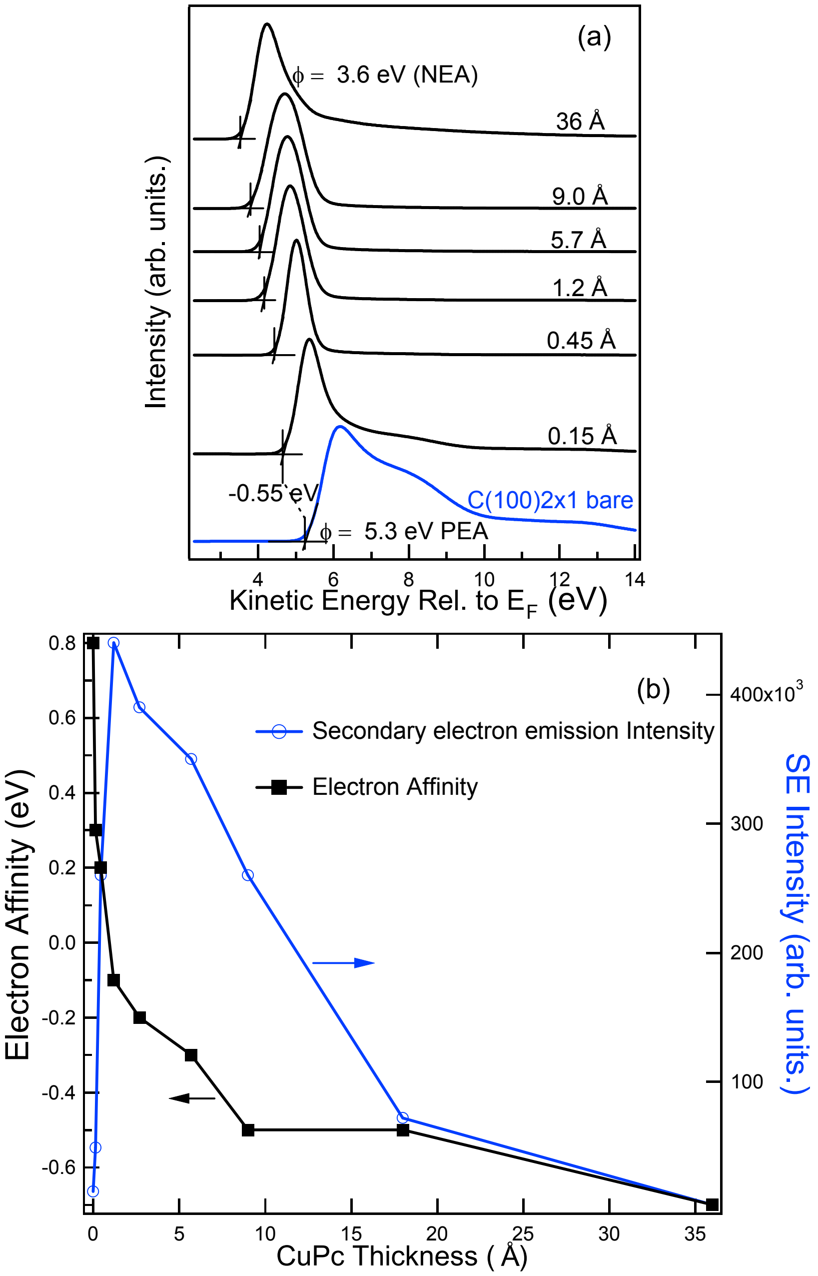

Figure 5.11. (a) Secondary electron emission of bare diamond with increasing CuPc thickness (photon energy, 60 eV). The KE scale is corrected for an applied bias voltage of -5 V. The cut-off of emission (vertical line in graph) indicates the position of VL relative to Fermi level (E_F). The secondary electron emission peaks are all normalized to have the same height for better viewing. The actual peak height varies significantly as reported in (b). (b) EA and secondary electron emission intensity of bare diamond as a function of CuPc thickness.

Table 5.2. Energy levels of bare diamond and organic functionalized diamond with increasing CuPc thicknesses. $C_B(1s)$: C 1*s* BE of bulk diamond component; $E_F - E_{VBM}$: energy distance between Fermi level and VBM; $E_{CBM} - E_F$: energy distance between CBM and Fermi level; ϕ: WF; χ: EA.

Diamond Surface with CuPc [Å]	$C_B(1s)$ [eV]	$E_F - E_{VBM}$ [eV]	$E_{CBM} - E_F$ [eV]	ϕ [eV]	χ [eV]
Bare	284.90±0.05	1.0±0.1	4.5±0.1	5.3±0.1	+0.8±0.15
0.15 Å	285.05±0.05	1.1±0.1	4.4±0.1	4.7±0.1	+0.3±0.15
0.45 Å	285.10±0.05	1.2±0.1	4.3±0.1	4.5±0.1	+0.2±0.15
1.2 Å	285.12±0.05	1.2±0.1	4.3±0.1	4.2±0.1	-0.1±0.15
2.7 Å	285.06±0.05	1.2±0.1	4.3±0.1	4.1±0.1	-0.2±0.15
5.7 Å	285.05±0.05	1.2±0.1	4.3±0.1	4.0±0.1	-0.3±0.15
9.0 Å	285.05±0.05	1.2±0.1	4.3±0.1	3.8±0.1	-0.5±0.15
18 Å	285.05±0.05	1.2±0.1	4.3±0.1	3.8±0.1	-0.5±0.15
36 Å	N.A.	1.2±0.1	4.3±0.1	3.6±0.1	-0.7±0.15

It is apparent from Figure 5.11b that both the EA and secondary electron emission intensity change most significantly within the first CuPc monolayer coverage (below 4 Å) where these molecules are in direct chemical bonding with bare diamond. Recalling the Diels-Alder reaction of diamond with 1,3-butadiene and other small organic molecules which continuously tunes the diamond EA and secondary electron emission intensity through the surface dipole layer built within the reaction product (c.f. Chapter 4), a similar phenomenon observed here can be understood in analogy. We propose that the numerous C-H bonds of the outer benzene rings of CuPc potentially contribute a dipole layer which modifies the electrostatic potential outside the surface. Although the chemical reaction between diamond and CuPc molecules constrains the initially deposited molecules to lie flat, the formation of new covalent bonds leads inevitably to the loss of conjugation of the molecular system and eventually distorts the molecular geometry [101, 162]. As a result, the terminal C-H bonds of the outer benzene rings are possibly bent out of the molecular plane and point towards the vacuum side to form such interface dipole. Additional dipoles may originate from the charge rearrangement and interfacial charge transfer via newly formed covalent bonds. With increasing coverage of adsorbed molecules, the planar average of the electrostatic potential field of the dipole layer provides a potential step that lowers the VL. In comparison with the scenario of CuPc on hydrogenated diamond where no interface dipole layer is present, the crucial role of interfacial chemical reaction in inducing the interface dipole is unambiguously demonstrated.

Although the internal energy distribution of secondary electrons inside diamond is largely unperturbed by the organic functionalization, the ability to detect these electrons is highly dependent on the position of VL at the surface. As a result, the majority of the photoexcited electrons which thermalize to the CBM of diamond now have a lower barrier for vacuum emission, leading to a giant enhancement and narrower distribution of secondary electron emission with CuPc deposition. After the bare diamond surface is completely passivated, the subsequently deposited molecules no longer react with diamond and retain their flat geometry. Consequently, the dipole moments of the terminal C-H bonds average out in every direction owing to the internal symmetry of molecules, resulting in no net perpendicular component of the dipole moment. Therefore, the WF and EA changes very slowly in the later deposition stage, and this relatively small change is attributed to the “band bending”-like energy shift within the CuPc multilayer.

As hot electrons from diamond CBM travel through the molecular layers, they are largely attenuated by the unreacted CuPc overlayers through inelastic scattering,

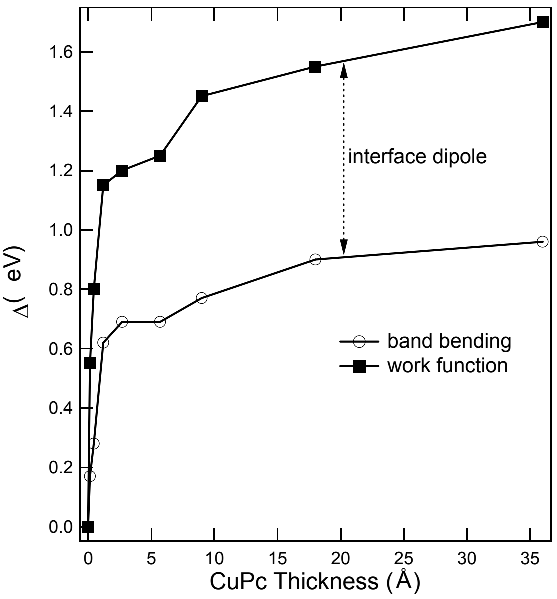

Figure 5.12. WF and band bending magnitudes as a function of CuPc thickness on bare diamond surface. The band bending is calculated as the sum of diamond C 1*s* peak BE shift and CuPc N1 peak BE shift.

leading to a rapid decay of the secondary electron emission intensity. However, the sharp emission peak feature is still retained for CuPc thickness below 9 Å, which indicates secondary electrons originating from diamond CBM still dominate. The slight shifting of the emission peak to lower kinetic energy direction is consistent with the downward band bending of diamond after organic deposition. At large CuPc thickness (e.g. 36 Å) the secondary electrons originally emitted from diamond CBM are largely inelastically scattered down to molecular unoccupied states and its energy distribution does not reflects the internal energy distribution of electrons in diamond any more [177-178]. As a result, shape of the secondary electron emission of 36 Å CuPc is very different from that from thinner films.

In order to quantitatively evaluate the interface dipole induced by the adsorbed molecules, the “band bending” contribution to the measured WF variation should be isolated [133]. It is noted that both band bendings in diamond and in the organic film, manifested by the BE shifts of the corresponding core-level components in the PES spectra, contribute to the decrease in WF upon CuPc deposition. In Figure 5.12, the decrease in WF is plotted together with the sum of band bending in diamond and CuPc film (i.e. the BE shift of diamond C 1s peak and CuPc N1 peak) as a function of CuPc nominal thickness. The change of WF can be clearly divided into two transition regimes. In the submonolayer regime (< 4 Å), the abrupt decrease ($\Delta \sim 1.2$ eV) in WF is predominantly induced by the intramolecular dipole moment due to reacted CuPc molecules. In multilayer regime (> 4 Å), the WF decreases slowly ($\Delta \sim 0.5$ eV) with CuPc thickness, concurrent with the band bending. For all film thicknesses, the change in WF is substantially larger than the band bending, with the difference gradually enlarging with increasing thickness and stabilizing at about 0.7 eV above 4 Å thickness. This value is indicative of the magnitude of the intramolecular interface dipole induced solely by the reacted CuPc molecules. This evolution is consistent with the scenario whereby the interface dipole is fully developed within the first monolayer of CuPc and subsequent variations in WF as well as EA are mainly attributed to “band bending” inside the CuPc film. The 0.7 eV interface dipole induced by reacted CuPc is comparable to that caused by the Diels-Alder reaction with 1,3-butadiene, and considerable less than that formed on hydrogenated diamond (i.e. 1.9 eV, see Chapter 3.3.2.2), implying a much lower density of effective C-H dipoles.

5.3.3 Energy level alignment

Figure 5.13 depicts the schematic energy level diagram across the heterojunction of CuPc on bare diamond. Pristine bare diamond has a PEA of + 0.8 eV (c.f. Chapter 3). The first monolayer CuPc molecules undergo chemical reactions with the underlying diamond dimers by forming new covalent bonds. The reacted molecules also build an intramolecular dipole layer which significantly lowers the surface VL even below the CBM of diamond, transforming bare diamond into a NEA surface.

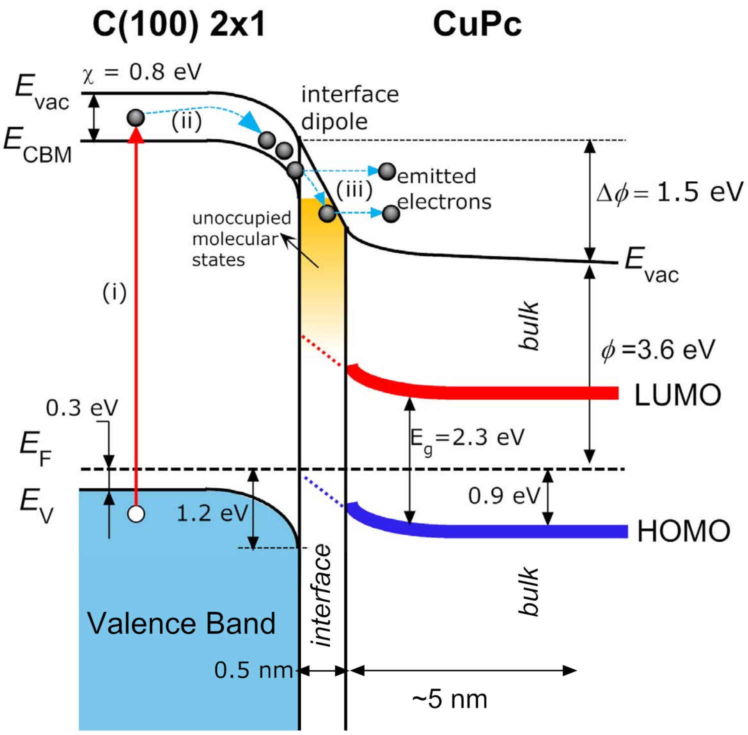

Figure 5.13. Schematic energy level diagram of CuPc on bare diamond surface. The LUMO position of CuPc is estimated by adding a CuPc transport band gap of 2.3 eV to HOMO position. All values are estimated to lie within an error of 0.1 eV.

The secondary electron creation and emission process in diamond can be described by three consecutive steps [179]: (i) Hot electrons are mainly excited into diamond conduction bands that lie outside the band bending region due to the large penetration depth of light (several μm); (ii) Electrons lose their energy through inelastic scattering processes, and some are accelerated towards the interface in the band bending potential and eventually accumulate in large numbers in the CBM at the interface; (iii) Finally, these hot electrons travel across the diamond/CuPc interface. When the CuPc film thickness is relatively low (i.e. submonolayer), most electrons tunnel directly into vacuum almost ballistically due to the lowered emission barrier and the strong electric field created by the surface dipole layer. Consequently, they constitute the sharp and intense secondary electron emission peak observed in Figure 5.11. A small portion of electrons that travel across the interface may be inelastically scattered into the unoccupied molecular states of CuPc with energies just below the diamond CBM but still above the VL. They are also emitted into vacuum and make up the rising edge of the secondary electron emission peak. However, as the CuPc film thickness increases, more and more hot electrons are inelastically scattered/relaxed into unoccupied molecular states below the VL and eventually the secondary electron emission decreases in intensity, representing the intrinsic emission from organic films.

A similar phenomenon of a sharp monochromatic emission peak in the low KE part of UPS spectra after organic functionalization of a solid surface has been observed recently in the system of self-assembled diamondoid monolayer (SAM) on metal substrates [180]. This is attributed to the facilitated electron conduction from an electron “reservoir” (i.e. metal) to the emission surface through the covalently attached molecular layer, combined with the NEA property of diamondoid molecules. By analogy to the metal-thiolate bonds formed between the SAM and metal substrate, the covalent bonds between diamond and CuPc also play a crucial role in the electron emission process by forming bridges facilitating electron conduction from diamond to molecules. Together with the lowered EA on the surface, the emission intensity is thus greatly enhanced.

After completion of the first monolayer, the subsequently deposited CuPc molecules are shielded from chemical reaction and retain their integrity. A downward energy shift in all molecular energy levels of CuPc which extends over 5 nm from the interface is also observed. The IP of the thick CuPc film (I = 4.5 eV), obtained by adding up the work function to HOMO-E_F, is smaller than that on hydrogenated diamond (I = 5.2 eV). This reduction in IP is probably related to the different molecular orientation of CuPc in thick molecular layers (i.e. standing-up on bare, lying down on hydrogenated surface). Indeed, the orientation-dependent IP has been observed in ordered molecular assemblies of archetypical π-conjugated molecular systems [181-183]. The intrinsic surface dipole, built by the negatively charged π-electron clouds and positively charged molecular plane below, give rise to the increased IP for the flatlying molecular layers, whereas no such dipole occurs at the surface of standing layers [183]. The difference between these two orientation phases can be as large as 0.8 eV. A similar effect is expected for the CuPc films in the present study.

5.4 NEXAFS and molecular orientation

In order to elucidate the effect of molecule-substrate interaction at the CuPc/diamond interface on CuPc supramolecular organization, angular-dependent NEXAFS were used to characterize the molecular orientation of CuPc on hydrogenated and bare diamond surfaces respectively. The C 1*s* core-level fitting results discussed above already suggest an orientation transition from lying-down to standing-up for CuPc on bare diamond. Moreover, the different IPs for bulk CuPc on hydrogenated and bare diamond surfaces also point to distinct molecular orientations. More accurate information on the molecular orientation within molecular assemblies can be acquired by angular-dependent NEXAFS [41].

In molecular systems, NEXAFS monitors the resonant excitations from the core-level of a specific atomic species of a molecule (e.g. C 1*s* or N 1*s*) to its unoccupied molecular orbitals (i.e. π^* or σ^*); the intensity of the resonances has a strong polarization dependence with the incident synchrotron light (i.e. the resonance is strongest when the electric field vector ***E*** of the incident linear polarized light is parallel to the π^* or σ^* molecular orbital, and weakest when ***E*** is perpendicular to the π^* or σ^* orbital). For a flat, conjugated molecular system such as CuPc, the π^* and σ^* orbitals are directed essentially out-of-plane and in-plane respectively [41]. Therefore, polariza-

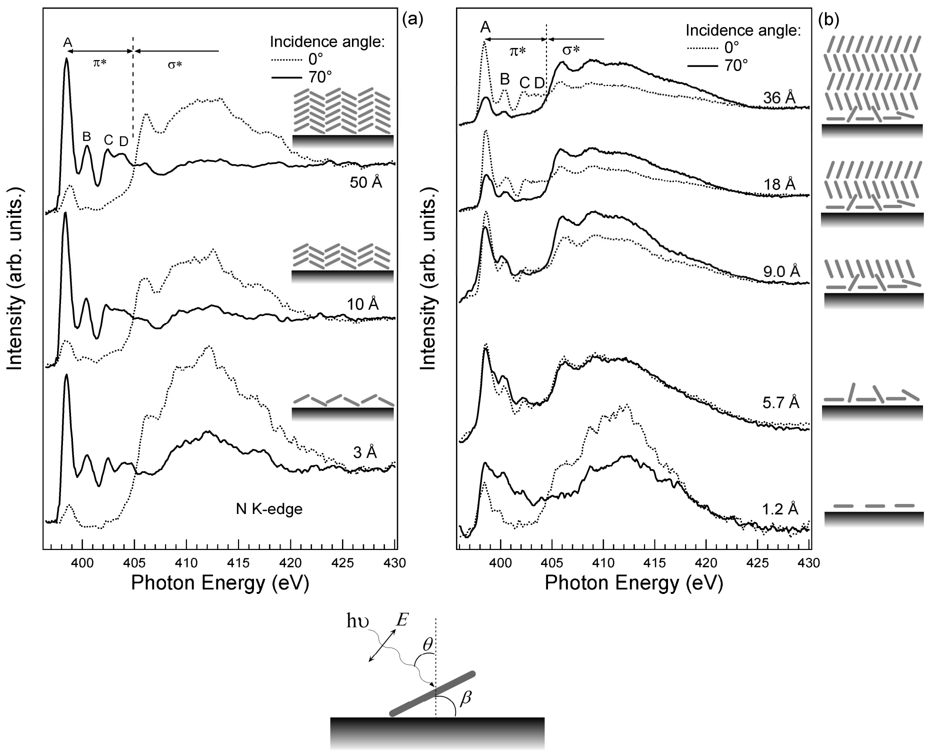

Figure 5.14. Angular-dependent N *K*-edge NEXAFS spectra for CuPc film with increasing thickness on (a) hydrogenated diamond and (b) bare diamond. The incidence angle θ is defined as the angle between the direction of the incident light and the normal direction of the substrate. All spectra are normalized to have the same adsorption edge step height. The insets show the schematic film structures during growth.

tion-dependent or angular-dependent NEXAFS is able to determine the molecular orientation.

Figure 5.14a shows the angular-dependent NEXAFS spectra of the N *K*-edge at various coverages of CuPc on hydrogenated diamond. The first four sharp absorption peaks labeled A through D are assigned to the transitions from N 1*s* core level to individual π^* orbitals, while the broad absorption features at higher photon energies correspond to transitions to σ^* states [152, 159, 163]. At all CuPc thicknesses, the π^* resonances are always much higher at grazing incidence angle (θ = 70º) than those at normal incidence (θ = 0º), whereas the σ^* resonances show the opposite behavior. The angular-dependence of these features clearly indicates that CuPc molecules are highly ordered and nearly parallel to the hydrogenated diamond surface at all thicknesses. Using the intensity ratio of the most prominent π^* resonance A at different incidence angles $R(\pi_A^*) = I_A(0°)/I_A(70°)$ and adopting 100% linearly polarized light, the average tilting angle (β) of molecular plane relative to the substrate can be calculated according to the equation [41]:

$$I(\theta) \propto 1 + \frac{1}{2}(3\sin^2\theta - 1)(3\cos^2\beta - 1) \ . \tag{5.1}$$

The resulting tilting angle β of the molecular plane is plotted against film thickness as shown in Figure 5.15 For comparison, the calculated values for the α and β polymorphs of CuPc single crystal are also shown in Figure 5.15, assuming that the deposited crystallites lie with their cleavage plane on the surface as sketched in the inset (also see Figure 5.2). As evident from Figure 5.15, CuPc molecules lie nearly flat at all thicknesses on the hydrogenated diamond surface with an average tilting angle around 27° ± 5°, close to the theoretical value (26°) for the α-form crystalline structure of CuPc with it's *a-c* plane parallel to the substrate. This indicates that the deposited CuPc molecules possibly self-organize into α-phase crystalline domains or crystallites on top of the hydrogenated diamond surface.

The NEXAFS spectra from CuPc on bare diamond in Figure 5.14b are similar in shape but display an entirely different angular dependence as compared to those of CuPc on hydrogenated diamond. At sub-monolayer coverage (1.2 Å), the π^* resonances are strongest at grazing incidence (θ = 70°), whereas they become the strongest at normal incidence (θ = 0°) at multilayer coverage. Moreover, at 5.7 Å thickness which is around 1 monolayer coverage, the angular-dependence of both π^* resonances and σ^* resonances almost vanishes. Considering that NEXAFS probes a large sample area, the absence of angular-dependence actually indicates a disordered molecular organization [152]. This change of angular-dependence against film thickness clearly suggests a reorientation of CuPc molecules from lying-down at sub-monolayer coverage to standing-up in multilayers, consistent with conclusions from PES results. The transition must start within the first monolayer resulting in the observed disordered molecular orientation. After the bare diamond surface is completely passivated by a monolayer of the molecules, the molecules subsequently grow standing up with improved order. The calculated average molecular tilting angle β as a function of film thickness shown in Figure 5.15 clearly reveals a gradual increase of the tilting angle with increasing film thickness and its upper limit reaches around 75º ± 5º, which is slightly larger than that of α-CuPc with *a-b* cleavage plane parallel to the substrate. Therefore, multilayer CuPc on bare diamond are also likely to be in the α-phase.

The organization and orientation of organic molecules, particularly conjugated

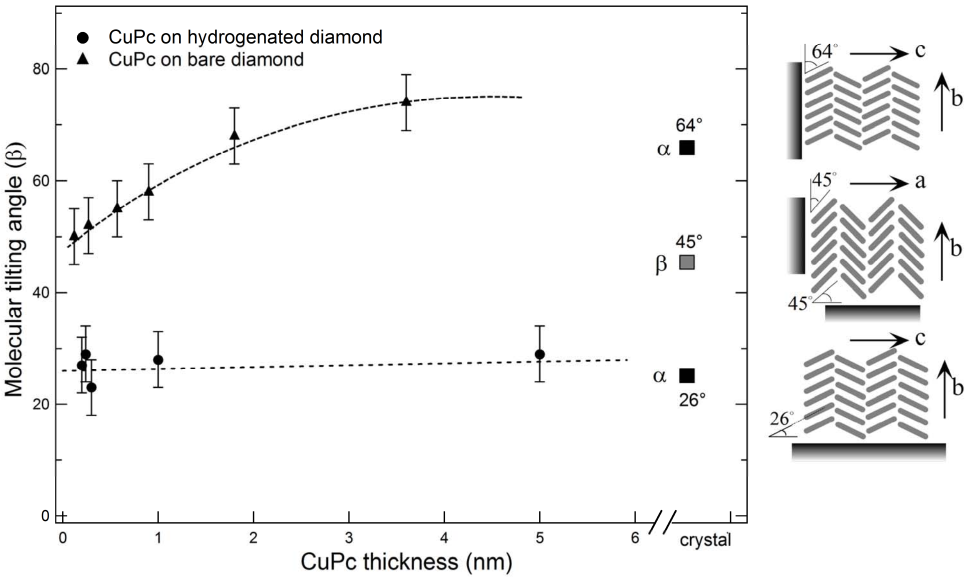

Figure 5.15. Molecular tilting angle as derived from the Eqn. (5.1) using the intensity variation of resonance **A** in the angular-dependent NEXAFS spectra for various CuPc film thicknesses on diamond substrates. The dotted lines through the data points serve as guides for the eye only. The squares denote the theoretical values as found for the known α-form and β-form single crystal structures of CuPc, assuming the crystals lie on different cleavage planes as depicted in the inset illustrations.

organic semiconductors, on solid substrates has been the subject of extensive research due to its importance to device performance [135, 184]. In general, it is governed by a complex balance between the intermolecular interactions and the molecule-substrate interactions. There have been numerous investigations on the molecular orientation of various phthalocyanine (Pc) systems on different substrates [152, 159, 167-173]. Summarizing briefly, Pc molecules tend to adopt a standing-up geometry on most inert surfaces such as oxidized inorganic substrates (ITO and SiO_x) as well as poly-crystalline metal substrates, where the stronger van-der-Waals type intermolecular interactions (e.g. π—π interactions due to intermolecular overlapping of π-orbitals, electrostatic quadrupoles interactions, London dispersion forces due to transient multipole interactions) [112] dominate over the weaker molecule-substrate interactions [166]. In contrast, a lying-down adsorption geometry is favored on most single crystal metals [154, 167-168], alkali-halides [169, 173] and reactive semiconductor surfaces [149-152, 161-162], where the molecule-substrate interactions are stronger than the intermolecular interactions. As shown in this work, no covalent bonds are formed between CuPc molecules and the hydrogenated diamond substrate. In spite of this absence of strong covalent interactions, the CuPc molecule contains N atoms and an extended π-conjugated electron system that allow it to form N···H−C [185] and π···H−C [186] hydrogen bonding with the terminal H atoms of the hydrogenated diamond. This directional hydrogen bonding energetically favors a planar or near planar adsorption geometry, because the N atoms and especially the π-electrons of molecules can interact with more H atoms on the diamond surface due to the cooperative effect of the π···H−C hydrogen bonding. As a result, the molecule-substrate (hydrogen bonding) interactions are at least comparable to the intermolecular interactions. This competition between the intermolecular and molecule-substrate interactions results in a configuration that maximizes the intermolecular interactions by π—π stacking in bulk-like herringbone structures, where at the same time the molecules tend to lie down on the substrate. The *α*-form CuPc crystal with its *a-c* plane parallel to the substrate could satisfy these two requirements simultaneously and therefore represents the most likely CuPc film structure on hydrogenated diamond (see Figure 5.14a inset). A similar molecular arrangement was previously observed for CuPc grown on other substrates as well [172].

In contrast, the strong chemical bonding at the bare diamond/CuPc interface causes the first layer molecules to adopt a lying-down geometry (Figure 5.14b). While approaching completion of the first monolayer, the subsequently deposited molecules experience increasing difficulty adopting planar orientations due to steric hindrance of neighboring adsorbed molecules and incline away from the substrate [152]. These different molecular orientations result in the observed disordered molecular organization within the first deposited monolayer. After the bare diamond surface is completely wetted by the first monolayer, the substrate is well screened and behaves like a weakly interacting van-der-Waals substrate such as oxidized substrates. Moreover, the disordered interfacial CuPc monolayer also induces a degree of roughness on the length scale of the molecules, further weakening the molecule-substrate interactions by reducing the effective adsorption site and preventing the lock-in of the initial lying adsorption geometry [170]. As a result, at higher thicknesses the molecule-substrate interaction becomes almost negligible, and the intermolecular interactions and surface energy become the dominant parameters influencing the film structure.

In thicker films, the CuPc molecules preferentially grow with face-to-face stacking in a standing up arrangement with respect to the substrate surface, forming a bulk-like herringbone structure between adjacent layers (see Figure 5.14b inset) [171]. This maximizes the intermolecular π—π interactions and minimizes surface energy [152, 170]. Hence, the molecular orientational order in thick films is significantly improved. This self-ordering behavior is mainly driven by the dominant intermolecular π-π interactions between molecular aromatic rings.

5.5 Chapter summary

In this chapter, we have studied and compared a model organic semiconductor (CuPc) on hydrogenated and bare diamond surfaces by synchrotron-based PES and angular-dependent NEXAFS. Significant dissimilarities have been found between these two substrates in terms of interactions, energy level alignment, and molecular organization. On hydrogenated diamond, CuPc molecules are found to weakly interact with diamond substrate via van-der-Waals-type interactions. Neither chemical reactions nor charge transfer are observed at the interface as indicated by PES. Molecules adopt a lying-down geometry throughout growth with a high degree of order as a result of the competing molecule-substrate interactions and intermolecular interactions. On bare diamond, CuPc molecules undergo chemical reactions with the underlying diamond dimers by forming new covalent bonds at the interface. The reacted molecules create an intramolecular dipole layer through distortion of the molecular plane which significantly lowers the surface VL even below the CBM of diamond, transforming bare diamond to a NEA surface with greatly enhanced secondary electron emission yield. The molecular orientation experiences a transition from lying-down at submonolayer coverage to standing-up in multilayer films, accompanied by an order-disorder-order transition during growth. These transitions are related to the switch from the dominant molecule-substrate covalent interactions in the first monolayer to weak intermolecular interactions in multilayers. These findings highlight the importance in understanding the complex interactions at the organic/inorganic semiconductor interface, and have important implications for the development of diamond-based organic electronic devices.

In particular, organic functionalization of diamond by an organic semiconductor results in a unique combination of NEA, high electron emission and electronic functionality of organic semiconductor. This would facilitate the integration of molecular electronics with diamond technology, a promise unparalleled by conventional surface functionalization with small and simple organic molecules. In particular, the strong C—C bonded interface by organic functionalization is more resistant than C—H interface of hydrogenated diamond to degradation through hydrolysis or moisture attack [187], making this an attractive route to fabricating more stable diamond-based NEA cathodes. Our approach also provides an understanding of the utilization of organic semiconductor molecules to tailor the surface electronic properties of conventional inorganic semiconductors via surface engineering, enabling the controlled tuning of device characteristics and functionalities.

CHAPTER 6

SURFACE TRANSER DOPING OF DIAMOND BY ORGANIC MOLECULES

6.1 Introduction

Doping of semiconductors, which is done to locally manipulate their charge carrier density and conductivity, lies at the heart of modern semiconductor technologies. Doping is conventionally achieved by incorporating impurity atomic-dopants with appropriate properties into the host lattice of the semiconductor. Depending on their number of valence electrons, the dopants (donors) can either donate excess electrons as negative free charge carriers to the semiconductor conduction band at moderate temperature (*n*-type doping), or they (acceptors) can take away additional electrons from surrounding host atoms to complete their covalent chemical bonding, leaving positively charged holes as charge carriers in the semiconductor valence band (*p*-type doping). This is shown schematically in Figure 6.1 for a group-IV elemental semiconductor. With the realization of both *n* and *p* type doping of semiconductors, the most basic structure of semiconductor devices, the *p*-*n* junction, could be built.

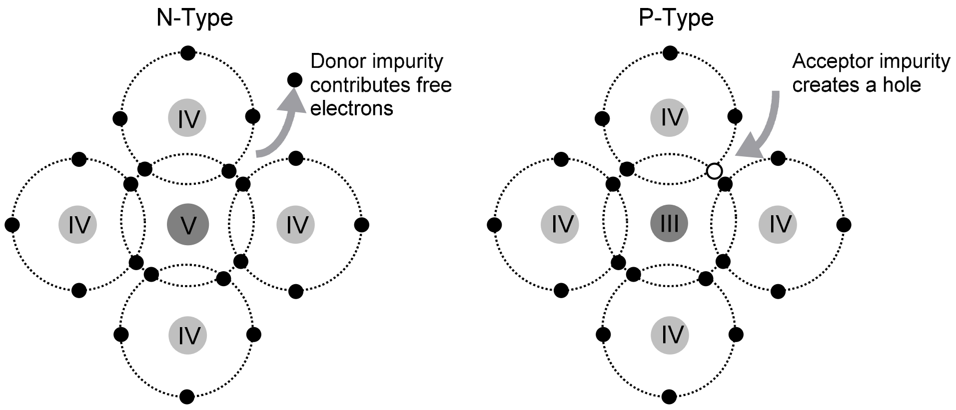

Figure 6.1. Schematic bond diagram for *n*-type doping of group-IV elemental semiconductor (Si, C, Ge, Sn) with group-V elements (N, P, As etc.) as dopants, and that for *p*-type doping with group-III elements (B, Al, Ga etc.)

6.1.1 Challenges of doping diamond

The large band gap of diamond inevitably leads to an extremely low charge carrier density of intrinsic diamond at RT ($n_\mathrm{i} = p_\mathrm{i} \sim 10^{-27}$ cm^{-3}). In other words, a diamond sample larger than earth is necessary to accommodate a single mobile charge at such low carrier density. Consequently, despite its exceptionally high electron and hole mobilities (Table 1.2), undoped diamond is considered a perfect electrical insulator. Doping diamond to achieve desirable conductivity is therefore essential for the successful application of diamond as an electronic material, utilizing its numerous extraordinary electronic properties (see Chapter 1.2.2).

The most common *p*-type dopant for diamond is boron (B), which is naturally present in type-IIb diamond. RT Hall measurements of type-IIb natural diamond with boron concentration of about 10^{16} cm^{-3} show moderate *p*-type electrical conduction with the hole concentration in the order of 10^{13} cm^{-3} and resistivity around 10^3 Ω·cm [188]. However, like other wide bandgap semiconductors, dopants in diamond suffer from high ionization energies, resulting in very low dopant activation at RT. As listed in Table 6.1, B has the lowest ionization energy among all the common dopants in diamond. However, an activation energy as large as 0.37 eV for B is still considerably high as compared to the thermal energy at RT ($kT = 0.026$ eV), therefore B acceptors are only weakly activated inside diamond at RT. Similarly, efficient *n*-type doping of diamond is much harder to achieve with common donor impurities. The exceedingly deep donor level 1.7 eV below diamond conduction band makes nitrogen (N) impractical as an *n*-type dopant, even though they are readily incorporated into natural diamond as one of the dominant impurities. The next candidate is phosphorous (P), which has a relatively lower activation energy of 0.6 eV. But the close packing and rigidity of diamond lattice result in very low solubility for P and other dopant atoms

Table 6.1. Common dopants and corresponding activation energy in diamond.

	Element	**Activation Energy** (eV)
p-type	Boron (B)	0.37[a]
n-type	Nitrogen (N)	1.7[b]
	Phosphorous (P)	0.6[c]

[a] A. T. Collins and W. S. Williams, J. Phys. C.: Solid State Phys. 4, 1789 (1970).

[b] R. G. Farrer, Solid Stete Comm. 7, 685 (1969).

[c] M. Katagiri, J. Isoya, S. Koizumi, and H. Kanda, Phys. Status Solidi A **201**, 2451 (2004).

with radius larger than C [189], thereby ruling them out as effective donors. In recent years, much effort has been paid in searching for alternative shallow donors, including sulfur [190], sulfur-hydrogen centers [191], N_2-H complex defects [192] and more recent co-doping scheme using a boron-hydrogen complex [193-194]. However, due to the lack of reproducibility of the claimed *n*-type conductivities as well as solid theoretical support, their roles as effective *n*-type dopants remain elusive [195-196].

The second challenge is the lack of reliable processing methods to dope diamond ultrathin films and nanostructures with controllable conductivity. Conventional doping process using ion implantation followed by thermal diffusion becomes futile in diamond owing to its extreme rigid and compact nature. In particular, ion implantation with high energy ion beams can lead to the graphitization of diamond surfaces [6]. Alternatively, impurity-containing molecules such as diborane (B_2H_6) and phosphine (PH_3) added to the gas mixture during CVD growth of diamond can successfully incorporate dopants into diamond lattice [197-198]. However, a well-defined and uniformly doped nanoscale layer for the realization of ultrashallow junction is hard to be achieved by this means. Finally, the extreme hardness and chemical inertness of diamond makes it difficult to pattern diamond films with micro- or nanoscale features [199].

In summary, bulk doping of diamond using conventional methods presents several technical challenges, which severely hampers the widespread commercialization of diamond as an electronic material despite its numerous outstanding electronic, thermal, and optical properties. In particular, the inability to effectively *n*-type dope diamond hinders the development of ambipolar diamond-based electronic devices such as the complementary circuits (i.e. CMOS) where both *n*-type and *p*-type transistor channels are required [14-15]. Consequently, most diamond devices realized so far are unipolar (*p*-type) and constructed in metal semiconductor field effect transistor (MESFET) device structure [14]. Therefore a novel doping scheme, that can tackle these challenges with controllable and reliable carrier densities in diamond, is needed to bring diamond-based electronic devices into fruition.

6.1.2 Diamond surface conductivity and its origins

Although intrinsic diamond is highly insulating, an intriguing surface conductivity (SC) of hydrogenated diamond was firstly discovered by Ravi and Landstrass on both natural diamond surface [200] and on CVD diamond thin films [201] exposed to hydrogen plasma. Through years of endeavour to study this peculiar SC of diamond [202-206], it is generally understood as *p*-type in nature with a value in the order of 10^{-4} to 10^{-5} Ω^{-1} at RT. The measured areal hole density responsible for the *p*-type SC lies in the range of 10^{12} — 10^{13} cm^{-2} with a Hall mobility between 10 and 100 cm^{2} V^{-1}s^{-1}. It is hardly temperature dependent between 150 K to RT. Based on this unique *p*-type SC several types of functional electronic unipolar devices have been successfully fabricated and demonstrated, including surface-channel MESFETs [24, 207-210], surface-channel metal-oxide semiconductor field-effect transistors (MOSFETs) [211-212], and a novel type of ion-sensitive field-effect transistor (ISFET) working in electrolyte with potential applications such as pH sensors [25, 213].

Since the SC is only observed on hydrogenated diamond and disappears when the surface undergo dehydrogenation or oxidation [214], it is intuitive to assume that hydrogen plays a indispensible role in the formation of a surface hole accumulation layer causing the SC. Based on this idea, several mechanisms focusing on hydrogen have been proposed to explain the origin of diamond SC. Ravi and Landstrass initially suggested that passivation of deep levels (e.g. trap states, gap states) by hydrogen incorporated in the subsurface region caused the observed SC [200-201]. Maki et al. later proposed that the SC was attributed to the formation of shallow acceptor states by hydrogen incorporated into the diamond subsurface at a depth of around 0.6 μm [203]. This model was further developed by Hayashi et al. who suggested that the subsurface hydrogen related point defects act as shallow acceptor states [202, 215] within a region 20 nm below the surface. However, the depth distribution of such hydrogen related shallow acceptors was disputed owing to the limited resolution of secondary ion mass spectroscopy (SIMS) for hydrogen profiling [216-217]. Moreover, no theoretical calculations could support the formation of such shallow acceptor states by subsurface hydrogen [196].

Work has also been done on possible acceptor-type energy states residing on the diamond surface. Shirafuji et al. and Kawarda et al. both proposed models in which hydrogenated diamond had an upward band bending to form a hole accumulation layer as a result of acceptor-type surface states related the surface C-H bonds with energy level around diamond VBM [218-219]. Although this upward surface band bending was later confirmed experimentally [220-221], the acceptor-type (unoccupied) surface states originating from surface C-H bonding were found residing far above the valence band in the diamond band gap [57, 78], and therefore cannot withdraw electrons from diamond valence band. Basing on the observation that the diamond SC is very sensitive to the ambient conditions, Gi et al. proposed a model in which solvated hydronium ions (H_3O^+) in a water layer naturally adsorbed on diamond acted as surface acceptors to induce electron transfer from diamond to these ions, with a hole accumulation layer in diamond surface formed as a result [204-205]. This primitive surface transfer doping model was further elaborated in 2000 by Maier et al. [23], who explicitly specified the indispensable roles of both hydrogen termination and air exposure in causing the SC.

Under the framework of the electrochemical surface transfer doping model [222], the reduction/oxidation (red/ox) couples involved in an electrochemical reaction in the adsorbed water layer provides the surface acceptor level necessary for initiating electron transfer across the diamond/air interface. The charge transfer proceeds until thermodynamic equilibrium is reached between the electrochemical potential of the electrons in the red/ox reaction and the Fermi level of the diamond. The responsible red/ox couple was initially suggested to be H_3O^+/H_2 by Maier et al. [23]. More recently, alternative O_2 red/ox couples (i.e. O_2/H_2O for acid condition, O_2/OH^- for basic condition) were proposed [223] and experimentally verified as surface acceptors that electrochemically facilitate interfacial electron transfer [224-225], owing to their lower electrochemical window than that of H_3O^+/H_2 red/ox couple[4] and the much higher concentration of O_2 dissolved in the adsorbed water layer.

---

[4] The electrochemical potential window for electrons involved in the H_3O^+/H_2 red/ox reaction ($2H_3O + 2e^- \leftrightarrow H_2 + 2H_2O$) is -3.6 eV to -4.6 eV referring to vacuum level in the pH range from 14 to 0. For comparison, the electrochemical potential window for electrons involved in the O_2 red/ox reaction ($O_2 + 2H_2O + 4e^- \leftrightarrow 4OH^-$) is -4.8 eV to -5.6 eV in the same pH range.

Although it is still under debate which red/ox couple is mainly responsible for inducing the SC, the surface transfer doping model is gaining acceptance over other competing models, due to considerable experimental evidence [226-233] as well as theoretical calculations [234-237]. It explains the *p*-type SC of diamond, and more importantly suggests a new route to dope diamond because of its obvious advantages over conventional bulk doping. For example, the ultrashallow junction of less than 10 nm as required by nanoscale devices is naturally achieved by surface transfer doping [212].

6.1.3 Surface transfer doping model and its applications

The surface transfer doping process is best illustrated by the schematic energy levels shown in Figure 6.2. When diamond adsorbs surface acceptors such as solvated electrochemical species (e.g. O_2 red/ox couple), isolated atoms or molecules, or adsorbates in condensed phase, the Fermi energy difference between diamond and surface adsorbates (or electrochemical potential for aqueous solution) will drive electrons from the diamond valence band to empty acceptor levels of surface adsorbates (i.e. red/ox couple for aqueous phase, LUMO for molecular adsorbates). As a result of the interfacial charge transfer, surface adsorbates become negatively charged, and compensating holes accumulate in the diamond valence bands. Together they build up a space-charge layer with associated upward band bending toward the diamond surface, which in turn raises the Fermi level (or electrochemical potential) of surface adsorbates to eventually align with the Fermi energy of diamond in equilibrium (Figure 6.2b). This upward band bending can be so strong that the Fermi level of diamond is forced below diamond VBM at the surface [221], resulting in a degenerate situation. The accumulated holes in the diamond valence band are highly mobile ($\mu_h \sim 70$ cm^{2}V^{-1}S^{-1}) parallel to the surface and lead to the substantial *p*-type SC of

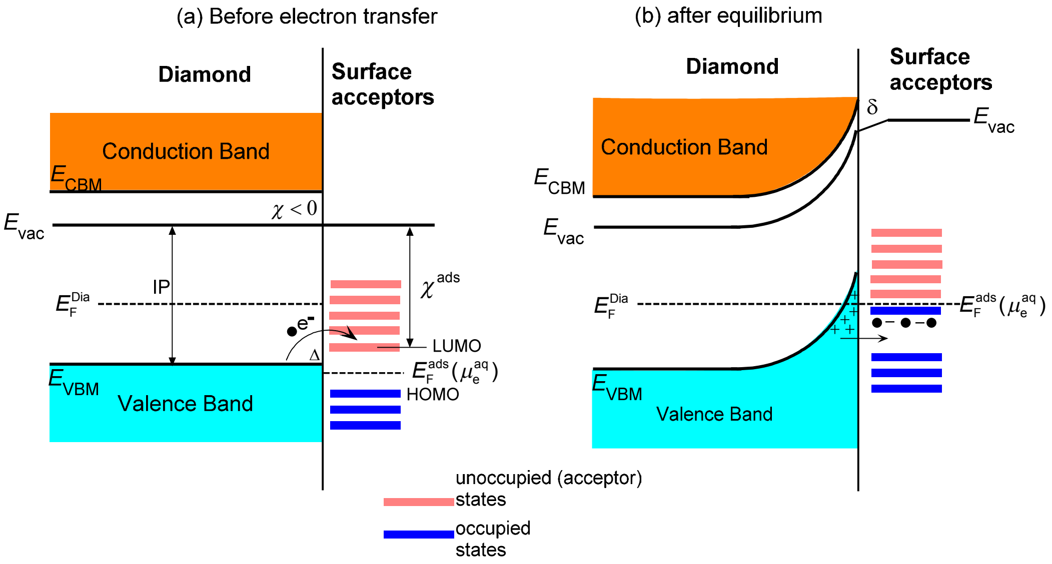

Figure 6.2. Schematic energy levels for surface transfer doping process. (a) Before electron transfer, the Fermi level (E_F^{ads}) or electrochemical potential (μ_e^{aq}) of the adsorbates is lower than that of the diamond. Electron transfer from diamond valence band to adsorbates' unoccupied acceptor states (e.g. LUMO) is energetically favored. (b) In equilibrium after electron transfer, Fermi levels on both sides are aligned and the diamond has a layer of accumulated holes at its surface, with equal amount of compensating electrons in adsorbates.

diamond, but they tend to be confined (squeezed) normal to the surface by the electric field created by the interfacial charge separation. The resulting space-charge layer width (of the order of several nm [222]) is much narrower than that of common depletion layers in semiconductors that easily extend over 100 nm [52]. Therefore, this hole accumulation layer in diamond surface is expected to behave as a quasi-2D hole gas with discrete quantum electronic states, as confirmed experimentally by Kalish et al. [238].

One prerequisite for effective *p*-type surface transfer doping of diamond is that the adsorbate layer must have its lowest unoccupied electronic level (acceptor level) below or close to the VBM of diamond, with their energy difference Δ analogous to the activation energy of conventional bulk dopants. Fulfilling this requirement is readily helped by the NEA property of hydrogenated diamond. Its NEA χ of -1.0 eV ~

-1.3 eV [61-62, 67-69] (c.f. Chapter 3.2.2.2) leads, in spite of the wide bandgap of diamond, to the lowest IP (4.2 eV ~ 4.5 eV) among all the known semiconductors. Therefore, diamond is much more amenable to surface transfer doping than other semiconductors.

For surface acceptors dissolved in the adsorbed water layer on diamond under ambient conditions, a pH level of 6 due to dissolved CO_2 places the electrochemical potential of the red/ox couple at 4.26 eV below VL for the H_3O^+/H_2 red/ox [23], or at 5.3 eV below VL for the O2 red/ox [225]. No matter which red/ox couple takes dominance in the water layer, their electrochemical potentials are either close to or lower than the VBM of diamond with reference to a common VL, thereby thermodynamically favoring the electron transfer from diamond valence band to these aqueous red/ox couples. For adsorbates in the molecular form or solid phase to act as effective surface acceptors, this requirement dictates that the EA of molecules (defined generally as the energy difference between VL and the LUMO) should be larger or close to diamond's IP (4.2~4.5 eV), which can be met by certain organic molecules with strong electron withdrawing properties. It should be noted that EA of molecular oxygen and other gas-phase oxidants (e.g. $\chi_{O_2} = 0.451$ eV [239]) in the absence of water is much smaller than their corresponding aqueous red/ox couple. Therefore, aqueous environment on a solid surface provides an essential condition for these gas-phase oxidants to act as effective electron sinks.

Surface transfer doping by atmospheric adsorbates in a complex aqueous system can readily induce substantial *p*-type SC in diamond. However, several problems are encountered in making this a practical doping scheme for diamond electronic device applications, such as the lack of the controllability of the induced hole concentration in diamond and the volatile device performance due to the poor thermal-stability of the physisorbed aqueous layer. Therefore, using organic molecules as surface transfer dopants would be a simpler and more reliable method [240-241] because of their good thermal-stability, non-volatility after adsorption on solid surfaces, compatibility with low-temperature or solution processing, ability to selectively dope and hence to pattern the diamond surface via thermal evaporation, tunability of their electronic properties by modifying the chemical structures, and the wide selection of molecules with suitable electron affinities. Therefore, organic molecular dopants with all of these advantages could overcome major challenges posed by conventional dopants and atmospheric surface dopants, and enable surface transfer doping to become a viable alternative to bulk doping for controlling the conductivity of diamond and other semiconductors [240].

A number of organic molecules have already been demonstrated by first principle calculations to be effective surface acceptors on diamond, including fullerene, fluorinated fullerene [242-244], CO_3H [245], and 2,3-dichloro-5,6-dicyano-1,4-benzoquinone (DDQ) [246]. Strobel et al. observed substantially increased SC of diamond induced by deposition of fullerenes and fluorinated fullerenes [247-249]. However, to our best knowledge, no direct measurement of charge transfer between diamond and surface adsorbates have been carried out so far, which would confirm the validity of surface transfer doping. Detailed characterization of the electronic structure at the diamond/adsorbate interface, crucial for both fundamental understanding and device application, is still lacking. The number of organic molecules investigated as surface acceptors is also limited. In this context, this chapter will carefully examine and compare a series of organic molecules with varying EA (electron-withdrawing ability) including F_4-TCNQ, TCNQ, fullerene, highly fluorinated fullerene and CuPc. By providing direct spectroscopic evidences of interfacial charge transfer, we aim to clarify the interfacial electronic structure and energy level alignments. More importantly, we hope to correlate the doping efficiency with molecular EA, thus paving the way for the selection of better organic molecular acceptors to control the SC of diamond.

6.2 Surface transfer doping of hydrogenated diamond (001) by organic molecules

6.2.1 Basic considerations

Figure 6.3 schematically displays the band edges of bare and hydrogenated diamond surface, along with several other semiconductors. Hydrogenated diamond indeed possesses the lowest IP among all semiconductors owing to its NEA. Placed on the right side are the HOMO-LUMO splittings of a series of organic molecules. These molecules have different EA in the range from 2.5 eV to 5.4 eV, which place their LUMO at different positions relative to the VBM of hydrogenated diamond. Among them, several molecules such as F_4-TCNQ (tetrafluro-tetracyanoquinodimethane) and $C_{60}F_{48}$ have very high EA (χ > 5 eV) with their LUMOs directly below diamond's VBM, so that they are expected to be effective surface acceptors on hydrogenated diamond. It should be noted that the IP and EA of organic molecules listed in Figure 6.3 is only valid for the *condensed phase* comprising at least several molecular monolayers. In the condensed state, the electronic polarization of molecules surrounding the ionized center molecule tends to screen the central charge, leading to a lowered IP (by the amount of P_+) and an increased EA (by P_-) as compared to those for isolated molecules in *gas phase* [104, 158, 247]. The electronic polarization energy (P_+ and P_-) for organic molecules can be as large as 1~2 eV [250]. Consequently, for certain organic molecules the formation of solid phase might be necessary to yield a sufficiently high EA to withdraw electrons out of diamond.

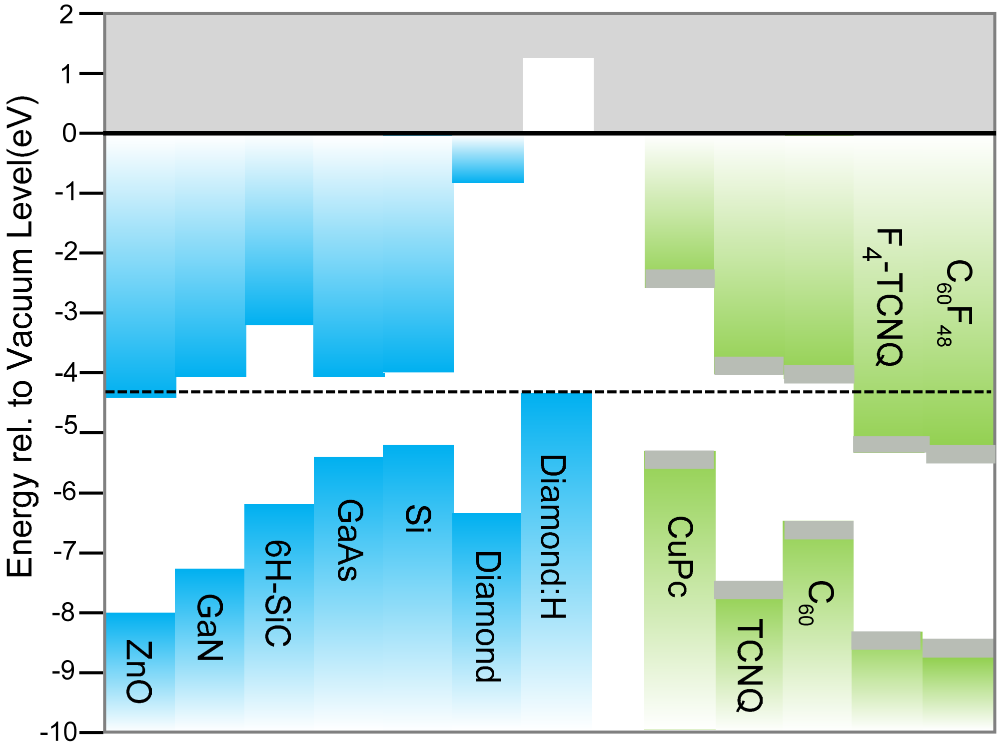

Figure 6.3. Band gaps of several semiconductors including bare diamond and hydrogenated diamond, and HOMO-LUMO splitting of organic molecules (in condensed phase). All energy levels are referenced to a common VL. The horizontal dashed line represents the energy position of the VBM of hydrogenated diamond.

The band alignment schematically shown in Figure 6.2 provides us several important spectroscopic insights on the surface transfer doping process. First of all, the upward band bending due to the hole accumulation in diamond should induce decreasing BEs in both the C 1*s* core-level and valence band features of diamond. Secondly, the electron-accepting molecules in direct contact with diamond become negatively charged anions. Excess electrons localized on certain atomic sites of the molecules might modify the local electrostatic potential of the related atomic core-level electrons, resulting in a lowered BE (i.e. chemical shift) [35]. Furthermore, depending of the orbital degeneracy [251] and the Jahn-Teller distortion [252], the excess electrons filling the LUMO of surface molecular acceptors can bring down the LUMO across the Fermi energy for partially-filled LUMO, or well below the Fermi energy for completely-filled LUMO [251]. Together with the relaxed HOMO in the new electronic configuration, they may form additional gaps states in the vicinity of Fermi level, which can be probed by UPS [253]. Finally, a common vacuum level alignment (Schottky-Mott limit) is no longer valid at this charge-transfer interfaces, and an interface dipole should be formed accompanying interfacial charge separation [104, 132-133, 254]. These phenomena can all be probed by PES experiments, and they are employed through out this chapter as important indicators to check whether surface transfer doping occurs.

However, it should be noted that the real situation may deviate from the ideal case discussed above, due to the very different properties of organic molecules. Depending on their electron-withdrawing abilities, the degree of charge transfer[5] to an individual molecule can vary from complete transfer ($Z = 1$) to only partial transfer ($Z \ll 1$) [255], resulting in very different interfacial electronic structure and energy alignment [251]. These issues will be addressed in subsequent sections.

6.2.2 2,3,5,6-tetrafluoro-7,7,8,8-tetracyanoquinodimethane (F_4-TCNQ)

Tetracyanoquinodimethane (TCNQ), with its four terminal strong electron-accepting cyano groups (–C≡N), represents one of the most widely used molecular acceptors in organic electronics. Its fluorinated derivative, tetrafluorotetracyanoquinodimethane (F_4-TCNQ) (Figure 6.4), possesses an even higher electron-accepting character with an exceptionally high EA of 5.24 eV in *condensed phase* [256-257]. Therefore, F_4-TCNQ is frequently used as a *p*-type dopant to enhance the hole conductivity in organic optoelectronic and photovoltaic devices [256, 258-260]. F_4-TCNQ on di-

---

[5] Degree of charge transfer Z is not a probability for a complete charge transfer. It should be understood as a mixing coefficient for an electron that occupies an orbital which is a linear combination of the acceptor state and donor state.

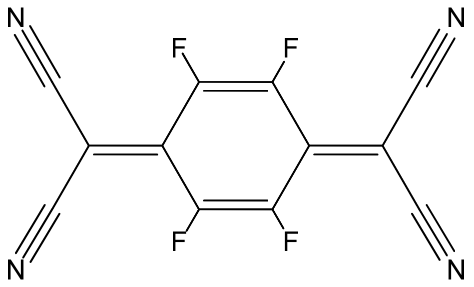

Figure 6.4. Chemical structure of F_4-TCNQ.

amond represents excellent test system to examine surface transfer doping since the diamond VBM lies directly above the LUMO of F_4-TCNQ (Figure 6.3), thereby thermodynamically favoring electron transfer from diamond to F_4-TCNQ.

PES spectra of N 1*s* evolution with increasing coverage of F_4-TCNQ is shown in Figure 6.5a. Initial deposition up to 0.5 Å leads to the formation of a pronounced peak

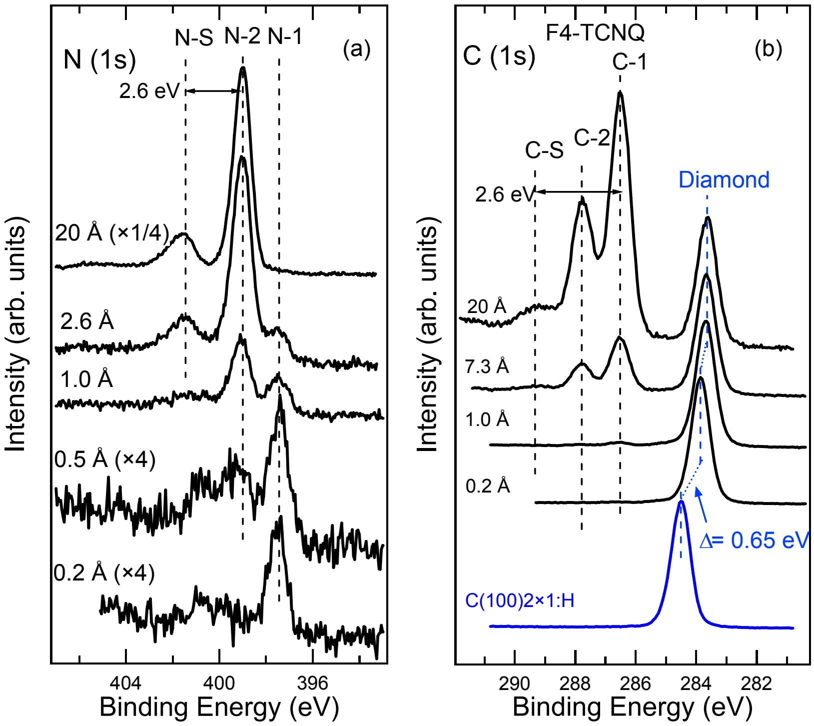

Figure 6.5. PES core-level spectra of (a) N 1*s* (photon energy of 500 eV) and (b) C 1*s* (photon energy 350 eV) of F_4-TCNQ on hydrogenated diamond with increasing thickness. C 1*s* spectra are all normalized to the same diamond peak intensity for better viewing.

at 397.50 eV (N-1) and a broad component at higher BE. At 1.0 Å nominal thickness, the higher BE component (N-2, 398.90 eV) becomes stronger than N-1. Further deposition results in a continuous increase in N-2 peak intensity and a decrease of N-1 which finally vanishes at the nominal thickness of 20 Å. The strong thickness dependences of N-1 and N-2 components clearly indicate that they are associated with interfacial and bulk molecular species respectively. In comparison with F_4-TCNQ on gold [261], the higher BE peak N-2 is assigned to neutral multilayer F_4-TCNQ^0 and the lower BE peak N-1 to anion molecules (F_4-TCNQ$^-$) in direct contact with hydrogenated diamond with their C≡N end groups withdrawing electrons from diamond [262-263]. Due to the high degree of electron localization within the molecule, the extra electronic charges reside predominantly at the cyano ends [264-265]. Consequently, the additional valence charges of N atoms in anion molecules give rise to a lower BE, and the corresponding chemical shift of 1.4 eV is close to that observed in the charge-transfer-complex involving its unfluorinated parent molecule TCNQ [266-267]. Peak N-S centered at 2.60 eV higher BE than peak N-2 is attributed to the shake-up processes of π-conjugated molecules [262]. The electrons transferred from diamond to the organic film remain localized at the interface, as shown by the rapid attenuation of photoemission signal from anion species with further F_4-TCNQ depositions. The charge localization also leads to the absence of a continuous molecular level shift for both C 1*s* and N 1*s* (or band bending in analogy to conventional semiconductor jargon). Another feature of this particular interface is the presence of neutral molecules even at the very early stage of molecular deposition where the coverage of molecules is far less than one monolayer (ML). This suggests a Volmer-Weber type growth mode of F_4-TCNQ on diamond, whereby molecular islands form from the very beginning without completely wetting the substrate surface first.

The loss of electrons (accumulation of holes) in the diamond surface region is further corroborated by the C 1*s* core-level spectra in Figure 6.5b. A substantial shift (0.65 eV) of the diamond peak to lower BE is immediately observed at the initial coverage as low as 0.2 Å. This shift continues to increase with subsequent deposition and saturates at 0.80 eV at the coverage of 1.0 Å. The low KE of detected C 1*s* photoelectrons (around 60 eV) limits the probing depth of our PES data to the surface region of diamond (around 1nm). Therefore, the shift of diamond peak indicates an upward band bending of 0.80 ± 0.05 eV towards the diamond surface, with hole accumulation to balance the negatively charged anion molecules at the surface. Further deposition leads to virtually no change of the diamond peak position, indicating a saturation of charge transfer. At large thicknesses, three new components (C-1,C-2 and C-S) related to carbon atoms in F_4-TCNQ can be clearly resolved after thick molecular layers are formed. The C-2 peak centered at higher BE of 287.75 eV is associated with fluorine bonded carbon atoms [268], whereas C-1 at lower BE of 286.50 eV is assigned to the rest C atoms within the molecule (Figure 6.4). The C-1 : C-2 intensity ratio is about 2:1, in agreement with the stoichiometry of the corresponding carbon atoms. Peak C-S, similar to N-S, is also related to shake-up processes [262]. The appearance of the anion F_4-TCNQ interfacial species together with the upward band bending inside diamond, unambiguously reveals electron transfer from diamond to the molecules, or *p*-type surface transfer doping.

More information on charge transfer and electronic structures at the interface can be deduced from valence band spectra. Figure 6.6a shows the evolution of valence bands of hydrogenated diamond with increasing F_4-TCNQ thickness. After the initial deposition of 0.2 Å, a rigid shift of 0.65 eV towards lower BE is observed, consistent with that of the diamond C 1*s* peak (Figure 1b), and thus attributed to upward band bending. Further deposition leads to an overall attenuation of diamond features and the emergence of new states from F_4-TCNQ molecular orbitals at higher BE. At the nominal thickness of 11.4 Å, various frontier orbitals of F_4-TCNQ can be clearly resolved, with its HOMO state centered at 3.20 eV ± 0.05 eV and its edge at 2.54 ± 0.05 eV, consistent with previous reports of F_4-TCNQ on Au [261]. At submonolayer coverage, additional intensities can be identified in the vicinity of Fermi level. Near the Fermi level in Figure 6.6b, two additional features centered at about 0.4 eV and 1.4 eV are observed, more clearly seen in the difference spectrum after subtracting the pristine diamond contribution (bottom spectrum in Figure 6.6b). These two gap states have been previously observed when F_4-TCNQ forms a charge-transfer-complex with various organic or inorganic substances [261, 269-270], and are assigned to the partially filled LUMO (LUMO′) of anion molecules after accepting excess electrons and to the relaxed HOMO (HOMO′) due to perturbation of the LUMO filling electrons, respectively [253, 267]. The intensity of these two peaks disappear rapidly after multilayer deposition (top spectrum in Figure 6.6b) where molecules are in their neutral state, indicating exclusive correlation of these gap states with charge transfer.

Another consequence of interfacial charge transfer is the formation of an interface dipole [104, 132-133, 254], usually indicated by an abrupt change in WF upon molecular adsorption. For molecules on inert substrates such as conducting polymers or passivated semiconductors where no interfacial chemical reactions are expected to occur, the substrate WF is sensitive to the interfacial charge transfer after molecular absorption. Hence, an upward shift of VL (increase of WF) occurs if electrons are transferred from substrate to adsorbate overlayers, or a downward shift of VL (decrease of WF) occurs when electrons are transferred in the opposite direction. The

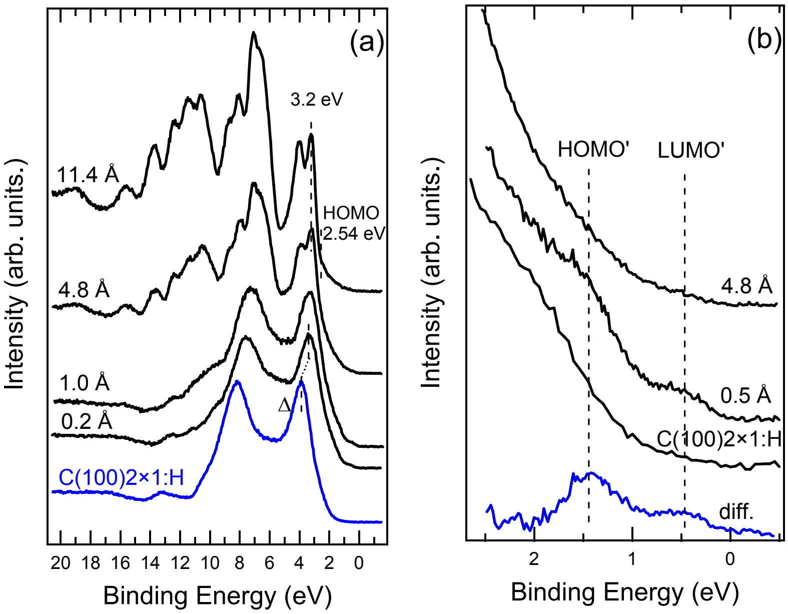

Figure 6.6. (a) UPS spectra (photon energy of 60 eV) of pristine hydrogenated diamond and after F_4-TCNQ deposition of increasing thickness; (b) a close-up near the E_F region of the UPS spectra.

interface dipole created by the resulting charge separation across the interface accounts for this abrupt VL shift.

Figure 6.7a displays the low KE part of the UPS spectra in which the emission peak cut-off indicates the VL (WF). Initial deposition of 0.2 Å causes a substantial increase of 0.70 eV in WF, and subsequent deposition increases the WF only moderately. The increase in WF upon F_4-TCNQ adsorption is consistent with the direction of interfacial charge transfer. However, the increase in WF after F_4-TCNQ deposition should also incorporate contributions from the band bending in diamond. To separate the interface dipole contribution, the increase in WF is plotted together with the shift of diamond C 1*s* peak as a function of F_4-TCNQ nominal thickness (Figure 6.7b). Throughout the deposition, the change of WF is substantially larger than the shift of diamond C 1*s* peak, and the difference between them gradually enlarges with increasing thickness and reaches a maximum of 0.6 eV, which is exclusively due to the

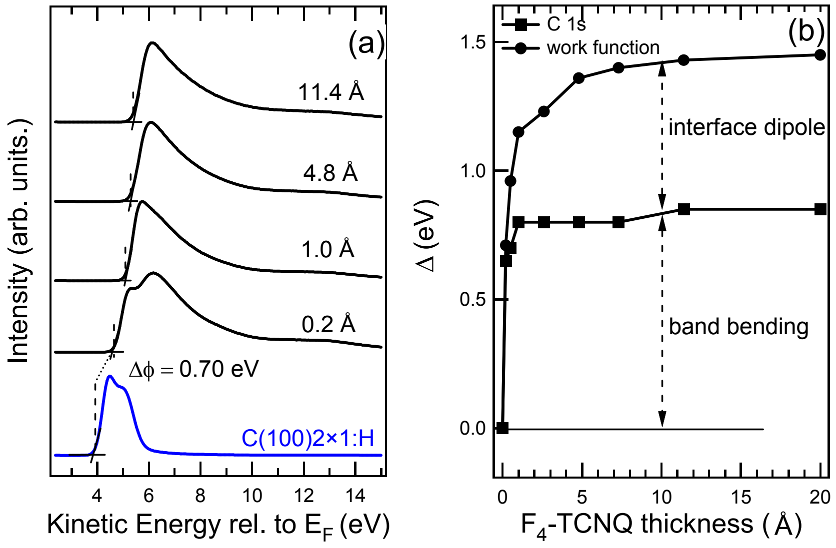

Figure 6.7. (a) Secondary electron emission cut-off of hydrogenated diamond with increasing F_4-TCNQ thickness, indicating the shifts of VL; (b) diamond C 1*s* core-level BE shift and WF change as a function of organic layer thickness.

interface dipole. As seen in Figure 6.7b, both WF and band bending change most rapidly below 4 Å thickness, equivalent to submonolayer coverage (assuming lying down molecules). This confirms that charge transfer only occurs at the diamond/F_4-TCNQ interface and the multilayer molecular film remains neutral.

Figure 6.8 schematically shows the energy level alignment before (panel a) and after surface transfer doping (panel b). The EA and IP for pristine hydrogenated diamond in vacuum is determined to be -1.1 eV (χ) and 4.4 eV (I) respectively, as described in Chapter 3. On the molecular side, the EA and IP of F_4-TCNQ molecule in condensed phase are 5.24 eV and 8.34 eV respectively, as determined separately by inverse photoemission spectroscopy (IPES) and UPS [257]. The corresponding HOMO-LUMO splitting of 3.10 eV is used to deduce the energy position of LUMO in the band alignment. After contact formation at the interface, the potential energy drop between the VBM of diamond and LUMO of molecules drives electrons to tunnel from the diamond valence band to the F_4-TCNQ LUMO until thermodynamic

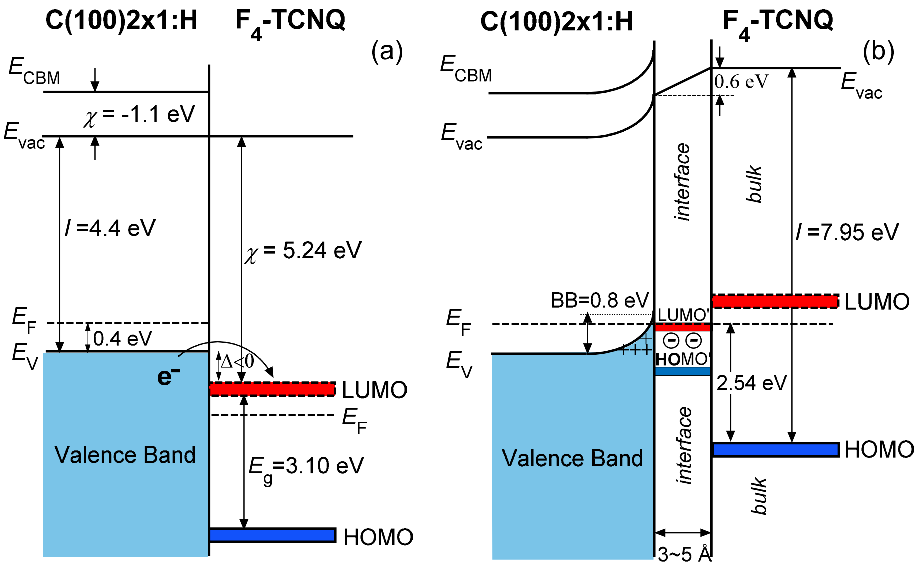

Figure 6.8. Schematic energy level diagram of (a) before surface transfer doping by F_4-TCNQ. (b) after surface transfer doping. LUMO′ and HOMO′ are the two gap states of the anion molecules at the interface. The position of LUMO is deduced by adding a band gap of 3.10 eV to the HOMO position.

equilibrium is reached. This results in an upward band bending of 0.8 eV with hole accumulation in diamond surface region and new gap states in anion molecules. The thickness of the charged interfacial molecular layer responsible for surface transfer doping is around 3~4 Å, and the strong interface dipole formed lifts the VL. On top of the anion F_4-TCNQ, the subsequent deposited molecules retain its neutrality. The IP of the F_4-TCNQ multilayer is determined to be 7.95 eV by simply adding WF to E_F-HOMO. This value is lower than the reported IP (I = 8.34 eV [257]) of F_4-TCNQ films, and this is possibly related to different film morphologies. In particular, molecular orientations are known to have a large influence on the IP of molecular assemblies [183].

It is evident from PES that significant charge transfer at the diamond/organic interface occurs at very low coverage of F_4-TCNQ, where molecules are still in molecular form with few neighbors. Although the EA of gas phase F_4-TCNQ is not known, it is estimated to be around 4.4 eV by adopting an average electronic polarization energy ($P_+ = P_- = 0.85$ eV) for planar π-conjugated organic molecules [158]. Consequently, the EA of isolated F_4-TCNQ molecules still matches the IP of hydrogenated diamond, thereby fulfilling the requirement of surface transfer doping. The highly efficient surface transfer doping ability of F_4-TCNQ is also endorsed by the appearance of anion molecule species as well as the gap state associated with partially occupied LUMO, suggesting a complete charge transfer to F_4-TCNQ ($Z = 1$). Similar degree of charge transfer has been commonly observed in charge transfer complex systems involving F_4-TCNQ [260, 270]. The Fermi level at diamond surface is pushed 0.4 eV below the VBM of diamond after surface transfer doping, leading to a degenerate semiconductor surface. A detailed calculation of the doping yield and efficiency which requires the knowledge of the areal acceptor molecule density as well as the areal hole density accumulated in diamond surface is discussed later.

6.2.3 7,7,8,8,-Tetracyanoquinodimethane (TCNQ)

TCNQ (Figure 6.9) is another commonly used molecular acceptor. Without fluorination of the central aromatic ring, its molecular energy levels including HOMO and LUMO are closer to the VL, leading to a smaller IP and EA than those of its fluorinated derivative (i.e. F_4-TCNQ). Consequently, the electron accepting ability of TCNQ is expected to be weaker than that of F_4-TCNQ. The EA of TCNQ molecules in gas-phase is determined to be 3.22 eV [271], which puts its LUMO far above the VBM of hydrogenated diamond. When condensed into the solid phase, the EA increases due to electronic polarization from surrounding molecules. Since an experimentally measured EA for TCNQ films is not available, it is estimated to be around 4.0 eV by adopting an average polarization energy of 0.85 eV for π-conjugated organic molecules [158]. The small activation energy (i.e. energy difference between

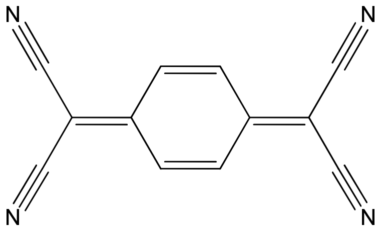

Figure 6.9. Chemical structure of TCNQ.

molecular LUMO and diamond VBM) suggests that TCNQ films can potentially induce surface transfer doping.

The N 1*s* and C 1*s* PES spectra of hydrogenated diamond surface with increasing TCNQ coverages are shown in Figure 6.10. The spectral evolution differs considerably with those of F_4-TCNQ in Figure 6.5 in several aspects: (i) The N 1*s* spectra (Figure 6.10a) comprises a single component along with its shake-up at all thicknesses, suggesting the absence of negatively charged TCNQ. This indicates that the degree of charge transfer to individual TCNQ molecule, if any, is significantly less than unity. (ii) Moderate hole accumulation is revealed by subtle shifts of the diamond C 1*s* peak, as indicated by the dashed lines in Figure 6.10b. In contrast to the substantial decrease of the diamond C 1*s* component upon F_4-TCNQ deposition, the corresponding C 1*s* peak shifts slightly to lower BE with increasing TCNQ thickness, and the shift saturates at 11.8 Å with a value of 0.2 eV. Upward diamond band bending being observed at relatively large TCNQ thicknesses indicates the formation of TCNQ films is required to yield sufficiently high EA to induce electron transfer. In the case of F_4-TCNQ, significant surface transfer doping of diamond is observable at very low coverage whereby the molecules are even isolated. The weaker doping efficiency of TCNQ compared to F_4-TCNQ is attributed to their distinct EAs in both gas-phase and solid-phase, despite possessing the same electron-withdrawing cyano

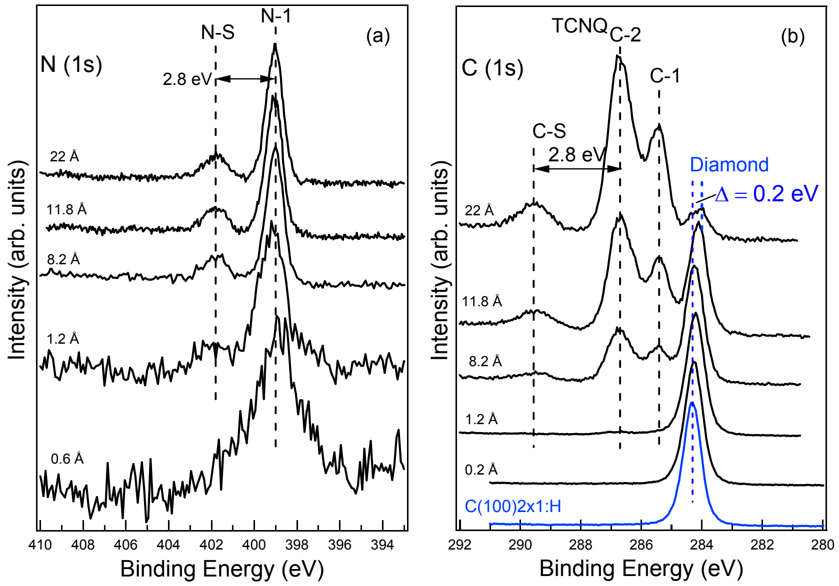

Figure 6.10. PES core-level spectra of (a) N 1*s* (photon energy of 500 eV) and (b) C 1*s* (photon energy 350 eV) of TCNQ on hydrogenated diamond with increasing thickness. N 1*s* spectra are all normalized to have the same N-1 peak intensity and C 1*s* spectra are all normalized to the same spectra height for better viewing.

ends. It underlines the important role of EA in determining the transfer doping efficiency.

Band bending of diamond is also revealed in Figure 6.11a which shows the evolution of diamond valence band structures with increasing TCNQ coverage. The band bending is clearly recognized by the subtle shift of the diamond *sp* band feature at around 13 eV to lower BE. The BE shift is thus in line with the diamond core-level shift due to the upward band bending. At large thicknesses, various orbitals originating from TCNQ are clearly resolved, with a HOMO peak at 3.2 eV and its leading edge at 2.65 eV. No BE shift of TCNQ frontier orbitals is observed, in agreement with the C 1*s* and N 1*s* core-level PES results (Figure 6.10). The absence of molecular energy level shift in TCNQ films suggests that the transferred electrons are mainly localized at the interface. Moreover, a close-up of the region near the Fermi level at all TCNQ thicknesses (not shown here) excludes the existence of gap states, in contrast to the formation of two gap states in anion F_4-TCNQ molecules (HOMO′ and LUMO′ in Figure 6.6b). The missing gap states suggest partial electron transfer to TCNQ ($Z \ll 1$). Consequently, the density of transferred electrons filling the molecular LUMO is too low to bring the LUMO below the Fermi level to form a gap state [251].

Unlike the diamond PES features with subtle BE shift (Figure 6.10), the WF variation upon molecular depositions is substantial (Figure 6.11b). The WF increases immediately from 4.0 eV for pristine hydrogenated diamond to 4.5 eV upon 0.6 Å TCNQ adsorption. It increases continuously with subsequent deposition and saturates at 5.2 eV at 20 Å thickness, with a net 1.2 eV WF increase. Although the overall WF increase after deposition of TCNQ on diamond is only slightly smaller than that of F_4-TCNQ (1.4 eV), its dependence on molecular coverage is dissimilar. In the case of F_4-TCNQ (Figure 6.7b), over 90% of the overall WF increase is completed below the thickness of 4 Å which roughly corresponds to a monolayer coverage. This suggests that majority of the interface dipole is built up at submonolayer coverage due to the large degree of electron transfer to F_4-TCNQ. In contrast, the WF increase at a TCNQ thickness of about 4 Å accounts for only about 60% of its total increase as shown in Figure 6.11c. A substantial part of the interface dipole continues to develop in TCNQ multilayers. This is in agreement with the conclusion from core-level PES that the formation of condensed TCNQ films is necessary to initiate electron transfer out of diamond. As the TCNQ overlayer thickness increases, its EA becomes lower due to increased polarization screening of neighboring molecules and more electrons are transferred from diamond to organic films. Consequently, charge separation continuously builds up across the interface, resulting in an interface dipole that extends several monolayers into the organic film. Separating the contribution from substrate

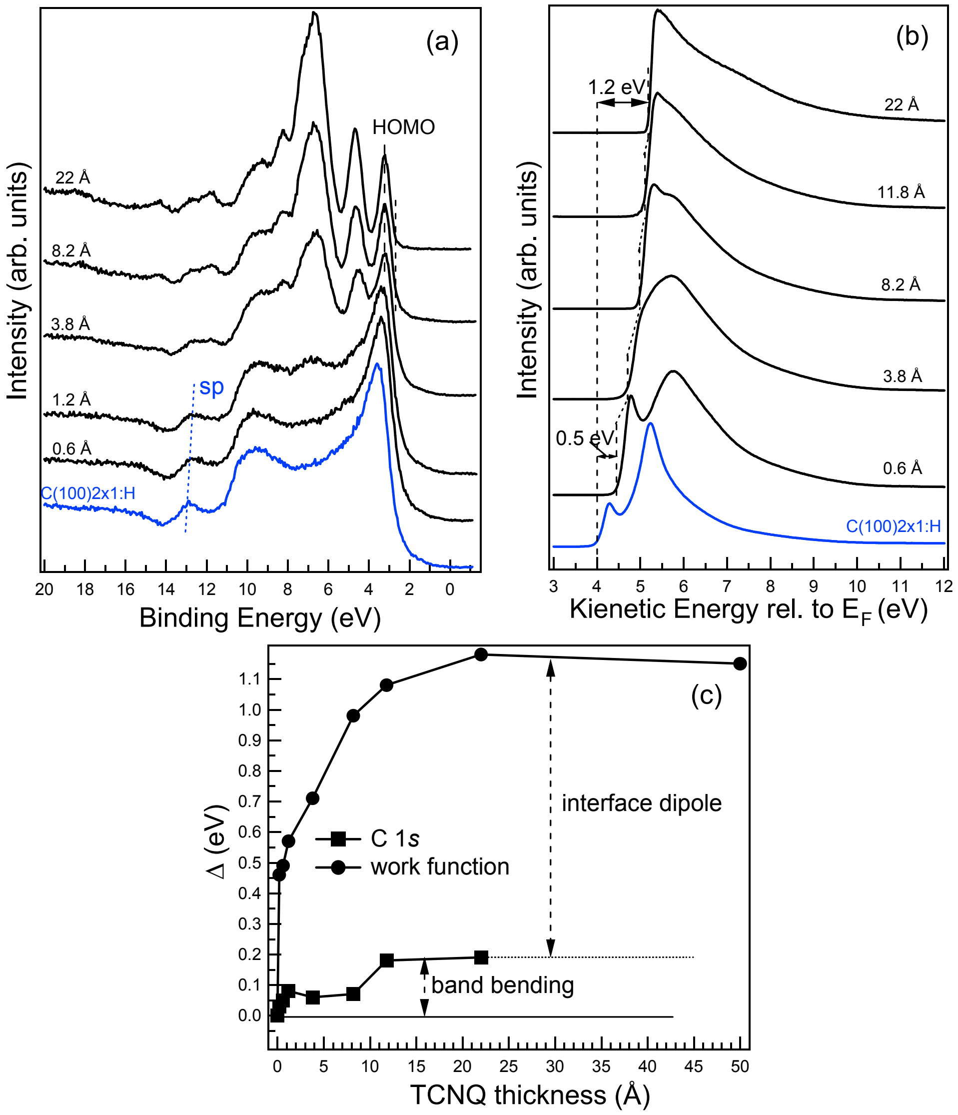

Figure 6.11. (a) UPS spectra (photon energy of 60 eV) of pristine hydrogenated diamond and after TCNQ deposition of increasing thickness. (b) Secondary electron emission cut-off of hydrogenated diamond with increasing TCNQ thickness, indicating the shifts of VL; (c) WF change and diamond C 1*s* core-level BE shift as functions of organic layer thickness.

band bending to WF increase, the interface dipole formed between TCNQ and diamond is estimated to be about 1.0 eV.

The energy band alignment across the interface between hydrogenated diamond and TCNQ is schematically shown in Figure 6.12. An EA of 4.0 eV and an IP of 7.4 eV [250] for neutral TCNQ before charge transfer are adpoted. Although the LUMO of TCNQ is slightly higher than diamond VBM with an activation barrier of 0.4 eV,

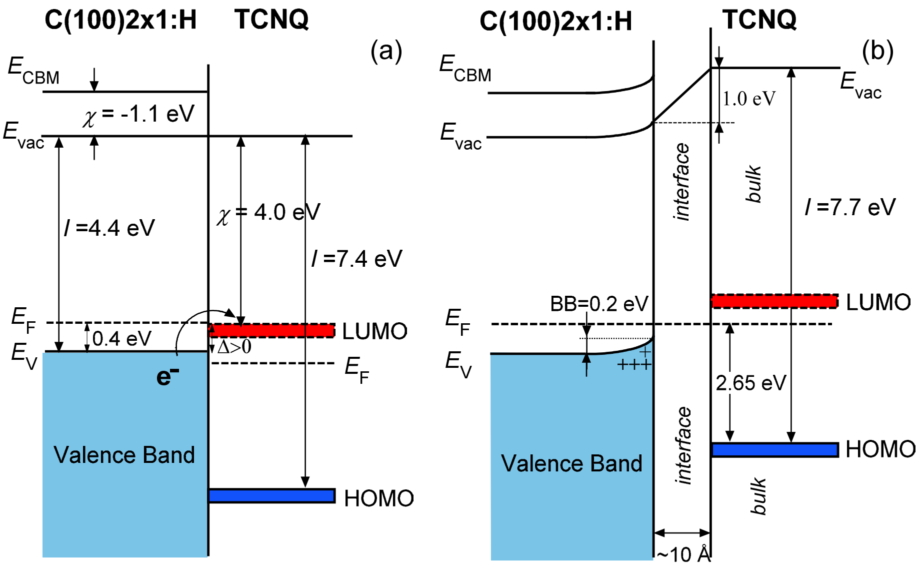

Figure 6.12. Schematic energy level diagram of (a) before surface transfer doping by TCNQ. (b) after surface transfer doping. The position of LUMO is deduced by adopting EA of 4.0 eV. All energy levels are estimated within an error of 0.1 eV.

electron transfer from diamond to TCNQ is still thermodynamically feasible. At equilibrium, the diamond side exhibits an upward band bending of 0.2 eV towards the surface with a hole accumulation layer formed. As a result of charge separation across the interface, an interface dipole of 1.0 eV forms, extending about 10 Å into the molecular bulk. The IP of TCNQ film is determined to be 7.7 eV by adding WF (5.05 eV) to E_F-HOMO (2.65 eV), consistent with the reported value [272].

In summary, TCNQ molecules can induce mild surface transfer doping of hydrogenated diamond. However, both the doping efficiency and degree of charge transfer of TCNQ as surface acceptor are much lower than its fluorinated counterpart F_4-TCNQ. The weaker surface transfer doping ability of TCNQ is directly related to its smaller EA as compared to F_4-TCNQ.

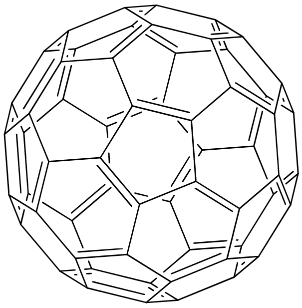

Figure 6.13. Chemical structure of C_{60}.

6.2.4 Fullerene (C_{60})

Fullerene (C_{60}, Figure 6.13) and its fluorinated derivative molecules (e.g. $C_{60}F_{36}$, $C_{60}F_{48}$) represent another group of molecular acceptors that can potentially dope diamond (Figure 6.3). The two lowest lying unoccupied molecular orbitals of fullerene with t_{1u} and t_{1g} symmetries respectively can each hold up to six electrons thanks to their three-fold degeneracy. Hence, fullerene is regarded as a potent electron acceptor [251]. Chemically modified fullerene molecules have been widely used as an electron acceptor material together with electron donors (usually conjugated polymers such as P3HT) in bulk heterojunction (BHJ) organic solar cells [273]. Surface transfer doping of diamond using fullerene and fluorinated fullerene has been experimentally demonstrated by Strobel *et al.* [247-249], who measured greatly increased SC of diamond after fullerene and fluorinated fullerene deposition. The measured SC are comparable (for C_{60}) or even higher (for $C_{60}F_{48}$) than that induced by atmospheric-adsorbates. The proposed electron transfer from diamond to fullerene and fluorinated fullerene overlayers is further supported by DFT calculations [242-244], although no detailed spectroscopic studies on this charge transfer system have been reported. Compared with TCNQ and F_4-TCNQ, fullerene has higher thermal and chemical stability. It is also more easily synthesized at very high purity, and reliable deposition

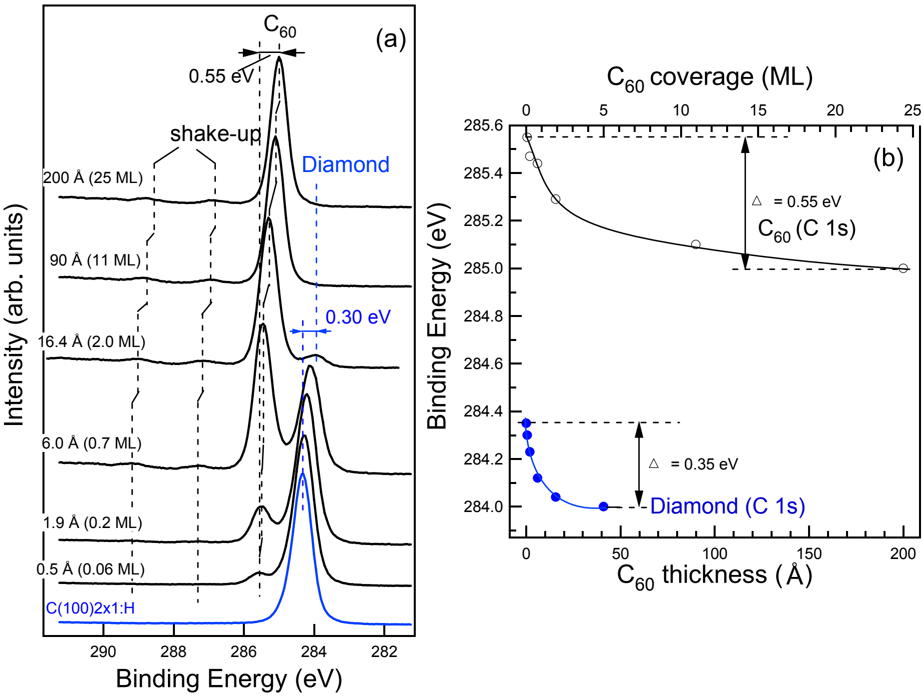

Figure 6.14. (a) C 1*s* PES spectra of C_{60} (photon energy, 350 eV) on hydrogenated diamond with increasing thickness. Spectra are all normalized to have the same spectra height. (b) BE shifts of C 1s component from diamond and C_{60}, respectively. Solid lines through points are guide for the eyes only.

techniques of fullerene in both solid phase and solution phase are readily available [273]. Therefore, the use of fullerenes is a more feasible route to practical surface transfer doping scheme.

Figure 6.14 shows the evolution of C 1*s* PES spectra with increasing C_{60} thickness. The coverage of C_{60} in units of ML is converted from its nominal thickness by assuming that C_{60} is arranged with its close-packed hexagon (111) plane of fullerene crystal parallel to diamond surface with an interlayer distance of 8.2 Å. The hydrogenated diamond C 1*s* component, initially at 284.30 eV, exhibits a gradual shift to lower BE within the first monolayer coverage, and approaches its saturation value of 0.35 eV at around 5 ML C_{60} coverage (also see Figure 6.14b). This shift, similarly to those observed for F_4-TCNQ and TCNQ, indicates an upward band bending toward diamond surface due to hole accumulation. It is apparent that several monolayers of solid fullerite are necessary to induce sizable band bending and charge transfer. This observation is consistent with the EA difference between isolated C_{60} molecules and its condensed fullerite phase. Although gas-phase C_{60} has a relatively low EA of 2.7 eV [274] which is far smaller than diamond IP, the electronic polarization increases EA to around 4.2 eV for a few monolayers of condensed C_{60} [275]. As a result, condensed fullerene (fullerite) has a small enough energy barrier (<0.2 eV) for electrons transferring from diamond valence band to molecular LUMO states. Surface conductivity measurements made by Strobel et al. also reveal that high surface conductivity only appears after at least several monolayers of fullerene is formed on diamond [248].

At higher thickness, the C_{60} C 1*s* components can be clearly identified and well separated from diamond component, comprising a main line with several shake-up peaks at higher BE associated with π to π^* or σ^* intramolecular transitions [276]. Closer inspection of the energy position of fullerene C 1*s* main line and its shake-up peaks reveals a gradual energy shift to lower BE as C_{60} thickness increases. The C_{60} main peak energy difference at smallest and largest coverage is 0.55 eV. Charging effects commonly observed in thick organic films can be ruled out since charging leads to a shift to higher BE. The change of electronic polarization energy used to explain the observed energy shift in organics such as CuPc on gold [154] and hydrogen-terminated silicon surfaces [157], cannot account for such a large energy shift. Therefore, this core-level energy shift explicitly indicates an upward electrostatic energy level bending away from interface in the organic overlayers.

Analogous to conventional inorganic semiconductors, the upward energy band bending is associated with an accumulation layer of negative space charges as a result of electron transfer from diamond to the molecular layers. The transferred electrons diffuse deep into C_{60} film bulk, resulting in a space charge width of more than 20 nm. This is quite different from the scenario of surface transfer doping of diamond by F_4-TCNQ and TCNQ, in which the transferred electrons remain localized at the interface (< 10 Å) and no shifts of the N 1*s* or C 1*s* components were observed in the multilayers. The apparent larger delocalization of transferred electron in fullerene films may be related to enhanced band-like transport of electrons in solid C_{60} due to more effective overlapping of molecular orbitals. Theoretical calculations [277] predict the electronic band formation in crystalline fullerene solids governed by the weak overlapping of the π-derived molecular orbitals. The bandwidth of the LUMO-derived conduction band is calculated to be about 0.5 eV, large enough for band-like transport of electrons in the conduction band with small effective mass and hence large mobility. Indeed, electron mobility of up to 6 $cm^2V^{-1}s^{-1}$ has been measured for highly crystalline C_{60} thin films [278]. In contrast, the electron mobility of TCNQ ($\mu_{TCNQ} \sim 3 \times 10^{-5}$ $cm^2V^{-1}s^{-1}$ [279]) is several orders lower.

The valence band photoemission spectra of hydrogenated diamond surface with C_{60} deposition is shown in Figure 6.15a. The spectra exhibit a transition from the valence band features of diamond to the molecular orbital-derived bands of fullerene films. In thick fullerene films, a number of peaks originating from the occupied molecular orbitals of C_{60} can be clearly indentified, resembling the valence band structure typically measured from solid C_{60} [276]. The states lying below 5 eV to E_F have a purely π character including the five-fold degenerate HOMO state with h_u symmetry, whereas those above 10 eV are mainly C 2*s*-derived σ states and those lying in between 5 eV to 10 eV have a mixed π and σ character. All the molecular states move closer to the Fermi level with increasing fullerene thickness (Figure 6.16a), in the same direction and magnitude as C_{60} C 1*s* components. This systematic

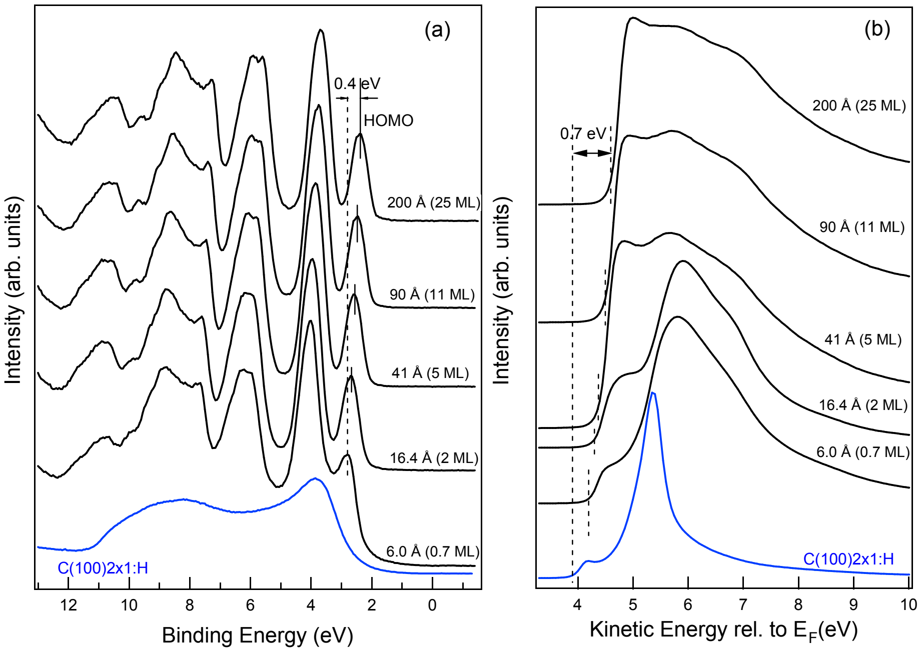

Figure 6.15. (a) UPS spectra (photon energy of 60 eV) of pristine hydrogenated diamond and after C_{60} deposition of increasing thickness. (b) Secondary electron emission cut-off of hydrogenated diamond with increasing C_{60} thickness, indicating the shifts of VL.

shift in all molecular energy levels is consistent with molecular band bending in the fullerene thin films associated with negative space charge layers.

In Figure 6.16a, the molecular HOMO and LUMO onset energies at different film thicknesses are shown together, clearly revealing the upward band bending. The Fermi level is very close to C_{60} LUMO at small thickness (the interface region) with an energy difference of less than 0.1 eV, indicating electron accumulation. Away from the interface at large thickness, E_F gradually moves back into the band gap at 0.4 eV below the LUMO, similar to that measured in bulk C_{60} films [280].

Although the electron transfer from diamond to C_{60} adsorbate layers has been confirmed by electrostatic band bending both in diamond and organics, careful examination of the valence band region close to the Fermi level excludes the existence of LUMO-derived gap states. Such states have been observed in alkali metal doped fullerenes (A_xC_{60}) by PES [251], where one or more alkali metal atoms such as potassium are intercalated into individual fullerene molecule and donate electrons to its LUMO orbitals. Since the triply-degenerate fullerene LUMO can accommodate a total of 6 electrons, up to 6 potassium atoms can be bonded to one fullerene, resulting in a partially or completely-filled LUMO state close to Fermi level. However, the appearance of gap states is only applicable to fullerene films with high potassium doping concentration so that many electrons are transferred to each C_{60} molecule. For fullerene films exposed to very low flux of alkali metal, a highly diluted solid solution of potassium in C_{60} is formed. The Fermi level in this case is pinned at donor levels close to the edge of LUMO-derived bands [280], thus causing a shift of the whole spectrum to higher BE as compared with that of pristine fullerene film. This scenario is similar to the present study where the degree of charge transfer to C_{60} should be much lower than unity. Hence, the fullerene film is better viewed as a semiconductor system with dispersive electronic bands instead of a simple collection of isolated molecules. Consequently, the surface transfer doping model in Figure 6.2 depicted under a molecular framework is no longer appropriate. Instead, a solid state picture in which the diamond/fullerite system resembles an extreme type II heterojunction formed between two semiconductors [53] should be adopted to describe the surface transfer doping process [247]. A detailed band alignment after surface transfer doping is discussed below.

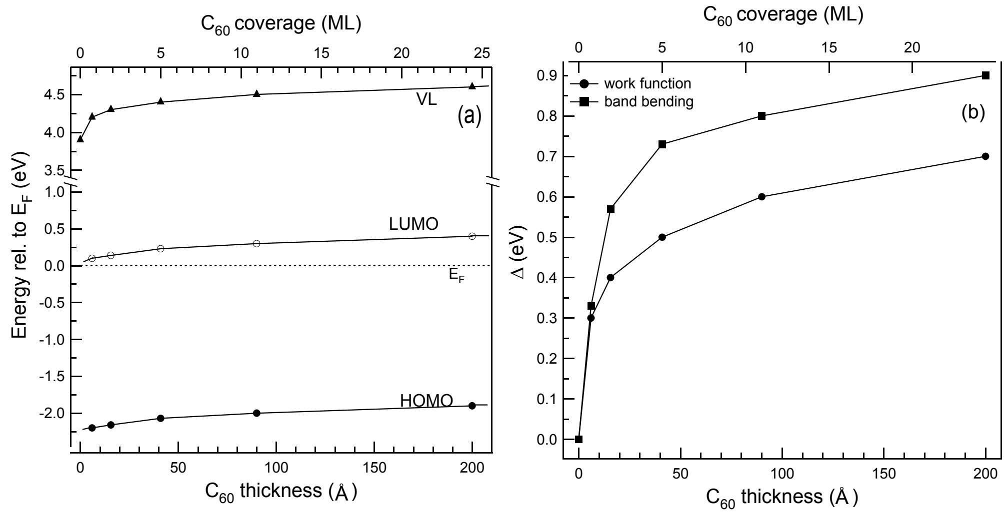

Figure 6.16. (a) Evolution of energy levels of C_{60} on diamond at increasing thickness. The energy position of HOMO edge is adopted to indicate the position of HOMO. The energy position of LUMO onset is obtained by adding a transporting band gap of 2.3 eV to that of HOMO [281]. (b) Changes of WF and band bending as a function of C_{60} thickness. The amount of band bending is calculated as the sum of energy shifts of diamond C 1*s* line and C_{60} C 1*s* main line. Solid lines through points are guide for the eyes only.

Figure 6.15b shows the low KE part of the UPS spectra. The VL shifts to higher KE (i.e. an increase of WF) with increasing fullerene film thickness, consistent with band bending and charge transfer. To evaluate the magnitude of the interface dipole from the change of WF and band bending in both diamond and fullerite (Figure 6.16b), it is noted that the band bending is constantly larger than the change of WF by about 0.2 eV. This differs from the results of F_4-TCNQ (Figure 6.7b) or TCNQ (Figure 6.11c) on diamond. At first glance, this deviation might indicate an interface dipole of 0.2 eV pointing toward the fullerene side (i.e. positive charges at fullerene, negative charges at diamond) that pulls down the vacuum level across the interface. However, this contradicts the charge transfer direction determined by PES. It should be noted that the calculation of interface dipole assumes that the IP (EA) of molecular overlayers is unchanged at all thicknesses, and therefore the local VL inside the molecular film has the same bending as that of HOMO (LUMO) states. In reality, the

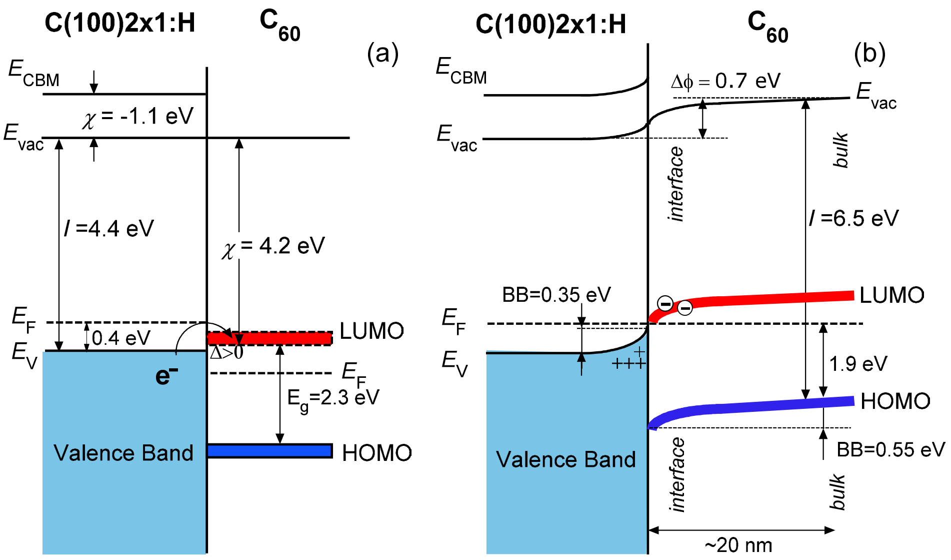

Figure 6.17. Schematic energy level diagram of (a) before surface transfer doping by C_{60}. (b) after surface transfer doping. The position of LUMO is deduced by adding a band gap of 2.3 eV to the HOMO energy position.

IP (EA) of a molecular system is influenced by the electronic polarizations, molecular orientations, and packing structures, etc. [183]. The observed small deviation might stem from small variations of the IP (EA) of fullerene films at different thickness. As a result, the interface dipole might not form across the diamond/C_{60} heterojunction. This conclusion is consistent with the delocalized nature of electron transfer in C_{60} layers. The electric field due to charge separation manifests as electrostatic band bending extends into the bulk of diamond and fullerite, rather than induce an abrupt and narrow interface dipole layer confined at the interface.

The energy level alignment diagram across the diamond/fullerene interface is shown in Figure 6.17. The high EA of condensed fullerene molecular solids puts the bottom edge of its LUMO derived band very close to the VBM of diamond with an activation barrier less than 0.2 eV. As a result, spontaneous electron transfer from diamond to fullerene overlayers occurs. After thermodynamic equilibrium is reached, the diamond surface is *p*-doped with a hole accumulation layer and a 0.35 eV upward

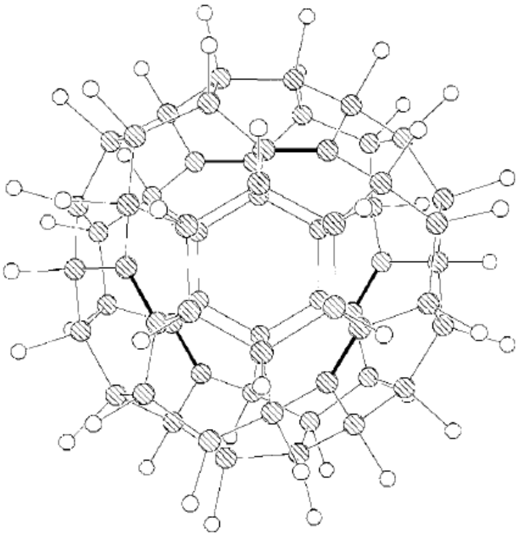

Figure 6.18. Relaxed molecular structure of the D_3 isomer of $C_{60}F_{48}$. The remaining 6 double bonds are indicated by bold lines. (Structure is taken from ref. [282])

band bending. However, *p*-type surface transfer doping of diamond by C_{60} is only effectively achieved with at least a complete fullerene layer. The accumulated holes on the diamond side are counterbalanced by excess electrons in the C_{60} film. Due to the high electron delocalization in C_{60} molecular solids, the transferred electrons are delocalized over a relative long distance into the film bulk. The resulting electron accumulation layer with a width over 20 nm in fullerite leads to a band bending of 0.55 eV. The VL is well aligned at the interface, but also bends systematically away from interface, similar to other energy levels. The VL alignment differs from that of F_4-TCNQ or TCNQ on diamond where a substantial interface dipole is formed (see Figure 6.8 and Figure 6.12).

6.2.5 Highly fluorinated fullerene ($C_{60}F_{48}$)

Similar to F_4-TCNQ, the electron withdrawing ability of fullerene molecules can be further promoted by fluorination. The inductive effects of electronegative fluorine atoms move the molecular energy levels away from the vacuum level [283], leading to increased EA and IP [284]. The large number of unsaturated C_{60} bonds results in all kinds of fluorinated fullerenes with varying fluorine amount ($C_{60}F_x$ $x = 2{\sim}48$). Among them, $C_{60}F_{48}$ is the most highly fluorinated fullerene that has been synthesized. It is expected to have the largest EA and the electron withdrawing abilities among all the fullerene derivatives.

The EA and IP of $C_{60}F_{48}$ in gas phase are experimentally determined to be 4.06 eV [285] and 12.0 eV [286] respectively, much larger than its parent fullerene molecules ($\chi_{\text{fullerene}} = 2.65$ eV, $I_{\text{fullerene}} = 7.6$ eV). The IP for $C_{60}F_{48}$ in the solid state is experimentally determined by UPS to be 8.4 eV [283], while reliable experimental value of EA for condensed phase $C_{60}F_{48}$ is still lacking. However, it can be deducted from its gas phase value by adding the electronic polarization energy. Although the experimental polarization energy P for an electron in fluorinated fullerene is not available, we can assume it to be the same as the value for C_{60} ($P_{-} = 1.3$ eV [247]). This leads to the EA for solid $C_{60}F_{48}$ of 5.4 eV, a value significantly larger than the IP of diamond. This EA is even slightly larger than the known value of F_4-TCNQ films. This suggests that $C_{60}F_{48}$ is potentially an excellent surface acceptor for diamond, with surface transfer doping ability close to or even superior to F_4-TCNQ. Indeed, conductivity measurements conducted by Strobel *et al.* showed an increase in diamond SC by several orders when exposed to very small amounts of $C_{60}F_{48}$, suggesting that this molecule is an effective surface acceptor even in isolated molecular form [248].

Figure 6.18 shows the relaxed molecular structure of the most stable isomer of $C_{60}F_{48}$. The attachment of 48 fluorine atoms to the carbon cage breaks most π-bonds between carbon atoms, destroying the conjugation of C_{60}. The remaining 6 double

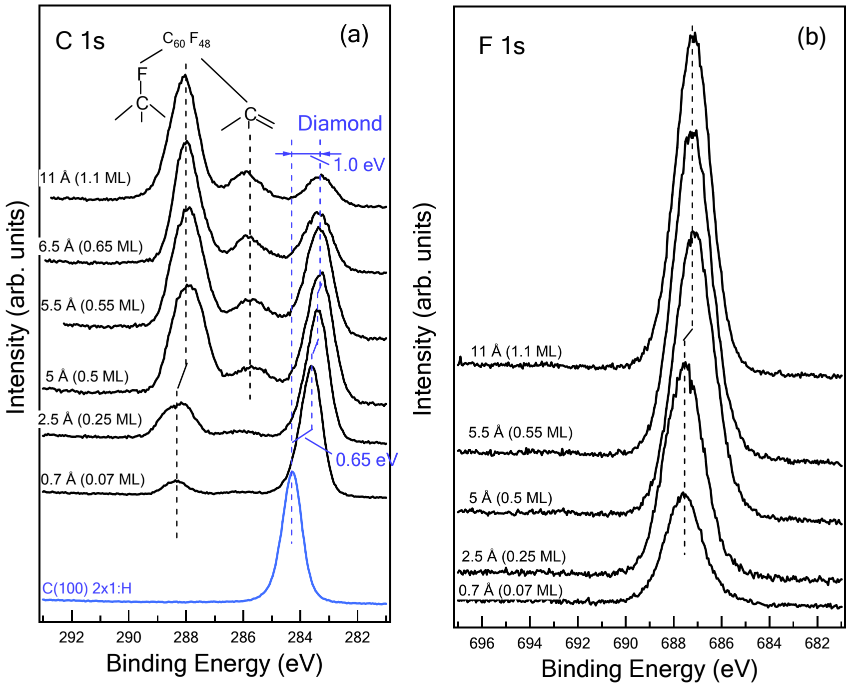

Figure 6.19. PES core-level spectra of (a) C 1*s* (photon energy of 350 eV) and (b) F 1*s* (photon energy 780 eV) of $C_{60}F_{48}$ on hydrogenated diamond with increasing thickness. C 1*s* spectra are all normalized to have the same overall spectra height for better viewing.

bonds are isolated. Therefore, the electronic structure of $C_{60}F_{48}$ should be significantly different from that of C_{60}.

Figure 6.19 shows the evolution of C 1*s* as well as F 1*s* PES spectra as a function of $C_{60}F_{48}$ thickness. After a series of depositions, two new components in the C 1*s* core-level spectra emerge on the left of the diamond peak. The component with higher BE stems from carbon atoms in the fullerene cage bonded to fluorine atoms, and the lower BE component is assigned to carbon atoms in threefold coordinated bonding configuration which retains the double bonds [248, 283]. The 2.2 eV chemical shift between these two components is the result of the reduced valence electron densities surrounding the fluorine bonded carbon atoms due to partial electron transfer to fluorine atoms. Furthermore, from the intensity ratio of these two components, we estimate an average stoichiometry of $C_{60}F_{46\pm2}$, corroborating the integrity of $C_{60}F_{48}$

molecules. The small difference may come from the existence of a small amount of lower fluorinated fullerene species in the organic source.

Inspection on the diamond C 1*s* main lines reveals a substantial shift of 0.65 eV to lower BE at very low coverage[6] of $C_{60}F_{48}$. The diamond band bending related shift continues to develop at a slower pace with increasing coverage and approaches saturation of 1.0 eV after 5 Å (~ 0.5 ML) deposition. The band bending behavior is similar to that of diamond surface after F_4-TCNQ adsorption but with a slightly larger magnitude. Therefore, as with F_4-TCNQ, $C_{60}F_{48}$ acts as a highly efficient surface transfer dopant that can induce substantial hole accumulation on diamond. The larger band bending suggests an even higher areal hole concentration on diamond than that induced by F_4-TCNQ doping. This strong surface transfer doping capability of $C_{60}F_{48}$ molecules is consistent with its high EA in both gas phase and condensed phase.

Although the band bending of diamond indicates electrons are transferred from diamond to the molecules, a closer inspection of the $C_{60}F_{48}$ derived C 1*s* and F 1*s* component (Figure 6.19) at low molecular coverages does not reveal any interfacial state related to anion molecular species. Only small shifts of about 0.4 eV to lower BE for both C 1*s* components and F 1*s* component are observed when the thickness of deposited molecules increases from 2.5 Å to 5 Å. This appears to contradict the conclusion drawn from diamond band bending that even isolated $C_{60}F_{48}$ molecules accept significant numbers of electrons from diamond forming anions. However, unlike F_4-TCNQ, the high fluorination ratio of a $C_{60}F_{48}$ molecule breaks the conjugation of its carbon cage. As a result, even for complete charge transfer to $C_{60}F_{48}$, the transferred electron may be highly localized within one or a few C-F bonds in direct

---

[6] The coverage in the unit of ML for $C_{60}F_{48}$ is estimated in a similar way to C_{60}. The interlayer distance (10 Å), however, is slightly enlarged as a result of the larger lattice constant of fcc single crystal of $C_{60}F_{48}$ (a=1.716 nm) than that of C_{60} single crystal (a=1.417 nm).

contact with diamond, leaving the remaining carbon and fluorine atoms largely unperturbed by the additional valence charges. Photoemission from the chemically shifted carbon and fluorine atoms thus comprise a very small percentage of the total atoms in the $C_{60}F_{48}$ molecule (estimated to be less than 3%). The observed 0.4 eV BE shift of $C_{60}F_{48}$ components are attributed to the interface dipole field induced by charge transfer.

The evolution of diamond valence band structures with increasing $C_{60}F_{48}$ thickness is shown in Figure 6.20a. At the thickness of 0.7 Å, the diamond valence band features above 5 eV are already largely suppressed by photoelectrons from adsorbed molecules. Nevertheless, the prominent feature A of pristine diamond can still be distinguished and exhibits a rigid shift towards the Fermi level, consistent with diamond band bending. After further deposition, features originating from $C_{60}F_{48}$ orbitals dominate the spectra at high BEs. The most prominent peak C located around 9 eV is mostly derived from the 2*p* lone pairs of fluorine atoms. The two broad features B and D located at each side of feature C are mainly attributable to the molecular orbitals with hybridizations between F 2*p* and C 2*p* orbitals [282-283]. Although *ab initio* calculations predict the existence of HOMOs which are purely C 2*p* in nature and localize on the remaining double bonds [282], the corresponding peak is missing in the UPS spectra at photon energy of 60 eV. This is due to the low DOS of the HOMOs as well as the low photoionization cross section of loosely bound π electrons [283]. The weak feature around 4 eV is believed to be the remnant intensity of diamond feature A rather than molecular HOMOs. It was reported that lower excitation energy of 11.7 eV can indeed probe the HOMO-related features of $C_{60}F_{48}$, with its threshold energy separated by 6.6 eV from the F 2p lone pair peak (C) [283].

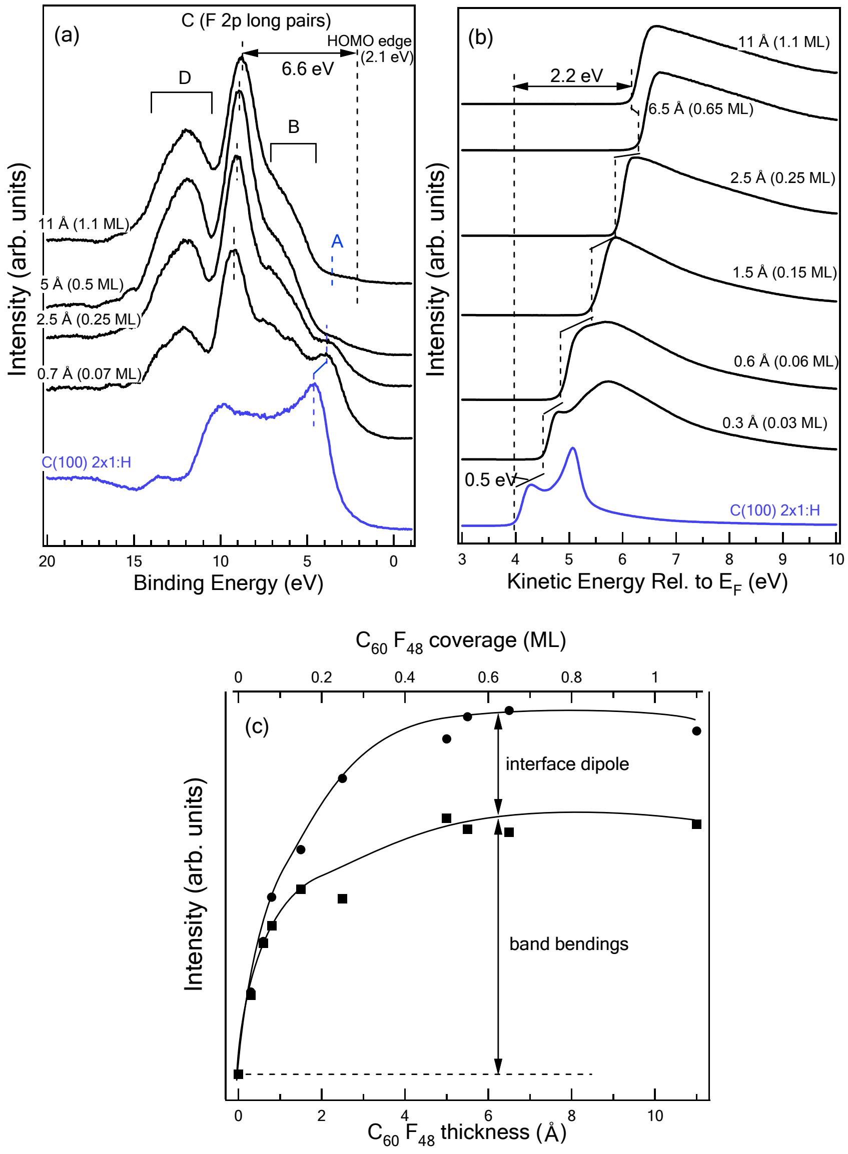

Figure 6.20. (a) UPS spectra (photon energy of 60 eV) of pristine hydrogenated diamond and after $C_{60}F_{48}$ deposition of increasing thickness; (b) Secondary electron emission cut-off of hydrogenated diamond with increasing $C_{60}F_{48}$ thickness, indicating the shifts of VL; (c) WF change (solid circles) and band bending (solid square) as function of organic layer thickness. Solid lines through points are guide for the eyes only.

Using this energy separation, we are able to deduce the HOMO edge position at 2.1 eV below the Fermi level.

Although electron transfer from diamond to $C_{60}F_{48}$ has been confirmed by diamond band bending, closer inspection of the region close to the Fermi level in the UPS spectra fails to reveal the existence of charge transfer states related to partially filled molecular LUMO and relaxed HOMO. This could also be due to the low photoionization cross sections of these orbitals. It is not clear at present stage whether we are able to observe these gap states using lower photon energy excitation due to the limitation of photon source.

As expected from interfacial charge transfer, the WF of diamond increases substantially with $C_{60}F_{48}$ deposition (Figure 6.20b). The overall VL shift reaches as high as 2.2 eV after deposition of 11 Å $C_{60}F_{48}$ molecules, which is much higher than the saturated WF change induced by F_4-TCNQ (Δ = 1.4 eV) and TCNQ (Δ = 1.2 eV). Since the change of WF is very sensitive to the amount of interfacial charge transfer, this anomalously high WF change supports the high surface transfer doping capability of $C_{60}F_{48}$. Figure 6.20c summarizes the change of WF as a function of $C_{60}F_{48}$ thickness. By separating the contribution from band bending, the interface dipole induced by charge transfer is estimated to be around 0.6 eV, similar to that of F_4-TCNQ on diamond.

The energy level alignment across diamond/$C_{60}F_{48}$ is schematically drawn in Figure 6.21. The extreme high EA for solid phase $C_{60}F_{48}$ puts its LUMO far below the diamond VBM. Even for $C_{60}F_{48}$ in isolated state, its gas phase EA of 4.06 eV results in a relatively small activation barrier (~ 0.3 eV). Therefore, spontaneous charge transfer occurs upon the adsorption of $C_{60}F_{48}$ even in molecular form. After thermodynamic equilibrium is reached (Figure 6.21b), the large upward band bending of 1.0 eV toward diamond surface puts the Fermi level 0.6 eV below the VBM at the surface, resulting in a highly degenerate surface region with large areal hole density. The VL is up-shifted sharply in the interface region due to the charge transfer. The IP for $C_{60}F_{48}$ layers is deduced from the HOMO position and work function to be 8.4 eV, in excellent agreement with previous reports on $C_{60}F_{48}$ thin films [283].

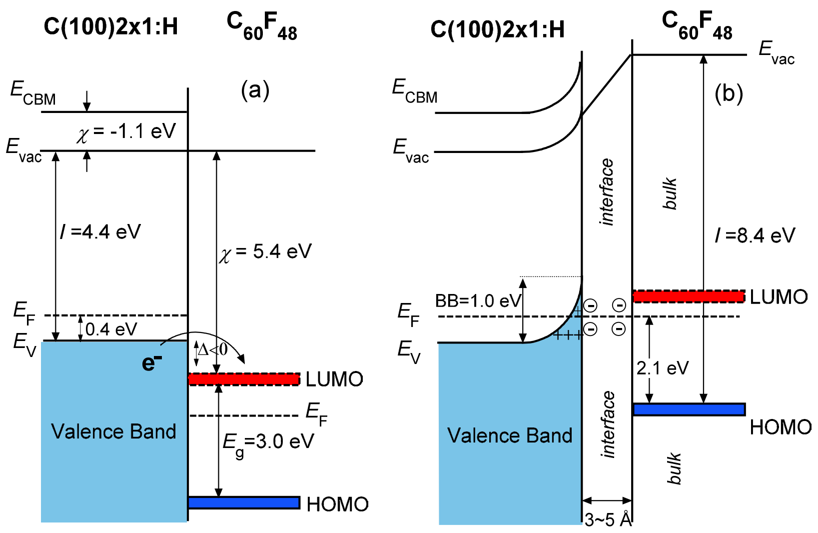

Figure 6.21. Schematic energy level diagram of (a) before surface transfer doping by $C_{60}F_{48}$. (b) after surface transfer doping. The position of LUMO is deduced by adding a band gap of 3.0 eV to the HOMO energy position.

6.2.6 CuPc revisited

The molecules studied in this chapter have condensed-phase EA close to or higher than the IP of diamond. To further investigate the influence of molecular EA on surface transfer doping of diamond, we choose a model organic molecule with a much smaller EA. CuPc serves this purpose very well, since its EA in condensed phase has a value in the range of 2.7 ~ 2.9 eV [156-158], which places its LUMO 1.7 to 1.9 eV above the VBM of diamond. The resulting activation barrier far exceeds the thermal energy of electrons at RT (~0.026 eV). Consequently, electron transfer from diamond VBM to CuPc LUMO is not energetically favored, and surface transfer doping of diamond is therefore not expected to proceed.

In Chapter 5, the PES results of CuPc deposited on hydrogenated diamond surface have been presented. In particular, the diamond C 1*s* peak remains at the same BE throughout CuPc deposition (Figure 5.3). The absence of band bending indicates that there is no hole accumulated region at the diamond surface. Moreover, as shown in Figure 5.5b, there is virtually no shift of the VL energy position within experimental error (~0.05 eV), indicating good VL alignment across the interface. The absence of band bending and interface dipole at diamond/CuPc interface unambiguously confirms that there is no charge transfer at the interface. CuPc thus does not serve as an effective surface acceptor for diamond.

6.2.7 Areal hole density and doping efficiency

Except for CuPc, all the organic molecules discussed in this chapter (i.e. F_4-TCNQ, TCNQ, C_{60}, $C_{60}F_{48}$) induce surface transfer doping of diamond. To compare their doping abilities, it is necessary to quantify the doping yield (i.e. induced areal hole density in diamond) as a function of molecular coverage.

The charge density and electrostatic potential profile of the space charge layers inside a general semiconductor due to the presence of surface states or surface adsorbates can be analyzed by combining Poisson's equation and Fermi-Dirac statistics [7]. Thus, the relationships between various important physical quantities such as the band bending amount, space charge density, and surface charge density etc. can be quantified. For wide bandgap semiconductors such as diamond, using the Boltzmann approximation and assuming a unipolar (holes only) semiconductor, a simple hole accumulation layer profile in diamond can be obtained [222]:

$$p_{\mathrm{s}}(u_{\mathrm{s}}) = \sqrt{2kT\varepsilon\varepsilon_0 N_{\mathrm{v}} / e^2} \cdot \exp(u_{\mathrm{s}} / 2kT) \tag{6.1}$$

This equation relates the integrated surface areal hole density p_{s} with the potential $u_{\mathrm{s}} = E_{\mathrm{VBM}} - E_{\mathrm{F}}$ at the diamond surface. k, T, ε, ε_0, e are the Boltzmann constant, temperature, relative dielectric constant (5.8 for diamond), vacuum permeability and elementary charge, respectively. N_{V} is the effective density of states at the valence band edge which is 2.7×10^{19} cm^{-3} for diamond at RT [222]. Hence, the pre-exponential factor in Eqn. (6.1) is calculated to be 2.1×10^{12} cm^{-2}. It should be noted that Eqn. (6.1) is only valid for the non-degenerate case where the diamond valence band is below the Fermi energy ($u_s<0$). For strong surface acceptors like F_4-TCNQ, the associated surface transfer doping can be so strong that the Fermi energy is well below the VBM at the surface as a result of large upward band bending, and the diamond surface becomes degenerate. In this case, the classical Boltzmann approximation is replaced by Fermi statistics approximated as a step function, and eqn. (6.1) becomes [222]:

$$p_{\mathrm{s}}(u_{\mathrm{s}}) = \sqrt{2kT\varepsilon\varepsilon_0 N_{\mathrm{v}} / e^2} \cdot \sqrt{1 + \frac{u_{\mathrm{s}}}{kT} + \frac{8}{15\sqrt{\pi}}\left(\frac{u_{\mathrm{s}}}{kT}\right)^{5/2}} \tag{6.2}$$

By combining Eqn. (6.1) and (6.2), the areal hole density induced by surface transfer doping on diamond can be explicitly estimated with the knowledge of the surface potential u_s. In practice, u_s is obtained by adding the band bending amount as deduced from core-level PES to the u_s of pristine hydrogenated diamond (u_s = -0.4 eV). From the above equations, a larger band bending always leads to higher areal hole density at the surface.

On the molecular acceptor side, excess electrons originating from diamond valence band fill the LUMO of surface acceptors. By only considering the molecules within the first monolayer in direct contact with diamond, the excess electron occupancy in the surface acceptors follows the Fermi-Dirac statistics under molecular framework and we have:

$$n = \frac{n_{\mathrm{A}}}{1 + \mathrm{e}^{(\Delta + u_{\mathrm{s}})/kT}} = \frac{n_{\mathrm{A}}}{1 + \mathrm{e}^{(\phi_{\mathrm{LUMO}} - E_{\mathrm{F}})/kT}} \tag{6.3}$$

for areal electron density n in the surface acceptor layer under thermodynamic equilibrium. n_A is the density of surface acceptors; Δ is the acceptor activation energy which equals the energy difference between molecular LUMO (ϕ_{LUMO}) and diamond VBM. Δ is a constant which remains unchanged before and after the equilibrium. In this way, the areal electron density is related to the surface potential u_s, which in turn is related with the areal hole density p_s in diamond. The addition requirement of overall charge neutrality in the system dictates that p_s must be equal to n. Combining with Eqn. (6.1) and (6.2), it is also possible to express u_s as a function of acceptor coverage n_A. It should be noted that the degeneracy factor was set to 1 in Eqn. (6.3), which implies at most only one unoccupied LUMO state per molecule can accommodate an extra electron charge even in the case of degenerate LUMO. This assumption is justified since the electron-electron repulsion (Coulomb repulsion) is very large when more than one electron is forced into one isolated molecule [287].

It is now straightforward to derive the effective doping efficiency of the surface acceptors using:

$$\eta = \frac{n}{n_A} = \frac{1}{1 + e^{(\Delta + u_s)/kT}} = \frac{1}{1 + e^{(\phi_{LUMO} - E_F)/kT}} \tag{6.4}$$

For surface acceptors such as F_4-TCNQ whose LUMO is a few kT below the Fermi level at equilibrium (Figure 6.8), the doping efficiency is expected to approach 100%. This is in agreement with our previous analysis that suggests the degree of charge transfer to each F_4-TCNQ molecule in the submonolayer regime is close to one.

In the top graph of Figure 6.22, we show the areal hole density (as well as sheet conductivity) as function of molecular coverage for various molecular acceptors. The areal hole density was calculated according to Eqn. (6.1) and (6.2). The sheet conductivity is then calculated according to $\sigma_{\square} = e\, p_s \mu_h$, where $\mu_h \approx 70$ cm^{2}V^{-1}s^{-1} [202] is the average hole mobility of diamond SC. The molecular coverage is expressed in the units of monolayer (ML, bottom axis) as well as in molecules/cm^2 (top axis).

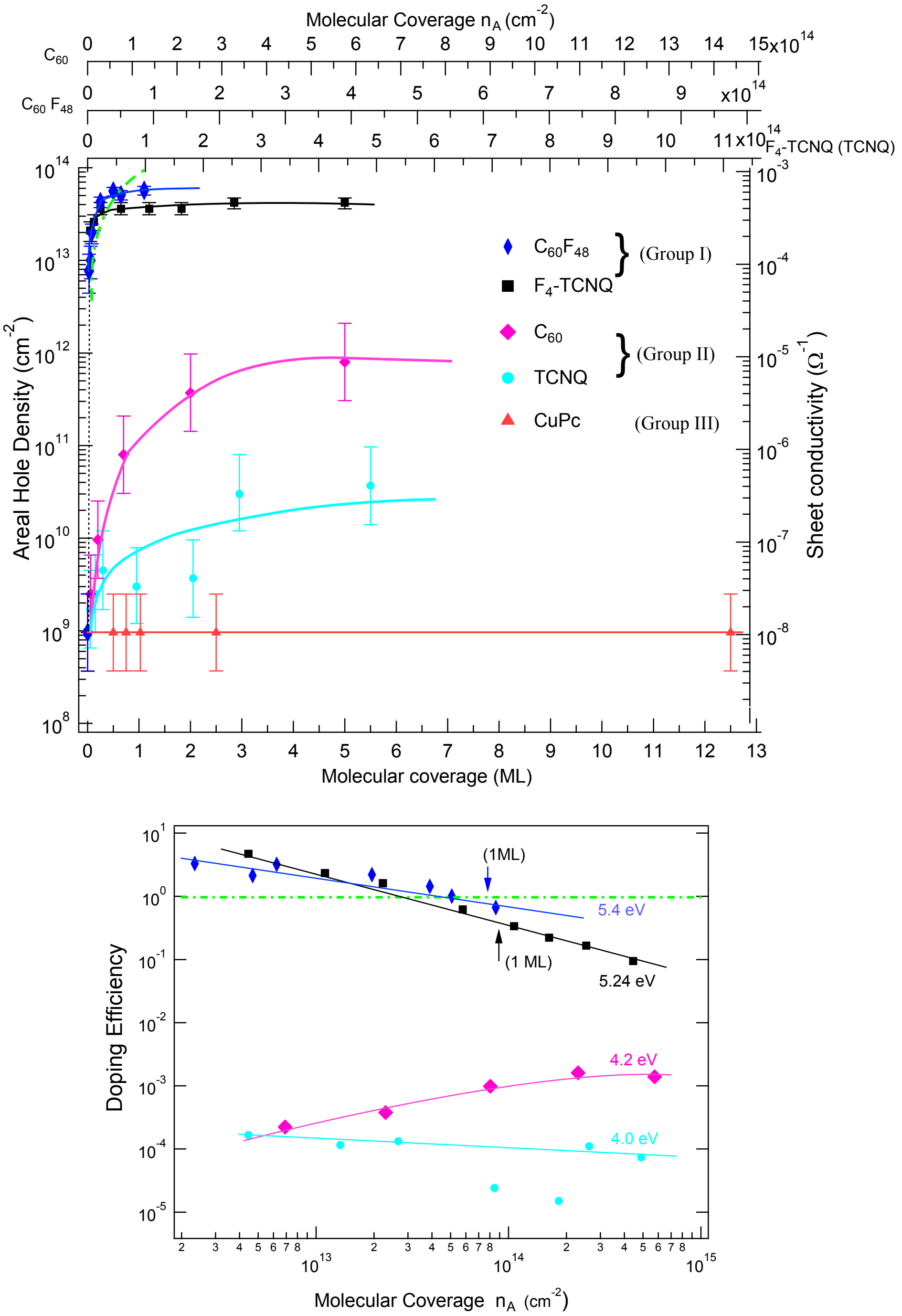

Figure 6.22. Top: calculated areal hole density and sheet conductivity at diamond surface induced by adsorption of organic molecules as a function of molecular coverage. A small areal hole density is present in pristine diamond due to moderate boron doping. The error bars are derived from the uncertainty in u_S. **Bottom:** doping efficiency as a function of molecular coverage. The green dashed lines in both panels represent doping efficiency equal to 1. The figures in the graph indicate the EA of molecules in *condensed phase*. The lines through markers are only guides for the eyes only.

The conversions from nominal thickness to ML for F_4-TCNQ, TCNQ and CuPc are achieved by assuming an average interlayer distance of 4 Å with lying down molecular orientation. This conversion is approximate especially when the growth mode deviates from layer by layer, but it nevertheless qualitatively illustrates the dependence of surface transfer doping on molecular coverage. The molecular density of 1 ML TCNQ has been estimated previously on Cu(111) to be about one molecule for every 20 surface copper atoms [288], which amounts to 8.9×10^{13} cm^{-2}. The resulting density is several times smaller than that of TCNQ single crystals (e.g. *ac* plane) [289], because the electrostatic repulsion between negatively charged anions tends to increase the neighboring molecular spacing. We use this density value to convert ML coverage to areal density for both TCNQ and F_4-TCNQ. For C_{60} and $C_{60}F_{48}$, a ML corresponds to a coverage of 1.15×10^{14} fullerene molecules/cm^2 and 7.8×10^{13} $C_{60}F_{48}$ molecules/cm^2 [248].

As seen in Figure 6.22, the doping behavior of different molecular acceptors studied can be divided into three groups according to the maximum areal hole density induced in diamond. In *group I*, F_4-TCNQ and $C_{60}F_{48}$ represents highly effective surface transfer dopants with the highest doping yield. The maximum areal hole density induced by these dopants reaches as high as 4×10^{13} cm^{-2} (F_4-TCNQ) and 6×10^{13} cm^{-2} ($C_{60}F_{48}$), over 4 orders of magnitude higher than the intrinsic hole concentration of boron-doped diamond. The saturated areal hole density induced by $C_{60}F_{48}$, which is slightly larger than that of F_4-TCNQ, is similar to the value derived from direct sheet conductivity measurements on $C_{60}F_{48}$ covered diamond surface [248], and is considerably higher than that observed under atmospheric conditions [202-206].

Group II consists of C_{60} and TCNQ with moderate surface transfer doping ability. The doping yield is in the range of 10^{10} to 10^{12} cm^{-2}. Although the induced hole densities are several orders smaller than those in *group I*, they are still significantly larger than that of pristine diamond. C_{60} has a higher doping yield; the saturated hole density after the formation of several monolayers of fullerite reaches 10^{12} cm^{-2}, consistent with the conductivity measurements on the same system [248]. The induced hole density and hence SC is at a level comparable to that induced by natural atmospheric species.

CuPc belongs to *group III*, and cannot induce hole accumulation in diamond at all. The distinct doping behavior of these three groups are consistent with their EA values. *Group I* molecules have EAs (condensed phase) above 5 eV, much larger than the IP of diamond, whereas *group III* molecules have EAs (condensed phase) smaller than 3 eV, well below diamond IP. *Group II* molecules with intermediate doping ability between *group I* and *III*, have EAs (condensed phase) close to diamond IP.

In addition to the different doping yield by these molecular adsorbates, their dependences of hole density on molecular coverage also reveal significant dissimilarities. The areal hole densities induced by F_4-TCNQ and $C_{60}F_{48}$ rises sharply to 10^{13} cm^{-2} at a few 10^{-2} of a monolayer, and reach saturation below 0.5 ML. Although the lowest deposited coverage in the present study is limited to slightly over 0.01 ML, it is reasonable to deduce that even smaller amounts of isolated molecules can induce significant surface transfer doping of diamond. Their ability to accept electrons in molecular form endorse their superior surface transfer doping efficiencies, and is related with their large *gas phase* EA which is already close to diamond IP. In contrast, for *group II* acceptors such as TCNQ and C_{60}, the induced areal hole densities in diamond increase slowly with molecular coverage, and the saturation doping yield is reached only after several monolayers are formed. This observation is consistent with the increase of EA that accompanies the formation of the solid phase [247]. Therefore, for *group II* molecules, realizing effective surface transfer doping of diamond relies on molecular ensembles rather than individual molecules.

The different doping abilities of the four studied molecular acceptors are best visualized by their doping efficiencies shown in the bottom panel of Figure 6.22. The doping efficiency is calculated from the doping yield (after subtracting the intrinsic hole density of pristine diamond) divided by the areal density of surface acceptors. Figure 6.22 clearly separates the *group I* and *group II* acceptors. The doping efficiency of *group I* molecules (F_4-TCNQ and $C_{60}F_{48}$) is close to one as expected from the complete charge transfer to individual molecules. Although the calculated doping efficiency is larger than 1 at low molecular coverages, it is unlikely that each molecules can accept more than one electron from diamond due to the large Coulomb repulsion in molecular systems [281]. The discrepancy is attributed to the uncertainty in the estimation of molecular coverage particularly at very low coverage.

In contrast, the doping efficiency of *group II* acceptors (C_{60} and TCNQ) is far below one, in agreement with their doping behavior. The dependence of doping efficiency on molecular coverage is also different for different molecules. For F_4-TCNQ and $C_{60}F_{48}$, the doping efficiency decreases with increasing coverage, whereas it remains almost constant or even increases with increasing TCNQ or C_{60} coverage. The different dependences on coverage is easy to understand since only molecules in the submonolayer contribute to surface transfer doping for *group I* acceptors, whereas the entire molecular films take part in the doping process for *group II* acceptors.

The above analysis points to the important relationship between surface transfer doping ability of a molecular acceptor and its EA. The higher the EA for a molecular acceptor, the higher is its doping ability in terms of its doping yield and doping efficiency. Furthermore, if the molecular EA in *gas phase* is close to diamond IP ($\Delta <$ 0.4 eV), they can act as effective surface acceptors even in isolated molecular form. Otherwise, the forming of molecular films is necessary to effectively dope diamond surface. If the EA in *condensed phase* is more than 1 eV smaller than diamond IP, the surface transfer doping cannot be achieved. It is, however, difficult to quantitatively model this relationship from the present study. More studies on a wider range of molecules with well determined EA values are needed to develop a reliable and predictive model.

6.3 Chapter summary

In this chapter, we demonstrated the surface transfer doping scheme as a promising route to achieve controllable and nanoscale doping of diamond surface. Five potential *p*-type molecular acceptors (F_4-TCNQ, TCNQ, C_{60}, $C_{60}F_{48}$ and CuPc) adsorbed on hydrogenated diamond (001) surface are carefully investigated by PES and classified into three groups based on their doping behavior. F_4-TCNQ and $C_{60}F_{48}$ induce substantial surface transfer doping of diamond even at submonolayer coverage, leaving a hole accumulation layer with an high areal hole density of over 10^{13} cm^{-2} on diamond. The interfacial charge transfer caused by TCNQ and C_{60} adsorption is lower than their fluorinated counterparts, and the formation of molecular thin films with several monolayer thicknesses is necessary to yield sufficiently high EA to initiate electron transfer from diamond. Finally, the adsorption of CuPc up to several tens of monolayers does not cause observable surface transfer doping of diamond, indicating its inability as an effective surface acceptor. The distinct surface transfer doping efficiencies of these three representative molecular groups are closely related to their EA in both *gas phase* and *condensed phase*, which in turn determines the relative alignment of molecular LUMO and diamond VBM.

Controllable surface transfer doping using carefully selected surface acceptors opens a new route to engineer the SC of diamond for a wide range of applications. Strong surface transfer dopants such as F_4-TCNQ and $C_{60}F_{48}$ can efficiently induce very high hole concentration in diamond with sheet conductivities well above 10^{-4} Ω^{-1}. On the other hand, moderate surface dopants such as C_{60} and TCNQ can achieve controllable low doping levels with surface conductivities between 10^{-7} to 10^{-4} Ω^{-1}.

CHAPTER 7

CONLUSIONS AND OUTLOOK

7.1 Thesis summary

The work presented herein aims to study the adsorption of organic molecules on diamond (001) by synchrotron based spectroscopies. Two important surface terminations of diamond — bare and hydrogenated — are investigated, and exhibit distinct interactions with adsorbed molecules. Focus is given to the electronic structure, electronic properties and energy level alignment at different diamond/organic heterojunction interfaces, revealing important implications for the development of diamond-based electronic devices.

First, the structural and electronic properties of hydrogenated and bare diamond (001) surfaces are characterized in Chapter 3. LEED and STM confirm the 2×1 reconstruction due to surface dimers on both surfaces with two orthogonally oriented 2×1 domains. The surface states originating from π-bonded dimers of bare diamond are clearly revealed by PES in both core-level and valence band domains. The associated unoccupied surface states with excitonic nature are also identified in the pre-edge NEXAFS spectra with significant polarization-dependence. In contrast, the surface states from hydrogenated surface dimers cannot observed by PES due to overlap with bulk diamond components. Nevertheless, the surface resonance associated with C1s→σ* resonant transitions within the surface C-H bonds is revealed by NEXAFS. The hydrogen termination passivates the π-bonded dimers of bare diamond, leading to the inert nature of hydrogenated diamond. The heteropolar C-H bonds create a surface dipole layer with an electrostatic potential step as large as 1.9 eV which effectively lowers the diamond vacuum level below the CBM, leading to the unique NEA (χ = - 1.1 eV) property of hydrogenated diamond. Consequently, hot electrons excited into diamond conduction bands accumulate at CBM through inelastic scattering and escape into vacuum without experiencing any energy barrier at the surface, giving rise to a sharp and intense secondary electron emission peak at the low kinetic energy region of PES spectra.

The π-bonded dimers on bare diamond (001) suggest susceptibility towards cycloaddition reaction with alkene-containing organic molecules, which is the topic of Chapter 4. The surface functionalization of diamond by 1,3-butadiene, an archetypical organic molecule, is studied by a combination of PES, NEXAFS and DFT calculations. The quenching of surface states (both occupied and unoccupied) upon molecular adsorption confirms the Diels-Alder reaction which involves the breaking of π-bonds and the formation of cyclohexene-like ring structures. Accompanying the interfacial chemical reaction is a significant reduction up to 0.7 eV of electron affinity and an enhancement of secondary electron emission. With the help of DFT calculations, we propose that the terminal C—H bonds in the covalently bonded organics on diamond give rise to a surface dipole that contributes to the tuning effect on diamond electron affinity and electron emission.

Functionalization of diamond with π-conjugated organic semiconductors represents a promising route to the integration of molecular electronics with diamond technology. Chapter 5 investigates the model planar organic semiconductor CuPc on hydrogenated and bare diamond surfaces. Significant dissimilarities have been found between these two substrates in terms of interfacial interactions, energy level alignment, and supramolecular organizations. CuPc molecules interact weakly with hydrogenated diamond surface *via* Van-der-Waals interactions without chemical reactions and charge transfer occurring at the interface. NEXAFS reveals that the molecules lie flat throughout growth with a high degree of order as a result of competing molecule-substrate interactions and intermolecular interactions. In contrast, CuPc are covalently attached to bare diamond dimers. PES shows the electron affinity of diamond is transformed from positive to negative with greatly enhanced secondary electron emission yield. This altering in diamond surface electronic properties is proposed to be due to an intramolecular dipole layer created by reacted molecules through distortion of the molecular plane, as well as the energy level bendings as a result of interfacial charge transfer. A novel electron emission process from diamond through covalently attached molecules to vacuum is described to explain the evolution of secondary electron emission profiles. Finally, the molecular orientation on bare diamond experiences a transition from lying-down at submonolayer coverage to standing-up in multilayers, accompanied by an order-disorder-order transition during growth. The switch from dominant molecule-substrate covalent interactions in the first monolayer to weak intermolecular interactions in multilayers accounts for the observed transition.

The last results chapter deals with charge transfer across the interface between hydrogenated diamond (001) and organic molecules. Surface transfer doping by organic molecules, which relies on this charge transfer, holds the promise of overcoming the doping difficulties of diamond and to achieve controllable nanoscale doping of the diamond surface. Five potential *p*-type molecular acceptors with varying electron affinities (F_4-TCNQ, TCNQ, C_{60}, $C_{60}F_{48}$ and CuPc) adsorbed on hydrogenated diamond (001) are carefully examined by PES and they are classified into three groups based on their doping behaviors. F_4-TCNQ and $C_{60}F_{48}$ can readily induce substantial electron transfer from diamond valence bands to molecular LUMOs even in their isolated molecular form, leaving a hole accumulation layer with an ultra-high areal hole density over 10^{13} cm^{-2} on diamond surface. The interfacial charge transfer caused by TCNQ and C_{60} adsorption is much less significant than their fluorinated counterpart, and the formation of solid-phase molecular thin films is a prerequisite to initiate electron transfer from diamond. Finally, the adsorption of CuPc up to several tens of monolayers does not cause observable surface transfer doping, indicating its ineffectiveness as molecular acceptors. The distinct surface transfer doping efficiencies of these three representative molecule groups are closely related to their electron affinity in both gas phase and condensed phase, which determines the relative alignment of molecular LUMO and diamond VBM. It is also worth mentioning that we have also successfully applied this novel doping scheme to achieve nondestructive, controllable doping of other semiconductor system including graphene and organic thin films [290-291], where conventional ion implantation method fails.

7.2 Future work

For pristine diamond surfaces, controversies still exist. Regarding the nature and origins of two surface resonances which show opposite polarization dependences with incident light direction, NEXAFS of *n*-type diamond would be helpful to discriminate between surface core-excitons and normal resonant transitions.

Although the interfacial electronic properties of 1,3-butadiene on bare diamond (001)-2×1 are now understood, the current understanding is based on macroscopic measurement techniques which lacks atomic-scale insights. STM imaging of the reacted surface with atomic resolution would be helpful to confirm the bonding geometry as predicted by DFT calculations. Important information such as molecular coverage and distribution would also be acquired. In particular, the diamond surface dimers with 2×1 symmetry could potentially provide a template allowing ordered self-assemblies of small organic molecules.

Future work involving more sophisticated DFT modeling and molecular dynamics (MD) simulation to understand the reaction scheme and bonding geometry of CuPc on bare diamond is needed. Although the complex structure of CuPc molecule and its numerous unsaturated bonds would apparently present many challenges to the theoretical modeling of its interaction with diamond, STM imaging could reduce the possible molecular configurations and reaction sites, thereby easing the calculation complexity.

For simple organics and organic semiconductors absorption on bare diamond surfaces, we observed lowered electron affinities with enhanced and narrowly distributed secondary electron emissions. This effect could potentially be exploited to develop diamond-based cold cathode or field-emission devices as an alternative to conventional hydrogenated diamond. Field-emission measurements would be needed to characterize these functionalized surfaces, providing important device-related parameters such as threshold voltage and emission current density. In particular, the stability of the functionalized surface, especially after it is exposed to air, would be vital for practical device operations.

Although we provide direct spectroscopic evidence for diamond *p*-type surface transfer doping of diamond, the areal hole density in diamond is indirectly estimated from diamond energy levels (i.e. the energy difference between VBM and Fermi level). Transport measurements (e.g. Hall measurement) in a device-like architecture would be necessary to reliably determine electrical characteristics (e.g. charge carrier type and concentration, carrier mobility) of the surface conductive channel, so that the surface transfer doping scheme can be validated in practice.

Future work on surface transfer doping should also involve the immobilization of molecular acceptors on diamond surface in order to enhance their thermal stability.

Although the charge transfer process by surface acceptors such as F_4-TCNQ and $C_{60}F_{48}$ is effective, a challenge for practical application is the rather weak bonding (usually in the form of physisorption) between surface acceptors and diamond surface, leading to thermal stability issues [249]. Strategies such as using dielectric capping layers [249] and photon assisted polymerization of organic overlayers [292] can potentially improve the thermal stability. A better solution would be to combine the organic functionalization of diamond and surface transfer doping by covalently attaching surface dopants on a hydrogenated diamond surface. This premise was recently demonstrated on a hydrogen-terminated diamond surface with hydroxyl functional groups [293].

Last but not least, only *p*-type surface conductivity of diamond is achieved in this work. For the realization of more advanced diamond surface-channel bipolar devices such LED and CMOS, *n*-type surface transfer doping is indispensible. Alkali metal donors such as potassium, and novel molecular donors such as cobaltocene ($CoCp_2$) [294-295] and pyronin B (PyB) [296] are potential candidates.

BIBLIOGRAPHY

[1] C. Sagan, and J. Agel, *The cosmic connection* (Anchor Press Garden City, NY, 1973).

[2] Created by Michael Ströck http://en.wikipedia.org/wiki/-File:Eight_Allotropes_of_Carbon.png

[3] J. Singh, *Physics of semiconductors and their heterostructures* (McGraw-Hill New York, 1993).

[4] K. Spear, and J. Dismukes, *Synthetic Diamond: Emerging CVD Science and Technology* (Wiley-Interscience, 1994).

[5] R. Davis, *Diamond Films and Coatings: Development, Properties, and Applications* (Noyes Publications, 1993).

[6] L. S. Pan, and D. R. Kania, *Diamond: Electronic Properties and Applications* (Kluwer Academic Publishers, Boston, 1995).

[7] S. M. Sze, *Physics of Semiconductor Devices* (Wiley, New York, 1981).

[8] D. Lide, *CRC handbook of chemistry and physics: A Ready-Reference Book of Chemical and Physical Data* (CRC Press, 2004).

[9] Y. V. Pelskov, A. Y. Sakharova, M. D. Krotova, L. L. Bouilov, and B. V. Spitsyn, *Photoelectrochemical properties of semiconductor diamond*, J. Electroanal. Chem. **228**, 19 (1987).

[10] W. Yang *et al.*, *DNA-modified nanocrystalline diamond thin-films as stable, biologically active substrates*, Nat. Mater. **1**, 253 (2002).

[11] C. E. Nebel, B. Rezek, D. Shin, H. Uetsuka, and N. Yang, *Diamond for bio-sensor applications*, J. Phys. D: Appl. Phys., 6443 (2007).

[12] A. Hartl *et al.*, *Protein-modified nanocrystalline diamond thin films for biosensor applications*, Nat. Mater. **3**, 736 (2004).

[13] W. M. Paul, *Diamond thin films: a 21st-century material*, Phil. Trans. R. Soc. Lond. A **358**, 473 (2000).

[14] C. J. H. Wort, and R. S. Balmer, *Diamond as an electronic material*, Mater. Today **11**, 22 (2008).

[15] R. Kalish, *Diamond as a unique high-tech electronic material: difficulties and prospects*, J. Phys. D: Appl. Phys. **40**, 6467 (2007).

[16] J. Isberg *et al.*, *High Carrier Mobility in Single-Crystal Plasma-Deposited Diamond*, Science **297**, 1670 (2002).

[17] S. Koizumi, K. Watanabe, M. Hasegawa, and H. Kanda, *Ultraviolet Emission from a Diamond pn Junction*, Science **292**, 1899 (2001).

[18] R. J. Tapper, *Diamond detectors in particle physics*, Rep. Prog. Phys., 1273 (2000).

[19] W. Adam *et al.*, *The development of diamond tracking detectors for the LHC*, Nucl. Instrum. Methods A **514**, 79 (2003).

[20] A. A. Rouse, J. B. Bernhard, E. D. Sosa, and D. E. Golden, *Variation of field emission and photoelectric thresholds of diamond films with average grain size*, Appl. Phys. Lett. **75**, 3417 (2006).

[21] G. T. Mearini, I. L. Krainsky, Y. X. Wang, J. A. Dayton Jr, R. Ramesham, and M. F. Rose, *Fabrication of an electron multiplier utilizing diamond films*, Thin Solid Films **253**, 151 (1994).

[22] M. W. Geis *et al.*, *A new surface electron-emission mechanism in diamond cathodes*, Nature **393**, 431 (1998).

[23] F. Maier, M. Riedel, B. Mantel, J. Ristein, and L. Ley, *Origin of surface conductivity in diamond*, Phys. Rev. Lett. **85**, 3472 (2000).

[24] P. Gluche, A. Aleksov, A. Vescan, W. Ebert, and E. Kohn, *Diamond surface-channel FET structure with 200 V breakdown voltage*, Electron Device Letters, IEEE **18**, 547 (1997).

[25] B. Rezek, H. Watanabe, D. Shin, T. Yamamoto, and C. E. Nebel, *Ion-sensitive field effect transistor on hydrogenated diamond*, Diamond Relat. Mater. **15**, 673 (2006).

[26] D. Awschalom, R. Epstein, and R. Hanson, *The Diamond Age of Spintronics*, Scientific American **297**, 84 (2007).

[27] Z. Ma, and F. Zaera, *Organic chemistry on solid surfaces*, Surf. Sci. Rep. **61**, 229 (2006).

[28] F. Rosei *et al.*, *Properties of large organic molecules on metal surfaces*, Prog. Surf. Sci. **71**, 95 (2003).

[29] J. Buriak, *Organometallic Chemistry on Silicon and Germanium Surfaces*, Chem. Rev. **102**, 1271 (2002).

[30] S. R. Forrest, *The path to ubiquitous and low-cost organic electronic appliances on plastic*, Nature **428**, 911 (2004).

[31] S. F. Bent, *Organic functionalization of group IV semiconductor surfaces: principles, examples, applications, and prospects*, Surf. Sci. **500**, 879 (2002).

[32] J. M. Buriak, *Diamond Surfaces: Just Big Organic Molecules?*, Angew. Chem. Int. Ed. **40**, 532 (2001).

[33] G. Binnig, H. Rohrer, C. Gerber, and E. Weibel, *Tunneling through a controllable vacuum gap*, Appl. Phys. Lett. **40**, 178 (1982).

[34] M. Van Hove, W. Weinberg, and C. Chan, *Low-energy Electron Diffraction: Experiment, Theory, and Surface Structure Determination* (Springer-Verlag, 1986).

[35] S. Hüfner, *Photoelectron Spectroscopy: Principles and Applications* (Springer, 2003).

[36] A. Enstein, Ann. Phys. **17**, 132 (1905).

[37] C. Berglund, and W. Spicer, *Photoemission Studies of Copper and Silver: Theory*, Phys. Rev. **136**, 1030 (1964).

[38] D. P. Woodruff, and T. A. Delchar, *Modern Techniques of Surface Science* (Cambridge University Press, 1994).

[39] J. Braun, *The theory of angle-resolved ultraviolet photoemission and its applications to ordered materials*, Rep. Prog. Phys. **59**, 1267 (1996).

[40] PES set-up illustration is adapted from source: http://en.wikipedia.org/wiki/X-ray_photoelectron_spec-troscopy

[41] J. Stöhr, *NEXAFS spectroscopy* (Springer, Berlin, 1992).

[42] B. D. Thoms, and J. E. Butler, *HREELS and LEED of H/C(100): the 2 × 1 monohydride dimer row reconstruction*, Surf. Sci. **328**, 291 (1995).

[43] B. D. Thoms, M. S. Owens, J. E. Butler, and C. Spiro, *Production and characterization of smooth, hydrogen-terminated diamond C(100)*, Appl. Phys. Lett. **65**, 2957 (1994).

[44] R. Stallcup, and J. Perez, *Scanning Tunneling Microscopy Studies of Temperature-Dependent Etching of Diamond (100) by Atomic Hydrogen*, Phys. Rev. Lett. **86**, 3368 (2001).

[45] S.-G. Ri, H. Watanabe, M. Ogura, D. Takeuchi, S. Yamasaki, and H. Okushi, *Hydrogen plasma etching mechanism on (0 0 1) diamond*, J. Cryst. Growth **293**, 311 (2006).

[46] X. J. Yu *et al.*, *New soft X-ray facility SINS for surface and nanoscale science at SSLS*, J. Electron. Spectrosc. Relat. Phenom. **144**, 1031 (2005).

[47] M. P. Seah, and W. A. Dench, *Quantitative electron spectroscopy of surfaces: A standard data base for electron inelastic mean free paths in solids*, Surf. Interface Anal. **1**, 2 (1979).

[48] Synchrotron Soleil http://en.wikipedia.org/wiki/File:Sch%-C3%A9ma_de_principe_du_synchrotron.jpg

[49] http://www.spring8.or.jp/en/about_us/sr/principle/publicfolder_view

[50] *http://ssls.nus.edu.sg*.

[51] H. O. Moser *et al.*, *Singapore Synchrotron Light Source - Status, first results, program*, Nucl. Instrum. Methods B **199**, 536 (2003).

[52] H. Lüth, *Solid Surfaces, Interfaces and Thin Films* (Springer Verlag, New York, 2001).

[53] W. Mönch, *Semiconductor Surfaces and Interfaces* (Springer, New York, 2001).

[54] A. V. Hamza, G. D. Kubiak, and R. H. Stulen, *Hydrogen chemisorption and the structure of the diamond C(100)-(2×1) surface*, Surf. Sci. **237**, 35 (1990).

[55] J. Furthmüller, J. Hafner, and G. Kresse, *Dimer reconstruction and electronic surface states on clean and hydrogenated diamond (100) surfaces*, Phys. Rev. B **53**, 7334 (1996).

[56] Y. M. Wang *et al.*, *Recent studies on diamond surfaces*, Diamond Relat. Mater. **9**, 1582 (2000).

[57] S. J. Sque, R. Jones, and P. R. Briddon, *Structure, electronics, and interaction of hydrogen and oxygen on diamond surfaces*, Phys. Rev. B **73**, 085313 (2006).

[58] K. Bobrov, A. J. Mayne, A. Hoffman, and G. Dujardin, *Atomic-scale desorption of hydrogen from hydrogenated diamond surfaces using the STM*, Surf. Sci. **528**, 138 (2003).

[59] R. Graupner, F. Maier, J. Ristein, L. Ley, and C. Jung, *High-resolution surface-sensitive C 1s core-level spectra of clean and hydrogen-terminated diamond (100) and (111) surfaces*, Phys. Rev. B **57**, 12397 (1998).

[60] K. Bobrov, G. Comtet, G. Dujardin, and L. Hellner, *Electronic structure of the hydrogenated diamond C(1 0 0)-(2×1):H surface*, Surf. Sci. **482-485**, 437 (2001).

[61] F. Maier, J. Ristein, and L. Ley, *Electron affinity of plasma-hydrogenated and chemically oxidized diamond (100) surfaces*, Phys. Rev. B **64**, 165411 (2001).

[62] L. Diederich, P. Aebi, O. M. Kuttel, and L. Schlapbach, *NEA peak of the differently terminated and oriented diamond surfaces*, Surf. Sci. **424**, 314 (1999).

[63] C. Bandis, and B. B. Pate, *Photoelectric emission from negative-electron-affinity diamond (111) surfaces: Exciton breakup versus conduction-band emission*, Phys. Rev. B **52**, 12056 (1995).

[64] R. L. Bell, *Negative Electron Affinity Devices* (Clarendon Press, Oxford, 1973).

[65] F. J. Himpsel, J. A. Knapp, J. A. VanVechten, and D. E. Eastman, *Quantum photoyield of diamond (111)- A stable negative-affinity emitter*, Phys. Rev. B **20**, 624 (1979).

[66] J. van der Weide, Z. Zhang, P. K. Baumann, M. G. Wensell, J. Bernholc, and R. J. Nemanich, *Negative-electron-affinity effects on the diamond (100) surface*, Phys. Rev. B **50**, 5803 (1994).

[67] L. Diederich, O. M. Kuttel, P. Aebi, and L. Schlapbach, *Electron affinity and work function of differently oriented and doped diamond surfaces determined by photoelectron spectroscopy*, Surf. Sci. **418**, 219 (1998).

[68] J. B. Cui, J. Ristein, and L. Ley, *Electron Affinity of the Bare and Hydrogen Covered Single Crystal Diamond (111) Surface*, Phys. Rev. Lett. **81**, 429 (1998).

[69] D. Takeuchi *et al.*, *Direct observation of negative electron affinity in hydrogen-terminated diamond surfaces*, Appl. Phys. Lett. **86**, 152103 (2005).

[70] I. L. Krainsky, V. M. Asnin, G. T. Mearini, and J. A. Dayton Jr, *Negative-electron-affinity effect on the surface of chemical-vapor-deposited diamond polycrystalline films*, Phys. Rev. B **53**, 7650 (1996).

[71] G. T. Wang, S. F. Bent, J. N. Russell, J. E. Butler, and M. P. D'Evelyn, *Functionalization of diamond(100) by Diels-Alder chemistry*, J. Am. Chem. Soc. **122**, 744 (2000).

[72] J. E. Yater, A. Shih, and R. Abrams, *Electron transport and emission properties of C (100)*, Phys. Rev. B **56**, 4410 (1997).

[73] S. Kono *et al.*, *UHV μ-electron beam evaluation of the CVD diamond particles grown on Si (001)*, Diamond Relat. Mater. **10**, 48 (2001).

[74] M. J. Rutter, and J. Robertson, *Ab initio calculation of electron affinities of diamond surfaces*, Comput. Mater. Sci. **10**, 330 (1998).

[75] Z. Zhang, M. Wensell, and J. Bernholc, *Surface structures and electron affinities of bare and hydrogenated diamond C (100) surfaces*, Phys. Rev. B **51**, 5291 (1995).

[76] J. F. Morar, F. J. Himpsel, G. Hollinger, G. Hughes, and J. L. Jordan, *Observation of a C-1s Core Exciton in Diamond*, Phys. Rev. Lett. **54**, 1960 (1985).

[77] K. Bobrov, G. Comtet, G. Dujardin, L. Hellner, P. Bergonzo, and C. Mer, *Surface electronic states of the partially hydrogenated diamond C (100)-(2×1): H surface*, Phys. Rev. B **63**, 165421 (2001).

[78] R. Graupner, J. Ristein, L. Ley, and C. Jung, *Surface-sensitive K-edge absorption spectroscopy on clean and hydrogen-terminated diamond (111) and (100) surfaces*, Phys. Rev. B **60**, 17023 (1999).

[79] A. Hoffman, G. Comtet, L. Hellner, G. Dujardin, and M. Petravic, *Surface near-edge x-ray adsorption fine structure of hydrogenated diamond films and Di (100) surfaces studied by H^+ and H^- ion desorption*, Appl. Phys. Lett. **73**, 1152 (1998).

[80] J. F. Morar, F. J. Himpsel, G. Hollinger, J. L. Jordon, G. Hughes, and F. R. McFeely, *C 1s excitation studies of diamond (111). II. Unoccupied surface states*, Phys. Rev. B **33**, 1346 (1986).

[81] R. Nakajima, J. Stöhr, and Y. U. Idzerda, *Electron-yield saturation effects in L-edge x-ray magnetic circular dichroism spectra of Fe, Co, and Ni*, Phys. Rev. B **59**, 6421 (1999).

[82] J. Ristein, W. Stein, and L. Ley, *Defect Spectroscopy and Determination of the Electron Diffusion Length in Single Crystal Diamond by Total Photoelectron Yield spectroscopy*, Phys. Rev. Lett. **78**, 1803 (1997).

[83] B. L. Henke, E. M. Gullikson, and J. C. Davis, *X-Ray Interactions: Photoabsorption, Scattering, Transmission, and Reflection at E = 50-30,000 eV, Z = 1-92*, At. Data Nucl. Data Tables **54**, 181 (1993).

[84] K. Bobrov, A. J. Mayne, and G. Dujardin, *Atomic-scale imaging of insulating diamond through resonant electron injection*, Nature **413**, 616 (2001).

[85] J. Wu, R. Cao, X. Yang, P. Pianetta, and I. Lindau, *Photoemission study of diamond (100) surface*, J. Vac. Sci. Technol., A **11**, 1048 (1993).

[86] G. Francz, and P. Oelhafen, *Photoelectron spectroscopy of the annealed and deuterium-exposed natural diamond (100) surface*, Surf. Sci. **329**, 193 (1995).

[87] R. Graupner, M. Hollering, A. Ziegler, J. Ristein, L. Ley, and A. Stampfl, *Dispersions of surface states on diamond (100) and (111)*, Phys. Rev. B **55**, 10841 (1997).

[88] P. K. Baumann, and R. J. Nemanich, *Surface cleaning, electronic states and electron affinity of diamond (100), (111) and (110) surfaces*, Surf. Sci. **409**, 320 (1998).

[89] J. Topping, *On the Mutual Potential Energy of a Plane Network of Doublets*, Proceedings of the Royal Society of London. Series A, Containing Papers of a Mathematical and Physical Character **114**, 67 (1927).

[90] M. A. Filler, and S. F. Bent, *The surface as molecular reagent: organic chemistry at the semiconductor interface*, Prog. Surf. Sci. **73**, 1 (2003).

[91] S. Bent, *Organic functionalization of group IV semiconductor surfaces: principles, examples, applications, and prospects*, Surf. Sci **500**, 879 (2002).

[92] W. Carruthers, *Cycloaddition Reactions in Organic Synthesis* (Pergamon Pr, 1990).

[93] R. J. Hamers *et al.*, *Cycloaddition Chemistry of Organic Molecules with Semiconductor Surfaces*, Acc. Chem. Res. **33**, 617 (2000).

[94] R. B. Woodward, and R. Hoffmann, *The Conservation of Orbital Symmetry* (Academic Press, New York, NY, 1969).

[95] G. Lopinski, D. Moffatt, D. Wayner, and R. Wolkow, *How Stereoselective Are Alkene Addition Reactions on Si (100)?*, J. Am. Chem. Soc. **122**, 3548 (2000).

[96] C. B. Duke, *Semiconductor Surface Reconstruction: The Structural Chemistry of Two-Dimensional Surface Compounds*, Chem. Rev. **96**, 1237 (1996).

[97] M. Z. Hossain *et al.*, *Diels-Alder reaction on the clean diamond (100) 2×1 surface*, Jpn. J. Appl. Phys **38**, L1496 (1999).

[98] D. R. Fitzgerald, and D. J. Doren, *Functionalization of Diamond(100) by Cycloaddition of Butadiene: First-Principles Theory*, J. Am. Chem. Soc. **122**, 12334 (2000).

[99] J. S. Hovis, S. K. Coulter, R. J. Hamers, M. P. D'Evelyn, J. N. Russell, and J. E. Butler, *Cycloaddition Chemistry at Surfaces: Reaction of Alkenes with the Diamond (001)-2×1 Surface*, J. Am. Chem. Soc **122**, 732 (2000).

[100] T. Ouyang, X. Gao, D. C. Qi, A. T. S. Wee, and K. P. Loh, *Cycloadditions on Diamond (100) 2×1: Observation of Lowered Electron Affinity due to Hydrocarbon Adsorption*, J. Phys. Chem. B **110**, 5611 (2006).

[101] I. Borriello, G. Cantele, D. Ninno, G. Iadonisi, M. Cossi, and V. Barone, *Ab initio study of electron affinity variation induced by organic molecule adsorption on the silicon (001) surface*, Phys. Rev. B **76**, 035430 (2007).

[102] T. He *et al.*, *Silicon/Molecule Interfacial Electronic Modifications*, J. Am. Chem. Soc. **130**, 1699 (2008).

[103] R. E. Thomas, *Diamond for Electronic Applications*, in MRS Symposia Proceedings, edited by D. Dreifus *et al.*1996), p. 263.

[104] H. Ishii, K. Sugiyama, E. Ito, and K. Seki, *Energy Level Alignment and Interfacial Electronic Structures at Organic/Metal and Organic/Organic Interfaces*, Adv. Mater. **11**, 605 (1999).

[105] P. S. Bagus, V. Staemmler, and C. Wöll, *Exchangelike Effects for Closed-Shell Adsorbates: Interface Dipole and Work Function*, Phys. Rev. Lett. **89**, 96104 (2002).

[106] F. Diederich, and C. Thilgen, *Covalent Fullerene Chemistry*, Science **271**, 317 (1996).

[107] T. Ouyang, Kian Ping Loh, D.-C. Qi, Andrew Thye Shen Wee, and M. Nesladek, *Chemical Bonding of Fullerene and Fluorinated Fullerene on Bare and Hydrogenated Diamond*, ChemPhysChem **9**, 1286 (2008).

[108] G. Kresse, and J. FurthmAuller, *Efficient iterative schemes for ab initio total-energy calculations using a plane-wave basis set*, Phys. Rev. B **54**, 11169 (1996).

[109] G. Kresse, and J. FurthmAuller, *Efficiency of ab-initio total energy calculations for metals and semiconductors using a plane-wave basis set*, Comput. Mater. Sci. **6**, 15 (1996).

[110] H. Y. Hoh, K. P. Loh, M. B. Sullivan, and P. Wu, *Spatial Effect of C-H Dipoles on the Electron Affinity of Diamond (100)-21 Adsorbed with Organic Molecules*, ChemPhysChem **9**, 1338 (2008).

[111] F. Gutmann, and L. Lyons, *Organic Semiconductors*, New York (1967).

[112] M. Schwoerer, and H. C. Wolf, *Organic molecular solids* (Wiley-VCH Germany, 2007).

[113] P. Peumans, A. Yakimov, and S. R. Forrest, *Small molecular weight organic thin-film photodetectors and solar cells*, J. Appl. Phys. **93**, 3693 (2003).

[114] A. Hagfeldt, and M. Gratzel, *Molecular Photovoltaics*, Acc. Chem. Res. **33**, 269 (2000).

[115] H. E. Katz *et al.*, *A soluble and air-stable organic semiconductor with high electron mobility*, Nature **404**, 478 (2000).

[116] B. Crone *et al.*, *Large-scale complementary integrated circuits based on organic transistors*, Nature **403**, 521 (2000).

[117] C. D. Dimitrakopoulos, and P. R. L. Malenfant, *Organic Thin Film Transistors for Large Area Electronics*, Adv. Mater. **14**, 99 (2002).

[118] Z. H. Xiong, D. Wu, Z. Valy Vardeny, and J. Shi, *Giant magnetoresistance in organic spin-valves*, Nature **427**, 821 (2004).

[119] W. Chen *et al.*, *Molecular orientation of 3, 4, 9, 10-perylene-tetracarboxylic-dianhydride thin films at organic heterojunction interfaces*, Appl. Phys. Lett. **91**, 114102 (2007).

[120] W. Chen, H. Huang, S. Chen, X. Y. Gao, and A. T. S. Wee, *Low-Temperature Scanning Tunneling Microscopy and Near-Edge X-ray Absorption Fine Structure Investigations of Molecular Orientation of Copper(II) Phthalocyanine Thin Films at Organic Heterojunction Interfaces*, J. Phys. Chem. C **112**, 5036 (2008).

[121] W. Chen, S. Chen, H. Huang, D. C. Qi, X. Y. Gao, and A. T. S. Wee, *Molecular orientation dependent interfacial dipole at the F_{16}CuPc/CuPc organic heterojunction interface*, Appl. Phys. Lett. **92**, 063308 (2008).

[122] S. Heutz, G. Salvan, T. S. Jones, and D. R. T. Zahn, *Effects of Annealing on the Properties of Molecular Thin Film Heterostructures*, Adv. Mater. **15**, 1109 (2003).

[123] S. Yim, S. Heutz, and T. S. Jones, *Influence of intermolecular interactions on the structure of phthalocyanine layers in molecular thin film heterostructures*, Phys. Rev. B **67**, 165308 (2003).

[124] S. Heutz, R. Cloots, and T. S. Jones, *Structural templating effects in molecular heterostructures grown by organic molecular-beam deposition*, Appl. Phys. Lett. **77**, 3938 (2000).

[125] L. Chen, W. Chen, H. Huang, H. L. Zhang, J. Yuhara, and A. T. S. Wee, *Tunable Arrays of C_{60} Molecular Chains*, Adv. Mater. **20**, 484 (2008).

[126] H. L. Zhang *et al.*, *C_{60} Molecular Chains on alpha-Sexithiophene Nanostripes*, Small (2007).

[127] P. Peumans, S. Uchida, and S. R. Forrest, *Efficient bulk heterojunction photovoltaic cells using small-molecular-weight organic thin films*, Nature **425**, 158 (2003).

[128] J. Xue, B. P. Rand, S. Uchida, and S. R. Forrest, *A Hybrid Planar-Mixed Molecular Heterojunction Photovoltaic Cell*, Adv. Mater. **17**, 66 (2005).

[129] F. Yang, M. Shtein, and S. R. Forrest, *Controlled growth of a molecular bulk heterojunction photovoltaic cell*, Nat. Mater. **4**, 37 (2005).

[130] F. Yang, K. Sun, and S. R. Forrest, *Efficient Solar Cells Using All-Organic Nanocrystalline Networks*, Adv. Mater. **19**, 4166 (2007).

[131] R. R. Lunt, J. B. Benziger, and S. R. Forrest, *Growth of an Ordered Crystalline Organic Heterojunction*, Adv. Mater. **19**, 4229 (2007).

[132] A. Kahn, N. Koch, and W. Gao, *Electronic structure and electrical properties of interfaces between metals and pi-conjugated molecular films*, J. Polym. Sci., Part B: Polym. Phys. **41**, 2529 (2003).

[133] D. Cahen, and A. Kahn, *Electron Energetics at Surfaces and Interfaces: Concepts and Experiments*, Adv. Mater. **15**, 271 (2003).

[134] G. Witte, and C. Wöll, *Growth of aromatic molecules on solid substrates for applications in organic electronics*, J. Mater. Res. **19**, 1889 (2004).

[135] F. Schreiber, *Organic molecular beam deposition: Growth sudies beyond the first monolayer*, Phys. stat. sol. **201**, 1037 (2004).

[136] S. R. Forrest, *Ultrathin Organic Films Grown by Organic Molecular Beam Deposition and Related Techniques*, Chem. Rev. **97**, 1793 (1997).

[137] W. Herbst, and K. Hunger, *Industrial organic pigments : production, properties, applications* (Wiley-VCH, Weinheim ; New York, 1993), pp. xiv.

[138] C. D. Dimitrakopoulos, S. Purushothaman, J. Kymissis, A. Callegari, and J. M. Shaw, *Low-Voltage Organic Transistors on Plastic Comprising High-Dielectric Constant Gate Insulators*, Science **283**, 822 (1999).

[139] A. F. Hebard *et al.*, *Superconductivity at 18 K in potassium-doped C60*, Nature **350**, 600 (1991).

[140] A. Facchetti, *Semiconductors for organic transistors*, Mater. Today **10**, 28 (2007).

[141] N. B. McKeown, *Phthalocyanine materials : synthesis, structure, and function* (Cambridge University Press, New York, 1998), pp. xvi.

[142] A. L. Thomas, *Phthalocyanine research and applications* (CRC Press, Boca Raton, Fla., 1990), p. 283 p.

[143] C. C. Leznoff, and A. B. P. Lever, *Phthalocyanines : properties and applications* (Wiley-VCH, New York, 1989).

[144] F. Evangelista *et al.*, *Electronic structure of copper phthalocyanine: An experimental and theoretical study of occupied and unoccupied levels*, J. Chem. Phys. **126**, 124709 (2007).

[145] M.-S. Liao, and S. Scheiner, *Electronic structure and bonding in metal phthalocyanines, Metal=Fe, Co, Ni, Cu, Zn, Mg*, J. Chem. Phys **114**, 9780 (2001).

[146] J. E. Downes *et al.*, *Electronic structure near the Fermi level of the organic semiconductor copper phthalocyanine*, Chem. Phys. Lett. **390**, 203 (2004).

[147] O. Berger, W. Fischer, B. Adolphi, S. Tierbach, V. Melev, and J. Schreiber, *Studies on phase transformations of Cu-phthalocyanine thin films*, J. Mater. Sci.: Mater. Electron. **11**, 331 (2000).

[148] G. Koller *et al.*, *Intra- and Intermolecular Band Dispersion in an Organic Crystal*, Science **317**, 351 (2007).

[149] F. Rochet *et al.*, *Copper phthalocyanine on Si(111)-7 × 7 and Si(001)-2 × 1: an XPS/AES and STM study*, Surf. Sci. **319**, 10 (1994).

[150] M. Kanai, T. Kawai, K. Motai, X. D. Wang, T. Hashizume, and T. Sakura, *Scanning tunneling microscopy observation of copper-phthalocyanine molecules on Si(100) and Si(111) surfaces*, Surf. Sci. **329**, L619 (1995).

[151] G. Dufour *et al.*, *Copper phthalocyanine on Si(111)-7×7 and Si(001)-2×1 surfaces: an X-ray photoemission spectroscopy and synchrotron X-ray absorption spectroscopy study*, Surf. Sci. **319**, 251 (1994).

[152] L. Wang, D.-C. Qi, L. Liu, S. Chen, X. Gao, and A. T. S. Wee, *Molecular Orientation and Ordering during Initial Growth of Copper Phthalocyanine on Si(111)*, J. Phys. Chem. C **111**, 3454 (2007).

[153] O. V. Molodtsova, and M. Knupfer, *Electronic properties of the organic semiconductor interfaces CuPc/ C and C/ CuPc*, J. Appl. Phys. **99**, 053704 (2006).

[154] H. Peisert, M. Knupfer, T. Schwieger, J. M. Auerhammer, M. S. Golden, and J. Fink, *Full characterization of the interface between the organic semiconductor copper phthalocyanine and gold*, J. Appl. Phys. **91**, 4872 (2002).

[155] L. Lozzi, S. Santucci, S. La Rosa, B. Delley, and S. Picozzi, *Electronic structure of crystalline copper phthalocyanine*, J. Chem. Phys. **121**, 1883 (2004).

[156] H. Peisert, M. Knupfer, and J. Fink, *Electronic structure of partially fluorinated copper phthalocyanine ($CuPCF_4$) and its interface to Au (100)*, Surf. Sci. **515**, 491 (2002).

[157] M. Gorgoi, and D. R. T. Zahn, *"Band bending" in copper phthalocyanine on hydrogen-passivated Si (111)*, Org. Electron. **6**, 168 (2005).

[158] I. G. Hill, A. Kahn, Z. G. Soos, and J. R. A. Pascal, *Charge-separation energy in films of π-conjugated organic molecules*, Chem. Phys. Lett. **327**, 181 (2000).

[159] S. Kera, M. B. Casu, K. R. Bauchspiess, D. Batchelor, T. Schmidt, and E. Umbach, *Growth mode and molecular orientation of phthalocyanine molecules on metal single crystal substrates: A NEXAFS and XPS study*, Surf. Sci. **600**, 1077 (2006).

[160] O. V. Molodtsova, V. M. Zhilin, D. V. Vyalikh, V. Y. Aristov, and M. Knupfer, *Electronic properties of potassium-doped CuPc*, J. Appl. Phys. **98**, 093702 (2005).

[161] G. Baffou, A. J. Mayne, G. Comtet, G. Dujardin, P. Sonnet, and L. Stauffer, *Anchoring phthalocyanine molecules on the 6H-SiC(0001)3 x 3 surface*, Appl. Phys. Lett. **91**, 073101 (2007).

[162] L. Wang, S. Chen, D.-C. Qi, X. Gao, and A. T. S. Wee, *Shielding copper atoms by distortion of phthalocyanine ring on Si(1 1 1)*, Surf. Sci. **601**, 4212 (2007).

[163] M. L. M. Rocco, K. H. Frank, P. Yannoulis, and E. E. Koch, *Unoccupied electronic structure of phthalocyanine films*, J. Chem. Phys. **93**, 6859 (1990).

[164] J. C. Buchholz, and G. A. Somorjai, *The surface structures of phthalocyanine monolayers and vapor-grown films: A low-energy electron diffraction study*, J. Chem. Phys. **66**, 573 (1977).

[165] C. J. Brown, *Crystal structure of β-copper phthalocyanine*, J. Chem. Soc. A, 2488 (1968).

[166] H. Peisert *et al.*, *Order on disorder: Copper phthalocyanine thin films on technical substrates*, J. Appl. Phys. **90**, 466 (2001).

[167] S. R. Forrest, *Ultrathin Organic Films Grown by Organic Molecular Beam Deposition and Related Techniques*, Chem. Rev. **97**, 1793 (1997).

[168] F. Evangelista *et al.*, *Au (1 1 0) induced reconstruction by p conjugated molecules adsorption investigated by photoemission spectroscopy and low energy electron diffraction*, Surf. Sci. **566**, 79 (2004).

[169] T. H. Akira Yamashita, *Organic molecular beam deposition of metallophthalocyanines for opto-electronics applications*, Adv. Mater. **8**, 791 (1996).

[170] H. Peisert *et al.*, *Molecular orientation of substituted phthalocyanines: Influence of the substrate roughness*, Surf. Sci. **600**, 4024 (2006).

[171] I. Biswas *et al.*, *Buried interfacial layer of highly oriented molecules in copper phthalocyanine thin films on polycrystalline gold*, J. Chem. Phys. **126**, 174704 (2007).

[172] R. Resel, M. Ottmar, M. Hanack, J. Keckes, and G. Leising, *Preferred orientation of copper phthalocyanine thin films evaporated on amorphous substrates*, J. Mater. Res **15**, 935 (2000).

[173] A. Koma, *Molecular beam epitaxial growth of organic thin films*, Prog. Cryst. Growth Charact. Mater. **30**, 129 (1995).

[174] G. Kaindl, T. C. Chiang, D. E. Eastman, and F. J. Himpsel, *Distance-Dependent Relaxation Shifts of Photoemission and Auger Energies for Xe on Pd(001)*, Phys. Rev. Lett. **45**, 1808 (1980).

[175] H. Peisert, M. Knupfer, F. Zhang, A. Petr, L. Dunsch, and J. Fink, *Charge transfer and doping at organic/organic interfaces*, Appl. Phys. Lett. **83**, 3930 (2003).

[176] W. Chen, X. Y. Gao, D. C. Qi, S. Chen, Z. K. Chen, and A. T. S. Wee, *Surface-Transfer Doping of Organic Semiconductors Using Functionalized Self-Assembled Monolayers*, Adv. Funct. Mater. **17**, 1339 (2007).

[177] N. Ueno, K. Sugita, K. Seki, and H. Inokuchi, *Low-energy electron transmission and secondary-electron emission experiments on crystalline and molten long-chain alkanes*, Phys. Rev. B **34**, 6386 (1986).

[178] N. Ueno, K. Sugita, O. Koga, and S. Suzuki, *Radiation effect in hexatriacontane thin film*, Jpn. J. Appl. Phys. **22**, 1613 (1983).

[179] H. Ding *et al.*, *Spin injection and spin dynamics at the CuPc/GaAs interface studied with ultraviolet photoemission spectroscopy and two-photon photoemission spectroscopy*, Phys. Rev. B **78**, 075311 (2008).

[180] W. L. Yang *et al.*, *Monochromatic Electron Photoemission from Diamondoid Monolayers*, Science **316**, 1460 (2007).

[181] N. Koch, I. Salzmann, R. L. Johnson, J. Pflaum, R. Friedlein, and J. P. Rabe, *Molecular orientation dependent energy levels at interfaces with pentacene and pentacenequinone*, Org. Electron. **7**, 537 (2006).

[182] K. Ihm *et al.*, *Molecular orientation dependence of hole-injection barrier in pentacene thin film on the Au surface in organic thin film transistor*, Appl. Phys. Lett. **89**, 033504 (2006).

[183] S. Duhm *et al.*, *Orientation-dependent ionization energies and interface dipoles in ordered molecular assemblies*, Nat. Mater. **7**, 326 (2008).

[184] G. Witte, and C. Wöll, *Growth of aromatic molecules on solid substrates for applications in organic electronics*, J. Mater. Res. **19**, 1889 (2004).

[185] G. A. Jeffrey, *An Introduction to Hydrogen Bonding* (Oxford University Press, New York, 1997).

[186] M. Nishio, Y. Umezawa, K. Honda, S. Tsuboyama, and H. Suezawa, *CH/π hydrogen bonds in organic and organometallic chemistry*, CrystEngComm **11**, 1757 (2009).

[187] H. Jin, Y. Dai, R. Long, M. Guo, B. Huang, and R. Zhang, *First principles studies for formation mechanism and properties of ethylene molecule adsorbing on diamond (100) surface*, J. Chem. Phys. **128**, 114710 (2008).

[188] B. A. Fox *et al.*, *Diamond devices and electrical properties*, Diamond Relat. Mater. **4**, 622 (1995).

[189] L. G. Wang, and A. Zunger, *Phosphorus and sulphur doping of diamond*, Phys. Rev. B **66**, 161202 (2002).

[190] I. Sakaguchi *et al.*, *Sulfur: A donor dopant for n-type diamond semiconductors*, Phys. Rev. B **60**, R2139 (1999).

[191] E. B. Lombardi, A. Mainwood, and K. Osuch, *Interaction of hydrogen with boron, phosphorus, and sulfur in diamond*, Phys. Rev. B **70**, 205201 (2004).

[192] T. Miyazaki, H. Okushi, and T. Uda, *Shallow Donor State Due to Nitrogen-Hydrogen Complex in Diamond*, Phys. Rev. Lett. **88**, 066402 (2002).

[193] Z. Teukam *et al.*, *Shallow donors with high n-type electrical conductivity in homoepitaxial deuterated boron-doped diamond layers*, Nat. Mater. **2**, 482 (2003).

[194] R. Kalish, S. Dhar, and L. C. Feldman, *Depth profiles, surface damage and lattice location of boron/deuterium co-doped diamond*, Diamond Relat. Mater. **14**, 1600 (2005).

[195] R. Kalish, A. Reznik, C. Uzan-Saguy, and C. Cytermann, *Is sulfur a donor in diamond?*, Appl. Phys. Lett. **76**, 757 (2000).

[196] S. J. Sque, *Bulk and Transfer Doping oF Diamond*, thesis.

[197] N. Fujimori, T. Imai, and A. Doi, *Characterization of conducting diamond films*, Vacuum **36**, 99 (1986).

[198] S. N. Schauer, J. R. Flemish, R. Wittstruck, M. I. Landstrass, and M. A. Plano, *Phosphorus incorporation in plasma deposited diamond films*, Appl. Phys. Lett. **64**, 1094 (1994).

[199] M. Schwitiers *et al.*, *Diamond-MESFETs - synthesis and integration*, in Radar Conference (IEEE, Arlington Virginia, 2005), pp. 1.

[200] M. I. Landstrass, and K. V. Ravi, *Hydrogen passivation of electrically active defects in diamond*, Appl. Phys. Lett. **55**, 1391 (1989).

[201] M. I. Landstrass, and K. V. Ravi, *Resistivity of chemical vapor deposited diamond films*, Appl. Phys. Lett. **55**, 975 (1989).

[202] K. Hayashi, S. Yamanaka, H. Watanabe, T. Sekiguchi, H. Okushi, and K. Kajimura, *Investigation of the effect of hydrogen on electrical and optical properties in chemical vapor deposited on homoepitaxial diamond films*, J. Appl. Phys. **81**, 744 (1997).

[203] T. Maki, S. Shikama, M. Komori, Y. Sakaguchi, K. Sakuta, and T. Kobayashi, *Hydrogenating effect of single-crystal diamond surface*, Jpn. J. Appl. Phys **31**, 1446 (1992).

[204] R. S. Gi *et al.*, *Hall Effect Measurements of Surface Conductive Layer on Undoped Diamond Films in NO_2 and NH_3 Atmospheres*, Jpn. J. Appl. Phys **38**, 3492 (1999).

[205] R. S. Gi, T. Mizumasa, Y. Akiba, Y. Hirose, T. Kurosu, and M. Iida, *Formation mechanism of p-type surface conductive layer on deposited diamond films*, Jpn. J. Appl. Phys **34**, 5550 (1995).

[206] H. J. Looi, R. B. Jackman, and J. S. Foord, *High carrier mobility in polycrystalline thin film diamond*, Appl. Phys. Lett. **72**, 353 (1998).

[207] H. Umezawa, K. Tsugawa, S. Yamanaka, D. Takeuchi, H. Okushi, and H. Kawarada, *High-Performance Diamond Metal-Semiconductor Field-Effect Transistor with 1 μm Gate Length*, Jpn. J. Appl. Phys **38**, L1222 (1999).

[208] A. Aleksov, A. Denisenko, U. Spitzberg, T. Jenkins, W. Ebert, and E. Kohn, *RF performance of surface channel diamond FETs with sub-micron gate length*, Diamond Relat. Mater. **11**, 382 (2002).

[209] H. J. Looi, L. Y. S. Pang, Y. Wang, M. D. Whitfield, and R. B. Jackman, *High-performance metal-semiconductor field effect transistors from thin-film polycrystalline diamond*, Diamond Relat. Mater. **7**, 565 (1998).

[210] M. Itoh, and H. Kawarada, *Fabrication and Characterization of Metal-Semiconductor Field-Effect Transistor Utilizing Diamond Surface-Conductive Layer*, Jpn. J. Appl. Phys **34**, 4677 (1995).

[211] K. Kitatani *et al.*, *MOSFETs on polished surfaces of polycrystalline diamond*, Diamond Relat. Mater. **8**, 1831 (1999).

[212] K. Tsugawa *et al.*, *High-preformance diamond surface-channel field-effect transistors and their operation mechanism*, Diamond Relat. Mater. **8**, 927 (1999).

[213] J. A. Garrido, A. Hartl, S. Kuch, M. Stutzmann, O. A. Williams, and R. B. Jackmann, *sensors based on hydrogenated diamond surfaces*, Appl. Phys. Lett. **86**, 73504 (2005).

[214] H. Kawarada, *Hydrogen-terminated diamond surfaces and interfaces*, Surf. Sci. Rep. **26**, 205 (1996).

[215] K. Hayashi, S. Yamanaka, H. Okushi, and K. Kajimura, *Study of the effect of hydrogen on transport properties in chemical vapor deposited diamond films by Hall measurements*, Appl. Phys. Lett. **68**, 376 (1996).

[216] A. Bergmaier, G. Dollinger, A. Aleksov, P. Gluche, and E. Kohn, *Deuterium depth profiles at CVD diamond surfaces*, Surf. Sci. **481**, L433 (2001).

[217] K. Kimura, K. Nakajima, S. Yamanaka, M. Hasegawa, and H. Okushi, *Hydrogen depth-profiling in chemical-vapor-deposited diamond films by high-resolution elastic recoil detection*, Appl. Phys. Lett. **78**, 1679 (2001).

[218] J. Shirafuji, and T. Sugino, *Electrical properties of diamond surfaces*, Diamond Relat. Mater. **5**, 706 (1996).

[219] H. Kawarada, H. Sasaki, and A. Sato, *Scanning-tunneling-microscope observation of the homoepitaxial diamond (001)-2×1 reconstruction observed under atmospheric pressure*, Phys. Rev. B **52**, 11351 (1995).

[220] D. Takeuchi, M. Riedel, J. Ristein, and L. Ley, *Surface band bending and surface conductivity of hydrogenated diamond*, Phys. Rev. B **68**, 041304 (2003).

[221] B. Rezek *et al.*, *Fermi level on hydrogen terminated diamond surfaces*, Appl. Phys. Lett. **82**, 2266 (2003).

[222] J. Ristein, *Surface transfer doping of diamond*, J. Phys. D: Appl. Phys. **39**, R71 (2006).

[223] J. S. Foord, C. H. Lau, M. Hiramatsu, R. B. Jackman, C. E. Nebel, and P. Bergonzo, *Influence of the environment on the surface conductivity of chemical vapor deposition diamond*, Diamond Relat. Mater. **11**, 856 (2002).

[224] V. Chakrapani, S. C. Eaton, A. B. Anderson, M. Tabib-Azar, and J. C. Angus, *Studies of Adsorbate-Induced Conductance of Diamond Surfaces*, Electrochem. Solid-State Lett. **8**, E4 (2005).

[225] V. Chakrapani, J. C. Angus, A. B. Anderson, S. D. Wolter, B. R. Stoner, and G. U. Sumanasekera, *Charge Transfer Equilibria Between Diamond and an Aqueous Oxygen Electrochemical Redox Couple*, Science **318**, 1424 (2007).

[226] J. Ristein, F. Maier, M. Riedel, M. Stammer, and L. Ley, *Diamond surface conductivity experiments and photoelectron spectroscopy*, Diamond Relat. Mater. **10**, 416 (2001).

[227] B. F. Mantel, M. Stammler, J. Ristein, and L. Ley, *The correlation between surface conductivity and adsorbate coverage on diamond as studied by infrared spectroscopy*, Diamond Relat. Mater. **10**, 429 (2001).

[228] C. E. Nebel *et al.*, *Hydrogen-induced transport properties of holes in diamond surface layers*, Appl. Phys. Lett. **79**, 4541 (2001).

[229] C. E. Nebel *et al.*, *Low temperature properties of the p-type surface conductivity of diamond*, Diamond Relat. Mater. **11**, 351 (2002).

[230] Y. Zhang, S. Yoshihara, T. Shirakashi, and T. Kyomen, *Electrochemical characteristics of boron-doped, undoped and nitrogen-doped diamond films*, Diamond Relat. Mater. **14**, 213 (2005).

[231] L. Hellner, A. J. Mayne, R. Bernard, and G. Dujardin, *Hydrogenated diamond crystal C (100) conductivity studied by STM*, Diamond Relat. Mater. **14**, 1529 (2005).

[232] J. Ristein, M. Riedel, M. Stammler, B. F. Mantel, and L. Ley, *Surface conductivity of nitrogen-doped diamond*, Diamond Relat. Mater. **11**, 359 (2002).

[233] M. Riedel, J. Ristein, and L. Ley, *Recovery of surface conductivity of H-terminated diamond after thermal annealing in vacuum*, Phys. Rev. B **69**, 125338 (2004).

[234] K. Larsson, and J. Ristein, *Diamond Surface Conductivity under Atmospheric Conditions: Theoretical Approach*, J. Phys. Chem. B **109**, 10304 (2005).

[235] D. Petrini, and K. Larsson, *Electron Transfer from a Diamond (100) Surface to an Atmospheric Water Adlayer: A Quantum Mechanical Study*, J. Phys. Chem. C **111**, 13804 (2007).

[236] D. Petrini, and K. Larsson, *Electron-transfer doping on a (001) surface of diamond: Quantum mechanical study*, J. Phys. Chem. B **109**, 22426 (2005).

[237] A. N. Andriotis, G. Mpourmpakis, E. Richter, and M. Menon, *Surface Conductivity of Hydrogenated Diamond Films*, Phys. Rev. Lett. **100**, 106801 (2008).

[238] L. Gan, E. Baskin, C. Saguy, and R. Kalish, *Quantization of 2D Hole Gas in Conductive Hydrogenated Diamond Surfaces Observed by Electron Field Emission*, Phys. Rev. Lett. **96**, 196808 (2006).

[239] J. A. Dean, *Lange's Handbook of Chemistry* (Mcgraw-Hill, New York, 1999).

[240] J. Ristein, *Surface transfer doping of semiconductors*, Science **313**, 1057 (2006).

[241] D.-C. Qi *et al.*, *Surface Transfer Doping of Diamond (100) by Tetrafluoro-tetracyanoquinodimethane*, J. Am. Chem. Soc. **129**, 8084 (2007).

[242] S. J. Sque, R. Jones, J. P. Goss, P. R. Briddon, and S. Oberg, *First-principles study of C_{60} and $C_{60}F_{36}$ as transfer dopants for p-type diamond*, J. Phys.: Condens. Matter **17**, L21 (2005).

[243] S. J. Sque, R. Jones, S. Öberg, and P. R. Briddon, *Transfer doping of diamond: Buckminsterfullerene on hydrogenated, hydroxylated, and oxygenated diamond surfaces*, J. Mater. Sci.: Mater. Electron. **17**, 459 (2006).

[244] S. J. Sque, R. Jones, S. Öberg, and P. R. Briddon, *Transfer doping of diamond: The use of C_{60} and $C_{60}F_{36}$ to effect p-type surface conductivity*, Physica B **376**, 268 (2006).

[245] J. P. Goss, B. Hourahine, R. Jones, M. I. Heggie, and P. R. Briddon, *p-type surface doping of diamond: a first-principles study*, J. Phys.: Condens. Matter **13**, 8973 (2001).

[246] J. P. Goss, R. J. Eyre, and P. R. Briddon, *Transfer doping of diamond via 2,3-dichloro-5,6-dicyano-1,4-benzoquinone (DDQ)*, phys. stat. sol. (a) **204**, 2903 (2007).

[247] P. Strobel, M. Riedel, J. Ristein, and L. Ley, *Surface transfer doping of diamond*, Nature **430**, 439 (2004).

[248] P. Strobel, M. Riedel, J. Ristein, L. Ley, and O. Boltalina, *Surface transfer doping of diamond by fullerene*, Diamond Relat. Mater. **14**, 451 (2005).

[249] P. Strobel, J. Ristein, L. Ley, K. Seppelt, I. V. Goldt, and O. Boltalina, *Surface conductivity induced by fullerenes on diamond: Passivation and thermal stability*, Diamond Relat. Mater. **15**, 720 (2006).

[250] N. Sato, K. Seki, and H. Inokuchi, *Polarization energies of organic solids determined by ultraviolet photoelectron spectroscopy*, J. Chem. Soc., Faraday Trans. 2 **77**, 1621 (1981).

[251] M. Knupfer, *Electronic properties of carbon nanostructures*, Surf. Sci. Rep. **42**, 1 (2001).

[252] O. Gunnarsson, *Jahn-Teller effect and on-site interaction for C_{60}^{n-}*, Phys. Rev. B **51**, 3493 (1995).

[253] W. R. Salaneck, R. H. Friend, and J. L. Brédas, *Electronic structure of conjugated polymers: consequences of electron-lattice coupling*, Physics Reports **319**, 231 (1999).

[254] N. Koch, *Energy levels at interfaces between metals and conjugated organic molecules*, J. Phys.: Condens. Matter, 184008 (2008).

[255] K. Walzer, B. Maennig, M. Pfeiffer, and K. Leo, *Highly Efficient Organic Devices Based on Electrically Doped Transport Layers*, Chem. Rev. **107**, 1233 (2007).

[256] W. Y. Gao, and A. Kahn, *Controlled p doping of the hole-transport molecular material N,N '-diphenyl-N,N '-bis(1-naphthyl)-1,1(')-biphenyl-4,4 '-diamine with tetrafluorotetracyanoquinodimethane*, J. Appl. Phys. **94**, 359 (2003).

[257] W. Y. Gao, and A. Kahn, *Electronic structure and current injection in zinc phthalocyanine doped with tetrafluorotetracyanoquinodimethane: Interface versus bulk effects*, Org. Electron. **3**, 53 (2002).

[258] X. Zhou *et al.*, *Very-low-operating-voltage organic light-emitting diodes using a p-doped amorphous hole injection layer*, Appl. Phys. Lett. **78**, 410 (2001).

[259] J. Blochwitz, M. Pfeiffer, T. Fritz, and K. Leo, *Low voltage organic light emitting diodes featuring doped phthalocyanine as hole transport material*, Appl. Phys. Lett. **73**, 729 (1998).

[260] M. Pfeiffer *et al.*, *Doped organic semiconductors: Physics and application in light emitting diodes*, Org. Electron. **4**, 89 (2003).

[261] N. Koch, S. Duhm, J. P. Rabe, A. Vollmer, and R. L. Johnson, *Optimized hole injection with strong electron acceptors at organic-metal interfaces*, Phys. Rev. Lett. **95**, 4 (2005).

[262] J. M. Lindquist, and J. C. Hemminger, *High-resolution core level photoelectron spectra of solid TCNQ: determination of molecular orbital spatial distribution from localized shake-up features*, J. Phys. Chem. **92**, 1394 (1988).

[263] C. Rojas, J. Caro, M. Grioni, and J. Fraxedas, *Surface characterization of metallic molecular organic thin films: tetrathiafulvalene tetracyanoquinodimethane*, Surf. Sci. **482**, 546 (2001).

[264] H. T. Jonkman, G. A. Van der Velde, and W. C. Nieuwpoort, *Ab initio SCF MO calculation of ionisation energies and charge distributions of TCNQ and its mono-and divalent anions*, Chem. Phys. Lett. **25**, 62 (1974).

[265] J. Giergiel, S. Wells, T. A. Land, and J. C. Hemminger, *Growth and chemistry of TCNQ films on nickel (111)*, Surf. Sci. **255**, 31 (1991).

[266] J. Fraxedas, J. Caro, A. Figueras, P. Gorostiza, and F. Sanz, *Surface characterization of thin films of tetrathiofulvalene 7,7,8,8-tetracyano-p-quinodimethane evaporated on NaCl(001)*, J. Vac. Sci. Technol., A **16**, 2517 (1998).

[267] W. D. Grobman, R. A. Pollak, D. E. Eastman, E. T. Maas, and B. A. Scott, *Valence Electronic Structure and Charge Transfer in Tetrathiofulvalinium Tetracyanoquinodimethane (TTF-TCNQ) from Photoemission Spectroscopy*, Phys. Rev. Lett. **32**, 534 (1974).

[268] G. Nansé, E. Papirer, P. Fioux, F. Moguet, and A. Tressaud, *Fluorination of carbon blacks: An X-ray photoelectron spectroscopy study: I. A literature review of XPS studies of fluorinated carbons. XPS investigation of some reference compounds*, Carbon **35**, 175 (1997).

[269] S. Braun, and W. R. Salaneck, *Fermi level pinning at interfaces with tetrafluorotetracyanoquinodimethane (F4-TCNQ): The role of integer charge transfer states*, Chem. Phys. Lett. **438**, 259 (2007).

[270] L. Romaner *et al.*, *Impact of Bidirectional Charge Transfer and Molecular Distortions on the Electronic Structure of a Metal-Organic Interface*, Phys. Rev. Lett. **99**, 256801 (2007).

[271] B. Milián, R. Pou-Amérigo, R. Viruela, and E. Ort, *On the electron affinity of TCNQ*, Chem. Phys. Lett. **391**, 148 (2004).

[272] R. J. Murdey, and W. R. Salaneck, *Charge Injection Barrier Heights Across Multilayer Organic Thin Films*, Jpn. J. Appl. Phys. **44**, 3751 (2005).

[273] C. J. Brabec, N. S. Sariciftci, and J. C. Hummelen, *Plastic solar cells*, Adv. Funct. Mater. **11**, 15 (2001).

[274] S. H. Yang, C. L. Pettiette, J. Conceicao, O. Cheshnovsky, and R. E. Smalley, *Ups of buckminsterfullerene and other large clusters of carbon*, Chem. Phys. Lett. **139**, 233 (1987).

[275] O. V. Molodtsova, and M. Knupfer, *Electronic properties of the organic semiconductor interfaces CuPc/C_{60} and C_{60}/CuPc*, J. Appl. Phys. **99**, 053704 (2006).

[276] J. H. Weaver *et al.*, *Electronic structure of solid C_{60}: Experiment and theory*, Phys. Rev. Lett. **66**, 1741 (1991).

[277] S. Saito, and A. Oshiyama, *Cohesive mechanism and energy bands of solid C_{60}*, Phys. Rev. Lett. **66**, 2637 (1991).

[278] T. Birendra Singh *et al.*, *Characterization of highly crystalline C_{60} thin films and their field-effect mobility*, phys. stat. sol. (a) **244**, 3845 (2007).

[279] A. R. Brown, D. M. de Leeuw, E. J. Lous, and E. E. Havinga, *Organic n-type field-effect transistor*, Synth. Met. **66**, 257 (1994).

[280] P. J. Benning *et al.*, *C_{60} and C_{70} fullerenes and potassium fullerides*, Phys. Rev. B **45**, 6899 (1992).

[281] R. W. Lof, M. A. van Veenendaal, B. Koopmans, H. T. Jonkman, and G. A. Sawatzky, *Band gap, excitons, and Coulomb interaction in solid C_{60}*, Phys. Rev. Lett. **68**, 3924 (1992).

[282] L. G. Bulusheva, A. V. Okotrub, and O. V. Boltalina, *Electronic Structure of the Fluorinated Fullerene $C_{60}F_{48}$*, J. Phys. Chem. A **103**, 9921 (1999).

[283] R. Mitsumoto *et al.*, *Electronic Structures and Chemical Bonding of Fluorinated Fullerenes Studied by NEXAFS, UPS, and Vacuum-UV Absorption Spectroscopies*, J. Phys. Chem. A **102**, 552 (1998).

[284] R. Taylor, *Why fluorinate fullerenes?*, J. Fluorine Chem. **125**, 359 (2004).

[285] C. Jin *et al.*, *Attachment of Two Electrons to $C_{60}F_{48}$: Coulomb Barriers in Doubly Charged Anions*, Phys. Rev. Lett. **73**, 2821 (1994).

[286] H. Steger, U. Mische, W. Kamke, A. Ding, M. Fieber-Erdmann, and T. Drewello, *Ionisation and fragmentation dynamics of highly fluorinated fullerenes $C_{60}F_{46,\ 48}$ and $C_{70}F_{54,\ 56}$ after excitation with synchrotron radiation*, Chem. Phys. Lett. **276**, 39 (1997).

[287] R. L. Hettich, R. N. Compton, and R. H. Ritchie, *Doubly charged negative ions of carbon-60*, Phys. Rev. Lett. **67**, 1242 (1991).

[288] W. Erley, and H. Ibach, *Vibrational spectra of tetracyanoquinodimethane (TCNQ) adsorbed on the Cu(111) surface*, Surf. Sci. **178**, 565 (1986).

[289] R. E. Long, R. A. Sparks, and K. N. Trueblood, *The crystal and molecular structure of 7,7,8,8-tetracyanoquinodimethane*, Acta Crystallographica **18**, 932 (1965).

[290] W. Chen, S. Chen, D.-C. Qi, X. Y. Gao, and A. T. S. Wee, *Surface Transfer p-Type Doping of Epitaxial Graphene*, J. Am. Chem. Soc. **129**, 10418 (2007).

[291] W. Chen, X. Y. Gao, D.-C. Qi, S. Chen, Z. K. Chen, and A. T. S. Wee, *Surface-Transfer Doping of Organic Semiconductors Using Functionalized Self-Assembled Monolayers*, Adv. Funct. Mater. **17**, 1339 (2007).

[292] H. Habuchi, S. Nitta, D. Han, and S. Nonomura, *Localized electronic states related to O_2 intercalation and photoirradiation on C_{60} films and C_{70} films*, J. Appl. Phys. **87**, 8580 (2000).

[293] P. Strobel, J. Ristein, and L. Ley, *Controlled hydroxylation of diamond for covalent attachment of fullerene molecules*, Diamond Relat. Mater. **17**, 1362 (2008).

[294] C. K. Chan, A. Kahn, Q. Zhang, S. Barlow, and S. R. Marder, *Incorporation of cobaltocene as an n-dopant in organic molecular films*, J. Appl. Phys. **102**, 014906 (2007).

[295] C. K. Chan, F. Amy, Q. Zhang, S. Barlow, S. Marder, and A. Kahn, *N-type doping of an electron-transport material by controlled gas-phase incorporation of cobaltocene*, Chem. Phys. Lett. **431**, 67 (2006).

[296] C. K. Chan, E.-G. Kim, J.-L. Brédas, and A. Kahn, *Molecular n-Type Doping of 1,4,5,8-Naphthalene Tetracarboxylic Dianhydride by Pyronin B Studied Using Direct and Inverse Photoelectron Spectroscopies*, Adv. Funct. Mater. **16**, 831 (2006).